N°d'ordre NNT : 2024ISAL0012

THESE de DOCTORAT DE L'UNIVERSITE DE LYON
Opérée au sein de
L'Institut National des Sciences Appliquées de Lyon

Ecole Doctorale N° ED162 : MEGA
Mécanique, Energétique, Génie Civil et Acoustique

Spécialité/ discipline de doctorat :

Mécanique-Génie Mécanique

Soutenue publiquement le 26/01/2024, par :
Amakoe K. AHYEE

Experimental and numerical study of the impact of the microstructure on the damage of shaft line bearings under indentation

---

Devant le jury composé de :

RICHARD Caroline	Professeur (Université de Tours)	Présidente
LEBON Frederic	Professeur (Université Aix-Marseille)	Rapporteur
KONDO Djimedo	Professeur (Sorbonne Université)	Rapporteur
NELIAS Daniel	Professeur (INSA Lyon)	Directeur de thèse
CHAISE Thibaut	Maître de Conférences (INSA Lyon)	Co-encadrant
DUVAL Arnaud	Ingénieur de Recherches-CNRS (INSA Lyon)	Invité
DETERRE Geoffray	Expert Roulements (Safran Aircraft Engines)	Invité
SERRES Baptistes	Ingénieur Roulement (Safran Aircraft Engines)	Invité

Département FEDORA – INSA Lyon - Ecoles Doctorales

SIGLE	ECOLE DOCTORALE	NOM ET COORDONNEES DU RESPONSABLE
ED 206 **CHIMIE**	**CHIMIE DE LYON** https://www.edchimie-lyon.fr Sec. : Renée EL MELHEM Bât. Blaise PASCAL, 3e étage secretariat@edchimie-lyon.fr	**M. Stéphane DANIELE** C2P2-CPE LYON-UMR 5265 Bâtiment F308, BP 2077 43 Boulevard du 11 novembre 1918 69616 Villeurbanne directeur@edchimie-lyon.fr
ED 341 **E2M2**	**ÉVOLUTION, ÉCOSYSTÈME, MICROBIOLOGIE, MODÉLISATION** http://e2m2.universite-lyon.fr Sec. : Bénédicte LANZA Bât. Atrium, UCB Lyon 1 Tél : 04.72.44.83.62 secretariat.e2m2@univ-lyon1.fr	**Mme Sandrine CHARLES** Université Claude Bernard Lyon 1 UFR Biosciences Bâtiment Mendel 43, boulevard du 11 Novembre 1918 69622 Villeurbanne CEDEX e2m2.codir@listes.univ-lyon1.fr
ED 205 **EDISS**	**INTERDISCIPLINAIRE SCIENCES-SANTÉ** http://ediss.universite-lyon.fr Sec. : Bénédicte LANZA Bât. Atrium, UCB Lyon 1 Tél : 04.72.44.83.62 secretariat.ediss@univ-lyon1.fr	**Mme Sylvie RICARD-BLUM** Laboratoire ICBMS - UMR 5246 CNRS - Université Lyon 1 Bâtiment Raulin - 2ème étage Nord 43 Boulevard du 11 novembre 1918 69622 Villeurbanne Cedex Tél : +33(0)4 72 44 82 32 sylvie.ricard-blum@univ-lyon1.fr
ED 34 **EDML**	**MATÉRIAUX DE LYON** http://ed34.universite-lyon.fr Sec. : Yann DE ORDENANA Tél : 04.72.18.62.44 yann.de-ordenana@ec-lyon.fr	**M. Stéphane BENAYOUN** Ecole Centrale de Lyon Laboratoire LTDS 36 avenue Guy de Collongue 69134 Ecully CEDEX Tél : 04.72.18.64.37 stephane.benayoun@ec-lyon.fr
ED 160 **EEA**	**ÉLECTRONIQUE, ÉLECTROTECHNIQUE, AUTOMATIQUE** https://edeea.universite-lyon.fr Sec. : Philomène TRECOURT Bâtiment Direction INSA Lyon Tél : 04.72.43.71.70 secretariat.edeea@insa-lyon.fr	**M. Philippe DELACHARTRE** INSA LYON Laboratoire CREATIS Bâtiment Blaise Pascal, 7 avenue Jean Capelle 69621 Villeurbanne CEDEX Tél : 04.72.43.88.63 philippe.delachartre@insa-lyon.fr
ED 512 **INFOMATHS**	**INFORMATIQUE ET MATHÉMATIQUES** http://edinfomaths.universite-lyon.fr Sec. : Renée EL MELHEM Bât. Blaise PASCAL, 3e étage Tél : 04.72.43.80.46 infomaths@univ-lyon1.fr	**M. Hamamache KHEDDOUCI** Université Claude Bernard Lyon 1 Bât. Nautibus 43, Boulevard du 11 novembre 1918 69 622 Villeurbanne Cedex France Tél : 04.72.44.83.69 direction.infomaths@listes.univ-lyon1.fr
ED 162 **MEGA**	**MÉCANIQUE, ÉNERGÉTIQUE, GÉNIE CIVIL, ACOUSTIQUE** http://edmega.universite-lyon.fr Sec. : Philomène TRECOURT Tél : 04.72.43.71.70 Bâtiment Direction INSA Lyon mega@insa-lyon.fr	**M. Jocelyn BONJOUR** INSA Lyon Laboratoire CETHIL Bâtiment Sadi-Carnot 9, rue de la Physique 69621 Villeurbanne CEDEX jocelyn.bonjour@insa-lyon.fr
ED 483 **ScSo**	**ScSo[1]** https://edsciencessociales.universite-lyon.fr Sec. : Mélina FAVETON Tél : 04.78.69.77.79 melina.faveton@univ-lyon2.fr	**M. Bruno MILLY** (INSA : J.Y. TOUSSAINT) Univ. Lyon 2 Campus Berges du Rhône 18, quai Claude Bernard 69365 LYON CEDEX 07 Bureau BEL 319 bruno.milly@univ-lyon2.fr

---

[1] ScSo : Histoire, Géographie, Aménagement, Urbanisme, Archéologie, Science politique, Sociologie, Anthropologie

Acknowledgements

These works result from a collaboration between LaMCoS (INSA Lyon) and Safran Aircraft Engines. First and foremost, I would like to express my deep gratitude to all the members of the jury, whose insightful advice and remarks contributed to improving the quality of this manuscript.

I wish to extend my heartfelt appreciation to my thesis supervisor, Daniel Nélias, for the trust he placed in me throughout this project. My thanks also go to my co-supervisor, Thibaut Chaise, and Arnaud Duval, for their involvement in my work. Despite the considerable autonomy granted to me, their guidance and unwavering support motivated me to successfully complete this thesis.

I would like to express special thanks to Sylvain Dancette for his invaluable assistance in setting up the nanoindentation tests at Mateis. My gratitude also extends to all the staff at Safran involved directly or indirectly in these works, particularly to Geoffray Deterrre, Baptiste Serres, and Espoir Koumi, for allowing me to work on an exciting topic for three years. A special thank to Baptise Serres for his operational supervision, and to Espoir Koumi for project setup and varied advice.

These works owe a great deal to Geoffray Deterre, whose expertise and technical knowledge led to many discussions and suggestions that were always pertinent and enriching.
I would like to warmly thank both the former and current PhD'students of the laboratory, as well as staff from other teams with whom I had the opportunity to exchange ideas in practical work or conferences.

A huge thank you to Efoe,Karine, Alexis, Victor, Martinien, Arif, Hussein, Julie, Adrien, Victor, Pierre, Nicolas, Zineb, Audrey, Loic, Joaquim, Mawuli, Raphael, Yvan, Ethel, Florian for their warm welcome and the valuable moments of exchange we shared. My thanks also go to Isabelle Comby, Sophie Oliveira, Carine Bruscella, and all the laboratory staff.

At the end, I would like to thank my parents for their support. I also express my gratitude to Emerenciel for support and assistance, Medard Ablodevi, Phillipe, Eric, and Soké for their support. As it was said by Isaac Newton, if i have seen further it is by standing on the shoulders of Giants.

Ces travaux résultent d'une collaboration entre le LaMCoS (INSA Lyon) et Safran Aircraft Engines. Tout d'abord, je tiens à exprimer ma profonde gratitude envers tous les membres du jury, dont les conseils et les remarques avisées ont contribué à améliorer la qualité de ce manuscrit.

Je souhaite adresser toute ma reconnaissance à mon directeur de thèse, Daniel Nélias, pour la confiance qu'il m'a accordée tout au long de ce projet. Mes remerciements vont également à mon co-encadrant, Thibaut Chaise, ainsi qu'à Arnaud Duval, pour leur implication dans mes travaux. Malgré la grande autonomie qui m'a été confiée, leurs conseils et leur soutien constant m'ont motivé à mener à bien cette thèse.

Je tiens à exprimer ma gratitude particulière à Sylvain Dancette pour son aide précieuse lors de la mise en place des essais de nanoindentation au Mateis. Mes remerciements s'adressent également à tout le personnel de Safran impliqué de près ou de loin dans mes travaux, notamment à Geoffray Deterrre, Baptiste Serres et Espoir Koumi, pour m'avoir permis de travailler sur un sujet passionnant pendant trois années. Un merci spécial à Baptise Serres pour le suivi opérationnel et son implication, et à Espoir Koumi pour le montage du projet et ses conseils variés.

Ces travaux doivent beaucoup à Geoffray Deterre, dont l'expertise et les connaissances techniques ont donné lieu à de nombreuses discussions et orientations toujours pertinentes et enrichissantes.

Je tiens ensuite à remercier chaleureusement les anciens et les nouveaux doctorants du laboratoire. Un immense merci à Efoe, Karine, Alexis, Victor, Martinien, Arif, Hussein, Julie, Adrien, Victor, Pierre, Nicolas, Zineb, Audrey, Loic, Joaquim, Mawuli, Raphael, Yvan, Ethel,Florian pour leur accueil chaleureux et les précieux moments d'échange que nous avons partagés. Mes remerciements vont également à Isabelle Comby, Sophie Oliveira, Carine Bruscella et à tout le personnel du laboratoire. Je n'oublie pas non plus les personnes des autres équipes avec qui j'ai eu la chance d'échanger lors des TD, TP ou de conférences.

Pour finir, je tiens à remercier mes parents pour leur soutien. Je remercie aussi Emerenciel pour le soutien et le support, Medard Ablodevi, Phillipe, Eric et Soké pour leur soutien. Comme l'a dit Isaac Newton, j'ai vu plus loin car j'ai été juché sur les épaules de Géants.

4

Abstract

Surface fatigue is currently the primary cause of bearing failures. This type of fatigue can originate from surface roughness or the presence of contaminants on the surface. Managing lubricant pollution, which leads to surface contamination, is complex and costly, especially as pollution exists in new lubricants, is continuously generated by lubricated systems, and is introduced during maintenance operations. Consequently, lubricants regularly carry particles of various origins into contact areas. When passing between surfaces, these particles are compressed, marking the surfaces and creating defects that become preferred sites for fatigue initiation in subsequent cycles. As surface indentation cannot be entirely prevented, a thorough understanding of indentation and indentation fatigue mechanisms is essential to ensure bearing reliability and reduce maintenance costs. To achieve this, our study is divided into four main parts.

The first part involves the mechanical characterization of bearing materials such as M50, 32CrMoV13, M50NiL, and M50NiLDH after undergoing thermochemical treatments (quenching, carburizing, nitriding, carbonitriding) to enhance surface properties. Nanoindentation tests provided microhardness measurements for different steels, enabling the establishment of monotonic loading behavior laws. Identifying material behavior laws was also carried out for cyclic loadings, revealing the adaptive behavior of steels within bearing solicitation ranges, making the use of an isotropic behavior law very close to observations. Consequently, among the studied steels, M50NiLDH exhibits the highest surface hardness, followed by M50NiL, 32CrMoV13, and M50. Numerical simulations of bearing loading showed that surface properties adequately describe material behaviors for low-volume loads. However, for high-level solicitations (>5 GPa), sub-layer properties become essential, indicating that M50 steel offers better resistance than the other three steels.

To identify sources of overpressures on bearing tracks, a numerical model incorporating free edge effects was developed within a semi-analytical contact resolution tool. This model covers different configurations, including a quarter space with one free edge, two free edges, a corner (eighth space), and four free edges (length-finite space). As a result, free edges increase the amplitude of the maximum Hertz pressure and cause a shift in the pressure field toward the infinite part of the space. Compared to Hertz solutions, free edge effects can induce pressure errors of up to 20% in the case of a length-finite space. However, these effects completely vanish and can be neglected at a distance of $d/a \geq 4$, where a represents the Hertz contact radius.

The indentation process will be replicated in the third part using finite element modeling. For this purpose, the CEL finite element model developed by Bonetto et al. will be modified and adapted to simulate surface indentation. A comprehensive

parametric analysis will be conducted to examine the influence of bearing operational parameters and the properties of the contacting materials on the indentation process. In summary, key parameters significantly impacting the indentation profile include size, nature, shape, orientation, and position of particles, residual stresses, presence of sliding, existence of a critical sliding rate, and bearing material properties. Conversely, the friction coefficient and speed have a moderate effect, while load has a moderately weak effect. To reduce calculation times and establish relationships between identified key parameters, analytical approximations have been developed to describe the evolution of certain parameters, such as the pile-up height or the dent diameter.

Surface fatigue primarily manifests as the emergence of microcracks localized on the side opposite to the friction forces of indentation. This microcrack formation and localization are analysed in the last part of this study. We employ a semi-analytical contact calculation tool to rapidly conduct rolling indentation simulations while considering material plasticity and residual indentation stresses. This study highlights the significance of shear effects in microcrack formation. The modified Dang Van criterion, developed by Bonetto et al., is used to identify crack initiation zones and accurately estimate critical planes. Concerning bearing fatigue, parameters influencing their lifespan include the applied bearing load, sliding, and the height of indentation bulges. Using developed analytical expressions, damage criteria have been proposed based on the lower endurance limit proposed by Jacq et al. In summary, a dent is considered damaged when its average slope exceeds or equals 0.05. The average bead height to reach this threshold is approximately 0.6 μm.

Keywords :

Nanoindentation,Hardening, Edge effect, Bearing, Residual stresses, Fatigue, Endurance limit, CEL, Semi-analytical method, Rolling contact, Analytical

La fatigue de surface est actuellement la principale cause de défaillances des roulements. Ce type de fatigue peut se développer à partir de la rugosité des surfaces ou de la présence de polluants en surface. La gestion de la pollution des lubrifiants, est complexe et coûteuse, d'autant plus que la pollution est présente dans les huiles neuves, générée en continu par les systèmes lubrifiés et s'introduit lors des opérations sur les moteurs. En conséquence, les huiles transportent donc régulièrement des particules de sources diverses vers les zones de contact. Lorsqu'elles passent entre les surfaces, ces particules sont comprimées et marquent les surfaces, créant ainsi des défauts qui deviennent des sites privilégiés pour l'initiation de la fatigue lors des cycles suivants. Puisque l'indentation des surfaces ne peut être évitée, une compréhension précise des mécanismes d'indentation et de fatigue d'indentation est nécessaire pour garantir la fiabilité des roulements et réduire les coûts de maintenance. Pour ce faire, notre étude a été divisée en quatre grandes parties.

La première partie concerne la caractérisation mécanique de matériaux de roulement tels que les aciers M50, le 32CrMoV13, M50NiL et M50NiLDH, ayant subi des traitements thermochimiques (trempe, cémentation, nitruration, carbonitruration) pour améliorer leurs propriétés de surface. Des essais de nanoindentation ont fourni des mesures de microdureté pour différents aciers, permettant d'établir des lois de comportement en charge monotone. L'identification des lois de comportement des matériaux a également été effectuée pour les chargements cycliques, révélant un comportement adaptatif des aciers dans les gammes de sollicitations des roulements, ce qui rend l'utilisation d'une loi de comportement isotrope très proche de l'observation. Il en ressort donc que parmi les aciers étudiés le M50NiLDH présente la meilleure dureté en surface, suivi du M50NiL, du 32CrMoV13 et du M50. Les simulations numériques de chargement des roulements ont montré que pour des charges sollicitant de faibles volumes, les propriétés de surface sont adéquates pour décrire les comportements des matériaux. Cependant, pour des niveaux de sollicitation élevés (>5 GPa), les propriétés en sous-couche deviennent essentielles, indiquant que l'acier M50 offre une meilleure résistance que les trois autres aciers.

Dans le but d'identifier les sources de surpressions sur les pistes de roulement, un modèle numérique intégrant les effets de bords libres a été développé dans un outil semi-analytique de résolution de contact. Ce modèle couvre différentes configurations, comme un quart de massif avec un bord libre, deux bords libres et un coin (un huitième de massif), ainsi que quatre bords libres (massif de dimensions finies). Il en résulte que les bords libres augmentent l'amplitude de la pression maximale de Hertz et provoquent un décalage du champ de pression vers la partie la plus infinie du massif. Face aux solutions de Hertz, les effets de bords libres peuvent induire des erreurs de pression allant jusqu'à 20% dans le cas d'un massif de dimensions finies. Toutefois, ces effets disparaissent complètement et peuvent être négligés à partir d'une distance $d/a > 4$, où a représente le rayon de contact de Hertz.

Dans la troisième partie, le processus d'indentation sera également reproduit par le biais d'une modélisation par éléments finis. Pour cela, le modèle éléments finis CEL développé par Bonetto et al. sera modifié et adapté pour simuler l'indentation en surface. Une analyse paramétrique exhaustive sera menée pour examiner l'influence des paramètres opérationnels du roulement ainsi que des propriétés des matériaux en contact sur le processus d'indentation. En résumé, la taille, la nature, la forme, l'orientation et la position des particules, les contraintes résiduelles, la présence de glissement, l'existence d'un taux de glissement critique et les propriétés des matériaux constituent les parametres clés ayant un impact significatif sur le profil de l'indentation. En revanche, le coefficient de frottement et la vitesse ont un effet modéré, tandis que la charge présente un effet moyennement faible. Afin de réduire les temps de calcul et d'établir des relations entre les paramètres clés identifiés, des approximations analytiques ont été développées, permettant de décrire l'évolution de certains paramètres tels que la hauteur du bourrelet ou le diamètre de l'indent.

La fatigue des surfaces indentées se manifeste principalement par l'émergence de microfissures localisées sur le côté opposé aux forces de frottement de l'indentation. Cette formation de microfissures et leur emplacement font l'objet de la dernière partie de notre étude. Nous employons un outil de calcul de contact semi-analytique pour effectuer rapidement des simulations de roulement sur indent en prenant en compte la plasticité des matériaux et les contraintes résiduelles d'indentation. Cette étude met en évidence l'importance des effets de cisaillement dans la formation des microfissures. Le critère de Dang van modifié, realisé par Bonetto, est utilisé pour localiser les zones d'amorçage des fissures et estimer précisément les plans critiques. En ce qui concerne la fatigue des roulements, les paramètres ayant un impact sur leur durée de vie sont la charge appliquée au roulement, le glissement et la hauteur des bourrelets d'indentation. A l'aide d'expressions analytiques développées, des critères d'endommagement ont été suggérés en se basant sur la limite d'endurance inférieure proposée par Jacq et al. En résumé, un indent est considéré comme endommageant lorsque sa pente moyenne est supérieure ou égale à 0,05. La taille moyenne du bourrelet pour atteindre ce seuil est d'environ 0,6 μm.

Mots-clés: Nanoindentation, Ecrouissage, Effet de bords, Roulement, Contraintes résiduelles, Fatigue, Limite d'endurance, CEL, Méthode semi-analytique, Contact roulant, Analytique

Contents

Contents

Contents

List of Figures

14

18

List of Tables

Nomenclature

Latin Letters

$[B,C,n]$ Swift isotropic constitutive law parameters

$[C,\gamma,Q_{inf},b]$ Chaboche combined constitutive law parameters

δ Rigid normal body displacement

μ Friction coefficient

ϕ_0,ϕ_p Reference size, particle size

ϕ_{dent} Dent diameter

ψ_i Corrective factors, $i=1,2$

σ_0 Yield strength

$\sigma_i(x,y)$ Component $i=1,2,3$ of stress tensor

$\sigma_x eq(x,y)$ Corrected tensile stress $\sigma_x x(x,y)$

$\tilde{}$ Fourier transform

a Elastic contact radius

A_c Contact area

b_0,b Reference contact half width, contact half width

d/a Normalize distance from the free edge of the quarter space

d_x/a Normalize distance from the free edge of the finite lenght space respect to x axis

d_y/a Normalize distance from the free edge of the finite lenght space resspect to y axis

E^* Equivalent modulus

E_1, E_2, E_3 modulus of contact materials 1,2,3

$F(p)$ Minimization founction in CGM algorithm

$g(x,y)$ Surface separation at time t

H, HV Micro-hardness

$h_0(x,y)$ initial bodies separation

H_1 Endurance limit of indented contact

h_d Dent's height

h_{min} represents the minimum oil film thickness

K_m, K_s Stiffness of machine and sample

L_x/a Normalize lenght of the finite lenght space respect to x axis

L_y/a Normalize lenght of the finite lenght space respect to y axis

mu Friction coefficient

N Discretization number

P, F_N Normal Applied load

$p(x,y)$ Contact pressure field

P_0 Hertz pressure of the homogeneous half-space

P_{moy} Mean pressure

R Sphere radius

R_a, R_{ms} represent the arithmetic and root mean square roughness values

R_d radius of the dent

s_m, s mean slope and slope of the pile-up

SRR Slide-to-roll ratio

U, v velocity of rolling contact elements

$u_i(x,y)$ Component $i = 1, 2, 3$ of displacement vector

General introduction

0.1 Bearings in aircraft engines: Presentation

In the aeronautics sector, Safran is taking a proactive approach to meet the climate challenge and contribute to the transition to carbon-neutral aviation by 2050. As a significant supplier of aeronautical equipment, Safran is committed to reducing emissions of CO_2 linked to its manufacturing processes and throughout its value chain. Optimizing the efficiency of bearings is one of the critical ways Safran works to reduce emissions. Bearings are crucial components in various applications, including engines, landing gear, air conditioning systems and others. By optimizing the design and performance of bearings, Safran can reduce friction and improve energy efficiency, thereby reducing emissions.

The aircraft engine (see cut view in Fig.1) is a critical component that continually undergoes improvements to address concerns such as fuel consumption, pollution, noise, and weight while enhancing reliability and performance. Among the key elements that can be optimized to achieve these objectives are the bearings. The fascinating history of rolling systems and their integral role in modern machinery is captivating to explore. In ancient Egypt, the innovative use of wooden logs to transport heavy objects showcased human ingenuity and adaptability. A significant advancement came with Leonardo da Vinci's discovery of combining a wheel with the log system to create the ball bearing, revolutionizing the efficiency and performance of various machines.

At the core of a bearing are the inner (3) and outer rings (4), which form the primary structural elements. The inner ring is equipped with a raceway (5), while the outer ring complements it. Between these rings, rolling elements (1) such as balls, rollers, or needles are incorporated to establish a low-friction interface as shown in Fig.2. This allows smooth movement between the rings. To ensure the rolling elements remain evenly spaced and prevent collisions during operation, metal or plastic cages(2) are used.

As a result of these design elements, the rolling elements can effortlessly travel along the tracks on the inner and outer rings, enabling seamless and efficient rotation. This has significantly transformed the way heavy loads are moved and facilitated the creation of larger and more intricate structures and machinery. The development of rolling systems and bearings has played a vital role in advancing technology and

28

expanding the possibilities of various industries.

Bearings are crucial in various industrial and mechanical applications by minimizing friction and enabling smooth and consistent rotation between two moving parts. The presence of rolling bodies, such as balls, rollers, or needles, helps reduce friction against a stationary surface, resulting in a more efficient transfer of loads.

The cage, also known as the separator, has the important function of maintaining a uniform distribution of the rolling bodies and preventing contact between them. This ensures optimal performance and longevity of the bearing. The inner and outer rings serve as the surfaces on which the rolling elements roll, enabling the desired rotational motion.

Bearings can be categorized based on their geometry, load-bearing capacity, rotational speed, precision, and other factors. Common examples of bearing types include ball bearings, tapered roller bearings, cylindrical roller bearings, and needle roller bearings. Each type is designed to meet specific application requirements.

When selecting a bearing for a particular application, it is crucial to consider factors such as load requirements, rotational speed, accuracy, expected lifespan, and maintenance needs. Proper bearing selection and installation are essential to prevent issues like premature system failure, excessive wear, or reduced performance. Careful consideration of these factors ensures optimal functioning and reliability of the bearing within the intended system.
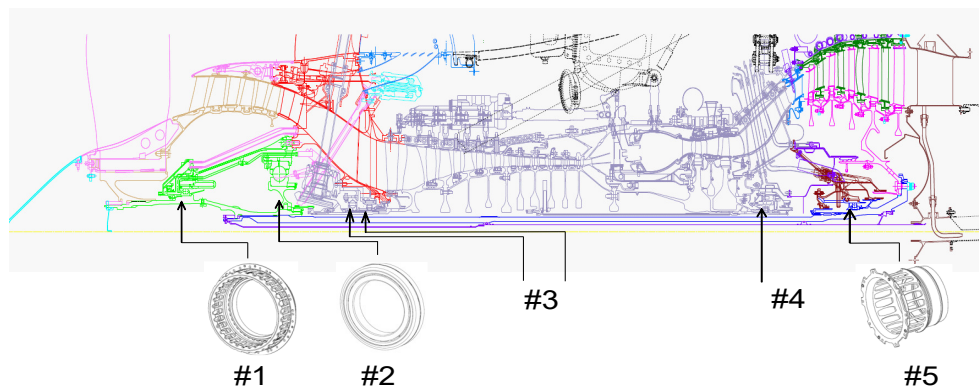
Figure 1: SAE LEAP engine presentation.

When considering the aircraft engine as illustrated in the Fig.1, five main bearings can be identified:

0.1.1 The rolling bearing 1

Located in front of the engine, bearing 1 is the largest of the five bearings and is designed to support the low-pressure shaft, whose inner ring rotates at the speed of the low-pressure shaft. This roller bearing is designed to withstand radial loads
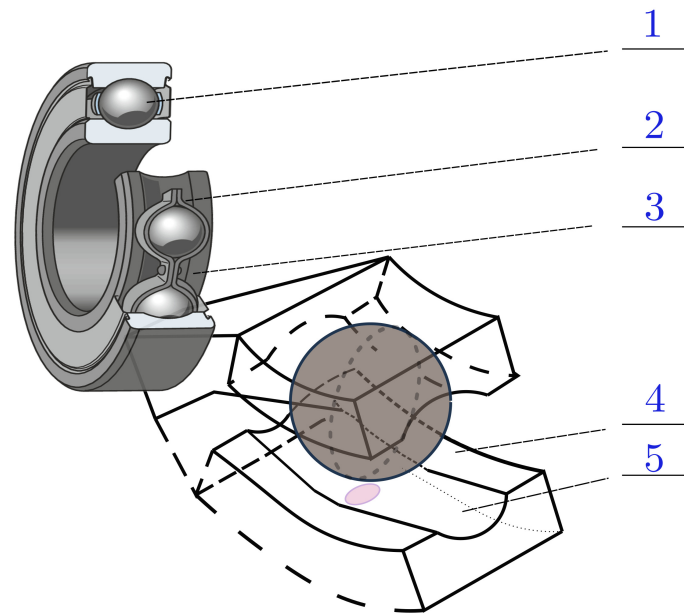
Figure 2: Ball bearing elements presentation

resulting from residual unbalance stress and engine thrust. Given the size and location of this bearing, it must be able to withstand significant loads and stresses while maintaining high levels of reliability and safety.

0.1.2 The rolling bearings 2

Bearings 2 are ball bearing. It is linked to the rotating low-pressure shaft by its inner ring. Bearing 2 is located at the front of the engine and is designed to support the low-pressure compressor rotor while bearing 5 is located at the rear of the engine and is designed to support the low-pressure turbine rotor. This bearings can withstand high axial loads resulting from the weight and rotational speed of the rotors. It is also designed to reduce friction and energy loss to improve the engine's efficiency.

0.1.3   The rolling bearing 3

A duplex bearing combines two or more types of bearings, typically a ball bearing and a roller bearing. In the case of rolling bearing 3, a duplex bearing supports the high-pressure shaft with a pair of twin bearings. This means that two bearings are mounted on the same shaft and designed to work together to increase load capacity and reliability. The ball bearing part of the duplex bearing is used to support the axial load, while the roller bearing part is used to support the radial load. This configuration allows for high load capacity and increased stiffness while maintaining a compact design. Duplex bearings are common in high-speed and high-load applications, such as aeronautics, where reliability and performance are critical.

0.1.4   The rolling bearing 4 and 5

Located towards the rear of the engine, bearing 4 is an intershaft roller bearing with the particularity of having two movable rings. Depending on the application, the rings can be co-rotating or counter-rotating. In the case of the CFM56 and Leap engines, the bearing rings are co-rotating, which means that they rotate in the same direction but at different speeds. The inner ring rotates at the speed of the low-pressure shaft, while the outer ring rotates at the speed of the high-pressure shaft. This configuration allows the bearing to support the radial loads generated by the high-pressure turbine while accommodating the differential rotational speeds between the low and high-pressure shafts. In addition, using roller bearings in this application allows for high load capacity and increased stiffness, which are essential for ensuring the reliability and safety of the engine. While bearing 5 is also located at the rear of the engine and is a roller bearing designed to support the low-pressure turbine rotor. These bearings can withstand high radial loads and rotational speed of the rotors. They allow to link stator part of the engine to the rotor parts.

0.2   Motivations and objectives

Bearing fatigue is the most critical source of bearing damage, and it typically occurs after a long process of wear and degradation of the elements. However, overload or poor assembly can also lead to premature bearing failure. The wear that results from the loading cycles can be caused by several factors, such as dry metal-metal contact, roughness on the surface of the bearings, and debris that can mark the tracks. While some of these causes can be mitigated through improvements in lubrication and material science, debris-induced wear remains a challenging problem to address.

Despite the improvements in lubrication techniques and bearing materials, the presence of debris in the bearing remains a primary source of damage. Crushing debris particles in the bearing contact can cause significant damage to the bearing elements and reduce their lifespan. Therefore, it is essential to monitor and control

the presence of debris in the bearing system to minimize the risk of damage. To better understand and prevent bearing damage caused by particle entrapment and crushing, it is important to study how particles become trapped and crushed within the bearing contact area and the resulting surface damage. This can involve analyzing the type and size of particles, the loading conditions, the geometry and material properties of the bearing and its components, and the lubrication and environmental conditions. By gaining a deeper understanding of these factors, engineers can work to develop better lubrication and maintenance strategies, as well as more advanced bearing designs and materials that are less susceptible to particle-induced damage.

0.3   Bearing damage

Bearing damage can occur for various reasons, such as wear, corrosion, overheating, contamination, improper lubrication, misalignment, overload, fatigue, etc. Some common types of bearing damage are:

0.3.0.1   Corrosion

Corrosion is the gradual deterioration of the bearing surface due to chemical reactions between the surface and the environment. It can be caused by moisture, acid, or other corrosive substances. The corrosion of a bearing manifests itself by pitting on the surface of the rolling elements or rings or on all the surfaces of the bearing.

0.3.0.2   Overheating

Overheating can cause the bearing to expand, resulting in loss of clearance and, eventually, bearing failure. It can be caused by excessive friction due to lack of lubrication, improper lubricant viscosity, or high operating temperatures.

0.3.0.3   Fatigue

Fatigue failure occurs due to repeated loading and unloading of the bearing. Cyclic stresses, improper bearing design, or overloading can cause it.

0.3.0.4   Contamination

Contamination occurs when foreign particles enter the bearing and damage the bearing surface. It can be caused by dust, dirt, water, or other contaminants.

0.3.0.5   Misalignment

Misalignment can cause excessive stress on the bearing and result in premature failure. It can be caused by improper installation, mounting, or shaft alignment.

0.3.0.6 Wear

Wear occurs due to the gradual material loss from the bearing surface. It can be caused by metal-to-metal contact, lack of lubrication, or abrasive particles in the lubricant.

0.4 Industrial issue

The presence of debris, such as dirt, metal chips, carbides, or other foreign particles, within a bearing, can introduce additional stresses on its surface, increasing the risk of rolling contact fatigue. This can lead to accelerated wear and damage. Furthermore, as the debris moves around within the bearing, it can create localized stress concentrations, further compromising the bearing's integrity. To prevent rolling contact fatigue in the presence of debris, it is firstly crucial to employ appropriate lubrication and sealing techniques. Adequate lubrication forms a protective film that reduces friction and wear between the rolling elements and the bearing surfaces. It also helps to flush out debris and contaminants, minimizing their detrimental effects. Effective sealing mechanisms play a vital role in preventing the entry of foreign particles into the bearing, thereby reducing the potential damage caused by debris.

Surface damage in bearings primarily occurs due to defects and debris that pass through the contact between the rolling elements and the rings. These factors exacerbate surface deterioration. This issue is complex and involves several parameters that are crucial to understand. Some of these parameters include:

1. Material properties optimization:
   Understanding the material properties of the rolling elements and optimizing them is essential. Factors such as hardness, fatigue resistance, and wear characteristics play a significant role in determining the bearing's ability to withstand damage.

2. Material behavior under repeated loading:
   When the rolling elements repeatedly pass through the contact area, plastic deformation can occur in the bearing material. Understanding the material's behavior under such conditions is crucial for predicting and mitigating surface damage.

3. Free edge and contact zone truncation problems:
   Problems related to edge effects and the truncation of the contact zone can arise when the rolling elements exceed the track. These effects can impact the distribution of stresses and increase the likelihood of surface damage.

4. Particle crushing process:
   Understanding the particle crushing process is important to put in place solutions to avoid it. Identifying the key parameters that govern this process can help design strategies to minimize particle-induced damage.

By comprehending these parameters and their interactions, engineers can gain insights into the complex mechanisms involved in bearing surface damage and improved bearing reliability and durability.

This why this study is carried out in collaboration with Safran Aircraft Engine (SAE) bearing team (IHENR). Consequently, the structure of this thesis study is:

1. In chapter one, we summarized the knowledge already acquired on the subject in order to define a new direction for the study.

2. Chapter two presents the characterization of bearing steels M50, 32CrMoV13, M50NiL and M50NiLDH which undergo thermo-chemical or heat treatments. Nanoindentation tests and reverse analysis techniques are employed for this characterization.

3. In the chapter three, material hardening analyses are conducted to identify first the material responses under cyclic indentation loading and the parameters for the material's elastic-plastic constitutive law.

4. Chapter four is focused in the analytical and numerical developpment to simulate the quarter space and the two-joined spaces problems.

5. Building upon the previous chapter, chapter five extends the analytical and numerical developpement on the quarter space problem to the case of the Eighth space and the finite space model.

6. A finite element modeling is used in this chapter six to simulate the particle crushing process within the contact. Key parameters influencing the dent profile are identified, and analytical approximations are developed to quickly calculate these parameters. These approximations are then used in a Monte-Carlo analysis to determine the distribution of dent diameter and pile-up height based on collected data.

7. This chapter seven focuses on the passage of rolling elements over dents and determines the critical pile-up based on the time-life model.

Chapter 1

Bibliography

In this chapter, a comprehensive overview of the study is presented, including a review of the current state of the art in the field. The chapter begins by providing a brief reminder of the various damage modes that can occur in bearings, highlighting the significance of surface damage mechanisms in rolling fatigue with indentation. Next, the chapter delves into an exploration of different contact fatigue life models. It discusses the existing physical models and their limitations in accurately predicting the life of indented contacts. The focus is on identifying the gaps in the literature and highlighting the need for a more robust and reliable lifetime model for indented contacts. Furthermore, the chapter outlines the resolution plan for the study.

Sommaire

1.1   The bearings

Aeronautical bearings are crucial components used in aircraft and aerospace applications, specifically designed to deliver precise and dependable performance under challenging conditions. These bearings are engineered to withstand high loads, extreme temperatures, high speeds, and vibrations commonly encountered in aviation. They are constructed using high-strength materials like steel, titanium, or ceramic, and their manufacturing processes involve strict adherence to precise tolerances to ensure accurate alignment and seamless operation. Aeronautical bearings (Fig.1.1) find extensive utilization in critical aircraft and aerospace systems, including engines, landing gears, and others.

Figure 1.1: Ball bearing

The friction coefficient plays a crucial role in the performance and efficiency of aircraft bearings during operation. Its impact on the system is significant. A low friction coefficient is highly advantageous as it minimizes energy losses caused by friction, leading to improved overall bearing efficiency. Moreover, a low friction coefficient helps in reducing heat generation during operation, which can prolong the bearing's lifespan and minimize wear.

However, maintaining a balanced friction coefficient is essential. Excessive slip between the rolling elements and the raceway may occur if the friction coefficient is too low. This excessive slip can result in bearing damage and a decrease in its lifespan. Therefore, the friction coefficient should not be excessively low.

Determining the ideal friction coefficient involves considering various factors, including the load on the bearing components, operating speed, lubrication conditions, and material properties. Each bearing application has unique requirements and operational characteristics. Hence, analysis is necessary to determine the optimal friction coefficient for a specific bearing application.

1.2 Bearing lubrication

Bearing lubrication is critical to bearing design and maintenance, particularly in high-speed and high-load applications such as those in the aeronautic industry. Lubrication reduces friction and wear between the bearing surfaces, dissipates heat, and protects the bearing from corrosion and other forms of damage. Several types of lubrication are used in bearings, including hydrodynamic, boundary, and mixed lubrication. There are four distinct lubrication regimes identified in bearing operation:

1. Elastohydrodynamic regime:
   In this regime, the load is transmitted through the lubricant film, and the contact between surfaces is smooth. Asperities may exist on the surface, but their height is so small that the overpressures they generate are negligible.

2. Micro-elastohydrodynamic regime:
   The load is still transmitted through the lubricant film, but the micro-geometry of the surfaces causes significant overstresses. This regime occurs when the asperities on the surface have a noticeable impact on the load distribution.

3. Mixed lubrication regime:
   In this regime, the lubricant film is incomplete, and direct contact between asperities may occur. The load is shared between the lubricant film and the direct contact between surfaces.

4. Limit lubrication regime:
   This regime occurs when the lubricant film thickness is very low, and the load is primarily transmitted through direct contact between asperities. The lubricant film is insufficient to fully separate the surfaces.

The (EHD) lubrication regime relates to the contact between the rings/cage and the rolling element/cage in bearings. In the EHD regime, when the rolling elements make contact with the rings, elastic deformations occur at the contact points. The severity parameter, denoted as $\Lambda = \frac{h_{min}}{R_{ms}}$, is a useful indicator for determining the lubrication regime. It represents the ratio between the minimum height of the elastohydrodynamic film in smooth contact and the quadratic average of the heights of the surface roughness. The transition from the elastohydrodynamic regime to the micro-elastohydrodynamic regime typically occurs when Λ is approximately equal to 1.

The elastohydrodynamic contact in bearings can be divided into three distinct zones:

1. Contact entry zone: This zone is characterized by hydrodynamic lubrication, where the contact pressure increases as the contact elements converge. As the

rolling element enters in contact with the ring, it displaces the lubricant and creates a pressurized area.

2. High-pressure zone: The contact experiences intense pressure in this zone, causing the lubricant to undergo temporary vitreousness. The surfaces in contact undergo elastic deformation due to the high load. This zone is where the lubricant's maximum pressure and significant elastic deformations occur.

3. Outlet zone: As the rolling element exits the contact, the lubricant is pushed out due to the divergence formed by the contact elements. This results in a decrease in oil film thickness at the outlet contact due to the conservation of flow. The lubricant is ejected from the contact in this zone.

The prediction of lubricant thickness in contacts has been a subject of study since the late 1930s to early 1940s. Researchers such as Ertel (ERT 39) and Grubin (GRU 49) used theories such as Hertz's theory for elastic deformation, the Reynolds equation for fluid flow, and Barus' law to describe the piezo viscosity of lubricants. They proposed analytical solutions, albeit approximate, for line contacts such as cylinder/plane contacts. In the 1960s, Higginson and Dowson (DOW 66) introduced the first numerical solutions for elastohydrodynamic problems in cylinder/plane contacts. Later, in the mid-1970s, Hamrock and Dowson (HAM 76; HAM 77) proposed numerical solutions for ellipsoid/plane contacts. These works enable the determination of lubricant thickness in contacts, which typically ranges from a few nanometers to one micron.

1.3   Lubricant pollution

Motor shaft line bearings, commonly used in industrial machinery, are susceptible to contamination from various sources, including external pollutants, wear particles, and lubricant contaminants. These contaminants can deteriorate the lubrication conditions, ultimately impacting the machinery's performance and reliability. External contamination can originate from dust, dirt, moisture, or environmental chemicals. Wear particles are generated by the rubbing surfaces of the machinery components. Additionally, the lubricant can undergo chemical or thermal breakdown, resulting in the formation of acidic compounds, sludge, varnish, and other contaminants. The type and source of contamination determine the nature of pollutants. Solid contaminants, like dirt and wear particles, can cause surface abrasive wear. Liquid contaminants, such as water and acids, contribute to the corrosion and chemical degradation of the lubricant and surfaces. The form of pollutants also affects the severity of degradation. Large particles can cause localized surface damage, while fine particles can infiltrate the lubricant film, increasing friction, and wear. Dissolved contaminants can alter viscosity, reduce film strength, and elevated operating temperatures, affecting lubrication properties. To mitigate the detrimental

effects of pollution on lubricants, it is crucial to monitor and control potential sources of contamination. Implementing appropriate filtration and maintenance practices helps reduce the accumulation of pollutants in the lubricant.

Lubricants used in industrial machinery can be subject to various sources of pollutants, including both external and internal contaminants. External contaminants encompass substances like dirt, dust, water, and other debris present in the surrounding environment. On the other hand, internal contaminants can arise from wear debris generated within the machinery, fuel, and coolant dilution and the formation of oxidation products over time. These contaminants can be solid particles, liquid compounds, or even gaseous substances. The nature and form of contaminants in lubricants can have diverse characteristics. Contaminants may exist in the lubricant as dissolved components or as suspended particles, and they can also accumulate as solid deposits on the surfaces that come into contact with the lubricant. The impact of contamination on lubrication conditions can vary significantly. Contaminants can generally lead to detrimental effects such as increased friction, wear, and energy dissipation. These factors can result in reduced efficiency and a shorter lifespan for the bearings.

The presence of debris in bearing lubrication can significantly impact the extremely thin lubricant film in the contact zones, typically on the order of a micron. The passage of debris can be particularly detrimental, depending on the characteristics of the debris itself, such as its geometry and mechanical properties.

There are multiple sources of particles in bearing lubrication. These particles can already be present in new oil, introduced during maintenance activities, or due to the wear of components between the oil reservoir and the lubricated contact. Figure.1.2 provides an overview of these different types of debris and categorizes them based on their geometries. The study will mainly focus on spherical particles, pieces, or pallets from the oil reservoir, tearing in the lubrication lines, or wear particles generated in the contact. For the sake of simplification in the digital models used in this study, we will consider these particles as spherical, neglecting their asymmetrical characteristics. These particles will become trapped in the contact and can leave marks, known as dents, on the surfaces of the bearing balls and/or rings.

Surface defects, such as dents and scratches, can act as stress amplifiers in bearing contact. As rolling elements pass over the raised edges created by these defects, it generates localized overpressure peaks. The magnitude of this overpressure is significantly influenced by the geometry of the dents formed by trapped particles in the contact. Indeed, completely eliminating all particles suspended in the lubricant is impractical and inefficient. The presence of small particles in suspension contributes to the lubricant's viscosity, which is essential for its proper functioning. Attempting to remove all particles through filtration would not only be expensive and dangerous (due to frequent filter clogging) but also compromise the lubricant's viscosity. Instead, it is necessary for the rolling materials, such as the bearings, to have the ability to withstand a certain level of pollution. Thermochemical treatments are commonly employed to enhance the material's resistance to the detrimental effects

40

of contamination. Therefore, bearings are inevitably exposed to this debris-laden environment and susceptible to its damaging effects. Consequently, it is crucial to study and understand the mechanisms of damage caused by these particles to assess the bearing's lifespan accurately.
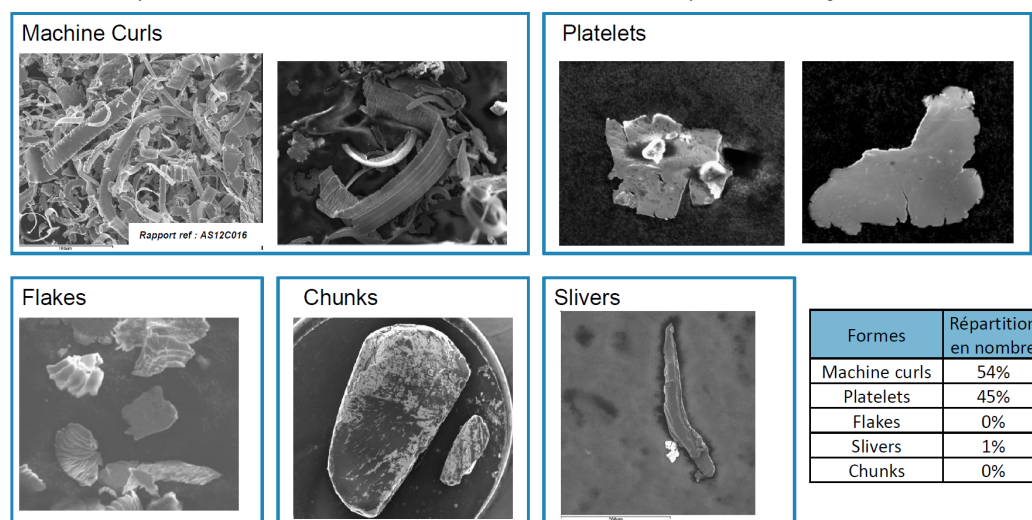
Figure 1.2: Different types of debris in bearing lubricant.

1.4 Bearing damage

Damage modes in bearings can be classified according to where the damage initiation occurs. Surface-initiated damage modes occur on the material's surface, including wear, dents, microcracks, and spalling. Friction, abrasive particles, or localized high stresses typically cause these damages. Surface wear can result from sliding contact between rolling elements and raceways, leading to material loss and surface roughness. Dents can be caused by debris passage into the contact between rolling elements and rings which can induce an excessive stress concentration. Spalling refers to the detachment of matter from the surface, which can occur as a result of fatigue, overstress, dent, and others.

On the other hand, sub-surface-initiated damage modes occur below the material's surface. A common sub-surface damage mode in bearings is rolling contact fatigue (RCF), which develops in the subsurface regions of bearing components due to repeated cyclic loading. RCF can lead to spalling, cracking, or pitting.

1.4.1 Sub-surface-iniated damage

When a material is subjected to cyclic loading, microcracks can initiate and propagate from subsurface defects, such as inclusions. These defects act as stress concentrators, causing localized stress concentrations that promote crack initiation. As the

cyclic loading continues, the cracks propagate, creating a distinct microstructural pattern called a fatigue butterfly as illustrated in Fig.1.3. Slip bands and regions of localized plastic deformation around the crack vicinity characterize this pattern.

The formation of slip bands and plastic deformation around the crack tip is a result of the repeated passage of load in the vicinity of subsurface defects. This plastic deformation is accommodated by the movement of dislocations, which are line defects in the crystal lattice. Some dislocations may become blocked or hindered during their reciprocating movement, leading to their gradual accumulation and the creation of microcracks. These microcracks are typically oriented at an angle of approximately 45° with respect to the surface. Under favorable conditions, such as continued cyclic loading, these microcracks can propagate and reach the surface, resulting in spalling and ultimately leading to the failure of the material.
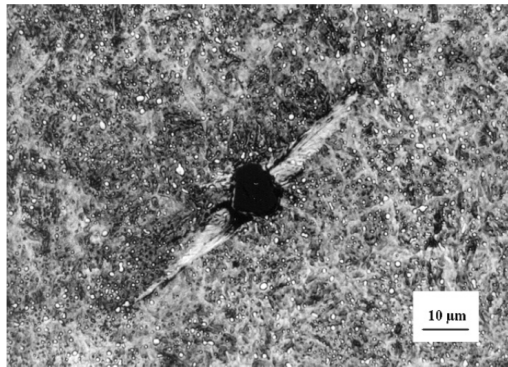
Figure 1.3: Fatigue butterfly in 100Cr6 around an alumina inclusion (SAN 93)

The damage initiated in the sub-layer has led to the development of two types of models: phenomenological models and physical models. Phenomenological models, such as the Weibull and Lundberg, and Palmgren models, were established in the mid-20th century. These models determine the probability of specimen survival based on the number of loading cycles, the maximum stress level, and a critical volume. The main difference between the Weibull model and the Lundberg and Palmgren model is adapting the Weibull model to consider a field associated with a volume at risk. Phenomenological models effectively describe the dispersion of fatigue life but do not provide a detailed understanding of the mechanisms involved in damage formation. To incorporate the mechanisms of damage formation, physical models have been developed. This is the case of the Lamcos and Mateis laboratories of INSA Lyon, which have conducted studies on physical models (JAC 01; TON 12b; AMU 16a). The work of Tanaka (TAN 81) served as a basis for developing criteria that have been further refined and utilized in numerous studies (LAM 96; STI 09). This criterion enables an accurate description of damage initiated at micro-heterogeneities within materials. However, with the continuous improvement of inclusion cleanliness in steels, damage initiated in the sub-layer

has become less frequent. As a result, the focus has shifted toward surface-related damage, which has become the primary source of bearing damage.

1.4.2 Surface damage

When examining surface damage in bearings, it can be categorized into two main types: damage caused by the presence of roughness and damage resulting from the creation of dents on the surface.

1.4.2.1 Damage initiated by roughness

The raceway surface of a rolling element bearing is crucial for its performance and durability. It serves as the contact surface on which the rolling elements (balls or rollers) move. The quality of the raceway surface plays a significant role in determining the bearing's performance. It should be smooth and free of defects to prevent premature wear and failure.

However, when the raceway surface is degraded, such as having significant roughness, it can lead to the generation of overpressures and the initiation of cracks on the surface. The level of roughness and the applied load can result in different modes of crack initiation. There can be cracks initiated in the subsurface layer, cracks initiated near the surface roughness, or a combination of both.

To quantify the severity of the surface condition, the lambda ratio (λ) is used as a parameter. The lambda ratio is defined as the ratio of the minimum oil film thickness to the composite surface roughness, which includes the roughness of the raceway and the rolling elements. It is calculated using the formula:

$$\lambda = \frac{h_{min}}{R_{ms}} \qquad (1.1)$$

Here, h_{min} represents the minimum oil film thickness, R_a and R_{ms} represent the arithmetic and root mean square roughness values, respectively. A higher lambda ratio indicates a smoother surface and better lubrication conditions, while a lower ratio suggests a rougher surface and a higher risk of metal-to-metal contact and surface-initiated damage.

Bearings are typically finished using grinding and superfinishing processes to achieve a smooth surface, minimizing the risk of overstressing due to roughness and promoting elastohydrodynamic lubrication. However, damage can still occur due to surface degradation caused by particles trapped in the contact area, resulting in indentations and excessive stress. This has become a primary source of bearing damage in modern applications.

1.4.2.2 Damage initiated by dents

Dents on the surface of bearings are characterized by their diameter, depth, and, most importantly, the height of the material displaced around the dent, known as

the pile-up height. The pile-up height can be significantly higher than the depth of the dent itself.

The pile-up height of an dent plays a critical role in determining the level of contact between the metal surfaces, even when lubrication is present. The higher the pile-up height, the greater the likelihood of metal-to-metal contact, which can lead to local overstresses and, ultimately, fatigue damage as presented in Fig.1.4. Therefore, it is crucial to control the size and shape of dents to prevent surface-initiated damage in bearing applications.
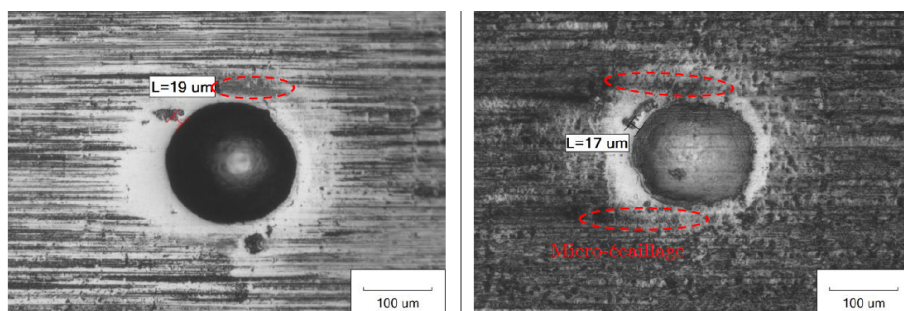
Figure 1.4: Spalling and micro-pitting at the edge of the dent in rolling-sliding condition (ROB 16).

A study conducted by Jacq et al. (JAC 03) under pure rolling conditions revealed that damage initiation due to dents occurs on both sides of the dent. However, there is a preference for damage initiation downstream of the dent with the rolling direction as illustrated in Fig.1.5. This preference is likely due to the accumulation of stresses and deformation in the material in the downstream direction, leading to a higher likelihood of damage initiation at that location. Additionally, the asymmetrical distribution of stresses and strains around the dent results in higher stress concentrations downstream.

The studies conducted by Tonicello (TON 12a), Robitaille (ROB 16) and Bonetto et al. (BON 20) allowed the application of fatigue criteria, which proved effective in localizing and predicting the orientation of cracks. Their research emphasized the significance of three parameters that reduce the service life of bearings: load, slip (sliding motion between contacting surfaces), and the height of the pile-up.

The presence of residual stresses resulting from thermo-chemical treatment, residual stresses caused by indentation, and the shape of the dent (including pile-up), as well as residual stresses generated during manufacturing processes (such as rectification, etc.), all play a critical role in causing damage. Therefore, based on these findings, it is imperative to enhance our understanding of this damage and accurately identify the key parameters that contribute to its occurrence.

44
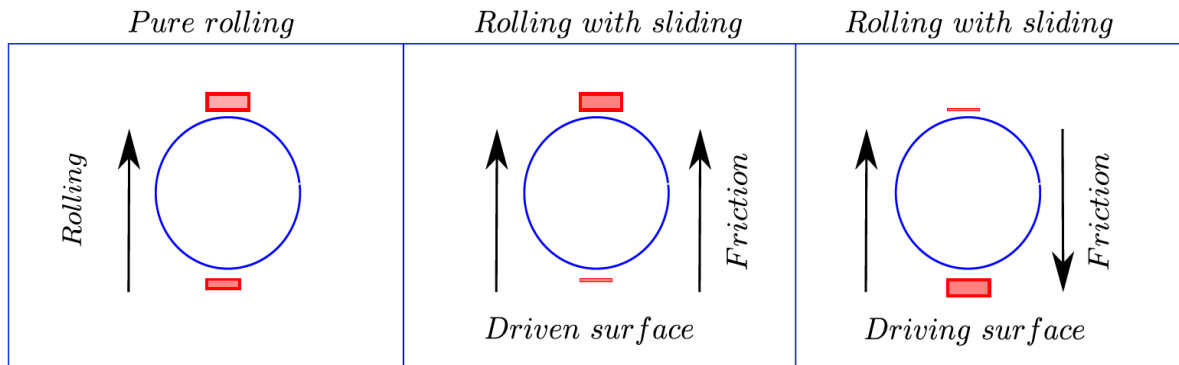
Figure 1.5: Sites of initiation of the damage in pure rolling or in presence of friction force.

1.5   The steel bearing

The traditional steel bearing is the most widely used bearing type in various applications, ranging from household appliances to heavy-duty industrial machines. It consists of an inner and outer race, rolling elements (balls or rollers), and a cage or retainer that keeps the rolling elements evenly spaced. Steel bearings are made from high-quality steel alloys with excellent mechanical properties, including high hardness, toughness, and wear resistance. These properties make them capable of carrying high loads and operating under harsh conditions, such as high temperatures, high speeds, and contaminated environments.

1.6   The ceramic hybrid bearing

Ceramic balls made of silicon nitride offer several advantages over traditional steel balls. Their higher stiffness and lower density result in lower deformation under load and lower centrifugal forces at high speeds, reducing the risk of ball skidding. The higher hardness and fracture toughness of silicon nitride also makes it more resistant to damage from surface defects and debris in the lubricant. However, ceramic bearings can be more brittle and have a higher risk of fracture under impact loads. The use of ceramics in hybrid bearings aims to combine the advantages of both materials and minimize their disadvantages.

Regarding contact fatigue, the hardness and Young's modulus of silicon nitride make it less susceptible to deformation from particle entrapment, leading to proportionally deeper dents with larger beads. However, implementing a ceramic rolling element among steel rolling elements can have a "smoothing effect" due to the strong plastic deformations of the pile-up generated by the ceramic rolling element, as observed in studies by Wan et al.(WAN 97) and Wang et al (WAN 07).

The addition of ceramics can positively impact the number of chipping cycles

and reduce the height of the pile-up, leading to a reduction in local overpressures. Including ceramics appears to increase the number of fatigue cycles in the vicinity of dents.

Another effect associated with the high Young's modulus of ceramics is an increase in the contact pressure under iso-force conditions. The contact area is reduced due to the minimized deformation of the rolling elements.

1.7 Endurance limit of indented contacts

1.7.1 Concept of lower bound of the endurance limit (H_1)

The concept is based on the ability of dislocations to accommodate localized plastic deformation. When the applied load exceeds the micro-elastic limit, dislocations are expected to move and accumulate before causing damage. Thus, the maximum stress denoted as H_1, represents the highest stress that keeps the material within the elastic range at any point. The absence of dislocation emission ensures infinite durability and serves as a lower bound for the endurance limit. H1 corresponds to the maximum Hertz pressure in the case of smooth contact without any localized plasticization.

In the presence of inclusions within the material, overstresses occur in the case of smooth contact. These overstress depend on the mechanical properties of the inclusions, as well as their geometry and position relative to the contact area. An H_1 value needs to be determined for each type of inclusion, along with identifying the most detrimental position near the maximum shear rate depth.

In the case of an indented contact, similar to the presence of an inclusion, overstresses arise when the rolling body passes over the dent. However, the difference lies in the presence of a residual stress state resulting from the indentation. Consequently, the micro-elastic limit of the material is not uniform throughout the contact area, and the lower bound of the endurance limit is defined as the maximum pressure (still in the case of a smooth contact) that does not exceed the micro-elastic limit. It is evident that this lower bound of the endurance limit heavily relies on the material properties, as well as the operating conditions in contact fatigue (such as contact pressure, contact geometries, presence of sliding, etc.) and the geometry of the associated dent in the state of residual stresses caused by indentation.

1.7.2 The lower bound of the endurance limit in the presence of indentation (H_{1I})

Simulation studies of contact in the presence of indentation have been conducted considering the material's elastic behavior (JAC 01). The objective is to identify the regions where dislocation movement occurs, indicating exceeding the material's elastic micro-limit. These simulations also consider the modifications of the elastic

micro-limit during the indentation phase.

For a smooth contact with an equivalent radius of 15mm, it has been observed that the yield micro-limit is exceeded at a depth of approximately 800μm under the pressure of 2.65GPa, considering the evolution of the yield micro-limit in the thermo-chemically treated layer of 32CrMoV13. However, the effect of indentation is limited to a depth of less than 350 μm in most cases. Consequently, Jacq focused on exceeding the near-surface micro-yield strength in the vicinity of the dent. To establish a lower bound of the endurance limit, it is sufficient to determine the lowest value of H_1 between that for a smooth contact (referred to as H_{1L} by Jacq) and that for an indented contact (referred to as H_{1I}).

An analysis of H_{1I} for all dent geometries has been conducted, revealing the dent geometries prone to rolling fatigue. These studies indicate that small-radius indenters, combined with high indentation loads, quickly lead to plastic deformations and are, therefore, susceptible to damage. Conversely, dents created with large-radius indenters under small loads have a significantly higher H_{1I} limit, suggesting a lower risk of damage in the vicinity of these dents.

Furthermore, these observations highlight that the average slope of the dents is a valuable parameter for characterizing their harmfulness. Jacq proposes a simplified representation of this slope, neglecting the spring back of the material, the deformation of the indenter during the indentation phase, and the presence of a bead. The representation allow the determination of the dent's height (h_d).

The relationship between the radius of the dent (R_d) and the average slope (s_m) can be expressed using the constant average pressure (P_{moy}) during indentation and the applied load (F_{Ni}) dependent only on the material. The equation is given as:

$$s_m \approx (1/2)R_d/(\pi P_{moy}) \tag{1.2}$$

By combining this equation with the previous equations, it has been demonstrated that the average slope (s_m) follows the same trend as the ratio called I_R, defined as:

$$I_R = (\pi * R_d/h_d) \approx (p/F_N) * (R_d/h) \tag{1.3}$$

This equation allows for the classification of dents based on their severity. Their results illustrate three distinct areas. The first area, referred to as group H (High endurance limit), consists of dents with a low probability of causing damage. The second area, group B (Low Endurance Limit), includes dents that are likely to cause damage. The third area, group M (Average endurance limit), encompasses intermediate dents. So from their analysis, it can be deduce that dents that generate localized overpressure, exceeding the H_{1I} endurance limit in pure rolling condition, will also generate a Hertz pressure exceeding H1I in the presence of sliding showing the nocivity of the sliding.

By utilizing this lower limit of the endurance limit for indented contacts (H_{1I}), it becomes possible to classify dents based on their harmfulness and identify those

with the highest probability of causing damage. However, this method alone cannot guarantee damage occurrence for a given geometry. Therefore, other methods are necessary to provide a comprehensive description of the damage and estimate the service life.

1.8 Contact fatigue life models

1.8.1 ISO 281 standard

The ISO 281 standard, implemented in 1990 and subsequently revised, remains the industry standard for contact fatigue life prediction. It is based on the statistical approach proposed by Weibull in 1949 (WEI 49) and enriched by the model developed by Lundberg and Palmgren (LUN 47) during the same period.

$$\ln(S) = -\frac{\sigma_0^c N^b.a.l}{z_0^{1-h}} \tag{1.4}$$

The Lundberg and Palmgren model provides a probability of survival (S) after a certain number of cycles (N) under maximum stress (σ_0) at a specific depth (z_0). The geometry of the contact, represented by the semi-major axis (a) and the length of the bearing track (l), is taken into account. Other parameters (c, β, and h) are determined and adjusted through a series of fatigue tests.

Based on this model, the ISO 281 standard proposes a modified calculation for service life, described by the equation:

$$L_{nm} = a_1.a_{ISO}.L_{10} \tag{1.5}$$

where

$$L_{10} = \left(\frac{C_a}{P_a}\right)^n \tag{1.6}$$

This equation allows for the calculation of the modified lifetime L_{nm} based on the failure lifetime for a 10% failure rate L_{10}, which is determined using the basic dynamic capacity C_a and the dynamic load P_a. The service life L_{10} is then reassessed using two factors, a_1 and a_{ISO}. Factor a_1 enables the transition from a 10% failure rate to another desired failure rate, while the a_{ISO} factor accounts for the effects of material properties, lubrication, and potential contamination.

The a_{ISO} factor considers the effects of overstresses generated by indentation, oil film thickness, tight mounting of the rings leading to shrinkage stresses, temperature, and other factors. It can be expressed as:

$$a_{ISO} = f(\frac{\sigma_D}{\sigma}) \tag{1.7}$$

48

The parameter a_{ISO} is a function of the endurance limit σ_D divided by the actual stress σ experienced by the components under consideration. When σ is less than σ_D, the lifetime is assumed to be infinite. Conversely, if σ exceeds σ_D, the a_{ISO} factor decreases, indicating a shorter lifespan.

According to the standard, the ratio $\dfrac{\sigma_D}{\sigma}$ can be approximated by the dynamic limit capacity (Cu) ratio to the dynamic load (P). Therefore, the a_{ISO} factor can be expressed as:

$$a_{ISO} = f(Cu/P) \tag{1.8}$$

This factor takes into account all the factors that contribute to overstressing the dynamic limit capacity (Cu). However, considering the complexity of these factors, the standard proposes introducing new factors to account for various contamination and operating condition issues. The a_{ISO} factor should consider the following factors, as stated in the standard:

- Lubrication:
  This includes the type of lubricant, additives, viscosity, and other related properties.

- Operating environment:
  This involves the level of pollution, the use of filters, and other environmental factors.

- Particle characteristics:
  This includes the hardness, geometries (shapes and sizes) of particles present.

- Mounting precautions:
  The standard suggests considering specific precautions taken during the mounting process.

Therefore, additional factors can be incorporated into the formulation of a_{ISO}. These factors are a contamination factor e_C and a factor related to lubrication conditions κ. The expression for a_{ISO} becomes:

$$a_{ISO} = f\left(\frac{e_C.C_u}{P}, \kappa\right) \tag{1.9}$$

The e_C factor accounts for various aspects of pollution, such as the size, hardness, and quantity of foreign particles. On the other hand, the κ factor characterizes the thickness of the lubricant by calculating the viscosity ratio between the actual kinematic viscosity and a reference kinematic viscosity. The κ factor can be estimated using the severity parameter Λ, which represents the minimum oil film height ratio for elastohydrodynamic lubrication to the quadratic average of roughness heights.

The relationship used to evaluate the κ factor is approximately given by:

$$\kappa \approx \Lambda^{1.12} \tag{1.10}$$

Through numerous tests, charts have been developed to characterize the a_{ISO} parameter, taking into account these factors. The standard relies on phenomenological and statistical models that require a significant number of trials. To enhance predictability, it is advantageous to work with physical models of damage.

1.8.2 Physical models

Physical models differ from phenomenological and statistical models as they involve parameters that can be measured through specific experiments. These models do not require extensive bearing life performance tests except initial validation.

It is important to note that some physical models may only encompass some of the physical characteristics of the damage mechanism. For example, Blake and Cheng (BLA 91) proposed a damage prediction model specifically for microchilling of surfaces. This model considers the presence of a distribution of microcracks initially present in the material. The lengths of these microcracks are adjusted according to a normal distribution, and their growth is assumed to follow Paris law. However, the predicted lifespans from this model are generally lower than the observed ones.

In a more recent article, Cheng and Cheng (CHE 97) presented a fatigue model for contact, which includes crack initiation in slip bands formed within the material's grains. These slip bands are modeled using two stacks of opposite sign dislocations, with each stack having a length equal to that of the grains. The accumulation of dislocations occurs during cyclic stresses due to the irreversible movement of dislocations. This modeling approach is based on the work of Mura and his collaborators(TAN 81), who studied crack initiation in crystalline materials subjected to cyclic stress.

In Cheng and Cheng's approach (CHE 05), they combined their crack initiation model with a priori assumed Weibull distribution of lifetimes. This combination somewhat reduces the predictive nature of the model.

Another physically based model focused on crack initiation was developped at INSA Lyon's Mateis laboratory. This model predicts the number of cycles for crack initiation in steel subjected to fatigue rolling, specifically near inclusions. The idea is based on the concept of stress amplification in the vicinity of inclusions, which leads to crack initiation. The same assumption of stress amplification applies to crack initiation near dents. Initially developed for modeling inclusion neighborhoods, this model has been adapted for studying crack initiation near dents.

The foundation of this model was established by Champaud (CHA 88), and it was further developed by Gosset (SAN 93) and Lamagnère (LAM 96). The general process modeling approach can be summarized in six steps:

❋ Calculation of the macroscopic stress field resulting from the contact between the rolling bodies.

50

❈ Calculation of the local stress field near an inclusion located in a sublayer.

❈ Modeling the shape and size of the fatigue butterfly (region prone to crack initiation).

❈ Calculation of the number of dislocations emitted during the initial loading.

❈ Calculation of the evolution of the number of dislocations emitted as the number of cycles increases.

❈ Calculation of the number of critical dislocations in the fatigue butterfly required for crack initiation and the number of cycles needed to reach this critical density of dislocations.

In the presence of an inclusion, the stress field due to contact is locally altered. Therefore, calculating this local field using the semi-analytical method of the equivalent inclusion developed by Eshelby (ESH 59). This method accounts for the disturbance of an applied, uniform stress in an infinite, isotropic, and elastic matrix containing an ellipsoidal or spherical elastic inclusion with elastic constants different from those of the matrix. So, the modeling process concerns the calculation of the size, λ, and the shape of the fatigue butterfly. According to Gosset (SAN 93), the fatigue butterfly is delineated by the equilibrium position of the first dislocations emitted from the matrix/inclusion interface. This assumption provides a realistic representation of the shape and size of the butterflies, as observed in Fig.1.3. The equilibrium position of dislocations is determined by comparing the driving forces acting on the dislocations within their slip plane with the frictional force of the matrix.

In the subsequent step of the modeling process, the number of dislocations that accumulate during fatigue within the domain defined by the fatigue butterfly needs to be estimated. This calculation involves determining the number of dislocations that are geometrically necessary to accommodate the deformation incompatibility between the inclusion and the matrix. This number includes a component resulting from the initial loading and a component resulting from the irreversibility of movement during cyclic loading. To account for this irreversibility, L. Gosset (SAN 93) introduced an accumulation factor of damage, denoted as f^*, based on the work of Lin et al (LIN 86).

In the final step of the modeling, the critical density of dislocations for crack initiation in the fatigue butterfly is calculated. For this purpose, the accumulation of dislocations emitted during the cycles is represented as a double stack. Under these conditions, Friedel (FRI 64) demonstrated that cracking occurs when the climbing stress acting on the dislocations reaches the decohesion stress of the material. The climbing stress primarily depends on the density of dislocations in the stack, while the decohesion stress of the matrix is approximately equal to $\mu/5$, where μ represents the shear modulus.

The following relationship determines the crack initiation condition in the double stack:

$$\frac{\mu b}{\pi(1-\nu)h}Ln\left(\frac{n_N^2}{8}\right) \geq \frac{\mu}{5} \tag{1.11}$$

where b is the Burgers vector of the dislocation, h is the height of the double stack, n is the density of dislocations in the stack, N is the critical density of dislocations for crack initiation, μ represents the material's shear modulus and ν the Poisson's coefficient of the material.

The modeling of crack initiation was coupled with a microcrack propagation model developed by Champiot (CHA 97b) to predict the number of fatigue cycles until failure. This deterministic modeling approach was then integrated into a statistical distribution model of inclusions to predict the lifetime dispersion in a population of bearings made of 100Cr6 steel (PIO 00).

Later, Tonnicelo's study (TON 12b; TON 12a) provided new insights and, most importantly, allowed for modeling damage mechanisms in nitrided 32CrMoV13. Our focus was specifically on developing a crack initiation model, represented by the equation below, to predict the number of cycles required for the initiation of a contact fatigue crack in the presence of indentation.

$$n_c = \frac{2\bar{\omega}_s - \alpha(1-\nu)\frac{\sigma_N^2}{3\mu}}{f^*.d.\gamma_c.(\Delta t - 2\tau_f)} \tag{1.12}$$

The developed model relies on a comprehensive understanding of material properties. The study reveals that the regions prone to damage are primarily concentrated within the bead areas. Furthermore, the presence of cracks in the sub-layer, specifically to the right of the beads, further emphasizes their susceptibility to damage.

In 2020, Bonetto et al.(BON 20) conducted a study where they employed a Finite Element Method (FEM) with Euler-Lagrange Coupling (CEL) modeling to simulate the indentation process. This modeling approach allowed them to gain insights into the indentation process and identify important parameters that influence it.

Using a novel criterion that combined the Dang Van and Brown Miller criteria, they enhanced the prediction of crack initiation and determined their locations more accurately. Their findings revealed that the exit bead, which is higher than the entry bead, becomes the preferential site for fatigue damage. They also identified that the bearing load, presence of slippage, and height of the beads are influential parameters that significantly affect the fatigue life of the system.

It is worth mentioning that the propagation of cracks in contact fatigue has been studied by numerous authors, including Keer et al. (KEE 83a), Lee et al. (LEE 86), Murakami et al. (MUR 85), (MUR 94), Zhou et al. (ZHO 89), Fan et al. (FAN 93), Rock (ROC 94), Kuo et al. (KUO 97), and Lee et al. (LEE 97). However, this stage of material damage is not the focus of the current work.

1.9 Synthesis

The presented work aims to characterize and understand the surface damage mechanisms in rolling fatigue, particularly in the presence of indentations. The existing literature needs physical models for predicting the fatigue life of indented contacts, which highlights the need for further research in this area.

To achieve a better understanding of the mechanisms involved in bearing surface fatigue, several research aspects will be explored. Firstly, the optimization of bearing steels will be pursued through thermochemical treatments such as quenching, nitriding, carburizing, and carbonitriding. The specific steels being studied include M50, 32CrMoV13, M50NiL, and M50NiLDH, and their characterization will be conducted.

In order to comprehend the evolution of the steel's plastic behavior during the repeated passage of rolling elements on the rolling track, cyclic tests will be carried out, and behavior laws will be identified. By investigating all sources of overpressure on the rolling tracks, including the influence of free edges on Hertz contact pressure, numerical modeling will be employed to assess their effects.

The final part of the study will focus on the analysis of the surface particle crushing process to identify key parameters that influence this process. All this study is schematized, on the diagram below in Fig.1.6.
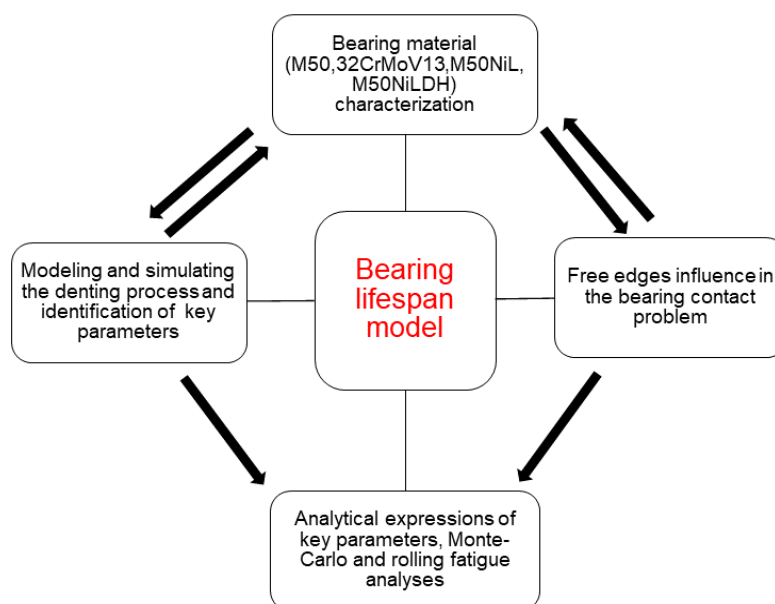
Figure 1.6: Synoptic diagram of the thesis work

1.10   Conclusion

This study aims to enhance the understanding and characterization of surface damage mechanisms in rolling fatigue with indentation. Despite this topic's significance, limited physical models are available in the literature that can accurately predict the lifespan of indented contacts. Therefore, this manuscript contributes valuable insights to the field of fatigue mechanics. Most existing physical models in the literature primarily focus on damage mechanisms near inclusions. However, surface damage mechanisms in rolling fatigue with indentation require separate consideration. While Jacq's (JAC 01) work provided endurance limits for contacts with dents, it did not establish a comprehensive lifetime model. In 2020, Bonetto (BON 20) conducted a study using a Finite Element Method (FEM) model based on the CEL approach to simulate the denting process. They identified key surface damage parameters and employed fatigue criteria to determine crack location and propagation. This work aims to deepen the understanding of surface damage mechanisms, identify key parameters, and develop a lifetime model specifically for indented contacts by incorporating physical models. To achieve this goal, it is crucial first to understand the mechanical behavior of the studied materials. Nanoindentation tests will be conducted on thermochemically treated materials, including M50, 32CrMoV13, M50NiL, and M50NiLDH. These tests will provide insights into the properties of monotonic plasticity and cyclic plastic behavior. The data obtained from these experiments will serve as a basis for developing a comprehensive lifetime model for rolling fatigue with indentation. Subsequently, numerical simulations will address free edges' influence by solving quarter, two-joined, and finite-length space problems. Finite Element Modeling will be employed to simulate the denting process and identify key parameters. Analytical expressions will be derived to determine these key parameter relationships, which will be used for subsequent damage criterion.

Chapter 2

Mechanical characterization of bearing steels

Characterizing the mechanical properties of bearing steels is crucial in understanding the different damage mechanisms that can occur during operation. In this chapter, bearing materials, such as M50, 32CrMoV13, M50NiL, and M50NiLDH, are studied. First, nanoindentation tests are performed to identify their mechanical properties, such as modulus and micro-hardness, and to establish their behavior laws. The results show that carburizing, nitriding, and carbonitriding increase surface hardness, but the hardness gradually decreases towards the material's interior. Quenching results in a uniform increase in hardness throughout the material. Swift's constitutive law parameters are determined for all the materials using an inverse approach. A direct link is established between the sample's treated depth, corresponding hardness, and Swift hardening parameters. Furthermore, numerical analysis of the materials under operating loadings is conducted to understand the influence of the gradient of properties on the surface and the entire deformation of the components. The study shows that the M50 steel has good surface and core properties and exhibited the highest resistance to high loading levels beyond 6.6 GPa. The M50NiLDH steel, which has the best surface properties, shows the best resistance in the 3.5-5.2 GPa range but starts to deform more than M50 at higher loading levels. The M50NiL and 32Cr-MoV13 steels show intermediate resistance levels between M50 and M50NiLDH, with M50NiL being more resistant than 32CrMoV13. However, at lower loading levels, the surface properties of the treated materials were found to play an important role in their mechanical resistance.

Sommaire

2.1   Introduction

In industry, local hardening treatments are commonly used to improve the surface properties of materials while maintaining their bulk properties. For example, case hardening techniques such as nitriding, carburizing, and carbonitriding can create a hardened layer on the surface of a material while preserving its core toughness. These treatments work by diffusing nitrogen, carbon, or both into the material's surface and hardening the resulting layer through heat treatment. Other methods, such as shot peening and laser shock peening, can also be used to create compressive residual stresses in a material's surface layer, improving its surface properties. These treatments work by inducing plastic deformation in the surface layer of the material, which then generates compressive residual stresses upon relaxation. Overall, local hardening treatments can effectively improve the surface properties of materials used in rolling element bearings, such as the track and rolling elements, while maintaining their overall strength and toughness. However, it is important to carefully select the treatment parameters and process conditions to ensure the material retains the required mechanical properties for its application.

The hardening mechanisms in bearing steels involve capturing dislocations through various means, such as hardening, foreign atoms, precipitates, and grain boundaries. While hardening treatments can create additional dislocations to interfere with the movement of dislocations, they often result in a loss of toughness. Thus, using nano-precipitates to prevent the movement of dislocations is a more attractive solution. Thermochemical treatments such as carburizing, nitriding, or carbonitriding can create these nano-precipitates. These treatments control the hardened zone's thickness and depth, allowing for local, deep, or shallow hardening. In this thesis, the bearing steels are treated through thermochemical treatments to achieve the desired hardness property.

2.2   The materials behavior

The study of material behavior within mechanical components refers to their response and interaction with external forces and loads. This involves a comprehensive examination of various mechanical attributes, including strength, stiffness, ductility, hardness, fatigue resistance, and creep resistance. Understanding material behavior is crucial in designing and modeling mechanical components to ensure their dependability, endurance, and optimal functioning across diverse operating conditions. Factors such as material composition, microstructure, heat treatment, and external loading conditions collectively shape how materials behave within mechanical components.

In circumstances of low stress, metallic materials exhibit elastic behavior, wherein the material deforms in response to applied stress, but this deformation is reversible

upon stress removal. However, when stress surpasses a specific threshold, the material undergoes plastic deformation, resulting in irreversible changes to its form and dimensions. This phenomenon arises from the movement of dislocations within the crystal structure, leading to enduring deformation even after stress removal. This elastoplastic behavior can be observed in various mechanical components, including bearings, which endure repeated cyclic loads during operation, potentially resulting in plastic deformation and eventual fatigue-related failure.

In normal operating conditions, bearings encounter static and dynamic loads that can trigger plastic deformation and fatigue failure. Plastic deformation arises when the bearing material experiences loads beyond its elastic limit, causing permanent shape alterations. Fatigue failure occurs due to the gradual accumulation of minuscule cracks induced by cyclic loading.

The plastic behavior of bearing material is characterized by parameters such as yield strength, ultimate tensile strength, and ductility. Yield strength signifies the stress level at which plastic deformation initiates, while ultimate tensile strength represents the maximum stress the material can withstand before failure. Ductility quantifies the extent of plastic deformation the material can endure before succumbing to failure.

Fatigue behavior in bearing materials is characterized by fatigue strength and life. Fatigue strength denotes the highest cyclic stress the material can withstand over a specified number of cycles before failure occurs, while fatigue life quantifies the number of cycles the material can endure before reaching failure.

2.3   Presentation of nanoindentation tests

Nanoindentation tests are a non-destructive, localized technique for characterizing the mechanical properties of materials at small scales. Unlike conventional tests like tensile or compression tests, nanoindentation tests can provide information on the mechanical behavior of a material at a specific location, such as the surface or a specific depth within the material. This makes them particularly useful for studying materials with gradient properties or heterogeneous microstructures. Additionally, since nanoindentation tests require only a small sample size, they can be used to characterize materials that are not suitable for conventional testing.

Nanoindentation is a widely used technique for the local characterization of mechanical properties of materials. It involves driving a tip of known geometry and properties onto the characterized material to extract its mechanical properties. The technique is non-destructive and can be used on small samples. Using the technique, one can locally estimate the mechanical properties of materials, such as hardness and Young's modulus. For example, the relationship between hardness and yield strength was predicted by (JOH 85) in 1985 using a spherical cavity model for the conical indentation of elastic-perfectly-plastic solids. Various authors

have developed methods to measure the mechanical properties of materials, including (OLI 92; FIE 93; S.P 09; JLL 86; HEN 95; TAB 51; DOE 86; JL. 95; PHA 02; OLI 04; DAO 01; GIA 02; BUC 03; CAO 04). One common effect encountered during indentation tests is the size effect, which is linked to wear or tip defects. Therefore, the profile of the indentation tip should be analyzed. This effect has been the subject of several studies conducted by (NIX 98; ELM 03; ARZ 98).

In recent years, the identification of material parameters and constitutive laws from indentation curves has been the subject of many studies. Advanced constitutive models have been implemented and tested with finite element codes to predict mechanical properties, such as the work by (ALV 04) and others (KLO 06; NAK 00; NAK 07; BOL 13; MOY 11). In addition, several authors have developed analytical and experimental methods using instrumented micro-indentation to estimate the elastic properties of graded materials. Some examples include the work of (GIA 99; HER 14; HER 15; NAK 00; NAK 07; NEL 65; MOY 11; MEN 16; CHE 10b; YAN 48; YAN 06; HEL 06; FIS 06). These methods allow for a more localized and non-destructive characterization of mechanical properties, which is particularly useful for materials with gradient properties (YAN 10; CAO 04; LEE 04; LEG 04; PRA 09; BOL 98; SNE 71; SNE 65; HAY 00; OLI 92; YAN 11; VAN 03; TAB 51).

2.4 Samples and thermo-chemical treatment

In this section, the bearing materials used in this study are presented. Thus as bearing steel, we have 32CrMoV13, M50, M50NiL, and M50NiLDH. These four steel grades have undergone thermochemical treatments.

2.4.1 32CrMoV13 steel

Nitriding is a surface hardening treatment that involves the diffusion of nitrogen into the surface of a material. In the case of 32CrMoV13 steel, gas nitriding is used to improve its surface hardness and mechanical properties. Gas nitriding involves heating the steel to a temperature between $500 - 600°C$ in a nitrogen-rich atmosphere. During this process, nitrogen atoms diffuse into the surface of the steel and react with the alloying elements to form nitrides, which are hard and wear-resistant compounds. The nitrided surface of the steel has a high mechanical surface resistance, which means that it is more resistant to wear and damage from contact with other surfaces. However, the core of the steel still retains its good ductility and resilience. This is important because it ensures the steel can withstand high stresses and loads without fracturing or breaking. Additionally, the nitriding process creates a profile of residual compressive stresses on the surface of the steel. These compressive stresses help to counteract the tensile stresses that are generated during the

operation of the bearing. This results in improved fatigue resistance and longer service life for the bearing. It is important to note that the nitriding process is carried out on a stabilized structure of 32CrMoV13 steel, which has been quenched and tempered at high temperatures (around $650°C$). This ensures the steel has good structural and mechanical stability even at the high temperatures used during the nitriding process.

Table 2.1: Chemical composition of 32CrMoV13 according to AMS 6481

Elements	C	C_r	M_o	V	M_n	S_i
Mass (%)	$0.29 - 0.36$	$2.8 - 3.3$	$0.7 - 1.2$	$0.15 - 0.35$	$0.40 - 0.70$	$0.10 - 0.40$

The microstructure of nitrided steel typically exhibits a gradient consisting of a combination layer and a diffusion layer. The combination layer, also known as the white layer, is generally composed of iron nitrides such as $Fe_4N - \gamma'$ and/or $Fe_{2-3}(C.N) - \varepsilon$ and is very hard but also prone to cracking. Thus, it is often removed during the finishing process. On the other hand, the diffusion layer has a thickness of up to 1mm. It exhibits a gradient of nitrogen in a solid solution of insertion or the form of intra or inter-granular nitrides. The nitrogen in the diffusion layer mainly contributes to hardening by forming fine nitride or carbonitride precipitates. In the case of 32CrMoV13 steel, deep nitriding can result in a constant nitrogen content up to a depth of $600 - 1000\mu m$. In addition, nitriding can also result in residual compressive stresses, which can promote fatigue resistance (JEG 12).

According to the AMS 6481 standard, the composition of this normalized steel includes approximately 3% Chromium (Cr), 1% Molybdenum (Mo), and 0.32% Carbon (C) as presented in Table.2.1.

In summary, the 32CrMoV13 steel, when subjected to this specific heat treatment process, offers a unique combination of strength and toughness. The composition is in accordance with the AMS 6481 standard, and the tensile strength is intentionally limited to maintain optimal toughness. For precise engineering applications, further details, such as the exact Vanadium content, may be required, and it is advisable to consult the latest material specifications and data sheets for the most up-to-date information.

2.4.2 M50 steel

In addition to its high hardness and strength, M50 steel exhibits excellent wear resistance and fatigue properties, making it ideal for use in high-load and high-speed bearing applications. M50 steel can be further modified through additional heat treatments such as tempering to achieve specific properties or surface characteristics.Tempering is a heat treatment process often performed after quenching to improve the toughness and ductility of the material while maintaining a desirable level of hardness. For M50 steel, the tempering process involves heating it to a

temperature between $150 - 500°C$, holding it at that temperature for a specified amount of time, and then cooling it to room temperature. The specific tempering temperature and time depend on the desired properties of the material. For example, tempering at a lower temperature and for a shorter time will result in a harder but more brittle material, while tempering at a higher temperature and for a longer time will result in a tougher but less hard material. Overall, M50 steel is a high-performance bearing steel with excellent mechanical properties and durability.

Table 2.2: Chemical composition of M50 steel according to AMS 6481

Elements	C	C_r	M_o	V	M_n	S_i
Mass percentage (%)	0.84	4	0.9	1.1	0.48	0.24

M50 steel is a high-speed tool steel commonly used in aeronautic and aerospace applications. It possesses several characteristics that make it suitable for these industries. M50 steel is part of a broader family of high-speed tool steels, and its composition is presented in Table.2.2. Its properties can vary depending on the specific grade and manufacturer. Engineers and manufacturers carefully select the appropriate grade of M50 steel based on the specific requirements of the aerospace component or application. Additionally, continuous advancements in materials science may result in variations or improvements in the properties of M50 steel over time.

2.4.3 M50NiL steel

M50NiL is a variant of M50 steel with some additional elements and less tungsten and carbon than M50 steel. The composition is given in Table.2.3. The steel is typically quenched and tempered to achieve the high hardness and strength and then carburized to improve its surface hardness and wear resistance further. Carburizing is a surface hardening process where carbon is diffused into the surface of the steel to increase its hardness. During carburizing, the steel is heated in a carbon-rich environment, such as a gas or liquid containing carbon, for a prolonged period of time. As a result, the carbon atoms diffuse into the steel and occupy interstitial positions in the crystal lattice, forming iron carbides. Carburizing can improve the steel's surface hardness and wear resistance, making it suitable for high-performance bearing applications. The depth of the carburized layer and the carbon concentration can be controlled by adjusting the carburizing temperature and time. However, carburizing can also reduce the toughness and impact resistance of the steel due to the formation of a brittle layer at the surface. Therefore, the carburized layer must be carefully controlled to balance the desired surface hardness with the required toughness and ductility for the specific application.

M50NiL steel is a specialized variant of M50 steel that finds application in high-performance aerospace and aeronautical contexts. What distinguishes M50NiL is its hypoeutectoid nature, characterized by a carbon composition of less than 0.35%.

Table 2.3: Chemical composition of M50NiL steel according to AMS 6481

Elements	C	C_r	M_o	V	M_n	S_i
Mass percentage (%)	0.13	4.1	4.2	1.2	0.13	0.18

This relatively low carbon content allows the carburizing treatment to be applied to this steel. M50NiL steel's low carbon content makes it a good candidate for carburizing. This process significantly improves its surface properties, making it more resistant to indentation and better suited for high-performance aerospace components.

2.4.4 M50NiLDH steel

The combination of carburizing and nitriding treatments is called carbonitriding, a surface hardening treatment used to improve steel's wear and fatigue resistance. In the case of M50NiLDH steel, the carbonitriding treatment is performed after carburizing and tempering to enhance further the surface hardness, wear resistance, and fatigue life of the material. The carbonitriding process introduces nitrogen and carbon atoms into the surface of the steel, creating a surface layer of nitrides and carbides that increases the surface hardness and provides additional protection against wear and fatigue. The M50NiLDH steel composition is presented in Table.2.4.

Table 2.4: Chemical composition of M50NiLDH steel according to AMS 6481

Elements	C	C_r	M_o	V	M_n	S_i
Mass percentage (%)	0.13	4.1	4.2	1.2	0.13	0.18

M50NiLDH steel is a further specialized variant of M50NiL steel, with additional treatment to enhance its surface properties for high-performance applications. The primary difference between M50NiL and M50NiLDH lies in the deployment of nitriding after carburizing. The combination of carburizing and nitriding results in a surface layer that is exceptionally hard, wear-resistant, and mechanically robust. This makes M50NiLDH steel well-suited for critical aerospace components subjected to extreme conditions and high-performance requirements, such as bearings, gears, and other parts in aircraft engines and propulsion systems.

2.5 Presentation of the samples

Preparing cylindrical bars as samples for material testing is common practice, as they can provide a representative cross-section of the material. The cylindrical bars used in the study are obtained as blanks with a diameter of $\phi = 10\ mm$ and a height of 10.6 mm by sawing and electro-erosion of the received material. These blanks are

then subjected to the necessary heat treatment processes for nitriding and carbonitriding. After heat treatment, the final geometry of the specimen is obtained by grinding the surfaces to ensure uniformity and accuracy. This ensures the samples are suitable for subsequent tests and accurately characterize the thermo-chemical layer. The polishing process started with SiC4000 paper and progressed to polishing with 1 μm diamond solution. This polishing process aims to obtain a surface free of scratches that could interfere with the characterization.

Surface flatness and roughness can significantly affect the accuracy and repeatability of the nanoindentation tests. Flatness can be checked using a surface profilometer, while roughness can be measured using techniques such as atomic force microscopy (AFM) or scanning electron microscopy (SEM). In addition, the calibration of the nanoindentor is crucial for obtaining accurate and reliable results. Therefore, the calibration should be performed before testing to ensure the applied force and displacement measurements are accurate. Calibration can be performed using a standard reference material with known mechanical properties, such as fused silica.

2.6 Micrographic analyzes of samples

In this section, micrographic analyses are employed to examine the resulting microstructures after the preparation of samples through cutting, polishing, and undergoing heat treatments. This allows for the identification of heat treatment zones and enables a comparison of the microstructure of the surface layers with the core metal. Techniques such as optical and scanning electrons microscopy can be used for microstructural and property analysis. In this study, optical microscopy and SEM after etching with 4% nital are performed to reveal the microstructure of metallic materials. Nital etching is a common technique used to reveal the microstructure of metallic surfaces. The resulting microstructure can be analyzed by observing essential features such as grain size, morphology, and distribution.

2.6.1 32CrMoV13 steel

In the nitrided 32CrMoV13 steel, we can distinguish three layers:

❋ The combination layer on the top

❋ The diffusion layer under the latter

❋ The bulk material

The combination layer is approximately 20-30 microns deep and is made up of an interwoven structure called "angel hair" as shown in Fig.2.2. The combination and diffusion layers are composed of iron nitrides and chromium formed from the
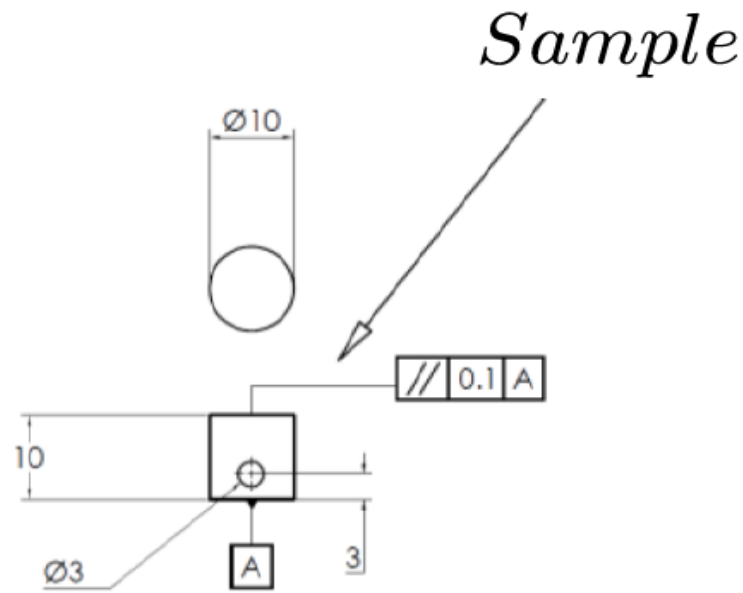
Figure 2.1: Geometry of the samples
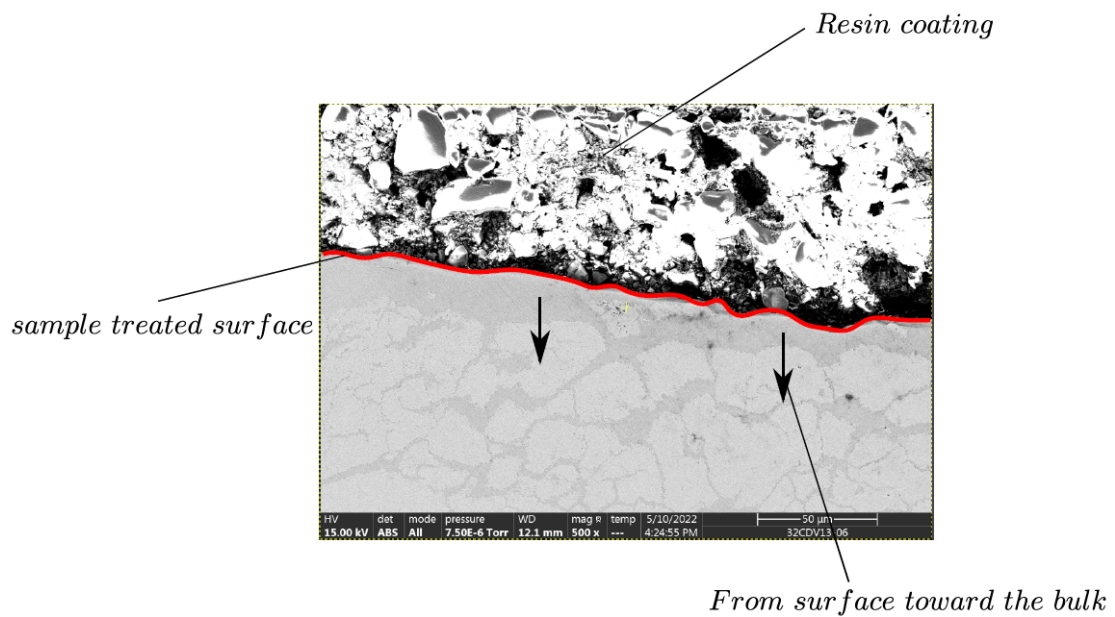
Figure 2.2: Typical micrograph of a nitrided 32CrMoV13 steel and its SEM observation with presence of nitrided layer

reaction between the substrate and the nitriding gas. The bulk of the material exhibits a martensitic microstructure, and the diffusion kinetics of nitrogen atoms in the substrate determines the microstructure of the diffusion layer. The diffusion layer's depth depends on the nitriding treatment's time and temperature.

2.6.2 M50 steel

M50 steel exhibits a dendritic microstructure at low magnification, mainly composed of martensite and carbides as we can observed in Fig.2.3, when observed at higher magnifications. The carbides include partially dissolved primary carbides, which are slightly larger and more numerous in the center of the cylinder, and small globular carbides distributed in the matrix that form during cooling at the quenching outlet. The appearance of martensite suggests that residual austenite may have existed after quenching and was destabilized by tempering operations.
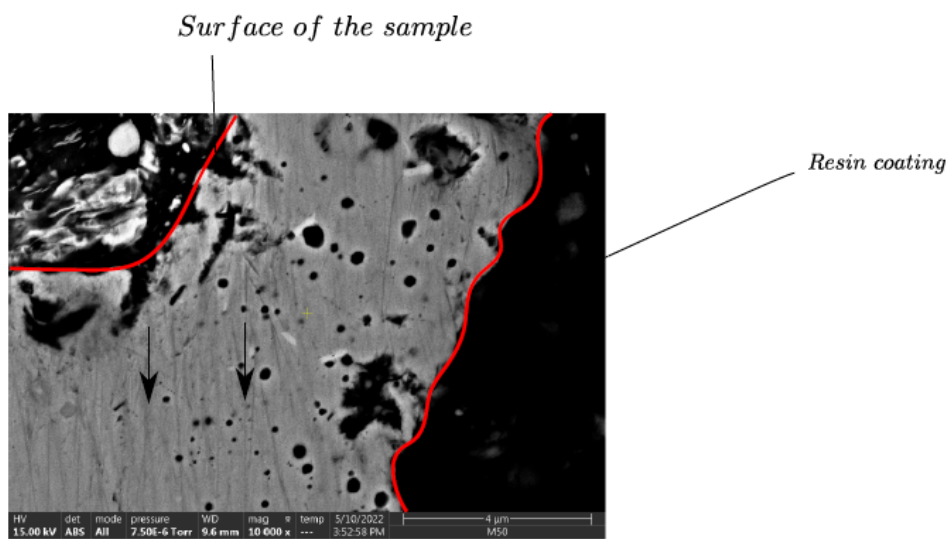
Figure 2.3: Typical micrograph of a quenching M50 steel and its SEM observation

2.6.3 M50NiL steel

At low magnification (x10), the cemented layer of the M50NiL steel is easily recognizable in the form of a light gray ring. The global microstructure consists of a martensitic matrix on all the sections examined as illustrated in Fig.2.4. The observation at higher magnifications (x200 - x500)and with the SEM highlights the microstructural differences between the edge of the sample (in the hardened layer), the interfacial zone between the hardened layer and the core of the sample, and the center of the sample.With regard to carburizing zone, two layers can be distinguished: a first layer of intragranular carburization followed by a second layer of intergranular carburization. The cemented layer is characterized by carbides located preferentially at the old austenitic grain boundaries. The interfacial zone (cemented layer-core) is composed of a martensitic structure free of carbide. Finally, in the

center of the sample (the core), a martensitic structure is also observed, with the presence of an intergranular precipitation phenomenon (marked grain boundaries).
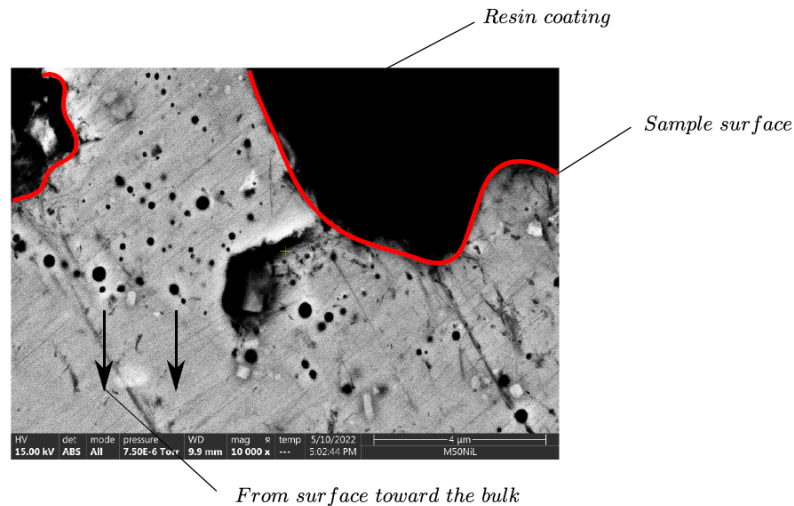
Figure 2.4: Typical micrograph of a carburizing M50NiL steel and its SEM observation with presence of carburized layer

2.6.4 M50NiLDH steel

The M50NiLDH material has a complex microstructure, with multiple layers formed through carburation and nitriding treatments as presented in Fig.2.5. The surface layer appears to have been treated with a combination of carburation and nitriding, resulting in a microstructure exhibiting characteristics of both treatments, including nitrided and carburized layers. Underneath this combination layer is a carburized layer extending down to the bulk material. The microstructure of the bulk material is mainly martensitic. Overall, the microstructure of M50NiLDH is likely to be more complex than that of M50NiL or M50 steel due to the multiple layers and treatments involved.

The nitriding treatment occurring after quenching on steel, the result is a matrix that will be overall martensitic (microstructure in the form of slats or needles) with residual austenite. In the nitrided parts, we will distinguish two main layers: the white combination layer on the surface, which extends over approximately 30 microns in depth, and the diffusion layer, which extends from below the diffusion layer towards the inside of the material, as can be seen in Fig.2.2.

2.6.5 Synthesis

The heat treatment diffused an insertion atom into the bulk of the studied materials, such as 32CrMoV13, M50, M50NiL, and M50NiLDH. In the case of M50 steel, which

66
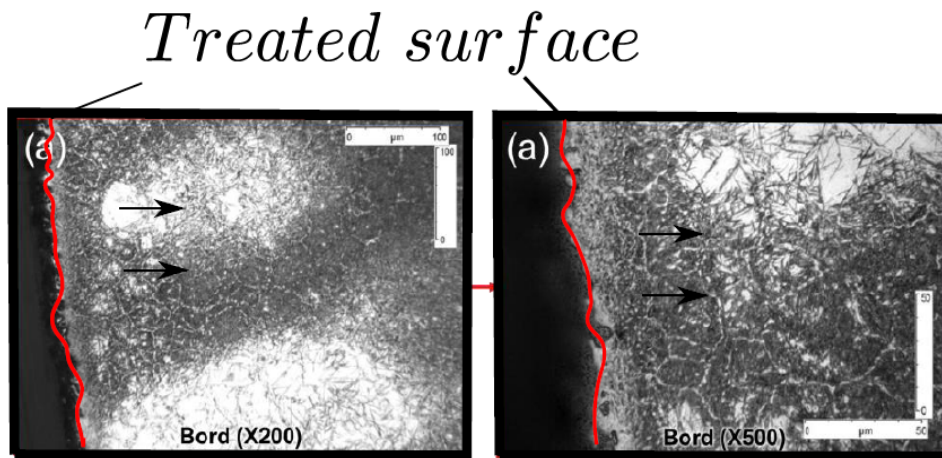
Figure 2.5: Typical micrograph of a carburizing M50NiL steel and its SEM observation with presence of carburized layer

was quenched in mass, its global properties were enhanced, and the appearance of gradient properties in the other materials (32CrMoV13, M50NiL, M50NiLDH). The microstructure of all the materials was globally martensitic in bulk, with either a nitriding or carburizing layer on the surface of the samples. Here it has been noted that there are variations in the level of treatment in different areas of the samples. However, the management of sample processing is outside the scope of this thesis, so we have used the samples as received. To identify the influence of heat treatment on these materials, appropriate characterization tests need to be conducted to track the evolution of the properties from the surface to the material's bulk. The nanoindentation test protocol can be used to track this gradient of properties at this scale

2.6.6 Material mechanical properties

Determining mechanical properties, such as hardness and elastic modulus, from indentation testing requires accurately calculating the contact area between the indenter and the sample. The shape and size of the indenter tip and the penetration depth into the sample all influence the contact area and, therefore, the mechanical properties derived from the indentation test. Therefore, accurate characterization of the indent geometry is crucial for obtaining reliable mechanical property measurements.

The contact area can be defined as the surface of the indent in contact with the sample or as the projection of the contact area developed on the surface of the sample. The contact height is the depth of the indentation, which can be measured using the displacement sensor on the indentation instrument. The contact area is an important parameter in determining the hardness of the sample. An accurate determination of the contact area is necessary to measure the mechanical proper-

67

ties of the material being tested precisely. The contact area can be calculated by measuring the depth of penetration (h) and the contact height (h_c) and using them to determine the contact area. This can be done using mathematical models, such as the Oliver-Pharr method (OLI 92) or the Hertzian contact theory, which relate the contact area to the indentation depth and contact height. The contact area can also be determined experimentally by measuring the size of the residual indent left on the sample's surface after the tip has been withdrawn.

Hardness is an important mechanical characteristic of a material that cannot be measured directly but is derived from other measurable quantities such as the test force, penetration depth, or indentation area. Various hardness testing methods, such as Vickers, Brinell, Knoop, Rockwell, etc., all follow the same principle of applying a known force to a punch (usually made of diamond) and measuring the resulting indentation. The conventional hardness value is then calculated as the ratio of the maximum force applied and the contact area between the indent and the surface.

2.7 Nanoindentation protocol

The principle of nanoindentation is based on pressing a sharp and rigid indenter (usually made of diamond) into the material's surface under a controlled load while continuously measuring the penetration depth and load applied. The force is typically applied with a continuously increasing load and then held for a specified period of time before being withdrawn. As the indenter penetrates the surface of the material, the load and depth of penetration are recorded, allowing for the calculation of various mechanical properties of the material, such as hardness, modulus, and yield strength. The analysis of the load-depth curve obtained from the nanoindentation test involves modeling the indentation process with an appropriate mathematical model to extract mechanical properties.

The nanoindentation tests are performed perpendicular to the treated surfaces following positions (a), (b), and (c), as shown in Fig.2.6. The Nanoindentation tests are carried out using a specialized instrument called the Nanoindentor G200, which Agilent Technologies manufacture. The tests are conducted at the Mateis laboratory located in INSA de Lyon. The Nanoindentor G200 is a high-precision instrument designed to measure materials' mechanical properties at the nanoscale. It uses a small probe with a sharp tip to indent the surface of a sample and measure its response to the applied load.

The "G-series hardness and modulus via load control cycles" method with the CSM stiffness measurement method is a well-established method for nanoindentation testing. However, this study modified the G-series(hmlcc) method into a single

load and unload cycle, allowing for more precise and controlled measurements. With the modified method, the maximum load imposed is 600 mN. This means the load gradually increased until it reached 600 mN, then decreased to zero. The indentation depth was measured during both the loading and unloading stages.

The nanoindentor device is typically composed of three main parts as illustrated in Fig.2.7:

❊ Column optics: This part of the device typically includes a microscope or other optical system to allow the operator to position and align the sample and the indenter accurately. It include lighting systems to ensure proper sample illumination and indenter illumination.

❊ Displacement table: This part of the device includes a mechanism for precisely controlling the movement of the sample relative to the indenter. This allows the operator to accurately position the sample and control the depth of the indentation.

❊ Indentation column: This part includes the indenter itself, which may be spherical, Vickers, Knoop, or other indenter types. The indentation column also typically includes a load cell to measure the force applied to the indenter during the indentation process.

These components allow the operator to apply a controlled load to the sample and measure the resulting indentation depth.
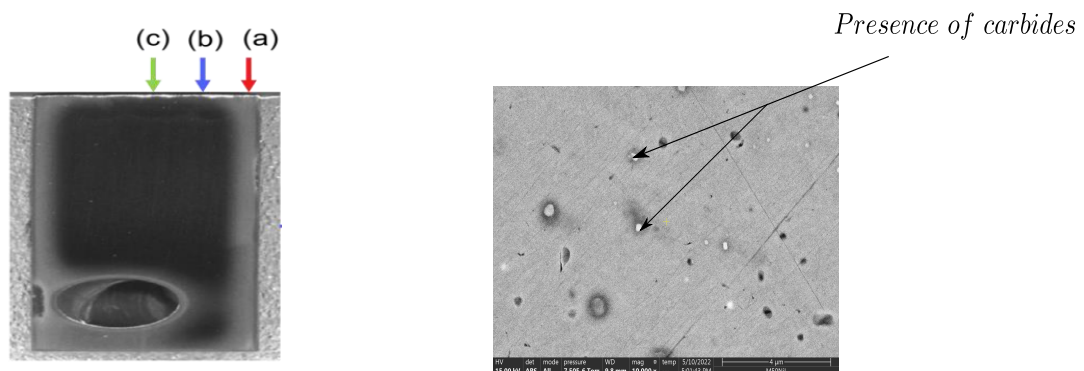
Figure 2.6: 1)Sample example with peripheral surface areas treated. identification of three treated areas a) b) c) 2)Presence of carbides in the treated material M50

Nanoindentation is a sensitive technique that requires careful execution and post-processing. The tip material and geometry choice is important for generating a homogeneous stress field and facilitating simulation. In this case, a spherical diamond tip of diameter 100 μm was used, with Young's modulus of 1100 GPa and a Poisson's ratio of 0.1. The tests were performed in load-controlled mode, with a maximum

69

load of 600 mN, and at least two indents were made at each depth to ensure repeatability. To avoid mutual influences, the distance between neighbor indentations was 100 μm. Calibration of the machine with a reference material, such as fused silica, was necessary, and the surfaces of the samples needed to be flat. The thermal drift threshold is also required to be low. Despite the relative simplicity of the technique, the interpretation and post-processing of the results were often delicate, requiring correction of the initial curve and several correction processes after the tests.
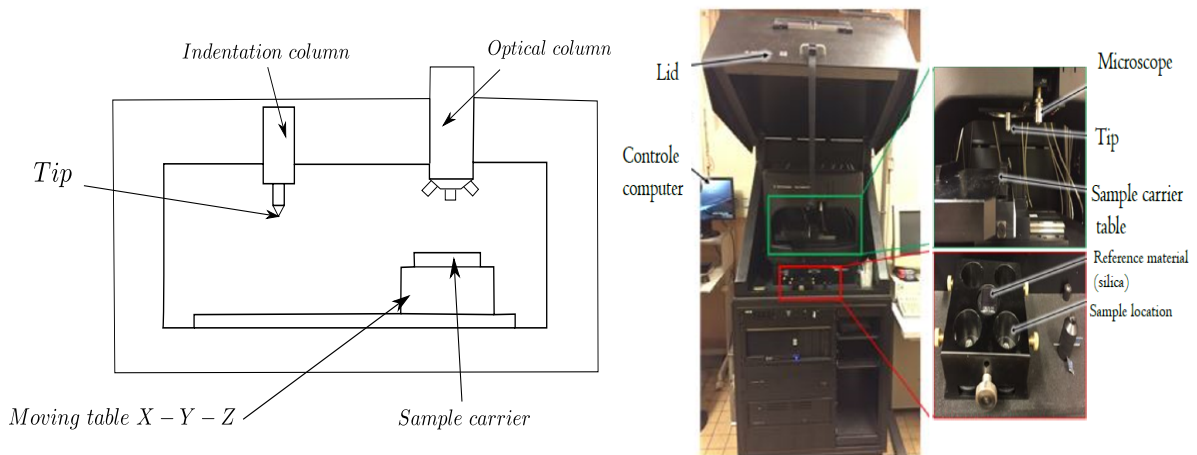
Figure 2.7: Nanoindentor machine presentation

2.7.1 Nanoindentation curve correction

To take into account the producibility of the data, a curve average is calculated over each sample depth as shown in Fig.2.8(a).

Correcting nanoindentation curves is typically done in three main steps. The first step involves making a point of contact coincide with the origin of the axes and aligning the beginning of the curve with the elastic Hertz curve of the material. This is done by subtracting the initial displacement of the piezoelectric sensor from the total displacement to obtain the true displacement of the indenter. The elastic Hertz curve is then simulated based on the geometry of the indenter and the material's mechanical properties. Finally, the initial part of the measured curve is fitted to this simulated curve to obtain the indentation depth at the start of the plastic deformation regime. The second step involves correcting for the compliance of the machine. The machine's compliance is typically determined by performing a reference measurement on a stiff material, such as fused silica, and comparing the measured stiffness to the known stiffness of the material. The determination of the stiffness of the machine is crucial for correcting the nanoindentation curves. One method to determine the stiffness of the device is to perform several nanoindentation

70
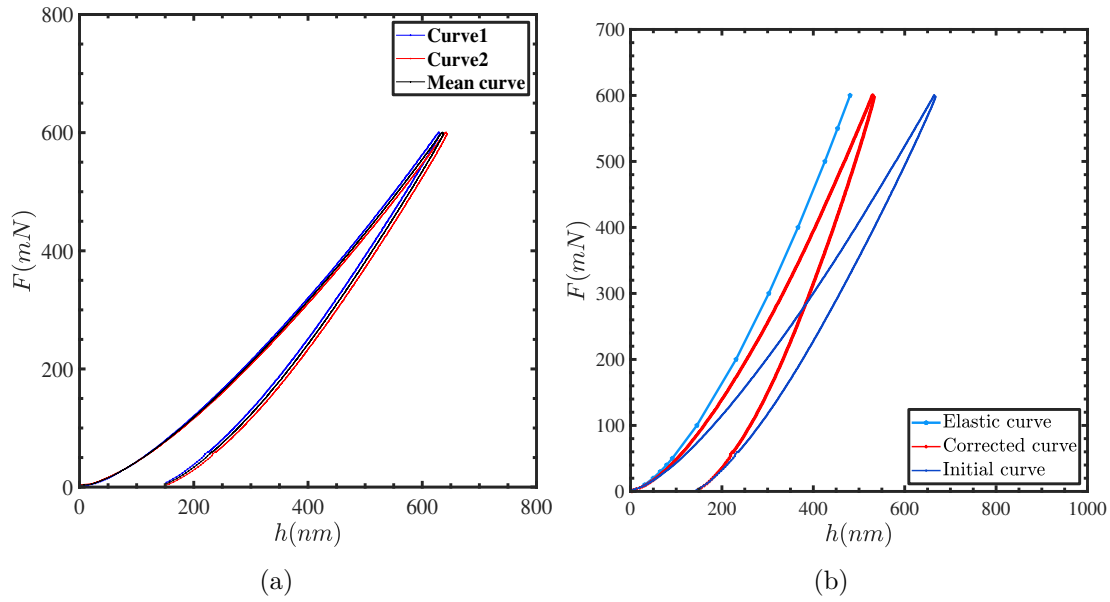
Figure 2.8: (a)Mean of data on one sample (b) Comparison between initial and corrected nanoindentation curve

tests on a reference material, such as fused silica. The point of intersection of the curve (stiffness-displacement) with the axis of the stiffness gives the stiffness of the machine, which can then be used to correct the indentation curves as illustrated in Fig.2.8. Another iterative method consists of varying the stiffness of the indentation curve of the reference material until obtaining the known elastic modulus of the material, which is $E = 75\ GPa$ for fused silica. This method can also be used to determine the stiffness of the machine. In this case, the machine stiffness was $K_m = 0.215 mN/nm$ with a linear correlation coefficient of $R^2 = 0.99$.

The correction for compliance is then applied to the force-displacement curve to obtain the true load-displacement curve as shown in Fig.2.9. Indeed the sample and the machine can be considered as the system of two springs in series whose stiffness is given by the relation:

$$\frac{1}{K_t} = \frac{1}{K_s} + \frac{1}{K_m} \tag{2.1}$$

Where K_t, K_s and K_m is respectively the stiffness of the system, of the sample and the machine.

The surfaces of our samples not being perfectly flat on the nanometric scale. To overcome the problems of flatness of the samples and the surface state, Young's modulus of our samples will be set at the value 210 GPa. Thus the determination of the modulus by adjustment of the unloading curve will make it possible to correct the curves.
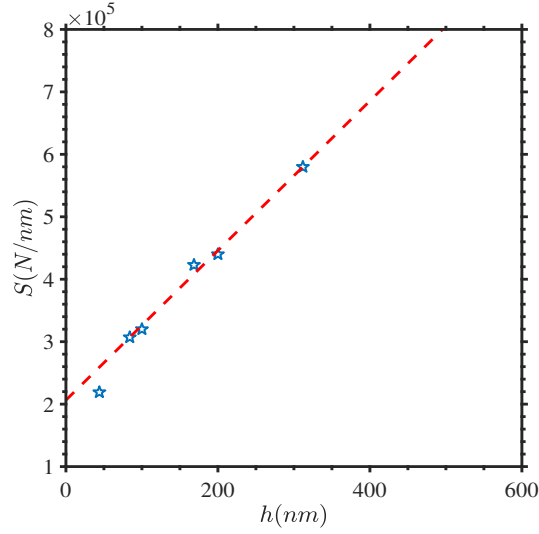
Figure 2.9: Determination of the machine (nanoindentor) stiffness allowing the indentation curve correction.

2.8 Theoretical description

To determine mechanical properties such as hardness and modulus, the analytical methods of Oliver and Pharr (OLI 04; PHA 02) will be used.

2.8.1 Oliver-Pharr method

The Oliver and Pharr (OLI 92) method proposes to decompose the indentation depth h_m into two parts: the contact depth h_c and the remaining depth h_s, such that $h_m = h_c + h_s$. This allows for determining the contact area, which is required to calculate mechanical properties such as hardness and elastic modulus. This method is the most common method for establishing the projected contact area and predicting the elastic modulus. This method stipulates the adjustment of the unloading curve by a power law given by:

$$F = B\left(h - h_r\right)^m \tag{2.2}$$

Where h_r is the residual displacement after complete unloading. B and m are the parameters to be determined.

By differentiating the adjustment law concerning the height h, we obtain the stiffness which is given by the relation:

$$C = \left(\frac{dF}{dh}\right)_{h=h_{\max}} = Bm\left(h_{\max} - h_r\right)^{m-1} \tag{2.3}$$

Based on the contact stiffness of Eq.2.3, the contact height h_c is given by the expression:

72

$$h_c = h_{\max} - \varepsilon \frac{F_{\max}}{C} \tag{2.4}$$

Where ε is a constant parameter which depends on the indenter geometry. The value of this parameter is suggested to be 0.75 for the spherical indentor tip. From the contact height, the projected contact area can be calculated by the expression:

$$A_c = \pi h_c (2R - h_c) \tag{2.5}$$
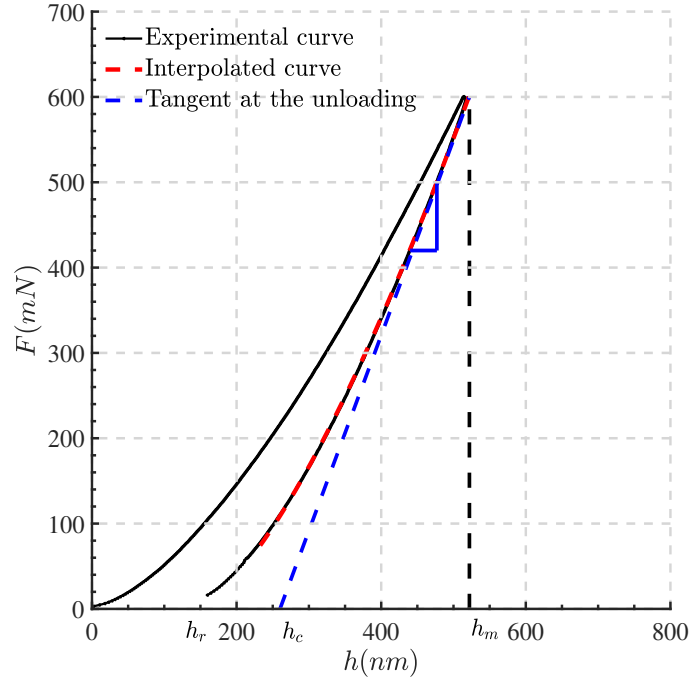
Figure 2.10: Indentation curve post-processing to determine the sample stiffness and the material modulus.

For an indentation curve, determining the modulus of elasticity involves determining the slope of the unloading curve as shown in Fig.2.10 because the unloading is purely elastic. This determination method is based on Hertz's theory. The development of the method will be made later by Sneddon (SNE 65), which makes it possible to express the reduced modulus in the function of the slope at the beginning of the unloading by:

$$E^* = \frac{\sqrt{\pi} C}{2\sqrt{A}} \tag{2.6}$$

This expression will be extended later to the cases of all indentors of a circular section by the introduction of a corrective factor β by King (O'S 88) to take into account the non-axisymmetric of the indentor. The corrected reduced modulus is given by:

73

$$E^* = \frac{\sqrt{\pi}C}{2\beta\sqrt{A}} \tag{2.7}$$

In our case, the used tip is spherical and axisymmetric so the factor $\beta = 1$. Then the modulus of elasticity of the sample is given by:

$$E_s = (1 - v_s^2)\left[\frac{1}{E^*} - \frac{1 - v_i^2}{E_i}\right]^{-1} \tag{2.8}$$

Where E_i and v_i designate respectively the modulus of elasticity and the Poisson's ratio of the indentor while the E_s and v_s designate the modulus and the Poisson's ratio of the sample.

The last step is therefore to determine the hardness which is given by the expression:

$$H = \frac{F_m}{A_c} \tag{2.9}$$

Using analytical methods like the one proposed by Oliver Pharr enables the determination of mechanical properties such as Young's modulus and hardness. Nevertheless, establishing a behavioral law in reverse remains highly intricate and necessitates applying an inverse approach.

2.9 Resolution by inverse approach

The inverse analysis is a numerical method that allows the determination of the material parameters of a constitutive model from the experimental data, such as the force-displacement curves obtained from nanoindentation tests. The principle of this method is to minimize the difference between the experimental results and the results obtained by simulation using a numerical model with a specific constitutive model. This minimization is done by adjusting the values of the material parameters until the difference between the experimental and simulated results is minimized. The inverse analysis is a powerful tool for determining material properties, especially in cases where experimental data is limited. However, it requires a good understanding of the physical phenomena involved and a suitable constitutive model that accurately represents the behavior of the material under study.

Typically, the inverse identification method is used to determine the constitutive law of a material from the force-displacement [F-h] curves obtained through nanoindentation tests (DAO 01; BUC 03; MEN 16). This approach involves solving the indentation problem using a contact resolution code, comparing the resulting numerical [F-h] curve with the experimental data, and identifying the parameters to minimize the error between the two responses. A sophisticated optimization algorithm, such as the Sequential Quadratic Programming (SQP) algorithm implemented in Matlab, is typically used for this purpose (KLE 93; Mat 02; NOC 06).

Sequential Quadratic Programming (SQP) is a nonlinear optimization algorithm that minimizes a differentiable function subject to constraints. It is particularly useful for solving problems with equality and inequality constraints. The algorithm starts by forming an approximation of the objective function and the constraints using a quadratic model. Then, it solves the quadratic programming subproblem to find a search direction and updates the approximation of the objective function and constraints based on the new point. This process is repeated until a termination criterion is met, such as achieving the desired accuracy or reaching a maximum number of iterations. SQP is known for its fast convergence, especially for problems with few variables and constraints.

The objective function is minimized using the least squares regression method. The least squares regression method minimizes the sum of the squared errors between the predicted and actual values of the dependent variable. For example, in the case of material constitutive law identification from nanoindentation data, the objective function is typically the sum of the squared differences between the experimental force-displacement [F-h] curve and the [F-h] curve predicted by the constitutive law, with the material parameters to be identified as the optimization variables. The objective function expression is given by the expression:

$$e_r^2 = \frac{1}{N^2} \sum_{i=1}^{N} \left(\widehat{h}_{expi} - h_{numi} \right)^2 \tag{2.10}$$

where $\widehat{h}_{expi}$ and h_{numi} represent respectively the experimental displacement and the numerical displacement.

To simulate the contact problem, the multiphysics contact resolution code called Isaac, developed in the Lamcos laboratory of INSA Lyon to model the contact problem between the spherical tip and the samples, is used. This code uses a semi-analytical formulation and can handle complex contact problems (GAL 10; KOU 15a). The mechanical behavior of the materials will be assumed to be elasto-plastic, with an isotropic and constant elastic behavior characterized by Young's modulus of 210 GPa and a Poisson's coefficient of 0.30. In this analysis, we will adopt a power law relation to describe the hardening work phenomenon, following the Swift isotropic hardening plastic law expressed by the relation:

$$\sigma = B(C + \varepsilon_p 10^6)^n \tag{2.11}$$

Where B, C, and n are three parameters to be identified. B is a strength parameter while C and n are material hardening parameters. To initiate the minimization analysis, a set of Swift plastic hardening parameters from literature (JAC 01) were utilized for numerical simulations. The initial parameters used were $B = 1280$ MPa, $C = 4$, and $n = 0.095$ for M50, M50NiL, and M50NiLDH steels, and $B = 1840$ MPa, $C = 16$, $n = 0.067$ for 32CrMoV13 steel as surface parameters. The flowchart

in Fig.2.11 illustrates the problem-solving approach, which involves defining the initial material parameter values, solving the contact problem using the Isaac code, and minimizing the error between the experimental and numerical curves until the objective function is minimized, thereby providing the solution parameter set.
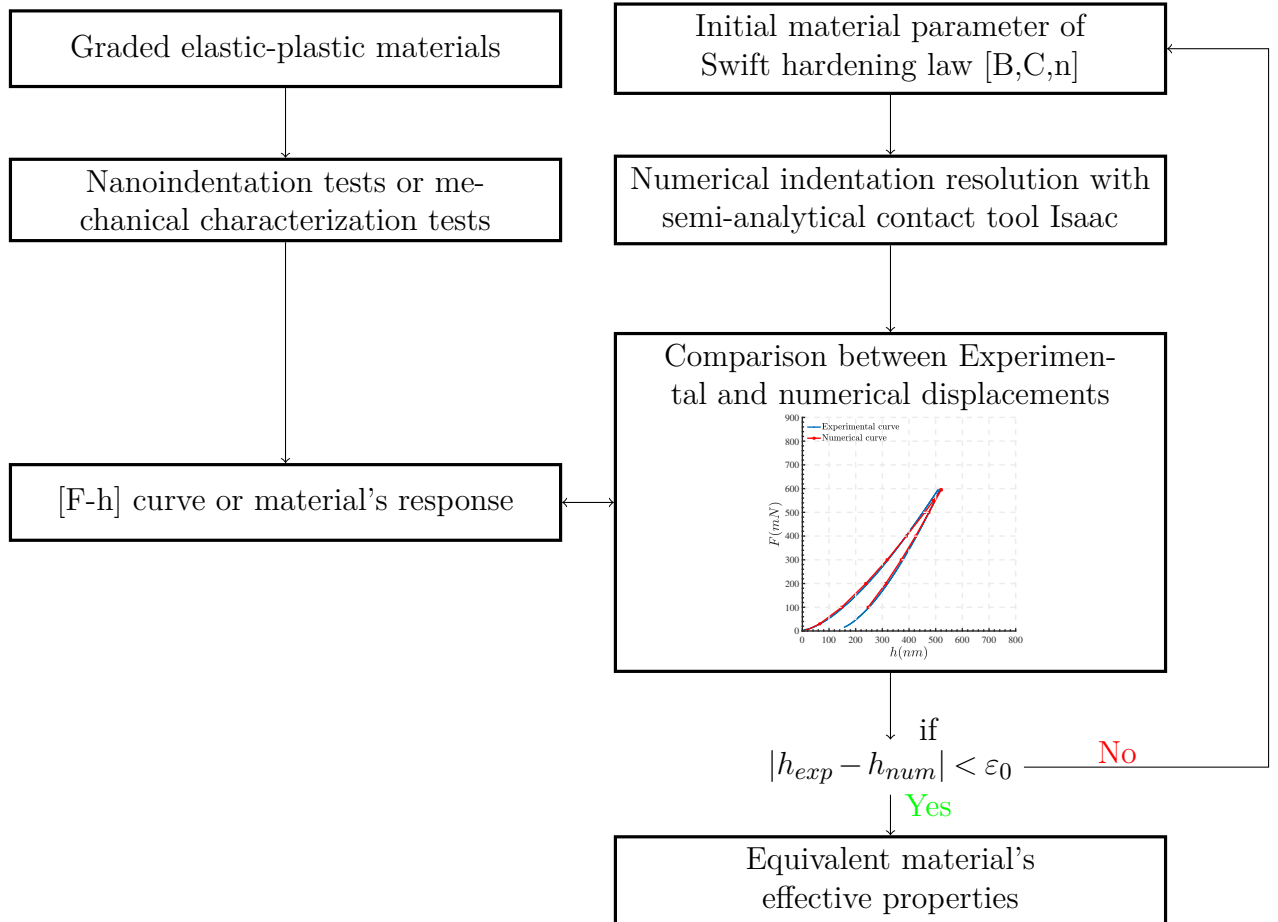
Figure 2.11: General algorithm for solving the indentation Contact Problem with an inverse approach.

2.10 Results

In this section, the results of the different methods (analytical and numerical) are presented.

2.10.1 Analytical method results

Using the analytical techniques developed by Oliver and Pharr (PHA 02), a microhardness profile was obtained for the different steel grades. The microhardness

profile for M50 steel shows a nearly constant value, as depicted in Fig.2.12. Based on the microhardness results obtained for M50, an average hardness value of $H = 5\,GPa$ and a standard deviation of $0.02\,GPa$ were identified for the measurements. The standard deviation value will account for the variation in microhardness measurements for the other steel samples.

Figure.2.12 displays the variation of microhardness in the 32CrMoV13 sample, revealing a gradient in microhardness ranging from $5.5\,GPa$ at the surface to $4.1\,GPa$ in the inner part of the material. Based on this result, the steel nitriding depth can be determined to be $150\,\mu m$.
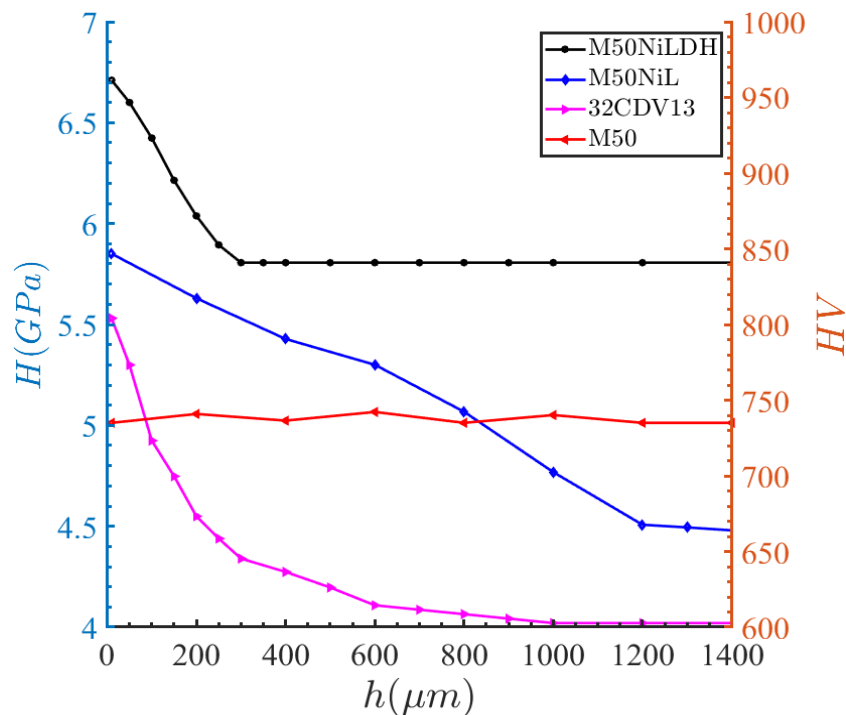
Figure 2.12: (a) Gradient evolution through the materials illustrastion , (b)Material micro-hardness filiation from surface to the bulk.

The microhardness profile of the M50NiL steel also exhibits a gradient, with a surface microhardness of $5.89\,GPa$ decreasing to $4.6\,GPa$ at the center of the material, as depicted in Fig.2.12. This indicates a carburization depth of approximately $1\,mm$. Here we observe a similar microhardness gradient in M50NiLDH steel, with a surface microhardness of $6.55\,GPa$ decreasing to $5.89\,GPa$ in the heart of the material, indicating a microhardness depth gradient of about $100\,\mu m$. A cross-treatment can be observed, which introduced M50NiL properties into the bulk material of this steel. The gradient shown in Fig.2.12 may give the impression that it is the gradient of the carbonitrided zone, while the cementation appears uniform throughout the sample. When considering a Vickers indentation, the hardness is typically given by the Vickers hardness number (HV). The HV is calculated by dividing the load

applied to the indenter by the surface area of the indentation. The formula for calculating the Vickers hardness number is given by:

$$HV = \frac{2P\sin(\frac{136}{2})}{d^2} = 1.8544\frac{P}{d^2} \tag{2.12}$$

By assuming that the average diameter of the imprints is equivalent between the spherical and the pyramidal tip, we obtain the following relationship between Vickers hardness (HV) and standard hardness in MPa:

$$HV = 0.147H(MPa) \tag{2.13}$$

Figure.2.12, gives a comparison of the hardness for different steel grades.

✴ The carbonitrided M50NiLDH steel has the highest surface and undercoat hardness. This can be attributed to the carbonitriding treatment performed on the steel. Additionally, crossing the carburizing treatments in the zones located in the center of the material creates almost homogeneous properties in these zones, leading to an even higher level of hardness.

✴ In the second place, the carburized M50NiL steel also has a good level of surface hardness.

✴ The nitrided 32CrMoV13 steel is in third place, with a good level of surface hardness that is better above the homogeneous properties of M50 quenched steel.

2.10.2 Approximation of the micro-hardness level of heat treatments

For this approximation, it is essential to note that approximating the micro-hardness level due to thermo-chemical treatments is a complex process that requires careful consideration of various factors, including the composition of the material, the heat treatment parameters, and the testing methodology. It is also important to ensure that the testing conditions are standardized and repeatable to produce accurate and reliable results. So in this analysis, we consider the Safran heat treatment standard condition of bearing metals to approximate the micro-hardness levels of steel due to heat treatments. By deploying this approximation, the approximate hardness value at different material depths based on the heat treatment conditions can be estimated. This information can be useful for determining the optimal heat treatment conditions for a specific application and for predicting the material's mechanical properties after heat treatment.

2.10.2.1   Approximation of nitriding treatment

The following equation can express the approximation of the nitriding micro-hardness with the nitriding depth:

$$HV(h) = a_n(h - h_{maxn}) + H_{0n} + 100 \qquad (2.14)$$

According to the nitrided samples used in this study, the approximated hardness law is given by:

$$HV(h) = -700(h - h_{maxn}) + H_{0n} + 100 \qquad (2.15)$$

Furthermore, an exponential approximation can be established to consider the curvature of the hardness filiation. For example, the following equation can express this approximation:

$$HV(h) = H_{0n} + 100 + a_n\left[1 - \exp(-k_n(h - h_{maxn}))\right] \qquad (2.16)$$

Where HV is the Vickers hardness at a given depth h, a_n in $HV.\mu m^{-1}$ is the slope in the linear regression case, h_{maxn} is the maximum nitriding height in micron, H_{0n} is the bulk material hardness. In the case of an exponential regression, a_n in HV, exp is the exponential function and k_n is the exponential evolution parameter according to the treatment condition in μm^{-1}. This equation assumes that the hardness increases exponentially with depth, which may be a better approximation for cases where the hardness curve is not linear. The constants a_n and k_n can be determined by fitting the equation to experimental data using regression analysis.

2.10.2.2   Approximation of carburizing treatment

The linear approximation of the hardness evolution with the treatment depth in the case of carburizing can be expressed as:

$$HV(h) = a_c(h - h_{maxc}) + H_{0c} \qquad (2.17)$$

According to our carburized samples, the approximated hardness law is given by:

$$HV(h) = -150(h - h_{maxc}) + 651 \qquad (2.18)$$

The exponential approximation of the hardness evolution with the treatment depth for carburizing can be expressed as:

$$HV(h) = H_{0c} + a_c\left[1 - \exp(-k_c(h - h_{maxc}))\right] \qquad (2.19)$$

With a_c in $HV.\mu m^{-1}$ is the slope of the line or in HV for the exponential case, h_{maxc} is the maximum carburizing height, H_{0c} is the bulk material hardness, and k_c is the exponential evolution parameter according to the treatment condition in μm^{-1}.

2.10.2.3 Approximation of carbonitriding treatment

In the case of carbonitriding, carburizing, and nitriding treatments are used to increase the hardness level in the treated zone. This results in a high gradient of properties from the surface to the bulk material. In the concerned zone, the hardness level linear approximation would be:

$$HV(h) = a_c(h - h_{maxc}) + a_n(h - h_{maxn}) + H_{0n} + 100 \qquad (2.20)$$

The exponential approximation would be:

$$HV(h) = H_{0n} + 100 + a_{cn}\left[1 - \exp(-k_{cn}(h - h_{maxcn}))\right] \qquad (2.21)$$

With $a_{cn} = -1000 HV.\mu m^{-1}$ the carbonitriding slope in the linear case, h_{maxcn} is the maximum carbonitriding height, H_{0n} is the bulk material hardness, and k_{cn} is the exponential evolution parameter according to the treatment condition in μm^{-1}.

2.10.3 Inverse approach results

This section will present the results of identifying the constitutive law by inverse analysis. Before that, we will first present the results of a sensitivity study that was carried out on the different sets of initial parameters. This study was conducted to determine the sensitivity of the inverse analysis to the choice of initial parameters. The results of this sensitivity study will help us understand the impact of the different parameters on the accuracy and reliability of the inverse analysis results.

2.10.3.1 Determination of the most sensitive constitutive law parameters

The sensitivity study involved varying the initial parameters of the constitutive law model over a range of values and analyzing the resulting changes in the identified material parameters. This was done for four steel grades: 32CrMoV13, M50, M50NiL, and M50NiLDH. Variations were made in the parameters' initial values related to the material's hardening behavior, such as the yield strength, the work hardening coefficient, and the strain hardening exponent.

The study revealed that for the samples with initial parameters [B, C, n], the B parameter varied significantly, the n parameter varied moderately, and the parameters converged towards 0.045. On the other hand, the C parameter remained almost constant. Therefore, for the identification process, the C parameter will be fixed at $C = 4$ and the n parameter at $n = 0.045$, while only the B parameter will vary to finalize the identification of the material laws. Since this optimization problem is convex, it lacks a global minimum, which implies that there are multiple parameters solutions.

2.10.3.2 Determination of constitutive law parameters

The Swift plastic law parameters $[B, C, n]$ have been identified for each [F-h] curve corresponding to the indentation data of the different steel samples. For the M50 steel, which has a homogeneous microhardness distribution, the Swift law parameters were determined to be $B = 1300 MPa \pm 20$, $C = 4$, and $n = 0.045$. Using this identification, a relative error of ± 20 MPa was estimated for parameter B, considering all errors made on the three parameters. This relative error value will be applied to the other steel samples. The identified parameters were then used to fit the indentation data for each graded material, as shown by the fitted curves in Fig.2.13.
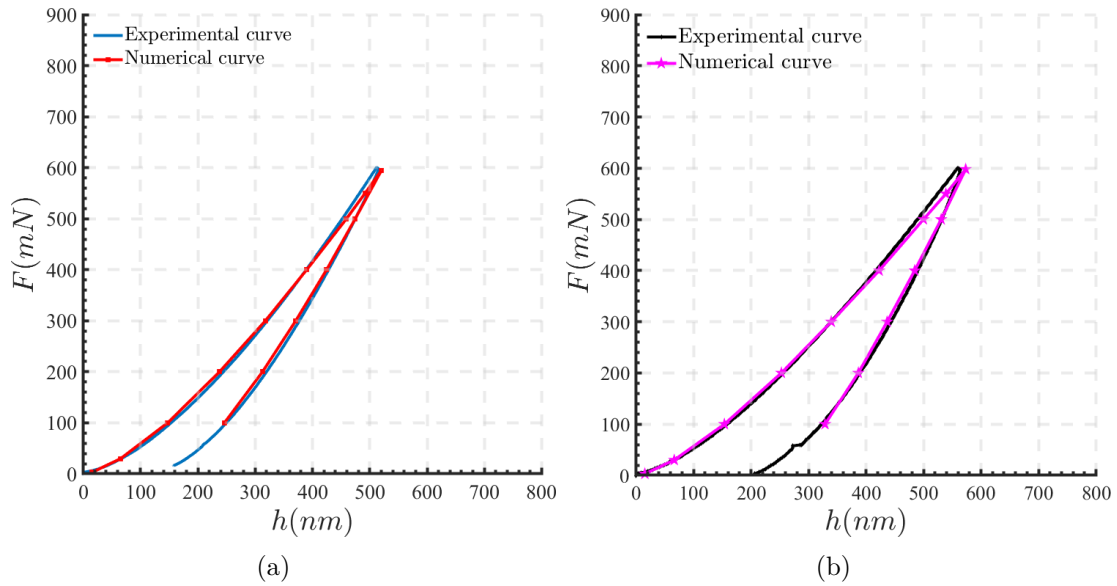
Figure 2.13: Fitting curve allowing the determination of the Swift's plastic law parameters (a) M50NiLDH steel at h=100 μm, (b) 32CrMoV13 steel h=100 μm.

Thus the Tables.2.5,2.6,2.7 present respectively the evolution of the parameters according to the depth in the 32CrMoV13 steel, M50NiL steel, and M50NiLDH steel.

The identification of the parameters of Swift's plastic law according to the depth allows the writing of the law in the form:

$$\sigma_z = B_z(C + \varepsilon_p 10^6)^n \tag{2.22}$$

Where B_z represents the value of B according to the depth. Figure.2.14(a) compares the hardening curve in the different grades of steels, while Fig.2.14(b) shows the same comparison but at the heart of the different steels. These curves make it possible to follow the evolution of the hardening law according to the various thermochemical treatments applied and in the basic materials. With the hardness approximation

Table 2.5: The identified Swift's parameters trought the depht on the M50NiL steel.

| Height [μm] | Swift Law Parameters | | | Relative error | Yield strength |
	B [MPa]	C	n	%	σ_0 [MPa]
10	1500	4	0.045	1.53	1597
200	1420	4	0.045	1.53	1511
400	1340				1426
600	1290				1373
800	1265				1346
1000	1245				1325
1200	1215				1293
1300	1200				1277
1400	1200				1277

Table 2.6: The identified Swift's parameters trought the depht on the 32CrMoV13 steel

| Height [μm] | Swift Law Parameters | | | Relative error | Yield strength |
	B [MPa]	C	n	%	σ_0 [MPa]
10	1440	4	0.045	1.53	1533
50	1400	4	0.045	1.53	1490
100	1378				1467
150	1362				1450
200	1340				1426
250	1320				1405
300	1302				1386
400	1286				1369
500	1260				1341
600	1240				1320
700	1225				1304
800	1203				1280
900	1185				1261
1000	1175				1251
1100	1175				1251
1200	1175				1251

made in the previous section, it is possible to deduce the parameters of Swift's plastic law from the heat treatment depth. Furthermore, the B parameter was found to vary linearly with the depth, as it is related to the hardness. Therefore, an approximation of the B parameter can be expressed as a function of the depth,

Table 2.7: The identified Swift's parameters trought the depht on the M50NiLDH steel.

Height [μm]	Swift Law Parameters			Relative error	Yield strength
	B [MPa]	C	n	%	σ_0 [MPa]
10	2000	4	0.045	1.53	2129
50	1900	4	0.045	1.53	2022
100	1810				1927
150	1730				1841
200	1660				1767
250	1590				1692
300	1535				1634
400	1500				1597
500	1500				1597
1200	1500				1597

given by the following expression:

$$\frac{B_z}{B_0} = \frac{HV_z(h)}{HV_0} \tag{2.23}$$

The relationship between the treatment depth and Swift's law parameter B depends on the type of treatment and its characteristics. With the previous results we can estimate the value of B for a given material. This relationship can be helpful in predicting the mechanical behavior of the material under different loading conditions.

2.10.4 Synthesis

The sensitivity study on the parameters of the [F-h] curves showed that the identified parameter values were relatively stable. This means that the parameters of the Swift constitutive law, identified from the indentation tests, can be considered reliable. Additionally, a correspondence can be established between the identified parameters and the microhardness results of the different heat treatments performed on the steels. A correspondence between the results of microhardness and parameters of the law of behavior can be established via the following relation on the steels:

$$\sigma_{0m} \simeq \frac{H(MPa)}{3}$$

where σ_{0m} is the microlimit of elasticity at 20.10^{-6}m/m strains. The analysis shows a nearly perfect agreement between the microhardness results and the parameters of the behavior law, with only slight differences that can be attributed to uncertainties in the data and analysis. These uncertainties stem from three main sources: the first being the error introduced by the reaction time of the nanoindentor, which can affect the value of Young's modulus and the accuracy of the data. The second is related
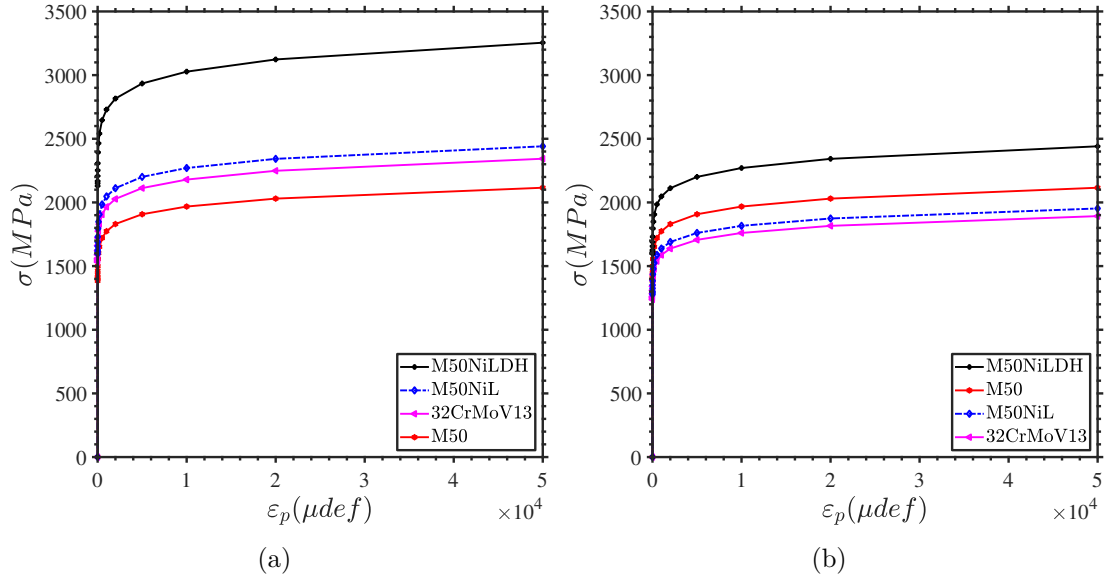
Figure 2.14: Swift hardening and constitutive law comparison of steels at surface (a) h=10 μm b) h=1500 μm

to the uncertainties in the optimization code used for the parameter estimation and the assumption that the hardening parameter n is fixed at 0.045 for all materials, even though it may vary slightly. However, the uniqueness of the solutions is not established in this study. The uncertainties in the results were evaluated. The third source of uncertainty is related to the indentation size effect (GAO 92).

The indentation size effect (ISE) is defined by an increase in stiffness as the indentation contact area decreases or the indentation scale decreases. So on a small scale, the materials seem harder than on a large scale. The indentor tip in the model was assumed to be spherical, while the true shape of the indenter tip may deviate significantly from this assumption. It is known that the hypothesis of an ideal tip geometry leads to substantial errors, leading to the need to calibrate each indenter tip to get the true contact area based on the indentation depth. The true geometry of the indenter tip may deviate significantly from the ideal assumption of a spherical tip, which can lead to substantial errors in determining the contact area and hence the measured properties of the material. Therefore, it is important to measure the real geometry of the tip and calibrate each indenter tip to get the true contact area based on the indentation depth. Therefore, this calibration was done, and the real geometry was measured. A numerical microscope observation was performed to evaluate the diameter of the spherical tip and identify any geometric defects, as depicted in Fig.2.15. This observation showed that the real diameter is 95.5 ± 2 μm . This value was found to be very close to the ideal tip diameter which value is 100 μm, indicating that the errors introduced by the tip geometry can be negligible. However, other factors, such as thermal drift, mechanical vibrations, fluctuations

in voltage, and frame stiffness, could affect the measured displacements during in-strumented indentation tests. These factors were all accounted for and eliminated through machine calibration.

(a)   (b)   (c)
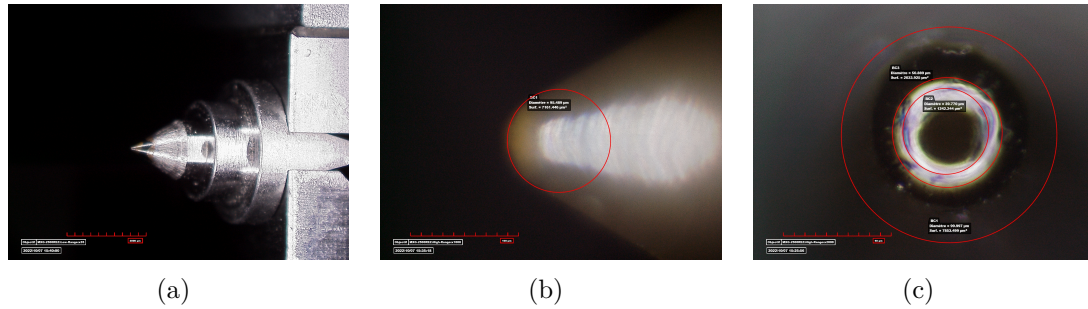
Figure 2.15: Different positions (a) (b) (c) of the indentation tip for its calibration.

The uncertainties related to the analysis can be at the origin of a strong variation of the parameter of hardening n which varies very strongly compared to the literature. The Swift's parameters obtained from the analysis were compared with those reported in the literature, and it was found that the values were very similar and in good agreement. However, there was a slight difference in the parameter values, which could be attributed to various factors such as measurement uncertainties, differences in the method of analysis, slight variations in material composition or heat treatment.

2.11   Behavior of materials under operating load

The purpose is to understand the deformation behavior of bearing materials when subjected to operating loads. Moreover, it is essential to investigate how the thermo-chemical treatment-induced gradient of properties influences this behavior. Additionally, understanding the plasticity evolution of the material under these operating loads is crucial. So to investigate the deformation behavior of the bearing material under operating load conditions, a loading simulation will be conducted. It is important to note that this simulation will not consider the effects of cross-heat treatments, and the property gradients being considered are those present in the service bearings. The M50 material is heat-treated in bulk using the identified properties from earlier analysis. First, the 32CrMoV13 material undergoes nitriding treatment to a depth of around 850 μm. Next, the M50NiL material is subjected to carburizing treatment to a depth of approximately 1mm. Finally, the M50NiLDH material is carburized to the same depth of about 1mm with surface nitriding treatment to roughly 150μm. The goal is to understand better how the material will deform and how its plasticity will evolve when subjected to these conditions.

This analysis is focused on simulating the contact between the rolling elements and the rings in a ball bearing. In this modeling, the contact is assumed to be ball-on-cylinder or annular linear contact. This type of contact allows for the representation of the contact zone and the maximum shear depth. This simplification is useful in modeling the behavior of the bearing material under operating conditions, as it provides a good approximation of the actual contact.

The elastoplastic behavior of the grade steel M50, 32CrMoV13, M50NiL, and M50NiLDH is analyzed in the contact between a sphere and a cylinder under a range of operating loads. All these materials follow Swift's elastoplastic law. The sphere has a diameter ϕ_1 of 20 mm with $\phi_1 > 0$, and the cylinder has a diameter ϕ_2 of 40 mm with $\phi_2 > 0$ and a length of $L = 100$ mm. The materials follow the elastoplastic constitutive law of Swift. The operating loads applied will range from 2 GPa to 7 GPa, and the behavior of each material will be noted at every loading step. Thus the pressure distribution and the materials' deformation will be analyzed. This contact problem is solved using the numerical code Isaac from LAMCOS at INSA Lyon.

When a load is applied to the materials, it is important to note that at a pressure of 2.5 GPa, all materials will undergo plastic deformation. This means they will change shape and permanently deform under the applied load. In this case, the M50 steel exhibits the highest level of plastic strains compared to the other materials. Additionally, the 32CDV13 steel deforms more than the M50NiL, which deforms more than the M50NiLDH, as illustrated in the Fig.2.16.

Figure.2.17 shows how the pressure field evolves for the different materials as they are loaded elasto-plastically. As the material becomes more plasticized, the pressure field's maximum value decreases, which means that it becomes smaller than the Hertzian elastic pressure. In other words, the more a material deforms plastically, the less it can withstand the same stress level without permanent deformation.
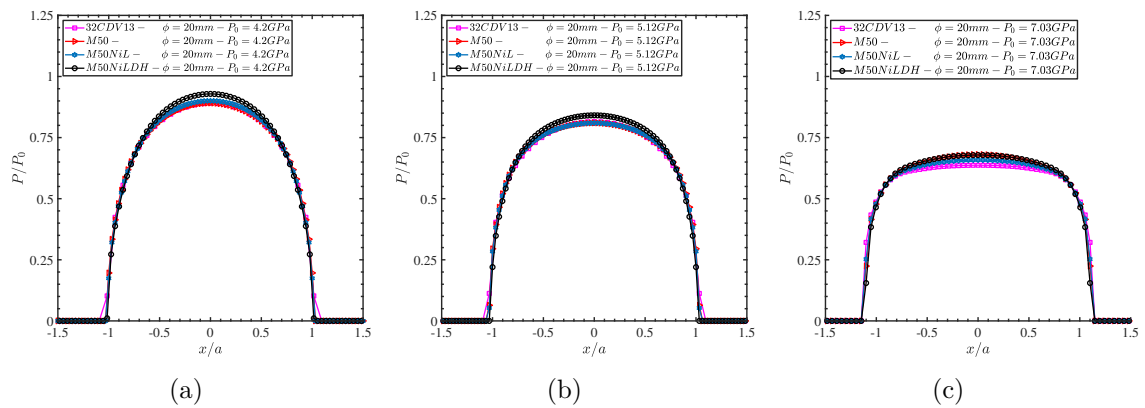
Figure 2.16: Elastoplastic pressure evolution in the materials at a)$P_0 = 4.2GPa$ b)$P_0 = 5.12GPa$ c)$P_0 = 7.03GPa$

When the load is increased gradually up to 4 GPa, it can be observed that the

M50NiLDH material has a higher resistance and deforms less compared to the other three materials. The deformations of the other three materials are almost the same. Upon closer examination, it can be noticed that the 32CDV13 material starts to deform more than the M50, while the M50NiL material deforms less than the M50. Figure.2.16 presents the evolution of the contact pressure distribution as a function of the residual displacement normalized by the contact radius associated with each loading level.
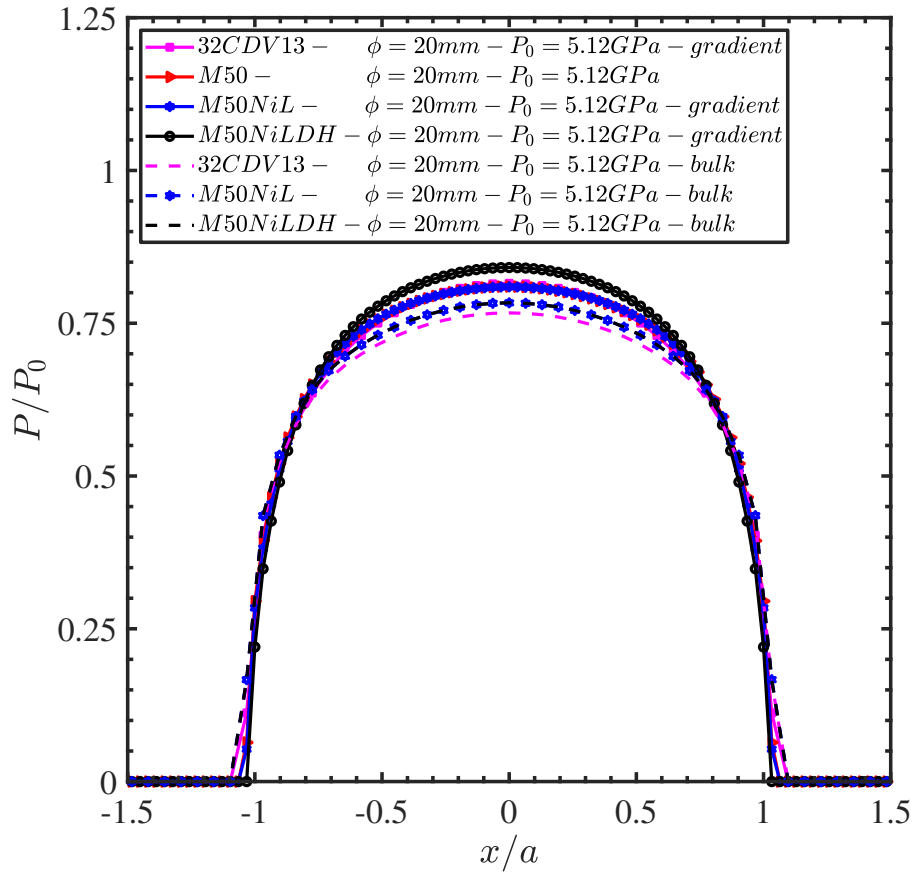
Figure 2.17: Elastoplastic pressure evolution in the materials at Hertz pressure $P_0 = 5.12 GPa$ for the property gradient materials against the bulk one

At a loading of 4.8 GPa, it becomes apparent from Fig.2.17 that the M50NiL material experiences a significant amount of plastic deformation and, as a result, begins to deform more than both M50 and M50NiLDH, which still show better resistance as shown in the Fig.2.18. However, at approximately 6.6 GPa, M50NiLDH starts to deform more than M50, causing M50 to become the most resistant material for loading levels beyond 6.6 GPa as shown in Fig.2.18.

The M50 material's good resistance to high loading can be attributed to its good surface and core properties. As the loading levels increase and more layers of material are solicited in-depth, the quality of the core properties becomes crucial.

However, for low loading that only requires a small amount of material in the treated layer, the surface properties can be used to model the material's behavior against surface attacks.

To show the influence of the heat treatment, a comparison between the behavior of materials that have undergone thermochemical treatments and their base materials (core materials) under operating conditions is made. The comparison shows that the treated materials have better resistance. Specifically, in the pressure range of $3.5 - 5.2\ GPa$, the level of residual deformation for M50NiLDH can reach up to 0.4 times that of the core material. For M50NiL, the level of deformation can reach up to 0.6 times that of the core material, and for 32CrMoV13, it can go up to 0.7 times that of the core material.

It is crucial to ensure that the shear height is within the treated layer to ensure the validity and applicability of the material response results. The depth of heat treatment divided by the smallest contact radius must be greater than or equal to 1. The shear height refers to the depth of maximum shear stresses during indentation loading, which is usually determined by the size and shape of the indenter used. For example, the maximum shear depth of bearings is 0.8a under operating conditions. However, outside this layer, it can be essential to consider other complex phenomena, such as interface problems..., that may occur in the material response.
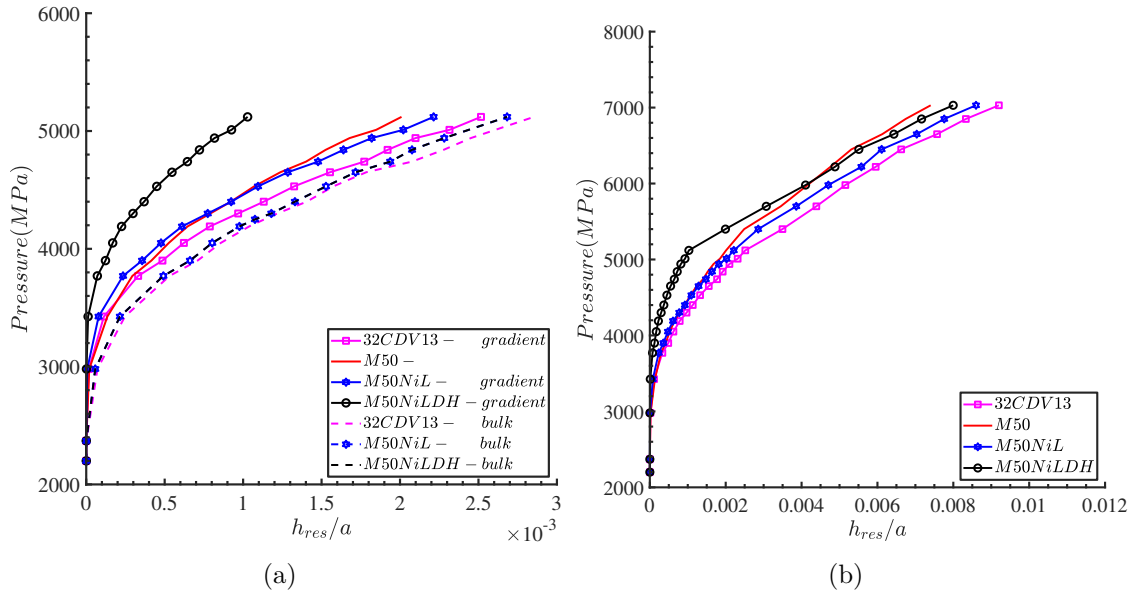
Figure 2.18: Evolution of the pressure with the residual displacement (a) Hertz pressure $P_0 = 2 - 5$GPa (b) Hertz pressure $P_0 = 2 - 7$GPa

2.12   Conclusion

In summary, this study focuses on determining the impact of thermochemical treatments, including quenching, carburizing, and nitriding, on the hardness gradient of M50, M50NiL, 32CDV13, and M50NiLDH steels. The research proposes an effective method for extracting these metals' microhardness gradient and elastoplastic constitutive law using nanoindentation tests. The characterization is done by combining two approaches:

- The Oliver Pharr's analytical approaches to determine Young's modulus and hardness.

- The inverse identification approach which made it possible to identify the parameters of Swift's behavior law for these materials.

The analysis conducted in this study revealed that specific treatments, such as carburizing, nitriding, and carbonitriding, increase surface hardness that gradually decreases towards the interior of the material. On the other hand, quenching leads to a uniform increase in hardness throughout the material. The treatments' depth was 150 μm for 32CrMoV13 steel, 1 mm for M50NiL steel, and 100 μm for nitriding and on M50NiLDH steel as the carburizing had created a homogeneous layer toward the bulk material. Additionally, the analysis allowed for the classification of the steel grades based on their surface hardness levels, with M50NiLDH exhibiting the highest level of resistance, followed by M50NiL, 32CrMoV13, and M50.

The study found a relationship between the depth of treatment, the level of hardness, and the parameters of Swift's law used to model the materials' behavior. Specifically, a linear and exponential approximation of the hardness evolution with the treatment depth was established for the different materials studied (AISI M50, AISI M50NiL, AISI M50NiLDH, and AISI 32CrMoV13). In addition, Swift's parameter B was approximated to have a linear evolution with the depth of treatment as the hardness decreases.

The results of the study showed that the operating resistance of the materials can be correlated with their surface and core properties, which are influenced by the different heat treatments. The M50 steel, which had a good surface and core properties, was the most resistant to high loading levels beyond 6.6 GPa. The M50NiLDH steel, which had the best surface properties, showed the best resistance in the 3.5-5.2 GPa but started to deform more than M50 at higher loading levels. The M50NiL and 32CrMoV13 steels showed intermediate resistance levels between M50 and M50NiLDH, with M50NiL being more resistant than 32CrMoV13.

So the M50 steel exhibited the highest operating resistance at high loading levels compared to the other materials tested, including the M50NiLDH, M50NiL, and 32CrMoV13. However, at lower loading levels, the surface properties of the treated materials were found to play an important role in their resistance to surface attacks.

Chapter 3

Bearing materials hardening under cyclic solicitation

In this chapter, the investigation focuses on identifying the material parameters that accurately model the response of four different steels: M50, 32CrMoV13, M50NiL, and M50NiLDH. These steels are martensitic and have undergone thermochemical treatments, which can result in a gradient of properties depending on the specific treatment applied. During the analysis, various types of behaviors were observed in the steels under cyclic uniaxial stress. These behaviors include elastic adaptation, elastoplastic accommodation, and ratchet. A combined type of work hardening will be employed to effectively model the elastoplastic behavior exhibited by the samples under cyclic loading. This combined work hardening approach incorporates both isotropic and kinematic work hardening. The study aims to identify sets of parameters for Chaboche's constitutive law for each grade of steel. This will be accomplished through an inverse resolution technique, which involves determining the material parameters that best match the observed behavior of the steels. The analysis will be conducted both at the surface and in the core of the samples to account for any potential variations in material properties. By identifying these sets of material parameters, the study aims to better understand the cyclic behavior of the investigated steels.

Sommaire

3.1 Introduction

In industrial machinery, mechanical components undergo repetitive loading over their operational lifespan. This is especially crucial in the context of aeronautical bearings, where it is necessary to examine how bearing materials respond to cyclic stresses.

When examining cyclic stresses, there are two types of formulations to consider: isotropic and kinematic formulations. Isotropic formulations are suitable when dealing with cyclic stresses that increase in loading amplitude as the number of cycles progresses. However, these formulations may need more precision as they must account for the translation of surface loads on materials, such as the Bauschinger effect. The Bauschinger effect pertains to a phenomenon observed in metallic materials under cyclic loading, where the yield strength decreases in the opposite direction after unloading. To accurately capture this effect, one must use kinematic formulations.

Kinematic formulations have shown significant improvements over isotropic formulations in some applications. They provide better predictions of local elastoplastic response and springback. Nevertheless, a combination of isotropic and kinematic formulations is often preferred due to the limitations of each approach. These combined formulations offer greater precision compared to purely isotropic ones and yield more accurate results in terms of local elastoplastic response and springback prediction. A detailed description of these specific formulations will be provided later in the text.

This chapter aims to identify the parameters of Chaboche's constitutive models implemented in Abaqus. These models describe the behavior of specific steel grades (M50, 32CrMoV13, M50NiL, M50NiLDH) under cyclic loading conditions. The focus is on comprehending how these steels react to repeated loading and unloading cycles.

Furthermore, in addition to parameter identification, this chapter will also explore the type of hardening exhibited by these steels based on the applied load levels.

3.2 Plasticity

Plasticity is a property exhibited by materials that undergo permanent deformation when subjected to external forces or loads. At any point on the stress-strain curve, the total strain ε is composed of an elastic strain ε_e and a plastic strain ε_p so that we can write:

$$\underline{\underline{\varepsilon}} = \underline{\underline{\varepsilon}}_e + \underline{\underline{\varepsilon}}_p \tag{3.1}$$

If we express the equation in terms of strain rates, Equation 3.1 becomes:

$$\underline{\underline{\dot{\varepsilon}}} = \underline{\underline{\dot{\varepsilon}}}_e + \underline{\underline{\dot{\varepsilon}}}_p \tag{3.2}$$

Here, $\dot{\underline{\underline{\varepsilon}}}$, $\dot{\underline{\underline{\varepsilon}}}_e$, and $\dot{\underline{\underline{\varepsilon}}}_p$ represent the tensors representing the rates of total, elastic, and plastic deformation, respectively.

In the stress space, there exists an elastic domain within which any variation in stress only leads to elastic deformation and no plastic deformation. On the boundary of this domain, the behavior is elastoplastic. The surface that delimits the elastic domain is called the yield surface, which can be described by the state function f of the stress state, known as the yield criterion.

Plastic deformation only occurs when the equivalent stress σ_{eq} is equal to the yield strength σ_{yield}. This condition can be expressed as:

$$f(\underline{\sigma}) = \sigma_{eq} - \sigma_{yield} = 0 \qquad (3.3)$$

and the loading point always remains on the yield surface. It is only when unloading the material that the equivalent stress σ_{eq} becomes lower than the yield strength $\sigma_{eq} < \sigma_{yield}$, hence $f = \sigma_{eq} - \sigma_{yield} < 0$, and the behavior becomes elastic with constant plastic deformation. Plastic collapse occurs when two conditions are simultaneously satisfied:

$$f = 0 \text{ and } \dot{f} = 0 \qquad (3.4)$$

The consistency condition states that during a stress variation that induces plastic deformation, the hardening evolution must occur in such a way that $f = 0$ is continuously maintained. However, the stress variation can cause the representative point of the loading state to move inward within the domain. This corresponds to elastic unloading characterized by $\dot{f} < 0$. The the plastic flow rule can be written as:

$$\dot{\varepsilon}_p = 0, \text{ if } f < 0 \text{ (elastic behavior)} \qquad (3.5a)$$

$$\dot{\varepsilon}_p > 0, \text{ if } f = 0 \text{ and } \dot{f} = 0 \text{ (indicating plastic flow)} \qquad (3.5b)$$

$$\dot{\varepsilon}_p = 0, \text{ if } f = 0 \text{ and } \dot{f} < 0 \text{ (indicating elastic unloading)} \qquad (3.5c)$$

When plastic flow occurs, the evolution of plastic strain is given by the relation:

$$\dot{\underline{\underline{\varepsilon}}}_p = \dot{\lambda} \frac{\partial f}{\partial \underline{\sigma}} \qquad (3.6)$$

where $\dot{\lambda}$ is the plastic multiplier, which represents the rate of equivalent plastic deformation. It needs to be determined based on the loading-unloading criterion.

3.3   Plasticity criteria

Plasticity criteria, also known as yield criteria or failure criteria, are mathematical expressions or conditions used to determine the onset of plastic deformation in materials. These criteria define the stress states at which materials transition from elastic to plastic behavior. Different criteria have been developed to describe the yield behavior of various materials under different loading conditions. Here are some commonly used plasticity criteria:

3.3.1   Von Mises Criterion

The Von Mises criterion, also known as the Von Mises yield criterion or the maximum distortion energy criterion, is widely used to describe the yielding behavior of ductile materials under isotropic loading conditions. It is based on the concept of equivalent stress. The mathematical expression for the Von Mises criterion is as follows:

$$\sigma_{eq} = \frac{1}{\sqrt{2}}\sqrt{(\sigma_1 - \sigma_2)^2 + (\sigma_2 - \sigma_3)^2 + (\sigma_3 - \sigma_1)^2} \tag{3.7}$$

There is inelastic deformations if:

$$\sigma_{\text{eq}} \geq \sigma_{yield} \quad \text{Yielding condition.}$$

In the Von Mises criterion, the symbols have the following meanings:

- σ_{eq} represents the von Mises equivalent stress.

- σ_1, σ_2, and σ_3 represent the principal stresses.

The yielding condition states that yielding occurs when the von Mises equivalent stress σ_{eq} exceeds or is equal to the yield strength σ_{yield}.

3.4   Behavior under cyclic load

The material hardening behavior is the hardening under the effect of its plastic deformation. It therefore corresponds to the modifications that material undergoes when the applied stresses are high enough to cause permanent plastic deformations. These modifications are of a metallurgical nature (modification of the internal structure) and generally have an influence on its mechanical properties. Experimental studies in the literature on materials reveal the presence of inelastic deformations when exceeding their elastic limits and that the plasticity surface evolution can be very complex. Thus, by plasticizing, materials can undergo expansion, translation and distortion as illustrated in several studies (LEM 90; BRO 08; CHA 08a; CHA 86; CHA 12; CHA 08b; DAR 15; DIA 13; DON 19; FEI 18; FEI 20; MOH 16).

Depending on the expansion or translation of the load surface, different types of work hardening can be distinguished, namely isotropic hardening and kinematic hardening.

3.4.1 Isotropic hardening

Isotropic hardening refers to work hardening where the load surface expands uniformly in all directions. It is often observed in materials that exhibit a relatively uniform distribution of dislocations during plastic deformation. The hardening response is characterized by an increase in the yield strength and a corresponding increase in the stress required to induce plastic deformation as we can observe in Fig.3.1. According to the isotropic hardening rule, the evolution of the loading surface is governed by a single scalar variable, denoted as R. This variable represents the isotropic hardening parameter. In the context of time-independent plasticity and isothermal plastic deformation, the yield surface can be described by the following equation, as formulated by Lemaitre and Chaboche (LEM 90):

$$\sigma = \sigma_0 + R \tag{3.8}$$

Here, σ represents the stress, σ_0 is the initial yield strength, and R is the isotropic hardening parameter. This equation indicates that the yield strength increases linearly with the isotropic hardening parameter. As plastic straining occurs, the isotropic hardening parameter R increases, leading to an overall expansion of the yield surface in all stress directions.

The isotropic hardening parameter, R, captures the additional yield strength induced by plastic deformation. It accounts for the accumulation of dislocations, changes in the microstructure, and other factors that contribute to the material's hardening behavior.

In order to account for the expansion of the loading surface in Abaqus, the Voce elastic-plastic constitutive law was implemented based on the work of Lemaitre and Chaboche (LEM 90; CHA 86). The size of the yield surface, denoted as $\sigma_0(\varepsilon_{pl}, \theta, f_i)$, is defined as a function of the equivalent plastic strain ε_{pl}, temperature θ, and field variables f_i. This dependency can be directly provided, coded in the user subroutine UHARD, or modeled using a simple exponential law for materials that cyclically either harden or soften:

$$\sigma = \sigma_0 + Q_{inf}\left(1 - \exp(-b\varepsilon_{pl})\right) \tag{3.9}$$

The exponential part determines the variation of the surface size. Here, $\sigma_0(\theta, f_i)$ represents the yield surface size at zero plastic strain, and $Q_{inf}(\theta, f_i)$ and $b(\theta, f_i)$ are additional material parameters that need to be calibrated based on cyclic test data.

3.4.2 Kinematic hardening

Kinematic hardening, on the other hand, involves a translation of the load surface without expansion as shown in Fig.3.2. It is also referred to as differential hardening. In kinematic hardening, the material's hardening response depends on its previous loading history and the direction of the applied stresses. This type of hardening occurs when there is an asymmetric distribution of dislocations or plastic strains in the
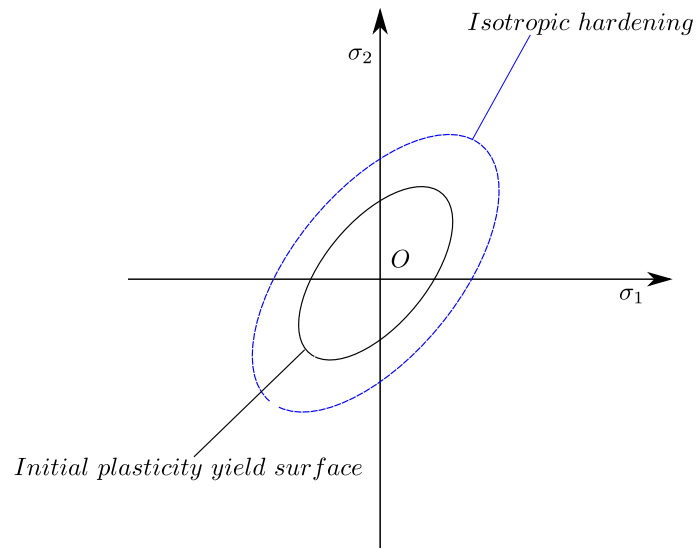
Figure 3.1: Isotropic hargening illustration

material. During cyclic loading, the material experiences non-proportional loading paths, leading to different stress-strain responses in different directions. Kinematic hardening is commonly observed in materials with anisotropic behavior, such as textured or polycrystalline materials.
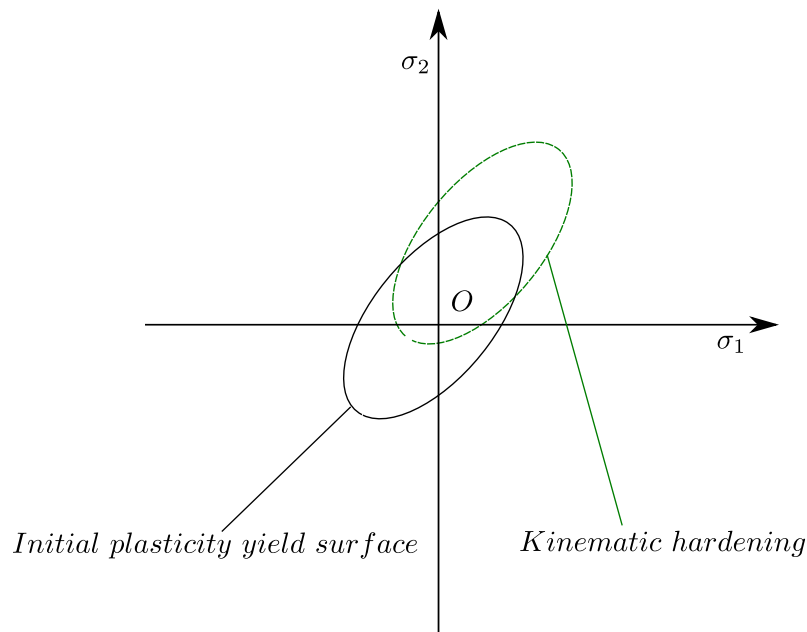
Figure 3.2: Kinematic hardening illustration

3.4.2.1 Linear kinematic hardening model

The linear kinematic hardening model is a simplified approach for modeling kinematic hardening in materials, particularly in the ABAQUS software. This model combines isotropic and kinematic hardening formulations and is commonly used to describe the material behavior in plastic deformation simulations.

In this model, the size of the yield surface, denoted as $\sigma_0(\theta)$, can be a function of temperature (θ) only. The evolution of the internal variable α, which represents the kinematic hardening parameter, is defined by Ziegler's hardening rule generalized to the nonisothermal case. The evolution equation for α is given by:

$$\dot{\alpha} = C \dot{\bar{\varepsilon}}_{pl} \frac{1}{\sigma^0} (\sigma - \alpha) + \frac{1}{C} \alpha \dot{C} \tag{3.10}$$

In this equation, C(θ) represents the hardening parameter, and $\dot{C}(\theta)$ is the work-hardening slope of the isothermal uniaxial stress-strain response, specifically the rate of change of stress (σ) with respect to plastic strain rate ($\dot{\varepsilon}_{pl}$), taken at different temperatures. The term $\dot{C}$ represents the rate of change of C with respect to temperature ($\dot{\theta}$).

This form of the evolution law for α indicates that the rate of α due to plastic straining is in the direction of the current radius vector from the center of the yield surface ($\sigma - \alpha$), while the rate due to temperature changes is directed towards the origin of stress space. This concept was presented more generally as:

$$\dot{\alpha} = \dot{\mu}(\sigma - \alpha) + h \alpha \dot{\theta} \tag{3.11}$$

The specific identification of $\dot{\mu} = C \dot{\varepsilon}_{pl} \frac{1}{\sigma^0}$ and $h = \frac{\frac{dC}{d\theta}}{C}$ in the above equation is assumed, and it defines the material behavior based on the isothermal, uniaxial work hardening data, represented by C(θ).

3.4.2.2 The non-linear kinematic hardening

The use of nonlinear hardening models enables the consideration of nonlinear kinematic hardening characteristics exhibited by materials. Among these models, the Armstrong-Frederick (ARM 66) nonlinear hardening model is widely employed and later enhanced by Chaboche. The modified Chaboche model is integrated into the finite element software Abaqus for implementation (SMI 19).

The non linear kinematic hardening component of this law is described by the equation:

$$dX = C_1(\sigma - X)d\varepsilon - \gamma d\varepsilon \tag{3.12}$$

where dX represents the change in the back stress tensor, σ is the stress, X is the back stress tensor, $d\varepsilon$ is the plastic strain increment, C_1 is the initial kinematic hardening modulus, and γ is the rate at which the kinematic hardening modulus decreases with increasing plastic deformation.

3.4.2.3 The combined hardening

Combined hardening refers to the simultaneous presence of isotropic and kinematic hardening in a material's response due to plastic deformation. Isotropic hardening involves changes in the yield strength and the size of the yield surface, whereas kinematic hardening pertains to the evolution of the shape of the yield surface. In materials exhibiting combined hardening, the yield surface expands or contracts with plastic deformation, and it undergoes translation as well as shown in the Fig.3.3. Kinematic hardening causes the yield surface to shift, resulting in an increase or decrease in the yield strength. On the other hand, kinematic hardening causes the yield surface to distort, leading to changes in the material's resistance to plastic deformation under different loading conditions. The combined hardening behavior of a material is typically characterized through constitutive models that incorporate both isotropic and kinematic hardening components. These models consider the evolution of yield surfaces and plastic deformation in response to external loading and provide a more accurate representation of the material's behavior under complex loading conditions. Combined hardening is crucial to accurately predict the response of materials subjected to cyclic or multiaxial loading, as it captures the interaction between isotropic and kinematic hardening mechanisms.
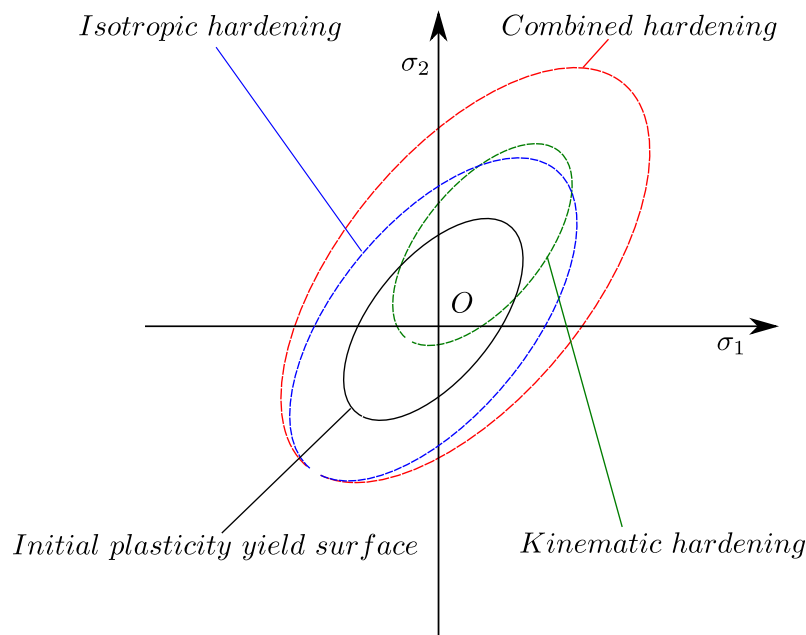
Figure 3.3: Isotropic/kinematic hardening illustration

The behavior of the hysteresis loop during cyclic loading depends on the material's ability to accommodate plastic deformation. When the material is able to adapt elastically to the applied stress, the hysteresis loop will close completely. However, in the case of elastoplastic accommodation, the loop will close until it stabilizes over a range of elastoplastic deformation, leading to a more open loop compared to

elastic adaptation. When an accomodation is present, the hysteresis loop closes more slowly, resulting in an even more open loop compared to the previous two cases. The behavior of the hysteresis loop during cyclic loading provides important insights into the material's ability to withstand repeated stress and strain cycles, which is critical in engineering applications such as the design of bearings and other mechanical components.

Under cyclic loading, materials often exhibit the Bauschinger effect, characterized by a decrease in the yield strength under compression after an initial loading in tension, and vice versa. This effect is commonly observed in uniaxial tension-compression or alternating torsion tests. Additionally, most materials and alloys demonstrate varying hardening properties during cyclic loading.

When conducting a strain-controlled test two types of behaviors can be observed, depending on the material being studied:

1. Hardening:
   Some materials exhibit an increase in the maximum stress with the number of cycles. This is referred to as hardening.

2. Softening:
   Other materials experience a decrease in the maximum stress with the number of cycles, indicating softening behavior.

These two types of behaviors, hardening and softening, are commonly observed in cyclically loaded materials and play a crucial role in their fatigue life and overall mechanical response.
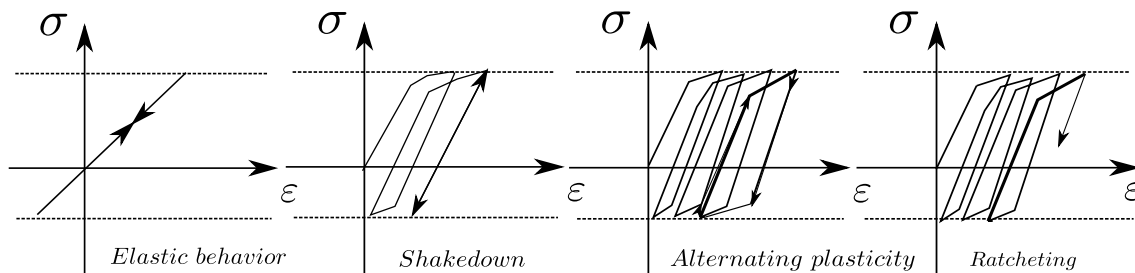
Figure 3.4: Schematic representation of cyclic elastoplastic behaviors.

When materials are subjected to cyclic loading, according to the loading path, the load level and the material properties, we can observe an elastic adaptation also called shakedown, an elastic-plastic adaptation called accommodation and the ratchet as illustrated in Fig.3.4.

3.4.2.4 Elastic adaptation or shakedown

Material shakedown refers to the phenomenon in which a material subjected to cyclic loading gradually stabilizes and exhibits elastic behavior, even though the applied

loads exceed the material's yield strength. This occurs when the cyclic loads are below a certain limit, known as the shakedown limit. During the initial loading cycles, the material may experience some plastic deformation due to the applied loads exceeding the yield strength. However, as the cyclic loading continues, the plastic strains gradually decrease until the material reaches a state of shakedown. In this state, the material undergoes purely elastic deformation, and the accumulated plastic strains become negligible.

3.4.2.5 Plastic adaptation or accommodation

Material plastic adaptation, also called elastic-plastic accommodation, denotes a material's capacity to modify its response when subjected to cyclic or repeated loading. The material experiences plastic deformation; however, as the loading is repeated, the material adjusts its behavior to attain a more stable plastic deformation loop.

Plastic adaptation involves the generation of residual stresses and strains within the material that counteracts the applied loads. These residual stresses and strains arise from dislocation rearrangements and the redistribution of internal forces. Consequently, the material attains a state where plastic deformation and elastic recovery strike a balance, resulting in a more stabilized plastic deformation loop.

3.4.2.6 Ratcheting

Ratcheting is a phenomenon observed in materials subjected to prescribed asymmetrical cyclic stresses. It results in a progressive increase in ratcheting strain with each cycle. However, different materials exhibit variations in their ratcheting behavior.

To capture this behavior, the nonlinear isotropic/kinematic hardening model is used.

The nonlinear isotropic/kinematic hardening model is known to provide more accurate results in many cases involving cyclic loading. For low mean stresses and low stresses, ratcheting is not often observed, resulting in zero ratchet strain. Conversely, at high mean stresses, the accumulated ratchet strain continues to increase steadily. A constant ratchet strain is predicted if only the nonlinear kinematic hardening component is considered without the isotropic hardening component.

3.4.3 Modeling of the cyclic behavior

For the reliable prediction of mechanical responses beyond the elastic limit in components and structures, it is typically recommended to describe the elastic-plastic behavior of metals accurately. Cyclic plasticity refers to the elastoplastic stress-strain response of materials subjected to closed and repeated loading paths. It encompasses various phenomena, such as the Bauschinger effect, cyclic hardening, relaxation, and ratcheting. Accurately predicting ratcheting is crucial for preventing catastrophic failure of structures. So an extensive experimental and numerical research has been conducted in recent years (SON 14; BRA 18; BRO 08; BUR 20; CAO 21; CHA 86;

CHA 97a; CHA 12; CHA 08b). To characterize the material behavior, various authors (CHE 18; CHO 13; CHO 17; CIZ 05; COU 17; DAU 21).have used uniaxial tests, including tests with different loading paths, such as nanoindentation tests.

Plasticity plays a crucial role in various industrial applications because of its ability to deform and retain its shape after the applied load is removed. It allows materials to withstand large strains and stresses, making them suitable for applications such as metal forming, structural design, and manufacturing processes. Plasticity has been the subject of several studies (DES 20; DIA 13; DON 19; EHL 16; ENO 12; FAR 19; FEI 18; FEI 20; FIS 12; FRE 06) to understand its mechanisms, to model its behavior, and to optimize its performance in different industrial contexts. Various forms of hardening can be distinguished in the presence of plasticity, as demonstrated by several authors (FU 19; GAL 12; GAL 13; GAO 20; GAO 20; GAR 20; GAR 21a; GAR 21b). Thus the prevalent use of a simple linear elastic model can be attributed to the limited information available on the material's constitutive behavior.

The Chaboche kinematic hardening model is one of the most commonly used constitutive models for metal plasticity. It combines Chaboche kinematic hardening with Voce isotropic hardening to create a comprehensive model known as Chaboche (or Chaboche-Lemaitre) combined isotropic-kinematic hardening (CIKH). Despite various modifications and new approaches introduced, the Chaboche model remains the benchmark for both the kinematic component and the combined isotropic-kinematic model. It is implemented in commercial finite element software packages like Abaqus (SMI 19).

To characterize the material response, uniaxial stress-strain-controlled cyclic tests are frequently conducted, revealing different behaviors such as purely elastic, elastic shakedown, plastic shakedown, or ratcheting, often with a steady strain increment.

In Fu et al. (FU 16), the model parameters for the Chaboche kinematic hardening model were determined using the virtual fields method in combination with full-field deformation measurements. They considered different numbers of backstress components to fit the initial loading cycles. Nath et al. (NAT 21) argued that accurate simulation of ratcheting tests requires the inclusion of isotropic hardening and emphasized evaluating the absence of isotropic hardening in cyclically stable materials on a case-by-case basis.

This analysis focuses on characterizing the material properties of different steel grades: M50, 32CrMoV13, M50NiL, and M50NiLDH. The characterization will involve identifying the parameters of the Chaboche constitutive law to describe their behavior.

3.5 Investigated materials and experimental campaign

In this section, we will present the materials used in the study and provide an overview of the experimental protocols.

3.5.1 Properties gradient in the samples

In this section, we will analyze and characterize the evolution of the elastoplastic and hardenable behavior of bearing steels M50, 32CrMoV13, M50NiL, and M50NiLDH. These steel grades have undergone different heat treatments, including quenching, nitriding, carburizing, and carbonitriding, which result in a gradient of elastoplastic properties as described in the previous chapter.

The objective is to examine how these treatments affect the materials' response to cyclic loading and loading level.

3.5.2 Nanoindentation protocol

The sample preparation and calibration of the nanoindentation machine followed the same procedures described in the previous chapter.

Nanoindentation tests were performed using the Nanoindentor G200 of the Mateis laboratory located at INSA Lyon. This machine uses a small probe with a sharp tip to indent the surface of a sample and measure its response to applied loads. The nanoindentation tests were carried out perpendicular to the treated surfaces. Two protocols were developed for the experimentation:

1. Cyclic Load Protocol:
   This protocol involved applying cyclic loads at different levels: 5 mN, 37 mN, 65 mN, and 500 mN. The selected levels corresponded to Hertz maximum pressures of 2427 MPa, 4730.4 MPa, 5707 MPa, and 11267 MPa, respectively. To implement this protocol, modifications were made to the "G-series hardness and modulus via load control cycles" method with the CSM stiffness measurement method. The modified protocol allowed loading 50 cycles at the same loading force.

2. Variable Load Protocol: This protocol applied four loading cycles at different levels: 75 mN, 150 mN, 300 mN, and 600 mN. After each loading step, an unloading step was performed until the applied load reached 10% of the maximum force of the step.

A spherical diamond tip with a diameter of 100 μm (the diameter observed under the numerical microscope is 95.5 $\pm 2\mu$m , as presented in section 2.10.4) was used for the nanoindentation tests. The tip had Young's modulus of 1100 GPa and a Poisson's

ratio of 0.1. The tests were conducted in load-controlled mode, with a maximum load of 600 mN. To ensure repeatability, at least two indents were made at each depth. Additionally, a distance of 100 μm was maintained between neighboring indentations to avoid mutual influences.

3.5.3 Investigated material cyclic responses

When deploying the first test protocol, which involves applying multiple loading cycles at a constant loading level, the behavior of the materials can be observed and distinguished based on the loading level:

1. At low loading :
   At this range of loading, the materials exhibit elastic adaptation. This means that the plastic deformations stabilize and occur within the elastic range after a certain number of cycles. Figure.3.5 illustrates this behavior, stabilizing plastic strains in an elastic cycle.

2. At moderately high loading :
   In this range of loading, the materials demonstrate elastoplastic adaptation, referred to as accommodation. Accommodation involves the stabilization of plastic deformations in an elastoplastic cycle. The materials exhibit a loop of plastic deformation, with plastic strains stabilizing over cycles.

3. At high loading:
   The materials generally exhibit a ratchet behavior. Ratchet behavior refers to an incremental increase in plastic deformations with each cycle. The materials experience increasing levels of plastic strains during cyclic loading. Figures.3.6,3.7 may illustrate a progressive increase in plastic deformations with each cycle due to ratchet behavior.

It is important to note that the behaviors described above depend on the loading levels and path and may vary for different materials and treatments.

By examining the Figs.3.5,3.6,3.7, we can observe a progressive increase in plastic deformation as the number of cycles remains constant. This observation indicates the existence of kinematic hardening in the mechanical characteristics of our various steel grades. Figures.3.5,3.6 reveal distinct behaviors for different materials at the surface. Specifically, the M50NiLDH, which possesses a higher hardness level, exhibits an initial elastoplastic response on the surface. This initial response is followed by the formation of an elastic loop. In contrast, the M50 material displays an elastoplastic behavior, but instead of an elastic loop, it undergoes another elastoplastic loop. However, after a certain number of cycles, the M50 material behavior eventually evolves into an elastic adaptation phase as we can observed it on the last cycle curves in Fig.3.8.
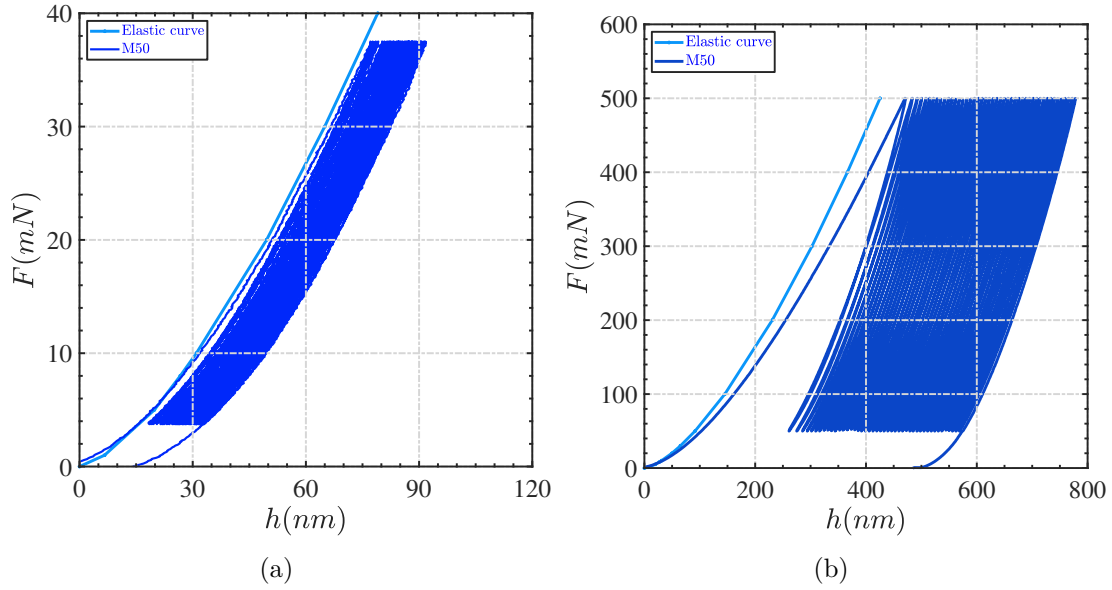
Figure 3.5: Cyclic indentation curve of M50 steel at depth $h = 10\mu m$ of the surface (a) Loading force $F = 37mN$ (b) Loading force $F = 500mN$

Figure.3.5 depicts the work-hardening progression of M50 steel under two distinct force levels: F=37mN and F=500mN, which correspond to Hertz pressures of 4.7GPa for an elastic contact radius of 2 μm and 11.2GPa for a contact radius of 5 μm, respectively. The respective number of cycles shown in the Fig.3.5 is 40 cycles and 100 cycles, with a loading frequency of 0.067Hz.

The phases for detecting the contact surface are conducted with extreme care, lasting approximately 5 to 10 minutes, depending on the servo speed set on the nanoindenter. As a result, an adjustment was made to the test method programmed into the machine to facilitate cyclic tests at a consistent loading level based on the number of cycles. Consequently, the cyclic tests are notably faster after the initial detection phase.

When comparing the materials, the 32CrMoV13 and M50NiL exhibit an elasto-plastic behavior characterized by a hysteresis loop, followed by an elastic adaptation phase. On the surface, the M50NiLDH quickly adapts elastically, similar to the M50 material. Conversely, the 32CrMoV13 and M50NiL materials demonstrate more open hysteresis loops compared to those observed on the surface. These larger hysteresis loops are then followed by an elastic adaptation phase.

Overall, the behavior of these materials varies depending on their hardness levels, with the materials displaying elastoplastic behaviors followed by elastic adaptation characterized by hysteresis loops and subsequent elastic adaptation phases.
The level of hardness, or more specifically, the elastic limit, plays a crucial role in determining the adaptation behavior of different steels.
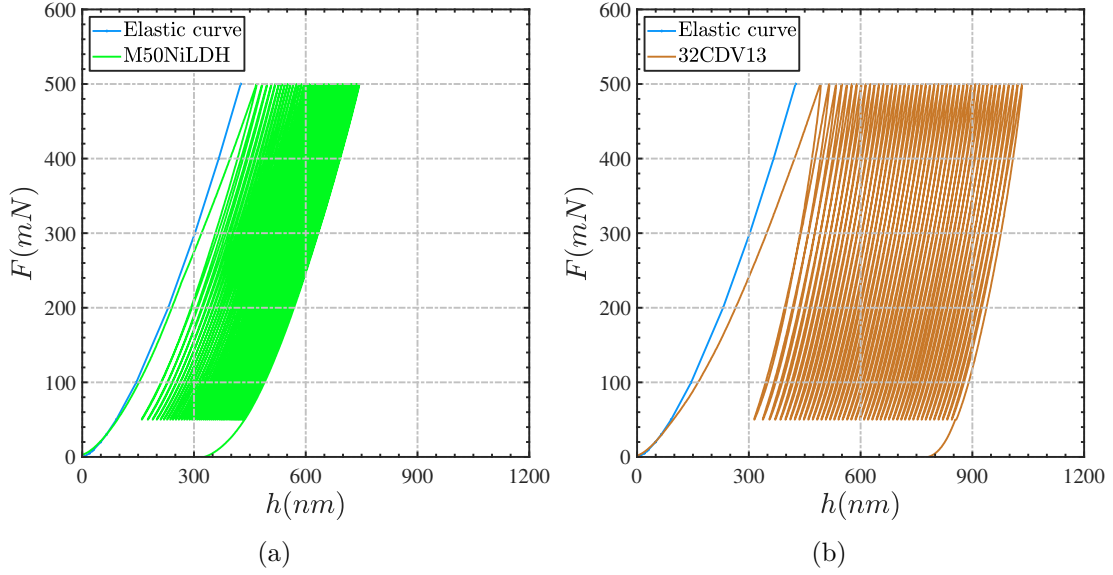
Figure 3.6: Cyclic indentation on bearing material at depth $h = 10\mu m$ with $F = 500mN$ (a) M50NiLDH (b) 32CrMoV13

Figure.3.9 depicts a cyclic indentation with varying loading levels of 75mN, 150mN, 300mN, and 600mN. Comparing this to a monotonic indentation curve at the maximum loading of 600mN, we observe the emergence of hysteresis loops. This demonstrates how the loading path influences the resulting response.

As the material undergoes a loading path with multiple load levels, it gradually deforms and becomes more plastic, initiating processes involving dislocations and defect movements that may not occur under monotonic loading. Similarly, it's evident that harder materials deform less, resulting in less significant dislocation movements. This accounts for the presence of smaller hysteresis loops on the M50NiLDH compared to the 32CrMoV13 curve.

By analyzing the evolution of work hardening in materials based on the loading level, it is possible to predict different behaviors, such as elastic adaptation, elastoplastic accommodation, and ratcheting, depending on the loading conditions following a specific loading path. Specifically, considering a loading level defined by the maximum pressure of Hertz, the following scenarios can be expected:

❆ For pressures below 3.5 times the initial yield strength ($P < 3.5\sigma_0$):
The material will undergo elastic adaptation after a certain number of cycles. This means the material will experience elastic deformation and recover its original shape when the load is removed. The behavior will primarily be characterized by elastic response without significant plastic deformation.

❆ For pressures between 3.5 times and six times the initial yield strength ($3.5\sigma_0 <$
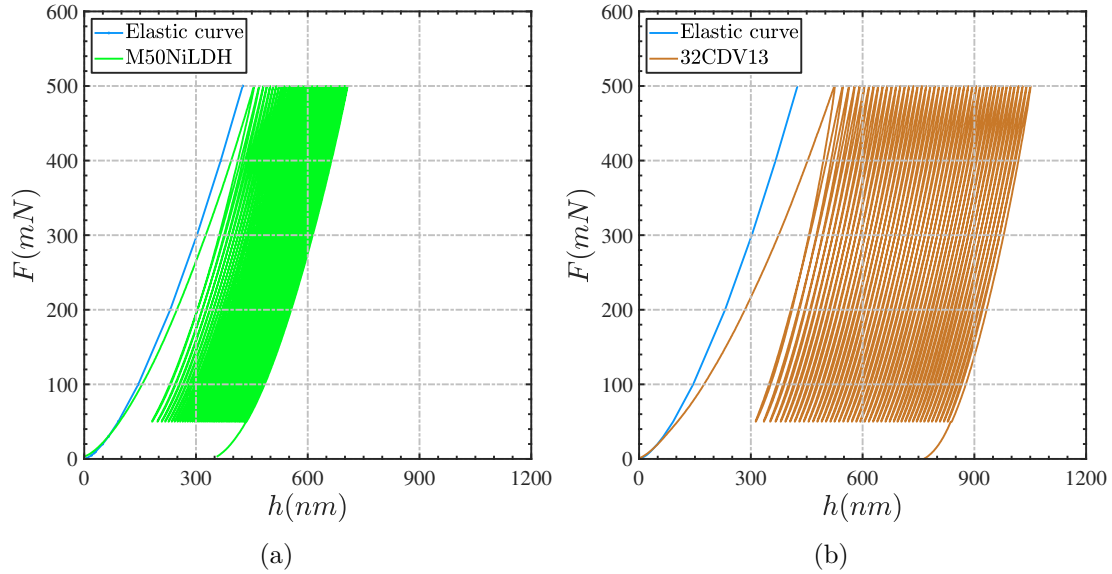
Figure 3.7: Cyclic indentation on bearing material at depth $h = 1500\mu m$ with $F = 500mN$ (a) M50NiLDH (b) 32CrMoV13

$P < 6\sigma_0$):
The material will stabilize in an elastoplastic cycle.

❅ For pressures exceeding six times the initial yield strength ($P > 6\sigma_0$):
The material will demonstrate work hardening of the ratchet type. In this case, the material will experience significant plastic deformation with each loading cycle. The plastic deformation will accumulate over time, leading to an increase in the material's overall strength and hardness. This behavior is commonly associated with progressive plastic deformation without complete recovery during the unloading phase.

When experimental protocol two is employed, it leads to the hardening of the steels at each level of loading. This means that the materials undergo an increase in their elastic limit, resulting in an enhanced ability to withstand higher stress levels without undergoing permanent deformation. Consequently, compared to a monotonous loading, where the material is subjected to a loading-unloading cycle, the levels of deformation observed during cyclic loading are decreased. The hardening effect observed in the materials during each loading cycle of protocol two can be attributed to several factors. One significant factor is the accumulation of dislocations within the material's crystal structure. The cyclic loading causes dislocations to move and interact, leading to their entanglement and the formation of subgrains or dislocation networks. This process increases the resistance to dislocation motion, thereby strengthening the material.

The endurance limit of materials is closely connected to their elastic limit and the behavior of their elastoplastic laws. Consequently, as depicted in Fig.3.10, most
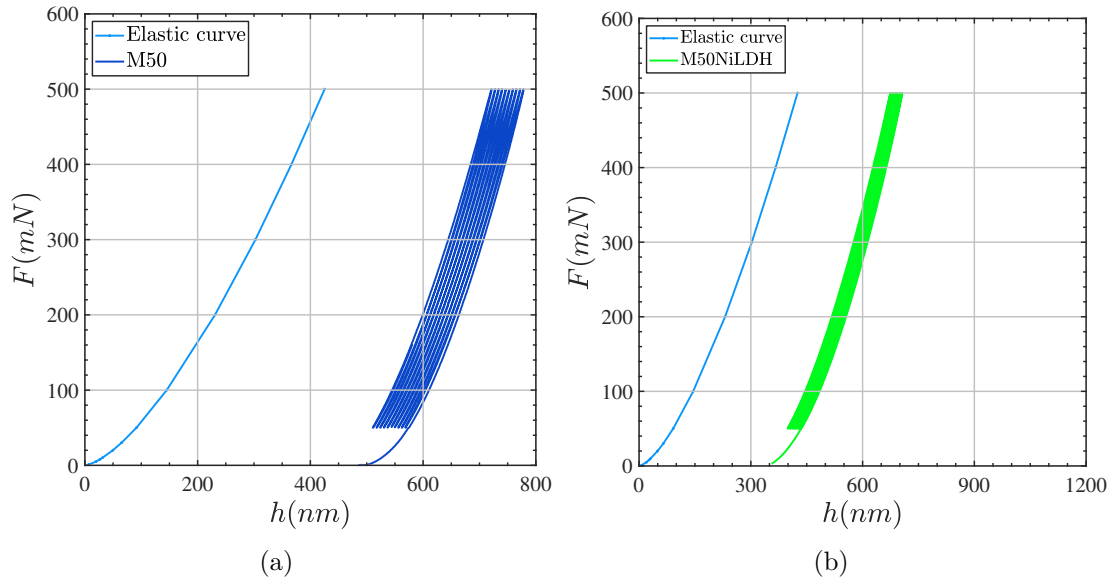
Figure 3.8: Last cycles of the cyclic indentation curve on material at depth $h = 1500\mu m$ with $F = 500mN$ (a) M50 (b) M50NiLDH

materials that demonstrate elastic adaptation will possess an unlimited endurance limit. On the other hand, materials exhibiting elastic-plastic accommodation behavior will typically have a limited endurance limit. Moreover, materials that display elastic-plastic ratchet behavior will have a low cycle endurance limit.

3.5.4 Material parameter identification

The identification procedure of the material parameters of the previous chapter will be adopted. It therefore consists in initially defining a set of material parameters, in calculating the simulated response, in comparing it with the experimental results, in reducing the error between the experimental and numerical results, in minimizing this error by means of an algorithm of optimization that will identify a new set of parameters and so on until this error is as minimal as possible.

To initiate this identification process, we will construct a finite element indentation model consisting of a diamond sphere with a modulus of 1100 GPa, a Poisson's ratio of 0.1, and a diameter of 100 μm. This sphere is used to indent a plane composed of four different steel grades: M50, 32CrMoV13, M50NiL, and M50NiLDH, as illustrated in Fig.3.11.

By iteratively updating the material parameters and minimizing the error between the experimental and numerical results, the identification procedure helps determine an optimal set of material parameters that accurately represent the material behavior in the Chaboche combined model.
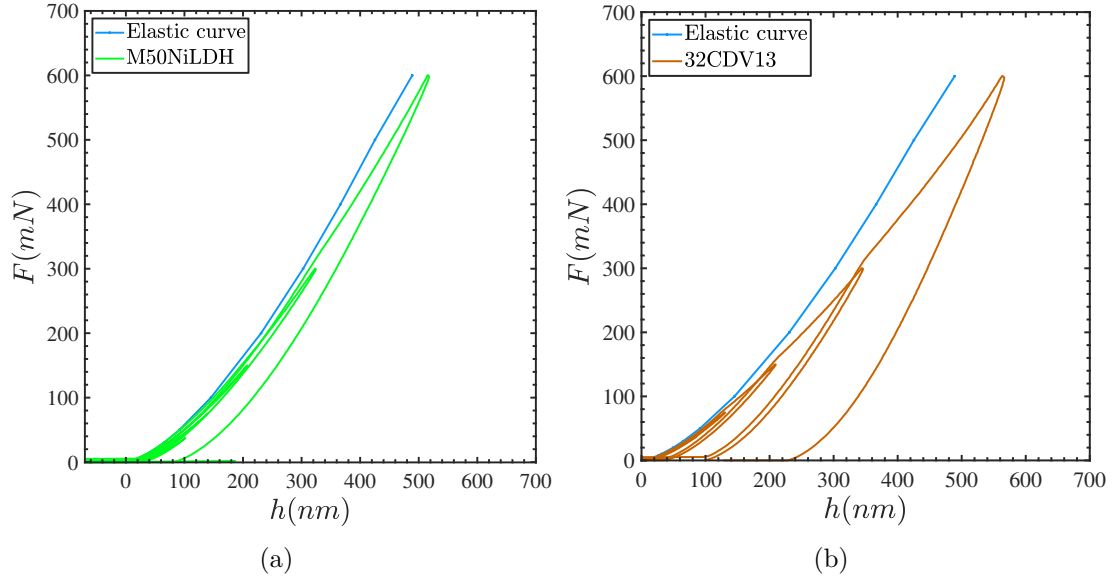
Figure 3.9: Cyclic indentation on bearing material at depth $h = 10\mu m$ with $F = 500mN$ (a) M50NiLDH (b) 32CrMoV13
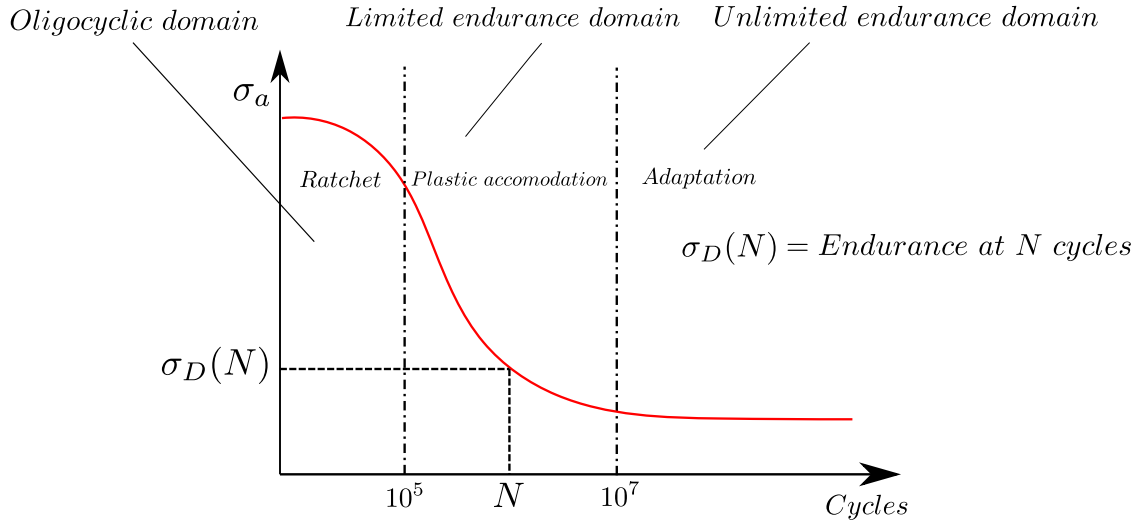
Figure 3.10:   Cyclic fatigue curve with material hardening behavior

$$\sigma = \sigma_0 + Q_{inf}\left(1 - \exp(-b\varepsilon_{pl})\right) \tag{3.13}$$

$$dX = C_1(\sigma - X)d\varepsilon - \gamma d\varepsilon \tag{3.14}$$

Here, $\sigma_0(\theta, f_i)$ represents the yield surface size at zero plastic strain, and $Q_{inf}(\theta, f_i)$ and $b(\theta, f_i)$ are additional material parameters that need to be calibrated based on cyclic test data. dX represents the change in the back stress tensor, σ is the stress, X is the back stress tensor, $d\varepsilon$ is the plastic strain increment, C_1 is the initial
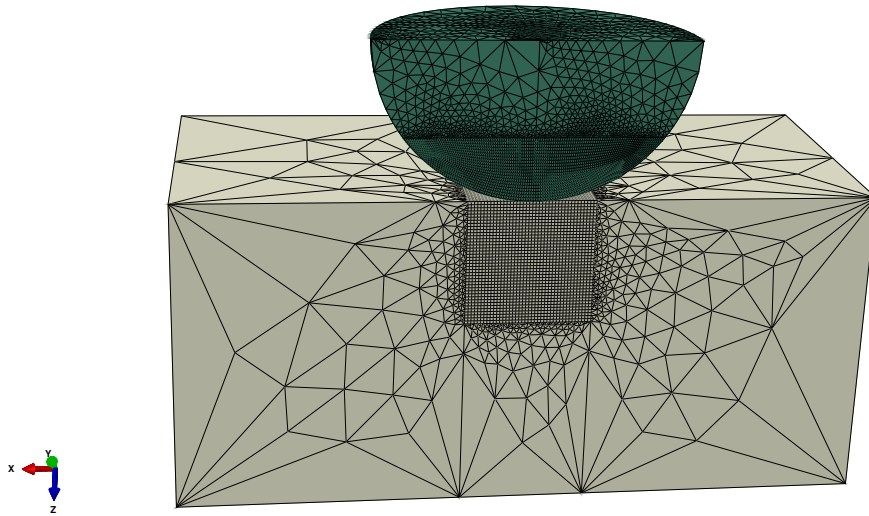
Figure 3.11: FEM model for simulating cyclic indentation
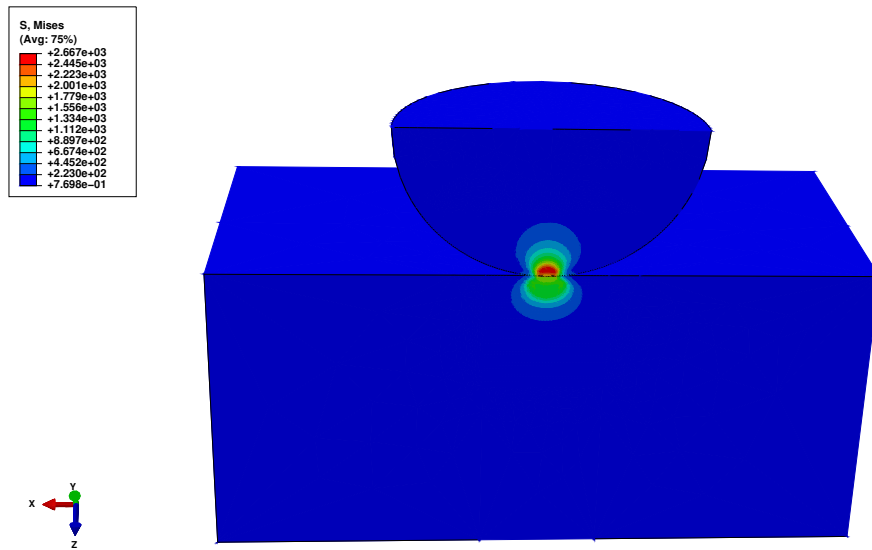
Figure 3.12: FEM model simulation result for the cyclic indentation

kinematic hardening modulus, and γ is the rate at which the kinematic hardening modulus decreases with increasing plastic deformation. In order to account for the observed softening or hardening of the samples during cyclic loadings, a combined law incorporating both isotropic (Voce) and kinematic (Chaboche) behaviors will be used in Abaqus software as illustrated in Fig.3.12. The identification process requires knowledge of the material's elastic limit, which should have been determined in a previous chapter by Swift's constitutive law.

Using the elastic limit as a reference, the coupling of Abaqus soft and the optimization algorithm will adjust the parameters to fit the force-displacement curves obtained from experimental data. This iterative process aims to identify the parameter values that best align with the experimental curves, considering the material's softening or hardening characteristics.
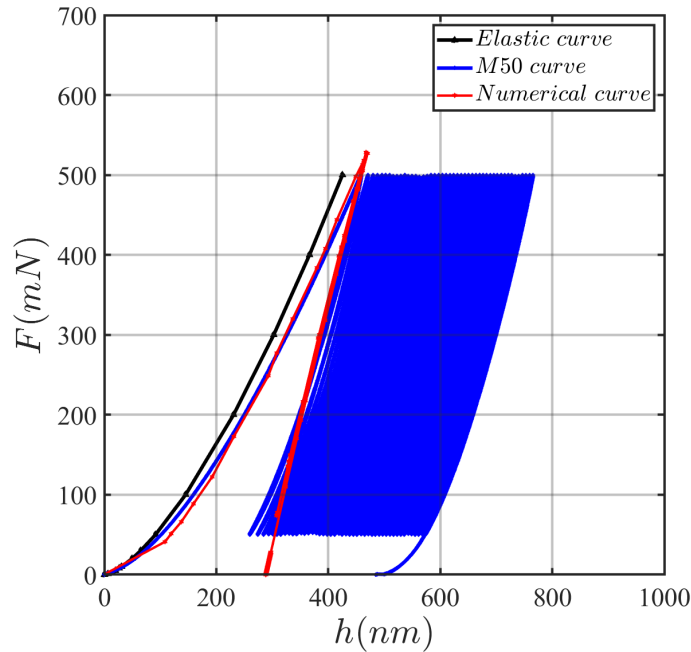
Figure 3.13: Fitting curve of the M50 steel under cyclic loading

To identify the parameters of the material's behavior law, a sensitivity study was conducted on four parameters: C (kinematic hardening modulus), γ (parameter determining the decrease of kinematic hardening), Q_{inf} (maximum change in the loading surface), and b (the rate at which Q_{inf} decreases).

The study revealed that the parameters b and Q_{inf} have a stronger influence on the evolution of the material's load surface, while the parameters C and γ have a relatively moderate influence. Based on these findings, it was decided to fix the parameters C, γ, and b around their average values of 30 GPa, 200, and 25, respectively.

However, to account for the evolution of work hardening, the parameter Q_{inf} will be specifically identified. This will allow for the evaluation of the influence of the material's level of hardness on the changes in plasticity surface.

Figure.3.13 presents the numerical fit conducted over the initial 5 cycles before the elastic adaptation of the behavior. By minimizing the errors between the experimental and numerical curves, the parameters of the mixed work-hardening law were determined. However, it is crucial to note that the numerical curves obtained are not an exact match to the experimental curves.

110

Based on the identification procedure described earlier, the parameters for steel M50 have been identified, taking into account the uncertainties in the parameter Q_{inf}. The identified parameter set for steel M50 is as follows: C = 30 GPa, $\gamma = 200$, $Q_{\text{inf}} = 200 \pm 20 MPa$, and b = 25.

In the case of materials that exhibit variations in properties with depth, the value of Q_{inf} has been fixed to 200 ± 20 MPa. This means that the parameter Q_{inf} remains relatively constant with minor variations as we move from the surface to different depths within the material. The value identified on the surface is used as a reference for the parameter throughout the material. Tables.3.1,3.2,3.3 contain the identified parameter sets for each steel grade, representing variations from the treated surface to different depths.

Table 3.1: The identified combined law parameters trought the depht on the M50NiL steel.

Height [μm]	Combined Law Parameters				Relative error	Yield strength
	C [GPa]	γ	Q_{inf} [MPa]	b	%	σ_0 [MPa]
10	30	200	100	25	10	1597
200	30	200	100	25	10	1511
400	30	200	100	25	10	1426
600						1373
800						1346
1000						1325
1200						1293
1300						1277
1400						1277

3.6 Synthesis

In the study, experimental protocols were developed and applied to analyze the behavior of M50, 32CrMoV13, M50NiL, and M50NiLDH steels under cyclic loading. These materials exhibit different types of behavior depending on the applied loading level: elastic adaptation, elastoplastic accommodation, or ratcheting. To model the behavior of these steels, the combined Chaboche constitutive law implemented in Abaqus is used. The identification process involves coupling an optimization algorithm with the Abaqus software to determine the appropriate parameters for each material. When performing the identification, it is essential to consider the presence of measurement uncertainties. In the process of identifying parameters for the constitutive law in this section, it's observed that the numerical results do not precisely align with the experimental curves. This discrepancy may arise from the inherent complexity of material physics at this scale, which might need to be fully captured by the behavior law, as well as variations in experimental results.

Table 3.2: The identified combined law parameters trought the depht on the 32CrMoV13 steel

Height $[\mu m]$	Combined Law Parameters				Relative error %	Yield strength σ_0 $[MPa]$
	C [GPa]	γ	Q_{inf} $[MPa]$	b		
10	30	200	80	25	10	1533
50	30	200	80	25	10	1490
100	30	200	80	25	10	1467
150						1450
200						1426
250						1405
300						1386
400						1369
500						1341
600						1320
700						1304
800						1280
900						1261
1000						1251
1100						1251

Table 3.3: The identified combined law parameters trought the depht on the M50NiLDH steel.

Height $[\mu m]$	Combined Law Parameters				Relative error %	Yield strength σ_0 $[MPa]$
	C [GPa]	γ	Q_{inf} $[MPa]$	b		
10	30	200	120	25	10	2129
50	30	200	120	25	10	2022
100	30	200	120	25	10	1927
150						1841
200						1767
250						1692
300						1634
400						1597
500						1597
1200						1597

Additionally, the fact that parameters b and C are not fixed could contribute to some differences in the response. Therefore, it would be valuable in future investigations to allow all parameters to vary and explore their influence on the fitted curves. These uncertainties can arise from several factors, including the dispersed nature of the test data due to the sensitivity of the experimental scale (such as the scale effect), uncertainties associated with the optimization software and codes, and the process of setting the parameters. The analyses conducted reveal that similar to

the case of monotonic loadings, M50NiLDH exhibits a lower degree of plasticization on the surface, followed by M50NiL, 32CrMoV13, and M50. This observation is attributed to the elastic adaptive behavior of M50NiLDH at Hertz pressure levels of P=11 GPa, contrasting with 32CrMoV13 and M50 steels, which initially adapt plastically. This underscores the significance of thermochemical treatments in the fatigue resistance behavior of these materials.

3.7 Conclusion

In this chapter, an analysis of the work-hardening evolution of various bearing steels, including M50, 32CrMoV13, M50NiL, and M50NiLDH, was conducted. Additionally, parameters for Chaboche's behavior law were identified.

The study revealed that the material's response, in terms of work hardening, depends on the level of loading and the thermochemical treatment it underwent. The materials exhibited different behaviors, such as elastic adaptation, accommodation, or ratcheting.

The results indicated that heat treatments not only increased the hardness level of the steels but also enhanced their endurance limit and resistance to contact fatigue. By identifying specific loading intervals, it became possible to observe different hardening behaviors in the materials.

For bearing steels experiencing loading levels within the range of 1 GPa to 3 GPa, work hardening was found to be adaptive. This adaptive behavior can be adequately modeled by an isotropic law without significant errors. However, a more comprehensive analysis of parameter variability and loading conditions can further enhance the study's findings and results.

Chapter 4

Quarter space contact problem resolution by SAM method

In various mechanical systems, the limited size of components often leads to challenges related to quarter-space contact, particularly when contact occurs near a free edge. This study is focused on addressing this specific issue. The chapter begins by exploring various methods aimed at resolving contact problems. It then proceeds to address the quarter-space, ellipse truncation, and two-joined space problems using a semi-analytical method (SAM) approach, which combines Hetenyi's mirror pressure technique with Guilbault's method to establish corrective factors known as ψ_1 and ψ_2. Subsequently, these factors are used numerically to predict the material's response. Our observations reveal that the pressure amplitude increases as the distance of the contact center (d/a) from the free edge decreases, while it decreases as this distance increases. Simultaneously, the contact zone diminishes in size as it nears the free edge and moves away. Specifically, at a distance of $d/a = 1$ from the quarter-space free edge, our model shows a maximum pressure increase of approximately 1.022 times P_0. The developed SAM models are validated and show good agreement with Finite Element Method (FEM) results. Additionally, we note that the influence of the free edge vanished at $d/a = 4$, beyond which the Hertz solution is suitable for modeling the contact problem. Investigating a truncated contact zone near the free edge reveals more pronounced pressure amplitudes and shifts in the pressure field. In cases of the two-joined space problem, where the third material -3 is stiffer than the indented material -2, the maximum pressure decreases as the contact zone is close to the interface. Moreover, the contact zone expands, potentially resulting in a noticeable pressure peak at $d/a = 1$. To evaluate the comparison between the obtained solutions and Hertz's solution, a series of parametric studies are conducted to illustrate the effects of the free edge on the contact response.

114

Sommaire

4.1 Introduction

Rolling element bearings play a critical role in machinery and are extensively employed in power transmission chains. However, during their operation, these rolling elements can migrate toward the edges of the rings, leading to quarter space or truncated contact issues. Such occurrences can escalate or prompt damage to the bearings. Consequently, comprehending the behavior of rolling elements near free edges and when their geometry is truncated is imperative. Numerous studies (ZAN 72; KAN 74; HAR 79; HAR 80; CHE 10a; JAC 01; AMU 16b; ZHA 17; BEY 19; BON 20; MER 22) have been carried out to enhance bearing reliability and gain deeper insights into their failure modes. These studies have underscored the significance of understanding edge effects and the impact of truncated geometries in contact to enhance predictions of contact-related damage to components.

Therefore, the objective of this study is to explore the elastic quarter space problem under normal loading and the truncated contact problem, since these issues can induce excess pressure on the bearing raceway. The chapter initiates by presenting the existing knowledge and understanding of the contact mechanics problem. The subsequent section is dedicated to resolving the quarter space problem.

4.2 Quarter space contact problem

While the Hertz theory of contact is a fundamental and widely used theory for contact problems in mechanics, it is limited to the assumption of a homogeneous half-space. In many real-world engineering systems, the surfaces in contact may have complex geometries (presence of free edges for example), material properties, and loading conditions that require more sophisticated and specialized analysis techniques. The study of contact problems in quarter space configurations, for example, has important applications in fields such as tribology, materials science, and structural engineering. Theoretical research and numerical simulations in this area can provide insights into the behavior of contact interfaces and guide the design and optimization of systems that involve contact mechanics. When we consider the elastic quarter-space problem, it has applications in many engineering systems, such as bearing raceways, railway tracks, pavement, foundations, and geotechnical engineering. Accurate analysis and prediction of the contact stresses and deformations in these systems are crucial for the design and maintenance of these structures. The solution methods for elastic quarter-space problems are constantly being developed and refined, and they often involve numerical techniques such as integral equations, Fourier transforms, Finite Element Methods (FEM) and Semi-Analytical Methods (SAM)(WAN 12; WAN 17; AHY 22). The solution of contact problems in quarter space problem has practical importance in various engineering applications, such as the analysis of the stresses and deformations in the contact of rail/wheel systems, bearings, and welded bodies. Theoretical research on quarter space problems has also led to the development of various numerical and analytical techniques for solv-

ing such problems, which have been applied to other types of contact problems as well. The appendix.A provides a comprehensive summary of the theories related to various types of contacts discussed in the literature, along with an overview of diverse resolution methods.

4.3 Presentation

The quarter-space contact problem, which involves a free edge very close to the contact zone, has been extensively studied under normal loading conditions by many researchers (HET 60; HET 70; HAN 89; HAN 90; HAN 91; GUI 11; WAN 12; WAN 17; AHY 22) in both industry and academia. This problem is of great interest because the mechanical components are of finite dimensions, and the edge effects can significantly impact the material's behavior or response. Practical mechanical systems such as rail wheels, cam followers, gears, and roller bearings commonly encounter this problem. In these cases, the contact limit is so close to the free edge that the edge effects cannot be ignored. Another scenario where edge effects modify the material's response is in nanoindentation or indentation tests, where the mechanical properties of samples are investigated up to the ends of the free edges. The Hertz assumptions are no longer valid in these different contact cases, and a quarter-space model is necessary to capture the more precise physical reality.

The elastic quarter plane problem under static loading was first investigated by Shepherd (SHE 35). The Mellin transform was used by Tranter (TRA 48) for solving the quarter plane problem with an arbitrary wedge angle. The analytical resolution of the quarter plane or quarter space problem is very complicated because of the nonseparability of the boundary conditions. Because of the complexity of the problem, several techniques have been developed by researchers and coupled with numerical approaches to reach for an effective solution. Among them, there is Hetenyi (HET 60; HET 70) ingenious technique of overlapping half plane or half space allowing to obtain results of an acceptable precision. In addition to normal loading, concentrated shear loads were investigated by Hetenyi (HET 60; HET 70) so that, loading of any type could be treated. The problem formulation in terms of two coupled integral equations was developed by Sneddon (SNE 71) and solved by the use of Mellin transform. Keer(KEE 84) applied Sneddon's method a little later to solve the quarter plane and quarter space problem numerically in the transform domain. Hetenyi's technique has been used by Constantinou (CON 86) for solving the orthotropic quarter-plane problem. Subsequently, Hanson(HAN 89; HAN 90; HAN 91) publish a series of extremely important papers on the subject considering diffent cases such as the frictionless contact problem between the quarter-space and a rigid cylinder, and the case of elastic-plastic and rolling and sliding contact. In 2010, Guenfoud (GUE 10) used the Ritz method to calculate with unprecedented precision the quarter space displacements. Inspired by Hetenyi technique, in 2011 Guilbault (GUI 11) implemented

a rapid correction method to solve a quarter space problem. Subsequently the case of two quarter spaces welded together, indented by a sphere rigid was studied by Wang et al. (WAN 12) and solved by the equivalent inclusions method. Inspired by Hetenyi and Keer works, in 2013 Zhang at al. (ZHA 13) proposed an explicit solution of the quarter space problem based on a matrix formulation. In 2014 Najjari (NAJ 14) studied the free edge effect on EHL of a cylindrical roller using an approximate correction factor method developed by Guilbault . In the same year Zhang et al. (ZHA 14) have investigated the effect of surface roughness characteristics on the elastic-plastic contact performance. In 2016 Zhang et al.(ZHA 16), extended the matrix formulation to the finite length space problem with two free surfaces. In 2017 researchers (WAN 17; GUO 17a; ZHA 17; GUO 17b) published a numerous of important studies on the quarter space problem to take into account the free edge effect and the finite line EHL. Recently in 2020 Guo et al. (GUO 20) have developed an explicit solution to a three-dimensional wedge problem considering two edges effect.

Regarding the ellipse truncation contact problem, this problem occurs for the example when the rolling elements reach the rim of the raceway due to excessive axial load, misalignment, or large deformations. This situation has the consequence to cut the elliptical contact between the rolling elements and the raceway. Recently in 2022 Juettner (JUE 22) investigated the influence of the undercut angle on the pressure distribution and the elastic and plastic deformation at the edge. According to the authors' knowledge, there is a scarcity of published studies that focus on elastic simulations involving truncated contact ellipses.

To solve numerically the quarter space problems some authors such as Bower(BOW 87) employed the finite element method (FEM) to analyse its plastic deformation under rolling contact loads. For a numerical resolution finite element method remain the most largely used method for any type of problem. This wide use is due to their ability to consider all kind of problems including contact problems, thermal effects, dynamic problems, plasticity, viscoplasticity.... However when finite element method are used, the required computational resources for precise results can be very prohibitive especially when the models become complex. One of the alternatives to overcome the problem of computation time is the boundary element method (BEM) which has the particularity of being more interesting when the modeling domains becoming infinite. So the problem resolution is made through the surfaces discretization of the bodies. Later the semi analytical methods (SAM) was developed. They are derived from boundary integral formulations, it consists in decomposing a complex problem into a sum of simple problems for which an analytical closed-form solution is known on each patch. After that, a numerical superposition of each elementary solution is then performed. The same procedure can be applied for a contact problem. So in the contact problem, by integrating the numerical superposition in a contact solver algorithm allows to obtain the solution of the mechanical problem. The semi analytical models also produce more precise results for a given mesh size and the preprocessing stage is straightforward. The first semi analytical

118

models were proposed by Bentall (BEN 67) and Paul(PAU 81) for contact problems under a static load. Later, Kalker (KAL 90a) proposed a first formalisation of this method using a Newton-Raphson algorithm.

SAM method being well adapted to the resolution of contact problems, it will be adopted for the quarter space problem resolution in this work. The resolution of the contact problem with SAM, whether normal and/or tangential, requires the establishment of a link between the distribution of the load on the one hand and the displacements and stresses that it induces on the other hand. This link was established by Boussinesq (BOU 85) and Cerruti (CER 82) potentials theory in the half space framework. Using a similar approach, Love (LOV 29) would later define the relation between uniform pressure acting on a rectangular area and the normal displacement it produces. Subsequently, Vergne(VER 85) has developed an equivalent solution for the tangential problem. The displacements and stresses computation is necessary for the resolution but turns out to be very expensive fact of the double summation over the domain which must be performed at each point. Hence the need to reduce the cost of this operation to maintain reasonable calculation times. In order to speed up these operations, the discrete convolution Fast Fourier Transform ($DC - FFT$) approach is widely used by many researchers. These operations complexity may be reduced from $M \times N \times L$ to $\ln M \times \ln N \times \ln L$. The proposed method by (JU 96) and later improved by Liu (LIU 02) consists in using the properties of discrete convolution products in the frequency domain. With this SAM developped method, a wide range of issues such as the resolution of normal and tangential contact(KAL 67), the take into account of the thermo-elastic and plastic behavior (BOU 05), heterogeneous viscoelastic behavior (KOU 15b), elasto-plastic layered behavior (WAY 11) and viscoelastic layered behavior (WAL 20; CAR 13). Recently a coupling of the semi analytical methods and the eXtended-Finite Element Method (SAM/X-FEM) was performed by Meray et al. (MER 22) for the simulation of 3D fatigue crack growth under rolling contact loading. In the present analysis, a contact problem on an elastic quarter space is investigated. A fast numerical model to solve the quarter space problem based on a new approach is proposed. This new approach consist in introducing two corrective factors ψ_1 and ψ_2 which will make it possible to better correct the influence of the free edge on the final solution. This approach is derived from Guilbault's (GUI 11) fast correction method. The model uses Hetenyi's mirror pressure superposition technique as well as semi-analytical methods optimized by Fast Fourier Transforms (FFT). At the end a modeling of the quarter space problem with the consideration of the contact ellipse truncation is carried out.

A numerical developments are performed in this chapter and the following in a homemade code called Isaac. Isaac is a semi-analytical multiphysics code that incorporates various aspects of contact modeling. It is developed to take into account various material properties, including elastic, elastic-plastic, viscoelastic, and the presence of inclusions, etc. Additionally, Isaac can handle complex material geometries and various configurations of contact problems, such as static, dynamic,

and rolling contact problems. The versatility of Isaac code allows for the accurate simulation of contact phenomena in different scenarios, considering the interaction between multiple physical phenomena. By incorporating various material properties and contact configurations, Isaac provides a comprehensive tool for studying and understanding complex contact problems.

4.4 Theoretical description

The quarter space can be geometrically obtained by first dividing the infinite space (defined by $-\infty \leq x \leq +\infty$, $-\infty \leq y \leq +\infty$, and $-\infty \leq z \leq +\infty$) into two halves along the z-axis, and then dividing one of the halves into two along the x-axis. This division process creates the quarter space defined by $x \geq 0$, $-\infty \leq y \leq +\infty$, and $z \geq 0$.

In the context of linear elasticity, the quarter space problem subjected to an arbitrary loading can be decomposed into two separate problems: the normal problem and the tangential one. In the normal problem, only the normal loading component is considered, which acts perpendicular to the contact surface. This problem focuses on the normal stress distribution and deformation caused by normal loading.

Similarly, in the tangential problem, only the shear loading component is considered, which acts tangentially to the contact surface. This problem focuses on the distribution of shear stress and deformation resulting from the shear loading.

By using the superposition properties of linear elasticity, the solutions to the normal and tangential problems can be obtained separately. Then, these solutions can be combined through superposition to obtain the overall solution for the quarter space problem subjected to arbitrary loading as illustrated in Fig.4.1.
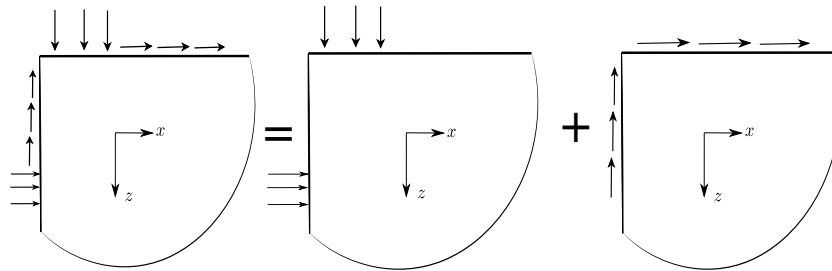
Figure 4.1: Decomposition of the quarter-space subjected to arbitrary loading on its both surfaces

Similarly, the quarter-space problem can be divided into two overlapped quarter-spaces when normal loadings are applied on horizontal and vertical surfaces, as depicted in Fig.4.2. By considering the solution of the normal problem for an elastic quarter-space with one loaded surface and one free surface as the kernel solution, solutions for various loading configurations can be obtained. An example where the quarter-space problem is applicable is when a ball or a roller reaches the free surface
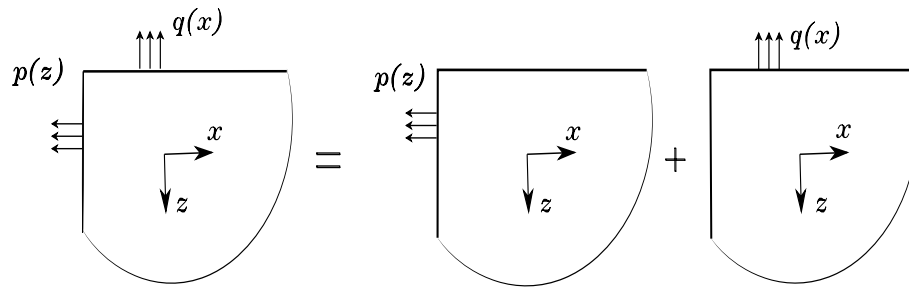
Figure 4.2: Decomposition of the quarter-space subjected to normal loading on its both surfaces

of a raceway. In such cases, the quarter-space problem arises, and we consider a quarter space subjected to normal loading at a normalized distance of d/a from the edge, as illustrated in Fig.4.3.

In this chapter, we propose a solution for the quarter-space problem. Furthermore, we extend the analysis to address situations where the Hertz contact area, which represents the solution for the half-space problem, is truncated. We also apply a similar approach to handle contact problems in two joined spaces with different material considerations. The quarter-space problem becomes particularly relevant when the contact area approaches the free surface. To illustrate this, let's consider a quarter-space subjected to normal loading by a sphere located at a dimensionless distance of d/a from the edge, as shown in Fig.4.3. Here, a represents the Hertz contact radius, and d is the distance between the free edge and the center of the contact.
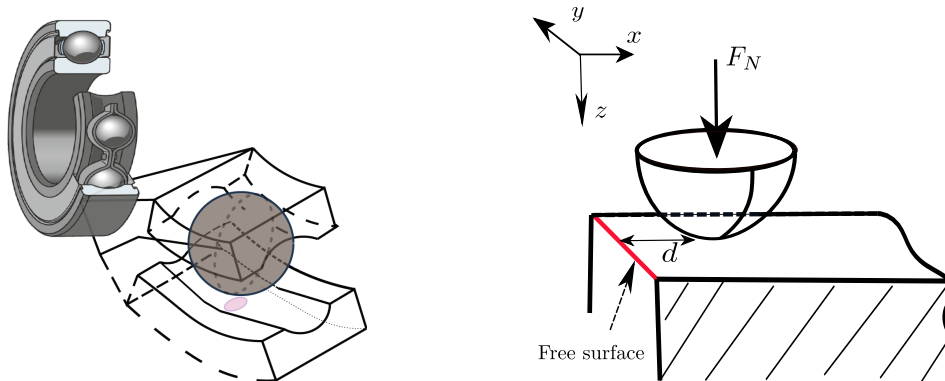
Figure 4.3: Quarter-space problem illustration: (a) The contact ellipse in a ball bearing may be truncated when it reaches the limit of the raceway, (b) Quarter-space subjected to a normal loading at distance d from the free edge

To address the quarter-space problem, Hetenyi(HET 60) introduced a technique known as the half-space overlap method, along with an iterative scheme to determine the free surface conditions. Building upon Hetenyi's approach, Guilbault (GUI 11) proposed a fast method to release the free surfaces of the quarter-space from shear

and normal internal stresses without significantly increasing computation time. This method involves the construction of a corrective factor derived from Hetenyi's correction process, which multiplies the mirrored pressure.

This section will describe Hetenyi's superposition technique using an arbitrary loading function $P(x,y)$. To facilitate the analysis, we adopt a 2D schematization known as quarter-plane schematization. Hetenyi's technique involves applying a pressure field $P(x)$ centered at x_0 and its symmetric counterpart $P(-x)$ centered at $-x_0$. This initial correction eliminates the shear stress in the (Oz) plane but generates an internal normal stress field. Its opposite is applied to cancel out this stress in the (Oz) plane. Consequently, shear stress arises in the (Ox) plane, which is then canceled by applying the corresponding mirrored loading. The overlapping technique proposed by Hetenyi is illustrated in Fig.4.4. In the subsequent analysis, $P(x)$ will be treated as a normal concentrated force P as shown in Fig.4.5.
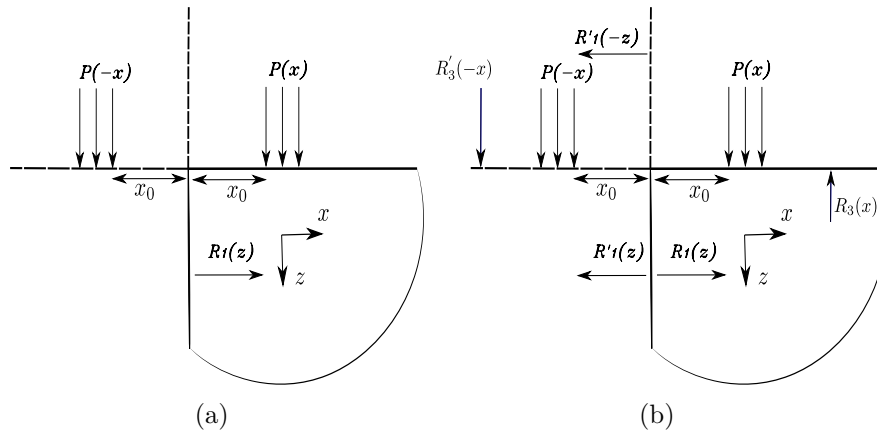
Figure 4.4: Quarter plane with loading $P(x)$ superimposing scheme at first and second iterations

When two concentrated forces are applied on a half-plane, as depicted in Fig. 4.4, the stress state at the point (x, z) can be expressed as follows:

$$\sigma_{xx} = -\frac{2P}{\pi} \left\{ \frac{z(x+x_0)^2}{(z^2+(x+x_0)^2)^2} + \frac{z(x-x_0)^2}{(z^2+(x-x_0)^2)^2} \right\} \tag{4.1a}$$

$$\sigma_{zz} = -\frac{2P}{\pi} \left\{ \frac{z^3}{(z^2+(x+x_0)^2)^2} + \frac{z^3}{(z^2+(x-x_0)^2)^2} \right\} \tag{4.1b}$$

$$\tau_{xz} = -\frac{2P}{\pi} \left\{ \frac{z^2(x+x_0)}{(z^2+(x+x_0)^2)^2} + \frac{z^2(x-x_0)}{(z^2+(x-x_0)^2)^2} \right\} \tag{4.1c}$$

At the interface defined by $x = 0$, the stress state becomes:

$$\sigma_{xx} = -\frac{4P}{\pi} \left\{ \frac{zx_0^2}{(z^2+x_0^2)^2} \right\} \tag{4.2a}$$

$$\sigma_{zz} = -\frac{4P}{\pi} \left\{ \frac{z^3}{(z^2+x_0^2)^2} \right\} \tag{4.2b}$$

$$\tau_{xz} = 0 \tag{4.2c}$$

To determine the lateral force that constrains the z axis, equation 4.2a needs to be integrated with respect to the variable x. The total lateral force can then be obtained as follows:

$$\int_0^{+\infty} \sigma_{xx} dz = -2P\frac{1}{\pi} \tag{4.3}$$
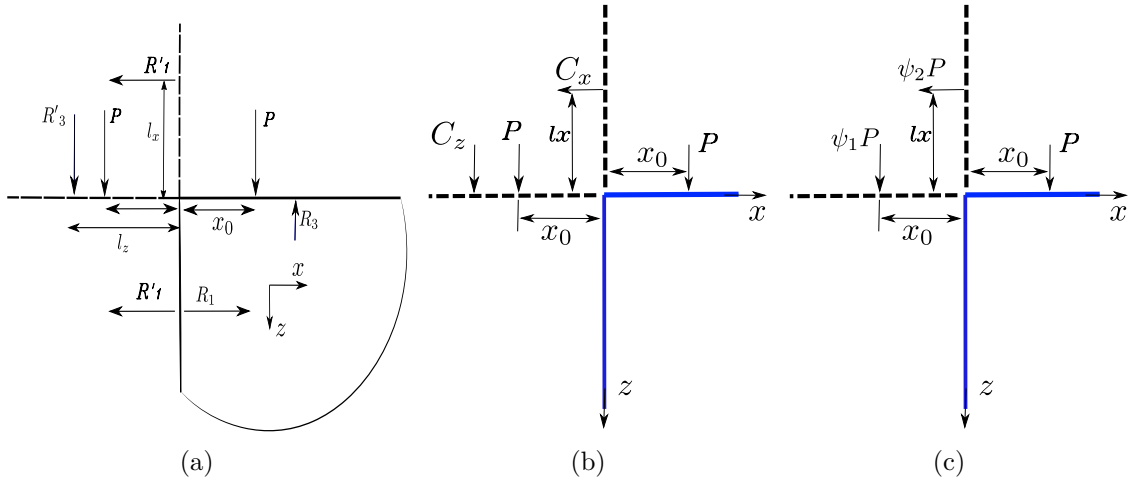
Figure 4.5: a) Quarter-space with the correction process at the third iteration with a normal loading, b) Quarter-space correction at the first iteration with a concentrated normal force, c) Quarter-space with the corrective factors applied on each plane.

Based on Eq.4.3, we can deduce that when two concentrated forces are applied along a particular axis, the resulting force magnitude on the second axis is obtained by dividing the total applied load by π. Therefore, correcting the system by counteracting the normal internal loading on the surface through a corrective force will generate an additional internal normal load on the initial boundary (z=0) equal to $(-2/\pi)^2 P$. Consequently, with each iteration, the induced internal normal stress is equivalent to the total applied load divided by π, and its position will shift away from the edge by a factor of $\frac{\pi}{2}$. This relationship can be expressed using the following equation.

$$\frac{\int_0^{+\infty} z\sigma_{xx} dz}{\int_0^{+\infty} \sigma_{xx} dz} = \frac{\pi}{2}x_0 \tag{4.4}$$

123

At the first iteration the corresponding point forces C_x, C_z as well as the lever arms is given by:

$$C_x = -\frac{2}{\pi}P, \quad l_x = -\frac{\pi}{2}x_0, \quad C_z = (-\frac{2}{\pi})^2 P, \quad l_z = (\frac{\pi}{2})^2 x_0$$

The convergence of this procedure was initially established by Hetenyi (HET 60). Guibault's method aims to eliminate the time-consuming and memory-intensive iterative process by introducing a corrective factor on the horizontal plane that considers the entire iterative process. The same resolution approach is employed in this analysis. When a half-space is subjected to a concentrated normal force P, the displacement fields in the z direction can be expressed as follows:

$$u_x(P) = \frac{P(1+\nu)}{2\pi E}\left\{\frac{xz}{\rho^3} - (1-2\nu)\frac{x}{\rho(\rho+z)}\right\} \tag{4.5a}$$

$$u_y(P) = \frac{P(1+\nu)}{2\pi E}\left\{\frac{yz}{\rho^3} - (1-2\nu)\frac{y}{\rho(\rho+z)}\right\} \tag{4.5b}$$

$$u_z(P) = \frac{P(1+\nu)}{2\pi E}\left\{\frac{z^2}{\rho^3} + 2(\frac{1-2\nu}{\rho})\right\} \tag{4.5c}$$

where

$$\rho = \sqrt{x^2 + y^2 + z^2}$$

When considering a quarter space, the influence of correction forces (C_x and C_z) depicted in Figure 4.5(c) on the displacement at the point of application can be evaluated using Eq.4.6.

$$u_z(C_x) = \delta(C_x) = \frac{C_x(1+\nu)}{2\pi E}\left\{\frac{xz}{\rho^3} - (1-2\nu)\frac{x}{\rho(\rho+z)}\right\} \tag{4.6a}$$

$$u_z(C_z) = \delta(C_z) = \frac{C_z(1+\nu)}{2\pi E}\left\{\frac{yz}{\rho^3} - (1-2\nu)\frac{y}{\rho(\rho+z)}\right\} \tag{4.6b}$$

$$u_z(P) = \delta(P) = \frac{P(1+\nu)}{2\pi E}\left\{\frac{z^2}{\rho^3} + 2(\frac{1-2\nu}{\rho})\right\} \tag{4.6c}$$

The new method involves applying two factors, ψ_1 and ψ_2, on each axis to consider the free edge effect on the contact zone, as illustrated in Figure 4.5. Consequently, the final displacement of the space can be expressed as follows:

$$\delta(P_{eq1}) = \delta(P) + \delta(C_z), \quad \text{on the horizontal plane} \tag{4.7}$$

$$\delta(P_{eq2}) = \delta(C_x), \quad \text{on the vertical plane} \tag{4.8}$$

The subsequent step involves quantifying the displacement of the equivalent forces with respect to each axis based on the displacement of the normal loading. This allows for the introduction of the corrective factors, which can be expressed as follows:

$$\psi_1 = \frac{\delta(P_{eq1})}{\delta(P)} = 1 + \frac{\delta(C_z)}{\delta(P)} \tag{4.9}$$

Thus we get on the horizontal plane:

$$\psi_1 = \frac{\delta(P_{eq1})}{\delta(P)} = 1 + \frac{2^5}{\pi^2(\pi^2 + 2^{2)}} \tag{4.10}$$

After Hetenyi n iterations, the factor become:

$$\psi_1 = 1 + \Sigma_n \frac{2^{4n+1}}{\pi^{2n}(\pi^{2n} + 2^{2n})} \tag{4.11}$$

Recall that this hyper-geometric series is convergent and gives:

$$\Sigma_n \frac{2^{4n+1}}{\pi^{2n}(\pi^{2n} + 2^{2n)}} = 0.29 \tag{4.12}$$

Hence:

$$\psi_1 = 1.29 \tag{4.13}$$

On the vertical plane, the corrective factor is given by:

$$\psi_2 = \frac{\delta(P_{eq2})}{\delta(P)} = \frac{\delta(C_x)}{\delta(P)} \tag{4.14}$$

At the first Hetenyi iteration we obtain:

$$\psi_2 = \frac{\delta(P_{eq2})}{\delta(P)} = \frac{1}{1-\nu}\left\{\frac{1}{\left[(\frac{\pi}{2})^2+1\right]^{\frac{3}{2}}} - \frac{1-2\nu}{\left[(\frac{\pi}{2})^2+1\right]^{\frac{1}{2}}\left[((\frac{\pi}{2})^2+1)^{\frac{1}{2}}+1\right]}\right\} \tag{4.15}$$

which gives after n iterations:

$$\psi_2 = \frac{1}{1-\nu}\left\{\Sigma_n\frac{1}{\left[(\frac{\pi}{2})^{2(2n+1)}+1\right]^{\frac{3}{2}}} - \Sigma_n\frac{1-2\nu}{\left[(\frac{\pi}{2})^{2(2n+1)}+1\right]^{\frac{1}{2}}\left[((\frac{\pi}{2})^{2(2n+1)}+1)^{\frac{1}{2}}+1\right]}\right\} \tag{4.16}$$

Knowing that:

$$\Sigma_n \frac{1}{\left[(\frac{\pi}{2})^{2(2n+1)}+1\right]^{\frac{3}{2}}} = 0.1717 \qquad (4.17)$$

and

$$\Sigma_n \frac{1}{\left[(\frac{\pi}{2})^{2(2n+1)}+1\right]^{\frac{1}{2}} \left[((\frac{\pi}{2})^{2(2n+1)}+1)^{\frac{1}{2}}+1\right]} = 0.25 \qquad (4.18)$$

it comes:

$$\psi_2 = \frac{1}{1-\nu}\left\{0.17 - 0.25(1-2\nu)\right\} \qquad (4.19)$$

To solve the contact problem, the two correction factors that have been identified will be introduced. In order to implement this numerically, the described process with the corrective factors will be deployed.

4.5 Contact model

In order to analyze the pressure, displacement, and stress fields in the quarter space, it is necessary to consider the contact problem. When two bodies are in contact over a region Γ, the boundary conditions of the contact problem can be described by the following system of equations and inequalities:

1. The surface separation:
   The distance between the contacting bodies denoted as $g(x)$, is determined by the summation of three components: the initial separation $g_i(x)$, the rigid body displacement δ_z, and the normal elastic surface displacement of both bodies $u_z^{\Omega_1+\Omega_2}(x)$:

$$g(x,y) = g_i(x,y) + \delta_z + u_3^{\Omega_1+\Omega_2}(x,y) \qquad (4.20)$$

2. The contact condition:
   The contact pressure is always non-negative:

$$(x,y) \in \Gamma_c; \quad g(x,y) = 0 \quad and \quad p(x,y) > 0 \qquad (4.21\text{a})$$

$$(x,y) \notin \Gamma_c; \quad g(x,y) > 0 \quad and \quad p(x,y) = 0 \qquad (4.21\text{b})$$

   where $p(x,y)$ denotes the pressure field and F_N is the normal load; g the final surface gap between the two bodies.

126

3. The load balance:
   The normal applied load, denoted as F_N, can be determined by integrating the contact pressure distribution $p(x,y)$ over the contact zone Γ_c. Mathematically, it can be expressed as follows:

$$F_N = \int_{\Gamma_c} p(x,y)dS \tag{4.22}$$

In order to numerically solve the contact problem, the two bodies in contact will be discretized into a $2D$ regular grid consisting of $N = Nx * Ny$ points. The grid points are spaced by Δx along the x-direction and Δy along the y-direction. Each grid point corresponds to a centered elementary rectangular zone with an area $dS = \Delta x * \Delta y$, where the pressure is assumed to be constant. Thus, the pressure distribution $p(x,y)$ is discretized into multiple patches with uniform pressure. By utilizing the linear elasticity theory, the elastic response of the contact interface can be determined by summing up the contributions from each grid element using influence coefficients, which are Green's functions. Consequently, the normal displacement can be expressed in the following discretized form:

$$u_z(n) = \sum_{m=1}^{N} K_z^p(m,n)p(m) \tag{4.23}$$

The influence coefficients K_z^p quantify the impact of a rectangular patch with uniform pressure at point m on the normal elastic displacement at point n.

The contact problem is formulated in a variational form, and its solution involves minimizing the complementary energy. The complementary energy can be expressed in the following form:

$$\begin{cases} \text{Minimize} \\ \boldsymbol{F}(\mathbf{p}) = \tilde{\mathbf{g}} \times \mathbf{p} + \frac{1}{2}\mathbf{p}^{\mathrm{T}} \times \mathbf{K} \times \mathbf{p} \\ \text{Subject to } p \geq 0 \end{cases} \tag{4.24}$$

In the given context, the matrix $\mathbf{K}$ represents the influence coefficients that establish the relationship between pressure and surface displacement. Additionally, $\tilde{g}$ denotes the geometrical interference between the two surfaces, which can be defined as $\tilde{g} = g_i - \delta_z$, where g_i represents the initial body separation and δ_z corresponds to the approach between the two surfaces.

The surface displacement of the quarter space can be expressed as the sum of two components. The first component, u_{z_h}, represents the surface elastic displacement of a homogeneous half-space. The second component, u_{z_q}, corresponds to the perturbed normal displacement on the surface due to the presence of a free edge near the contact area. Mathematically, it can be expressed as follows:

$$u_z = u_{zh} + u_{zq} \tag{4.25}$$

The surface elastic displacement of the homogeneous half-space, denoted as u_{z_h}, can be calculated using the FFT-based algorithm method, which provides highly efficient computational solutions. For elastic half-spaces, the displacement u_{z_h} can be expressed as follows:

$$u_{zh} = IFFT \left(\widetilde{K_p^{u_z}} * \tilde{p} \right)$$

The influence coefficients $\widetilde{K_p^{uz}}$ are associated with the half-space solutions and depend on the elastic properties of the material bodies as well as the mesh size. These coefficients are utilized in a convolution operation denoted by the asterisk symbol. For more detailed information about the resolution scheme, interested readers can refer to references such as (KEE 83b; HAN 90; HAN 91; POL 99), or (JAC 03; GAL 06a; NEL 07; KOU 14; KOU 15b) and others. Since the contact problem is an optimization problem with constraints, the conjugate gradient method (CGM) algorithm is employed to determine the pressure distribution and the displacement field. The flowchart illustrating the process of solving the elastic quarter space contact problem is presented in Fig.4.6.
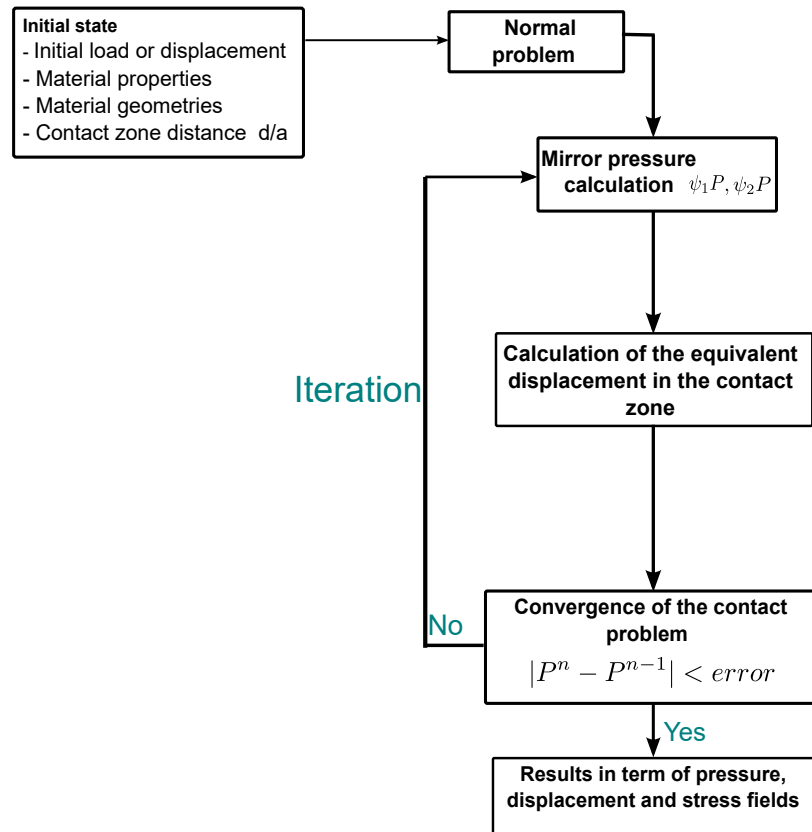
Figure 4.6:   Flowchart for solving quarter space contact problem.

The new correction method, based on the principle of mirror loadings, requires

a correction to obtain the correct tensile stress that is normal to the free surface. Although the numerical solution provides an initial stress state, it is only partially accurate, and a stress correction is necessary to achieve a more precise approximation. To correct the tensile stress σ_{xx} after applying the corrective factors, we observe that when applying a force of P at x_0 and $\psi_1 P$ at $-x_0$ on the half-space, the corresponding tensile stresses on each side are σ_{xx} and $\psi_1 \sigma_{xx}$, respectively. Therefore, the resulting tensile stress at the free edge, located at a distance $d = a$ from the edge (as depicted in Fig.4.7), is $(2-\psi_1)\sigma_{xx}$. Since the loadings are symmetrical, the tensile stress in the quarter space equals the tensile stress in the half-space, plus the tensile stress resulting from the mirror pressure acting on the free edge side. In this correction, only the effect of the ψ_1 factor is considered, as the effect of the ψ_2 factor on the stress field is negligible. To consider the influence of the distance d/a from the free edge on the stress state, the stress field can be approximated using the following expression:

$$\sigma_{xxeq} = \left[1 + (1-\psi_1)\frac{a}{d}\right]\sigma_{xx} \qquad (4.26a)$$

$$\sigma_{xzeq} = \left[1 - \frac{0.29a}{4d}\right]\sigma_{xz} \qquad (4.26b)$$
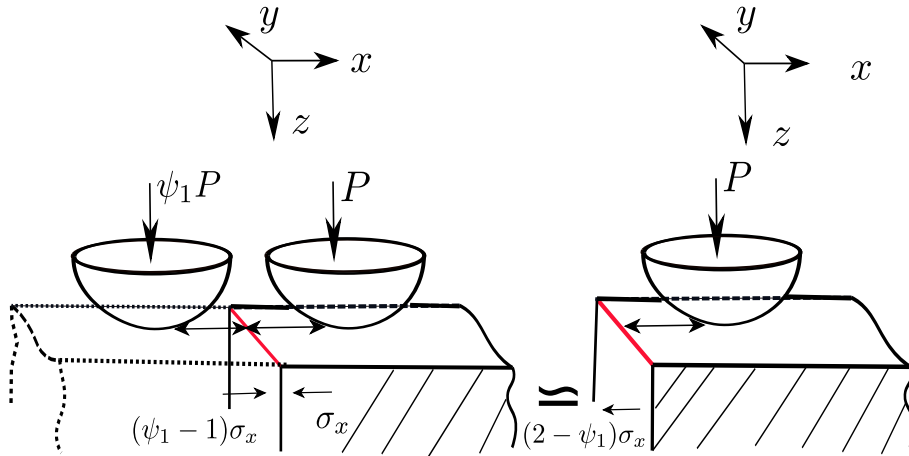
Figure 4.7: Quarter-space stress field correction at d = a, a being the Hertz contact radius and d the distance between the Hertz contact center and the free edge

4.6 Ellipse truncation analysis

The contact zone or ellipse truncation problem refers to a phenomenon that occurs when two bodies with elliptical contact areas come into contact, and the contact region is truncated or reduced in size.

The contact zone or ellipse truncation problem is important to consider because it affects the distribution of forces, stresses, and contact pressure between the bodies. Understanding the extent of truncation and its impact on the mechanical behavior of the system is crucial for accurate analysis and design considerations.

In this section, we will examine the phenomenon of contact zone truncation in the quarter-space contact problem. This situation commonly arises in contacts involving bearing or gear components, where rolling elements like balls or rollers can experience motion, and their geometries can be truncated relative to the ends of the rings. This truncation leads to the formation of an undercut that extends into the contact zone, resulting in the partial disruption of the elliptical contact between the rolling elements and the raceway.

By incorporating the correction method and factors discussed earlier, the authors extend their approach to analyze the effect of ellipse truncation in the quarter-space contact problem. This allows for the investigation of contact behavior and stress distribution in scenarios where the contact area is modified due to truncation caused by the presence of free edges.

Consider a situation where two bodies are in contact, and the contact zone is truncated due to the presence of a free edge, as illustrated in Fig.4.8(a).

(a)   (b)
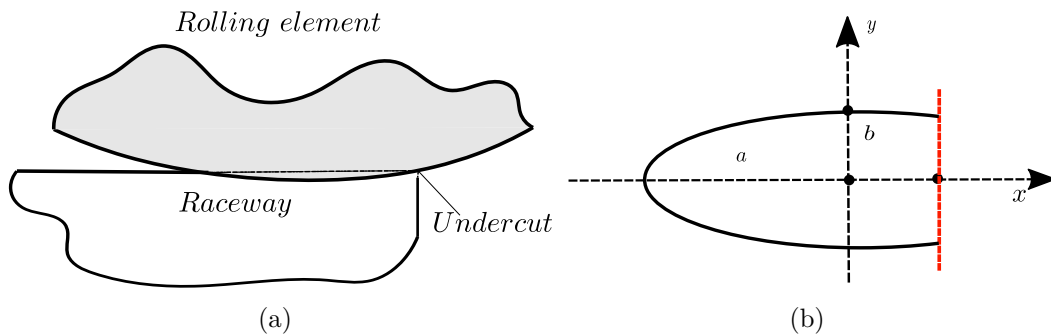
Figure 4.8: (a) Geometry truncation problem illustration, (b) Elliptical contact zone truncation

To handle the truncation of the contact zone in the resolution, the authors propose a modified approach to solve the quarter-space problem. This modified approach uses the same resolution method employed for the quarter-space case but incorporates the mirror pressure distribution on the truncated zone. The resolution process follows a similar procedure to the quarter-space problem, with the main distinction being the truncation of the pressure distribution to align with the geometry of the contact zone affected by the truncation, as depicted in Fig.4.8.

The resolution process encompasses the following steps:

❊ Define the contact problem conditions

❊ Define the loading, the geometry and material properties.

❋ Calculate the truncated pressure field numerically

❋ Apply the corrective factors on the mirror pressure

❋ Calculate the equivalent displacement field due to the mirror pressure

❋ Introduce the calculated displacement into the contact resolution

❋ Get the results in term of pressure, displacement and stresse fields

These steps are summarized in the flowchart in Fig.4.6.

4.7 Two joined space contact problem

The contact problem between two joined spaces refers to a scenario where two separate spaces or bodies come into contact with each other at their common interface or contact surface. The analysis of contact problems on two joined spaces is crucial in various applications, including mechanical engineering, structural analysis, biomechanics, and material science. It allows for the prediction of contact behavior, the optimization of design parameters, and the evaluation of structural integrity and performance under various loading conditions.

The welding process is widely used across various industries due to its efficiency and effectiveness in joining materials. Welded or joined components are commonly used in assembly processes across various industries due to their numerous advantages. Here are some of the benefits of welded or joined components in assembly:

✂ Structural integrity: Welded or joined components can enhance structural integrity compared to individual parts. By joining components, the resulting assembly can have increased strength and stiffness, allowing it to withstand higher loads and stresses.

✂ Simplified manufacturing: Joining components through welding or other joining methods can simplify manufacturing by reducing the number of separate parts. This can lead to cost savings, improved production efficiency, and reduced assembly time.

✂ Weight reduction: Joining components can eliminate the need for additional fasteners or connectors, resulting in weight reduction. This is especially important in the automotive, aerospace, and transportation industries, where reducing weight can lead to improving fuel efficiency and performance.

✂ Enhanced design Flexibility: Welded or joined components offer greater design flexibility, allowing for complex and intricate shapes to be created. This enables engineers to optimize designs for specific functional requirements, resulting in more efficient and innovative products.

✂ Improved aesthetics: Welded or joined components can provide a seamless and smooth appearance without visible fasteners or connectors. This contributes to improved aesthetics and can be desirable in consumer products or architectural applications.

However, contact problems on the joined surfaces may arise when joining components. The contact problem involves analyzing the interaction between two contacting surfaces, considering factors such as contact pressure distribution and contact area. Addressing contact problems in assembling welded or joined components is crucial to ensure proper functionality and reliability in this kind of components.
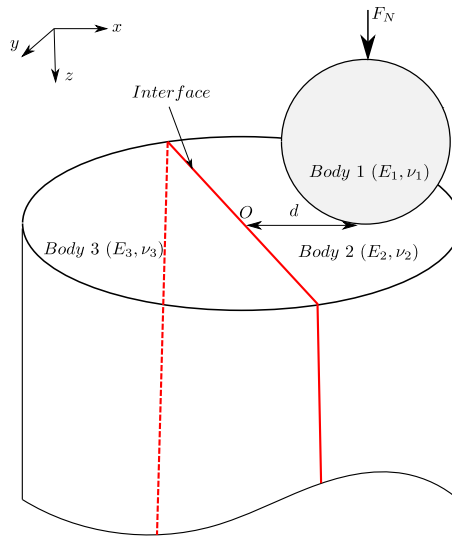
Figure 4.9: Two joined space contact problem illustration

To solve the contact problem between a sphere and two joined spaces as shown in Fig.4.9, the quarter-space problem method will be deployed. In this resolution, the sphere will be referred to as $material-1$, with properties (E_1, ν_1). The main indented space will be referred to as $material-2$, with properties (E_2, ν_2), the third space will be referred to as $material-3$, with properties (E_3, ν_3).

To take into account the influence of $material-3$ in the contact zone, an approximation technique is used. This approximation involves defining the influence of $material-3$ based on its modulus and the distance between the interface and the contact center. The approximation expression is as follows:

$$E_3^m = \frac{\frac{13(0.73E_3 + 1.27E_2)}{2E_2}}{\exp\left(\frac{1.95d}{a}\right)} \tag{4.27}$$

where E_3^m represents the $material-3$ modulus influence in the contact according to the distance d/a, E_3 is the modulus of $material-3$, d is the distance between the interface and the contact center, and a is the contact radius of Hertz. This

132

approximation allows for incorporating the influence of $material-3$ in the contact zone by considering its modulus and the spatial relationship between the contact center and the interface.

The mirror pressure field on the space of $material-3$ can be calculated based on the previous approximation. The expression for the mirror pressure field is as follows:

$$P_3(x,y) = \frac{2a_3 E_3^{eq}}{\pi R} \tag{4.28}$$

where a_3 represents the contact radius on the half-space of $material-3$, R is the radius of the sphere, and E_3^{eq} is the equivalent modulus defined by:

$$E_3^{eq} = \left[\frac{1-\nu_1^2}{E_1} + \frac{1-\nu_3^2}{E_3^m}\right]^{-1} \tag{4.29}$$

Indeed, the pressure difference between $material-2$ and $material-3$ will significantly influence the interface's behavior, which in turn affects the pressure distribution and the contact zone as the contact approaches the interface. The pressure difference between the two materials will generate some effects to be transmitted across the interface, leading to changes in the contact mechanics. By applying the corrective factors to the pressure field difference and following the entire procedure described in Fig.4.6, the solutions to the contact problem between the sphere and the joined spaces can be obtained.

4.8 Numerical results and discussion

In this section, an analysis of frictionless contact will be conducted between a quarter space, a truncated space, and a two-joined space with different materials. The material parameters for all bodies are specified as $E = 210$ GPa and $\nu = 0.3$. The normal force is assumed to be applied at the center of the rigid sphere.

The study will involve a parametric analysis of the response of the quarter-space and the finite-length space based on their distances from each free edge. The contact center is located at the origin of the coordinate system, and the parameter d represents the distance between the contact center and the left-side free edge. In the case of the finite-length space, two distance parameters d_x and d_y are considered, describing the position of the contact center with respect to the reference edges along the x and y directions.

Table 4.1 provides an overview of the material parameters and contact conditions used in the analysis. To normalize the results (pressure, stresses, and displacements), the maximum Hertzian pressure P_0 and contact radius a from the corresponding homogeneous contact case of the half-space are used as reference values.

The simulation domain employed for the analysis spans $(-5a, 5a) \times (-5a, 5a) \times (0, 6a)$ in the x, y, and z directions, respectively. The domain is discretized uniformly into $251 \times 251 \times 40$ cuboids grid.

Parameter	Symbol	Unit	Value
Normal load	P	(N)	1923
Indentor Young's modulus	E_1	(GPa)	Rigid
Indentor radius (sphere)	R	(mm)	20
Quarter and other spaces Young's modulus	E_2	(GPa)	210
Quarter and other spaces Poisson's ratio	ν_2		0.3
Hertz's maximum pressure	P_0	(MPa)	3672.76
Hertz's contact radius	a	(mm)	0.5
Quarter-space distance from the free surface	d/a		from 0 to 3
Joined space distance from the free surface	d/a		from 0 to 3

Table 4.1: Parameters and contact conditions

4.8.1 Model verification

In this section, the validation of various SAM models is conducted by comparing them with the Finite Element Method (FEM).

4.8.1.1 Quarter space model validation

The simulations for various cases were conducted on a personal computer with a 2.6 GHz i7 CPU. The purpose was to calculate and compare the results with the Finite Element Method (FEM). To perform the three-dimensional finite-element analysis, the commercial software package ABAQUS 2019 was utilized. In order to reduce the computation time of the FEM model, the model's symmetry was taken into account by applying symmetrical boundary conditions on the section where $y = 0$ as illustrated in Fig.4.10. The zone of interest in the FEM model was meshed with C3D8R elements (eight-node linear bricks with reduced integration and hourglass control) of size 0.04 mm, while the remaining parts of the model were meshed with C3D4 elements. The sphere was modeled as an analytically rigid shell. The simulations were carried out by varying the dimensionless distance d/a and setting the friction coefficient μ_f to 0. The comparison between the pressure fields along the x-axis of the quarter space obtained from both methods is presented in Fig.4.11.

Figure 4.11 presents a comparison of the normalized contact pressure P/P_0 obtained using the Finite Element Method (FEM) and the Semi-Analytical Method (SAM) for varying values of d/a. The plot showcases the evolution of the pressure field and the contact zone as the distance d/a increases from the free edge of the quarter space. Notably, a good agreement is observed between the SAM model and the FEM results. From these results, The following key observations can be made :

♥ The presence of a free edge close to the contact zone leads to an increased pressure field compared to the case of a half space.
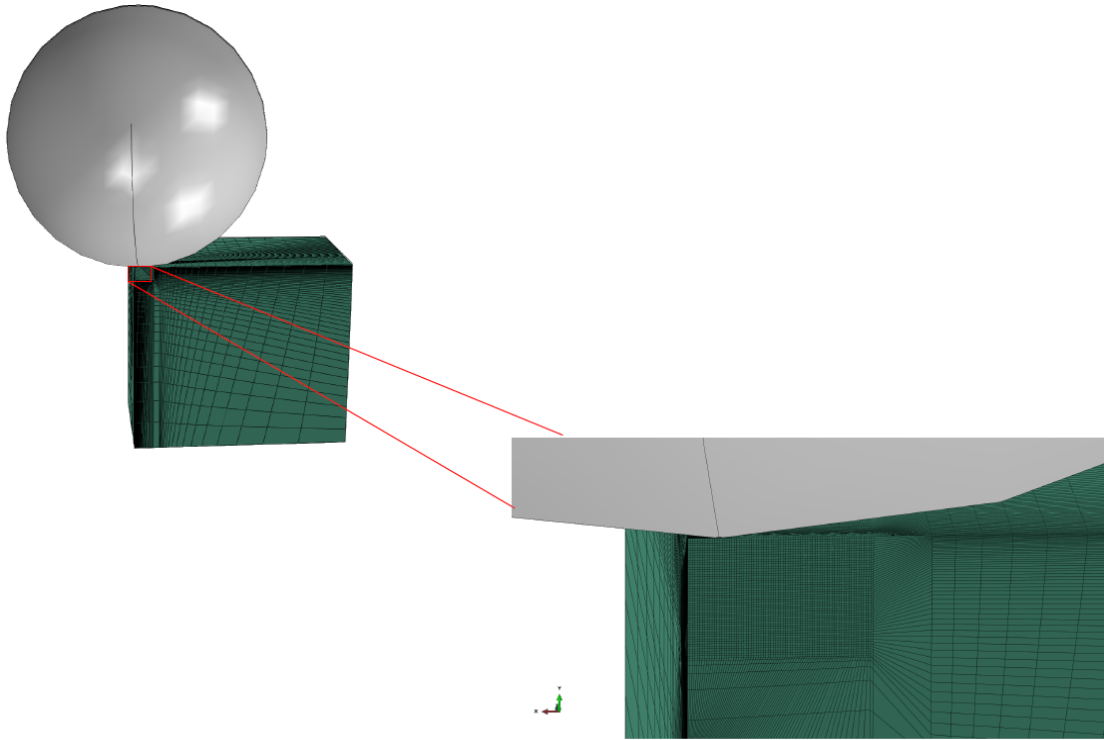
Figure 4.10: Sphere and plane contact problem model in FEM

♥ The presence of a free edge close to the contact zone causes a shift in the direction of infinity compared to the case of a half-space.

The existence of a free edge introduces nonlinearity to the contact problem. When contact problems involving edges are analyzed, a very fine mesh is required due to the high-stress concentration gradients. However, using the Finite Element Method (FEM) necessitates a large number of elements and significant computational resources. On average, FEM simulations take approximately four hours to complete. As a result, the Semi-Analytical Method (SAM) is increasingly advantageous for contact calculations, as it offers significantly faster computation times for many practical scenarios compared to FEM.

The SAM approach achieves accurate results by introducing corrective factors to account for edge effects without increasing the computation time. The SAM method is faster and consumes considerably less memory than FEM. In the SAM model, the same element size is used for the mesh, and the computation time is around one minute. It is worth noting that the SAM model can achieve similar result quality with a coarser mesh, highlighting the efficiency and speed of SAM compared to FEM. Additionally, the SAM method provides a higher grid resolution in the contact zone compared to FEM. In FEM, a larger simulation domain of $(-10a, 10a) \times (-10a, 10a) \times (0, 10a)$ is required to satisfy the half space conditions.
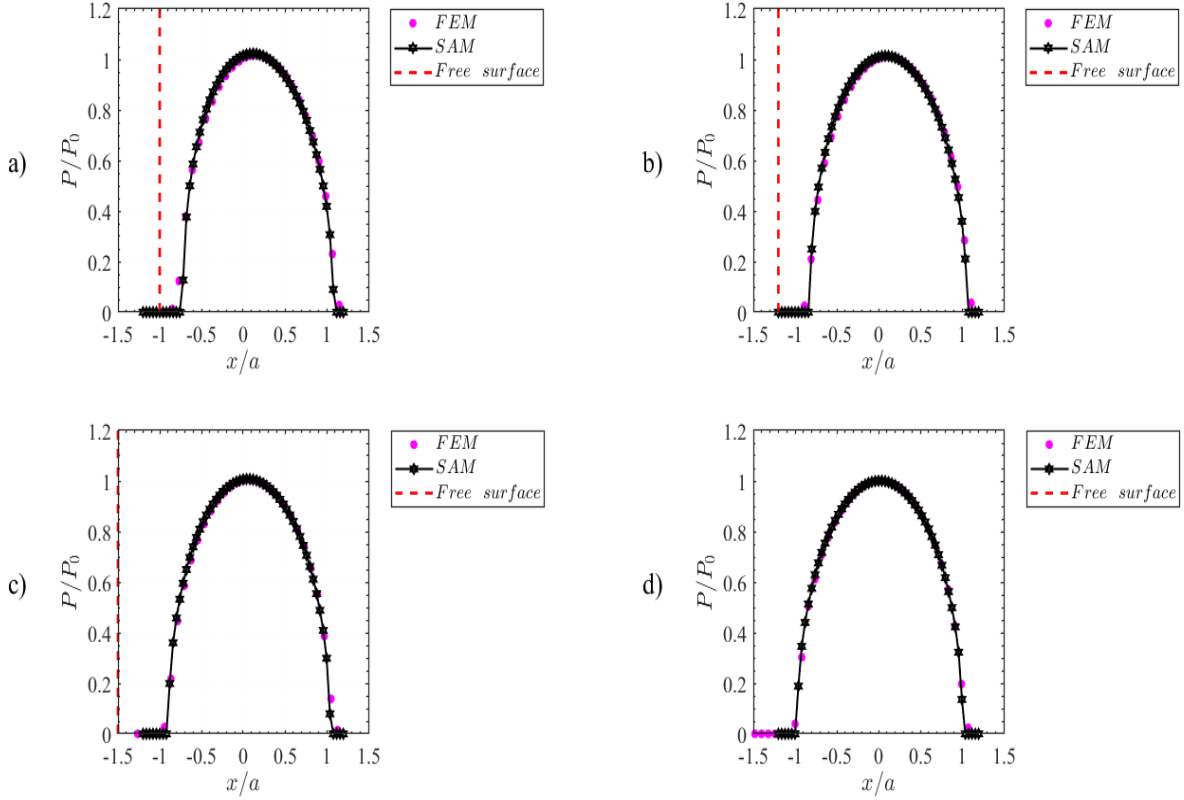
Figure 4.11: Quarter space pressure field evolution in fonction of the distance d/a from the free edge   a) $d = a$ b) $d = 1.2a$ c) $d = 1.5a$ d) $d = 3a$

Figure 4.12(b) compares the stress field in the quarter space at a depth of $z = 0.72a$ between the new SAM model and FEM. The results exhibit good agreement between the two methods. In Fig.4.12(b), further observations can be made:

> When a free edge is located close to the contact zone, it results in an increase in the normal stress compared to the case of a half-space.

> The presence of a free edge very close to the contact zone causes a decrease in the tensile and shear stresses compared to the half-space case.

Figure.4.12(b) shows the comparison of the quarter space stress field at depth $z = 0.72a$ of the new model with that of the FEM. There is a good agreement between the two results.

From the Fig.4.12(b) it can be deduced that the presence of a free edge very close to the contact zone will induce an increase in the normal stress while the shear and tensile stresses will decrease compared to the case of the half space. Figure.4.12(a) illustrates the progression of the pressure profile with the distance from the free edge, d/a. It demonstrates an increase in the maximum pressure as the contact

Figure 4.12: Quarter space pressure profil evolution according to the distance d/a (a) Pressure maximum value according to the distance d/a (b) Quarter space stress validation with FEM results.

zone moves closer to the free edge and ashift of the contact zone toward the infinite side of the body.

Figure.4.13 shows the validation of the quarter space model under identical conditions, except for Poisson's ratio set at 0.45. It demonstrates once again a good agreement between the solution derived from the developed model and the Finite elements one. Similar observations were noticed regarding the changes in the pressure field and the shift of the contact zone.

A top view of the contact area and the pressure profile is presented in Fig.4.14. We can observe the asymmetry of the pressure field when we approach the free edge. The effort being concentrated on a smaller contact surface, it increases the maximum pressure.

4.8.1.2 Truncation ellipse model validation

In this section, we conducted analyses using the ellipse truncation model. Furthermore, a validation process was performed by comparing the results obtained from this model with those from a finite element analysis (FEM) model. The comparison, as depicted in Fig.4.15(a), demonstrates a good agreement between the two models.

However, it is important to note that a slight difference in the pressure shift near the singularity was observed compared to the FEM results. This discrepancy may arise from the inherent approximations made in the semi-analytical approach employed in the present model.

The modeling results, presented in Fig.4.15, reveal that when the contact ellipse

137
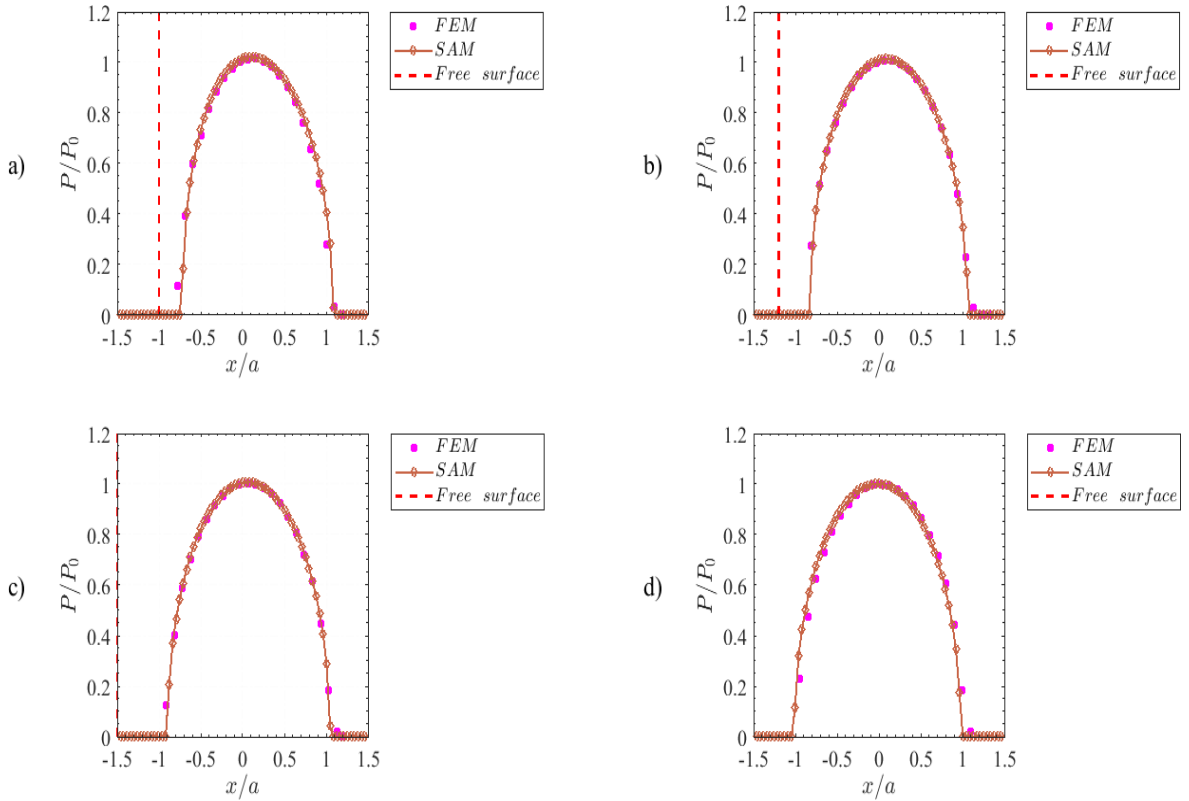
Figure 4.13: Quarter-space pressure distribution function of the distance d/a from the free edge for $\nu = 0.45$: a) $d = a$, b) $d = 1.2a$, c) $d = 1.5a$ and d) $d = 3a$

is truncated, the magnitude of the pressure field increases, and the pressure distribution shifts further away from the center compared to the case of a quarter-space model without truncation. This observation indicates that the truncation of the contact ellipse has a significant effect on the pressure distribution. The pressure field can reach a maximum value of 1.12 times the Hertz maximum pressure due to the truncation.

Figure.4.16 shows the evolution of the pressure field and the contact zone according to the distance d/a.

4.8.2 Two joined space contact problem validation

In this section, we analyze the results obtained from the modeling of the two joined space contact problem. These results demonstrate good agreement with the finite element analysis as shown in Fig.4.17. However, a slight difference is observed when the contact extends beyond the interface of the two materials. This discrepancy can be attributed to the approximation technique used in this study.

It is important to highlight that the proposed model can effectively handle the presence of materials with different properties. In all the investigated cases, our re-
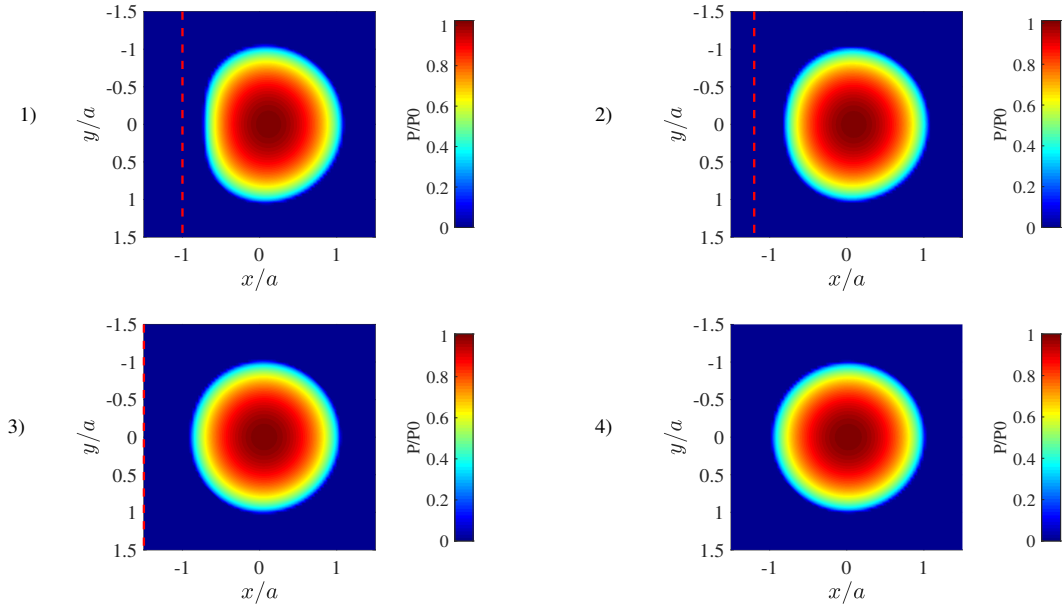
Figure 4.14: Pressure field evolution according to the distance d/a a-1) Quarter space pressure at $d = a$ a-2) Quarter space pressure at $d = 1.2a$ a-3) Quarter space pressure at $d = 1.5a$ a-4) Quarter space pressure at $d = 3a$

sults exhibit a good agreement with the finite element analysis (FEM) results. This indicates the capability of our model to accurately capture and predict the behavior of contact problems involving materials with diverse properties.

The properties of $material-3$ can lead to different scenarios in the contact problem. For instance, when $E_3 = 4E_2$, $material-3$ is significantly stiffer than the principal indented material. In this case, the contact's behavior near the interface can differ from other scenarios, particularly when $E_3 = E_2$ or $E_3 = 0$. When $E_3 > E_2$ and the contact approaches the interface, the contact zone expands and moves towards the interface separating the two joined spaces. This results in a decrease in the pressure field and the emergence of a pressure peak when $d = a$ as depicted in the Fig.4.18(a). Figure.4.19, in turn, offers a top-down view of the pressure profile. It allows us to observe an extension of the contact zone crossing the interface of the two materials, explaining the pressure peak's emergence. It induces a decrease in the maximum pressure.

When $E_3 = E_2$, except in cases involving interfaces or welds particular problems, the two blocks behave as a single unit, resembling a half-space behavior as depicted in Fig.4.18(b).

On the other hand, when $E_3 < E_2$, the pressure field initially moves away from the interface. The contact zone shrinks, and the magnitude of the pressure field increases until $E_3 = 0$ (corresponding to the quarter space case), where the increase
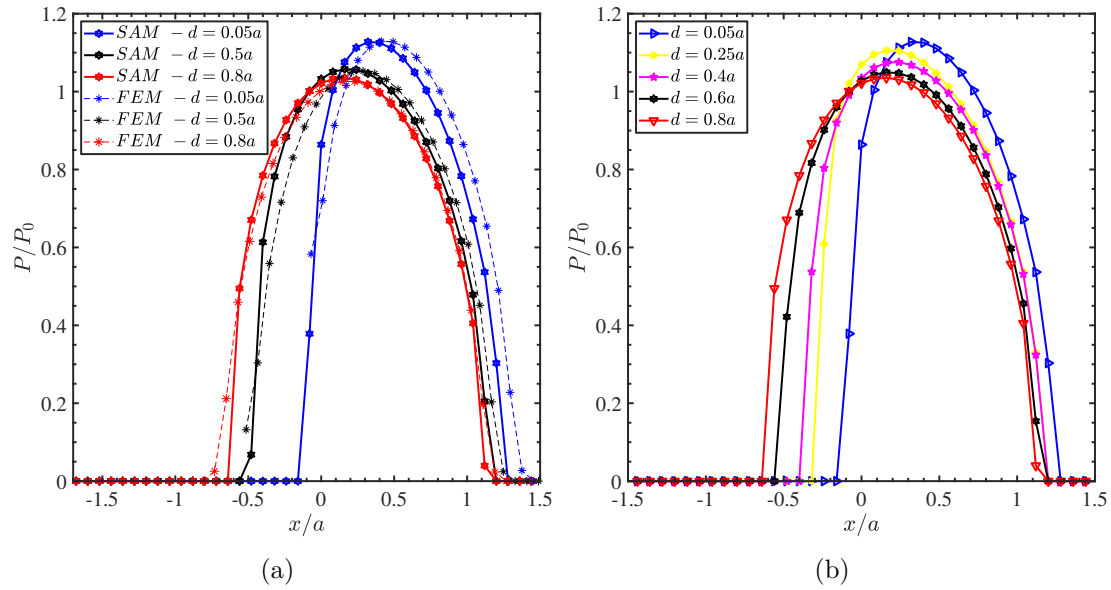
Figure 4.15: Pressure field evolution according to the distance d/a, a) Pressure field comparison with FEM, b) SAM pressure field evolution function of the distance d/a.
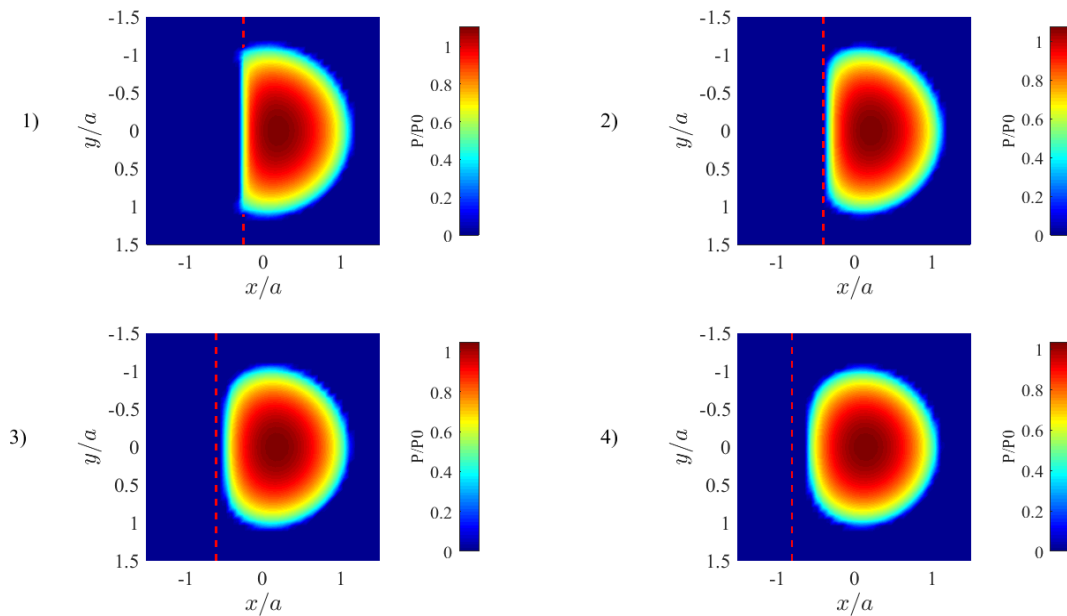
Figure 4.16: Pressure field evolution of truncated quarter-space in function of the distance d/a: 1) $d = 0.4a$, 2) $d = 0.6a$, 3) $d = 0.7a$ and 4) $d = 0.8a$

in the pressure field is even more significant (see Fig.4.20).

In the two-joined space model, it is important to note that when $E_3 = 0$, the solution reverts to the quarter space model.
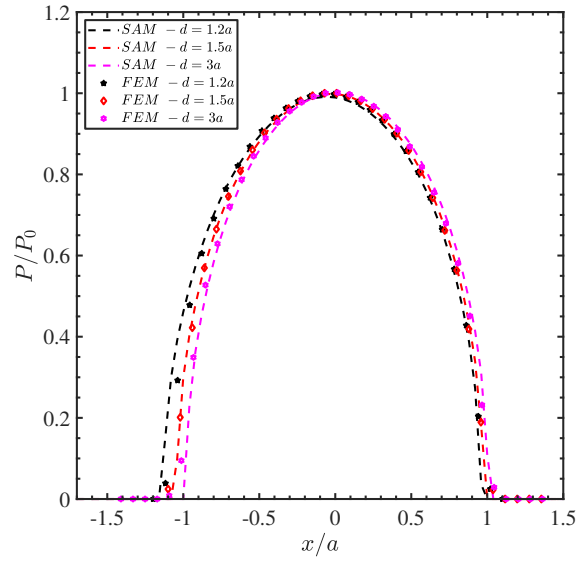
Figure 4.17: Joined spaces pressure validation according to the distance d/a for $E_3 = 4E_2$
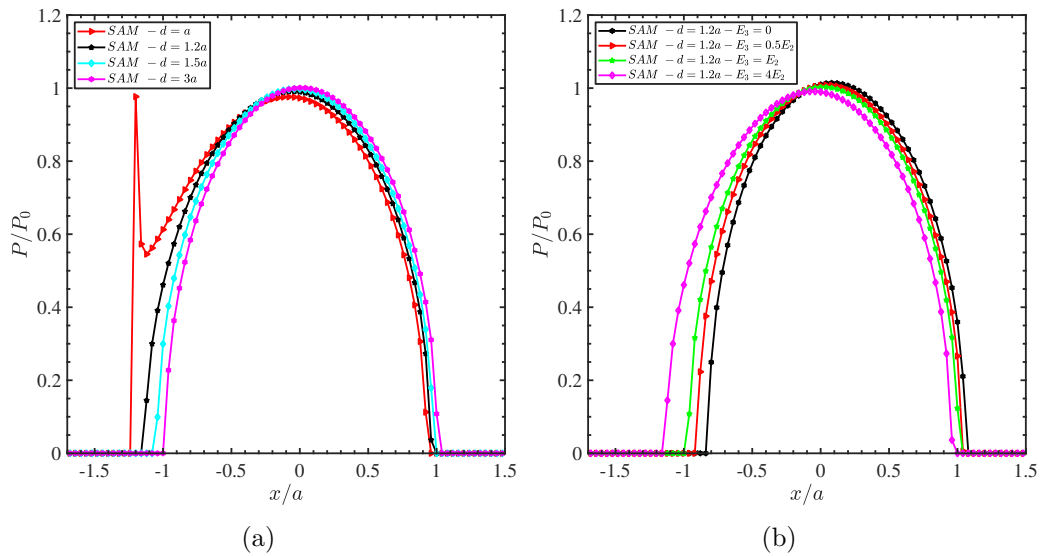
Figure 4.18: Two-joined space pressure parameter evolution according to the distance d/a (a) Pressure profil evolution according to the distance d/a for $E_3 = 4E_2$ (b) Joined space pressure evolution at distance $d/a = 1.2$ for different properties of the third $material - 3$.
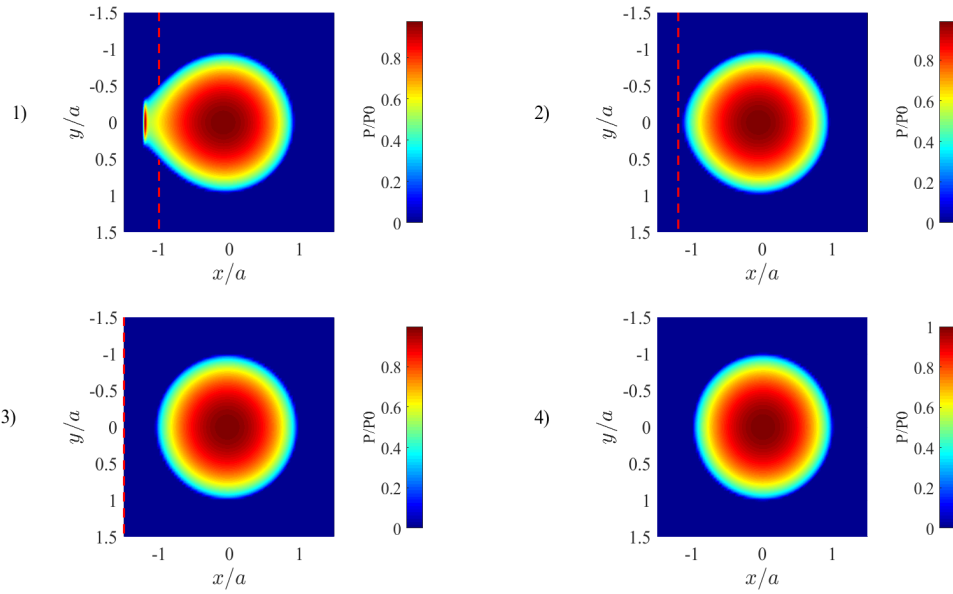
Figure 4.19: Pressure field evolution of two-joined space for $E_3 = 4E_2$ in function of the distance d/a: 1) $d = a$, 2) $d = 1.2a$, 3) $d = 1.5a$ and 4) $d = 3a$
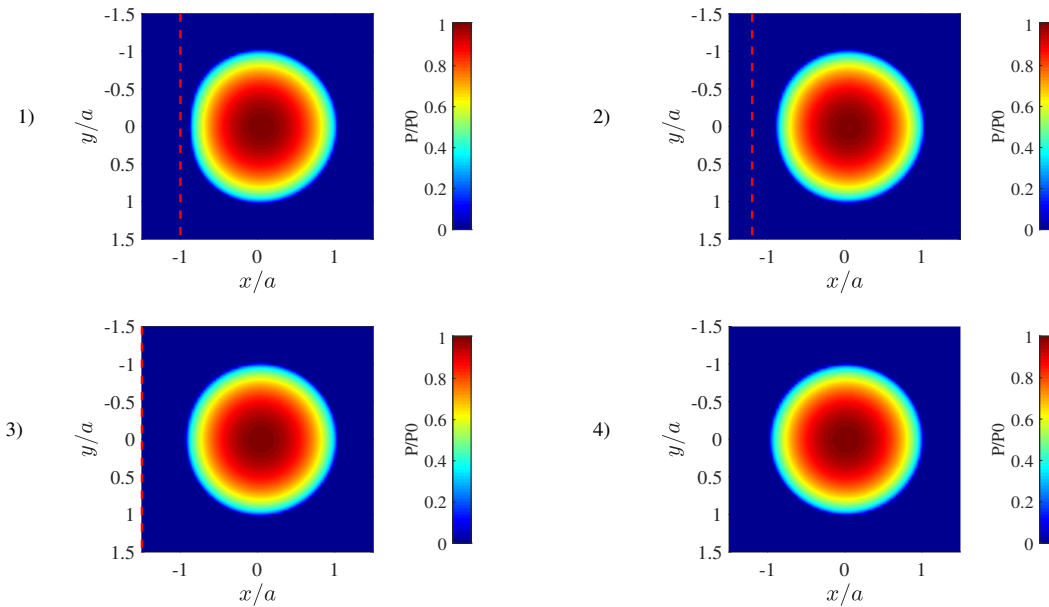
Figure 4.20: Pressure field evolution of two-joined space for $E_3 = 0.5E_2$ in function of the distance d/a: 1) $d = a$, 2) $d = 1.2a$, 3) $d = 1.5a$ and 4) $d = 3a$

4.8.3 Synthesis

4.8.3.1 Effect of free surface distance d/a

Comparing the half-space problem with the quarter space, the ellipse truncation model, and two-joined-space problems, we observe different profiles of the pressure fields, and contact zone which in turn result in different deformation and stress fields due to the presence of free surfaces or additional materials, as shown in Fig.4.12 and Fig.4.18.

Figure.4.12(a) shows the superposition of the pressure fields for different free edge distances d/a. Figure.4.12(a) provides a clearer visualization of the increased pressure field and its relative shift as the free edge distance varies.

Figure.4.14 provides a top view of the pressure field and the corresponding contact area. In Figure.4.14, we can observe an asymmetry in the pressure field and contact zone as we approach the free edge. Additionally, there is a shift of the pressure field towards the positive x-axis, which represents the infinite part of the quarter space. The presence of the free edge leads to an increase in the pressure field due to the same loading being applied on a smaller contact zone compared to the half-space case.

When considering the ellipse truncation model, we observe similar observations as before, with an increase in the pressure magnitude and a reduction in the contact zone size as the distances d/a change, as shown in Fig.4.16. Therefore, in the presence of a truncated contact zone, the pressure magnitude increases and shifts towards the infinite part of the space.

In the case of the two-joined-space modeling, we observe a decrease in the pressure field as we get closer to the interface, especially when the third material is stiffer. The contact zone extends and shifts towards the interface. Therefore, when using the same welded materials, the two-joined space behaves similarly to a single space, exhibiting half-space characteristics. On the other hand, when considering a third material that is less stiff, there is an increase in the pressure magnitude and a shift towards the infinite part of the space.

We observe a similar shift in stress fields compared to the pressure field. Depending on the distance d/a, the stress field can increase in amplitude and shift towards the infinite side of the space if $E_3 < E_2$. Conversely, the stress field can decrease in amplitude and shift towards the interface of the space as the distance d/a increases.

The correction method proposed is based on Hetenyi's mirror pressure technique applied to the surface. As a result, there may be a slight difference between the stress states obtained in depth using this method and those obtained from the FEM analysis, particularly about the tensile stress σ_{xx}. This discrepancy can be attributed to the fact that the correction factors are derived in the proposed model based on resultant forces rather than the distribution of stresses. However, since the magnitude of the shear stresses is much smaller than that of the normal stresses and the difference between the developed model's stresses and the FEM results in depth is small, the normal stress component σ_{xx} remains dominant, and the difference in

143

shear stresses can be neglected without significant error.

In the case of the quarter space model, as the distance d/a approaches 4, the influence of the free edge becomes negligible, and the pressure profile tends to resemble Hertz's pressure distribution. Therefore, all the effects associated with the edges, such as the pressure field's shift, increase, and asymmetry, become negligible. This behavior is illustrated in Fig.4.21, where it can be observed that when d/a is sufficiently large; specifically $d/a \geq 4.0$, the influence of the free edge on the stresses in the quarter space tends to zero.

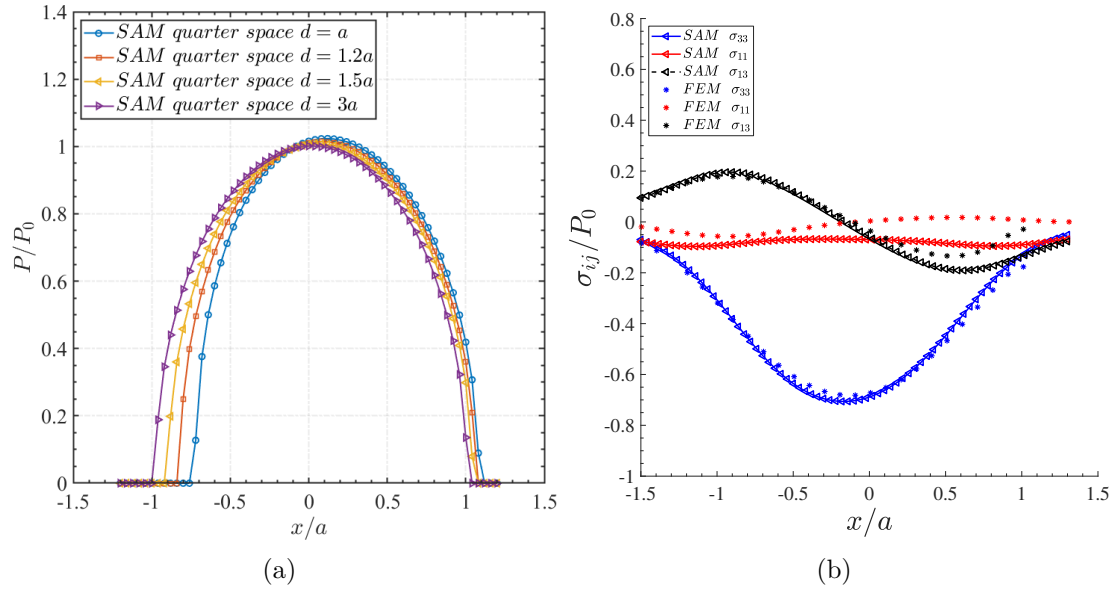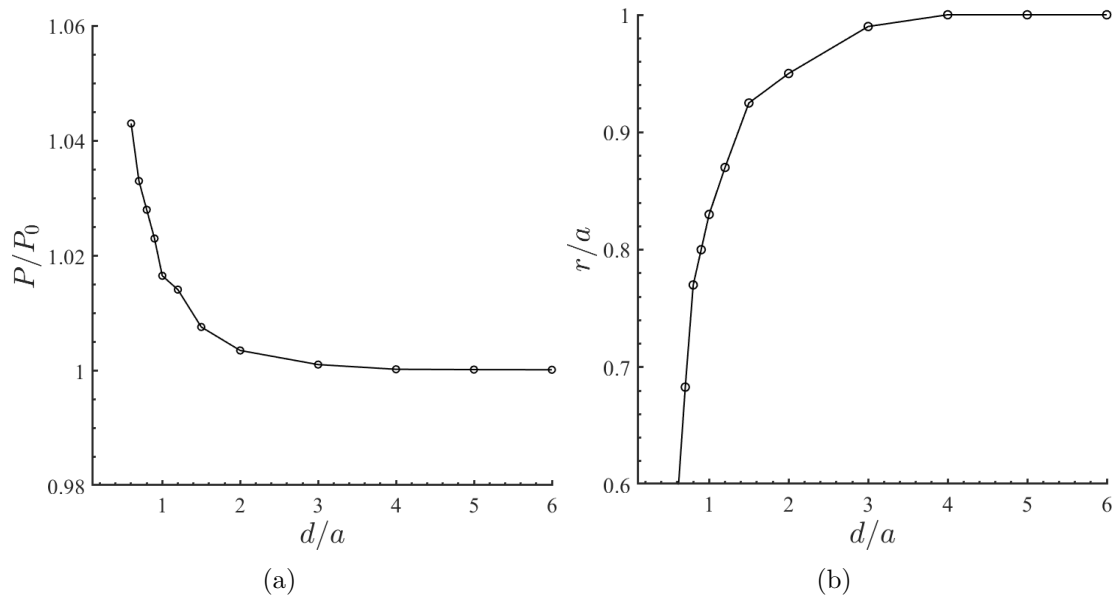**Figure 4.21:** Quarter space parameter evolution according to the distance d/a (a) Pressure maximum value according to the distance d/a (b) Radius evolution according to the distance.

4.8.3.2 Plasticity

In this section, an attempt has been made to incorporate plasticity into the quarter space contact problem. The technique used involves considering the plastic strains in a half-space and incorporating them into the contact analysis until convergence is achieved. However, it has been observed that the resulting pressure field presents a small difference (at $d/a = 3$ from the free edge) from that obtained using the Finite Element Method (FEM) as observed in Fig.4.22.

This discrepancy can be attributed to the fact that the current approach does not account for the calculation of mirror plastic strains resulting from the plasticization of the symmetrical space. In order to obtain accurate results, it is necessary to incorporate the calculation of mirror plastic strains in future work.

144

By including the calculation of mirror plastic strains, the influence of plasticity on the contact problem can be properly accounted for. This will lead to a more accurate prediction of the pressure field and overall behavior of the contact interface. Further research and development are required to refine the methodology and ensure the input of plastic strains in the analysis.
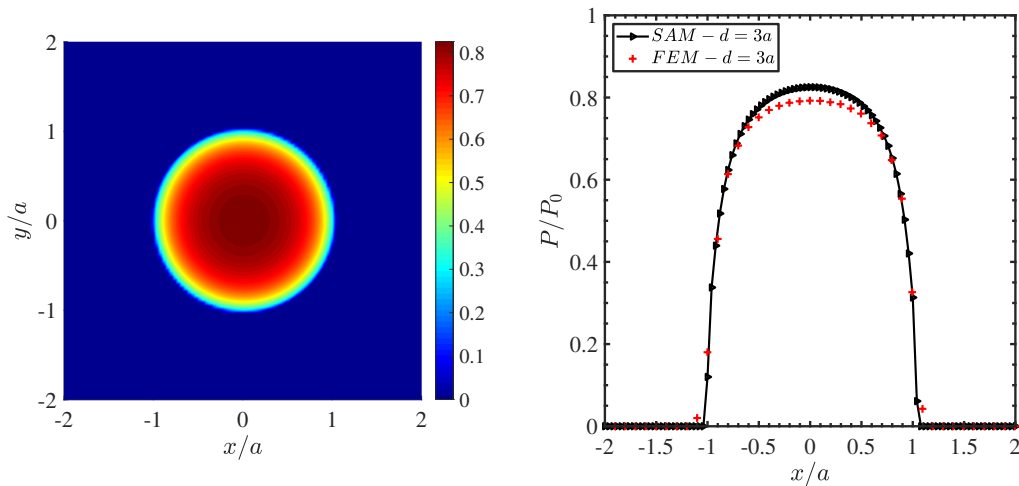
Figure 4.22: Quarter space elastic-plastic pressure distribution in the left and comparison between SAM and FEM in the right

To assess the accuracy of the Semi-Analytical Method (SAM) with the plasticity model, a validation study is conducted by comparing its results with those obtained from the finite element model (FEM). Figure.4.22 presents the comparison of the pressure fields at a distance $d/a = 3$. While the SAM and FEM solutions tend towards that of the half-space, a slight difference between the two can be observed. As we approach the free edge in the SAM with plasticity model, the difference between its solution and the FEM solution becomes more pronounced as shown in Fig.4.23.

Figure.4.23 presents the pressure profile obtained from the finite element method (FEM) for the quarter space problem with plasticity. The material in consideration follows an elastoplastic law, specifically the Swift law. The material's parameters are as follows: $B = 1100$, $C = 4$, $n = 0.045$.

Several observations can be made as the contact zone approaches the free edge.

- Firstly, the pressure field shifts towards the infinite side of the body, indicating a redistribution of stresses in the material. This shift is a consequence of the presence of the free edge, which influences the stress distribution near the contact zone.

- Secondly, the material experiences a higher degree of local plastification as the pressure field's amplitude increases compared to the case of a half-space.
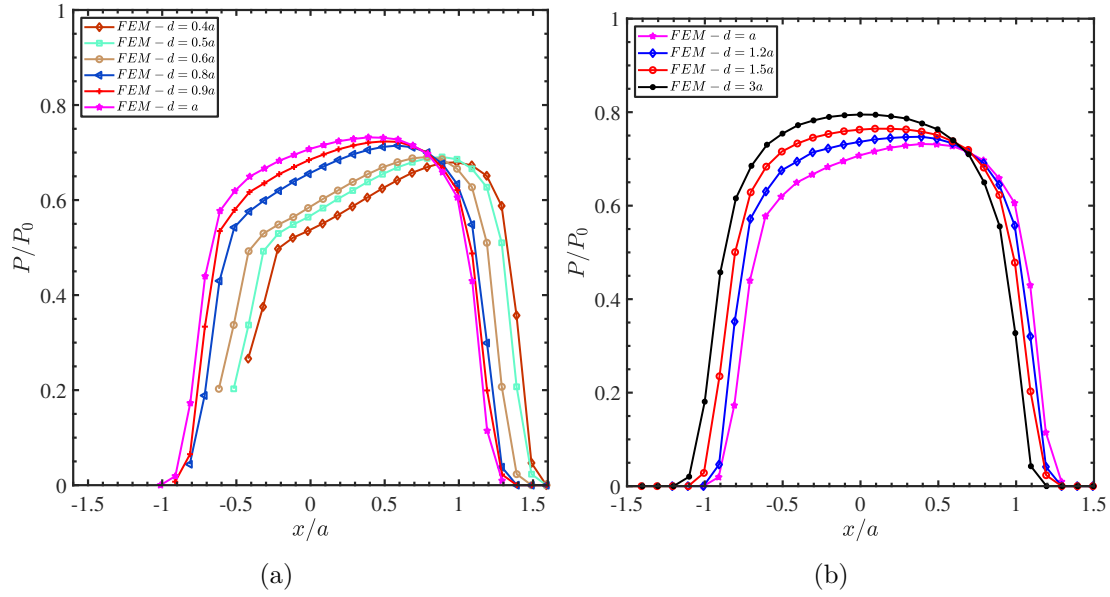
Figure 4.23: Quarter space elastic-plastic pressure evolution according to the distance d/a at $P_0 = 3672MPa$ (a) Pressure profile for $d/a < 1$ (b) Pressure profile for $d/a > 1$.

The larger contact radius induced by plasticity leads to a larger area of plastic strains in the material.

- Thirdly, the material undergoes significant relaxation in the region near the edge. This relaxation occurs due to the release of stresses in the material, resulting in a redistribution of the pressure field. As a result, an asymmetry in the pressure field is observed, indicating the free edge's influence on the material's deformation behavior.

In the case where the contact zone is truncated as shown in Fig.4.23(b) with respect to the free edge, an even greater degree of plasticization and relaxation is observed. The truncation of the contact zone leads to an increased concentration of stresses near the truncated edge, causing more pronounced plastic deformation and relaxation effects. Additionally, the pressure field experiences a more significant shift due to the truncation.

Overall, plasticity in the quarter space problem introduces complex deformation and relaxation phenomena influenced by the proximity to the free edge and the truncation of the contact zone.

4.9 Conclusion

This chapter proposes a novel numerical approach for solving the elastic quarter space contact problem, ellipse truncation, and two-joined space contact problem. The method is inspired by Hetenyi's mirror pressure technique and Guibault's fast correction method, and it is implemented within a semi-analytical framework (SAM). The approach incorporates two corrective factors to account for the presence of the free edge.

To solve the problem, the Conjugate Gradient Method (CGM) and Fast Fourier Transform (FFT) algorithm are integrated, enhancing computational efficiency. The results obtained using this method are compared with corresponding Finite Element Method (FEM) solutions, and a good agreement is observed. The computational efficiency of the proposed method is advantageous compared to FEM.

In the case of the quarter space model, the consideration of the free edge leads to an increase of the maximum contact pressure, a reduction in the size of the contact zone, and a shift towards the infinite side as the distance d/a approaches 1. The influence of the free edge diminishes as d/a exceeds 4.0, and the Hertz solution becomes applicable.

For the ellipse truncation model, the truncated contact zone induces a more significant increase in pressure magnitude and a shift in the contact zone. The two-joined space contact problem highlights the influence of a third material with different properties in the contact area, particularly when the contact zone is close to the interface. This results in an extension of the contact zone, a decrease of the maximum pressure magnitude, and a shift towards the interface for a stiffer material. Conversely, for a softer material, the contact zone decreases similarly as the quarter space case.

The newly developed approach enables the modeling of these different contact scenarios and effectively simulates the corresponding phenomena. It provides a versatile framework for studying and analyzing various contact problems with different geometries and material properties.

Regarding perspective, including mirror plastic strains in plasticity analysis in the quarter space problem can lead to more accurate results.

Chapter 5

Eighth-space and finite-length space contact modeling

This chapter introduces a semi-analytical method (SAM) to address the eighth space and finite-length space contact problems commonly encountered in applications such as gears or roller bearings. These issues involve contact stress distribution affected by the presence of free edges. The method extends the resolution technique used for the quarter space problem to consider the impact of multiple free edges on the contact zone. The SAM developed approach involves the use of corrective factors ψ_1 and ψ_2 and employs a space overlapping technique. Validation is performed by comparing SAM results with those obtained from finite element method (FEM) analysis, revealing a good agreement between the SAM and FEM results. The findings emphasize the mutual influences of free edges, resulting in higher pressure magnitudes and more noticeable shifts towards the farthest free edge. In cases involving finite-length spaces, the maximum pressure can increase by approximately 1.2 times the maximum Hertz pressure (P_0). To assess the deviation of the obtained solutions from Hertz's solutions, the chapter includes several parametric studies illustrating the effects of free edges on contact responses. These studies offer valuable insights into the influence of free edges, contributing to a deeper understanding of contact behavior in practical scenarios.

148

Sommaire

5.1 Introduction

The finite-length space contact problem is a common occurrence in practical engineering applications, especially within mechanical components like gears, cams, and roller bearings. Differing from the commonly used Hertz contact theory for approximating finite-length problems, the finite-length space contact problem involves at least two free surfaces and corners, resulting in distinctive pressure and stress distributions with unique characteristics.

This problem is an extension of the quarter-space contact problem, which has garnered substantial attention from researchers over the past decades. Many scholars, as referenced in (HET 60; HET 70; SNE 71; KEE 83b; CON 86; HAN 89; HAN 90; HAN 91), and (ZHA 13; WAN 17; GUO 17a; ZHA 17; GUO 17b), have devoted their research efforts to comprehending and resolving quarter-space contact problems. They have considered various factors, such as material properties, contact geometry, load conditions, and boundary conditions.

In this chapter, the methodology introduced in the previous chapter for solving the quarter-space problem is extended to address more intricate scenarios involving multiple free edges. Specifically, two cases are examined: the eighth space contact problem, encompassing two free edges and one corner, and the finite-length contact problem, which includes four free edges and four corners. The objective is to develop an approach capable of effectively handling these situations and providing precise solutions for stress distribution in the contact region.

5.2 Theoretical description

In Hertz contact conditions, the contact problem is typically analyzed assuming an infinite space, where the contact pressure is uniformly distributed over the entire contact area. However, in practical situations involving finite-length space contact, the contact area is limited by the presence of free surfaces, such as edges or corners. As a result, the pressure and stress distribution in these contact problems is significantly influenced by the presence of these free surfaces. Sophisticated methods and models are required to predict the pressure and stress distribution accurately in finite-length space contact problems. These methods go beyond the assumptions of infinite space and consider the specific geometric constraints imposed by the free surfaces. The finite-length space contact problem can be seen as an extension of the quarter-space contact problem, where the effects of multiple free edges and corners are taken into account. By addressing the finite-length space contact problem, researchers aim to provide more realistic and accurate solutions for practical applications such as gears, bearings, and other contact systems where free surfaces significantly affect stress distribution.

The eighth-space concept is obtained geometrically by dividing the infinite space along the z-axis into two equal parts. One of these halves is further divided along the x-axis, resulting in a quarter space defined by $x \geq 0$, $-\infty \leq y \leq +\infty$, and $z \geq 0$.
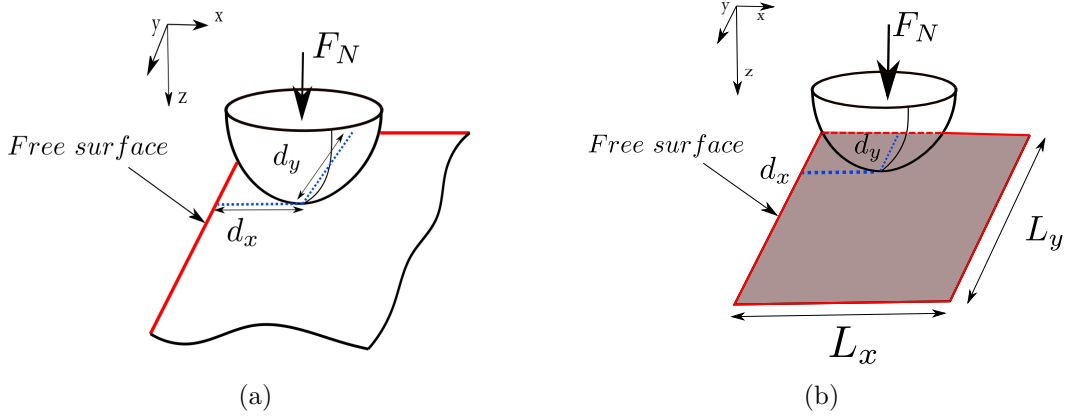
Figure 5.1: (a) Eighth space contact problem illustration according to the distances d_x/a, d_y/a (b) Finite-length space contact problem illustration according to the distances d_x/a, d_y/a.

Subsequently, by dividing the quarter space along the y-axis, we achieve the eighth space defined by $x \geq 0$, $0 \leq y \leq +\infty$, and $z \geq 0$, as depicted in Fig.5.1(a).

On the other hand, the finite space is geometrically defined by specifying the dimensions L_x, L_y, and L_z. It represents a bounded space with finite extents in the x, y, and z directions. The finite space is obtained by further dividing the eighth space along the x and y axes, resulting in specific lengths L_x and L_y for the respective dimensions, as illustrated in Fig.5.1(b).

To address and solve the eighth-space and finite-length space contact problems, the methodology employed in the previous chapter focused on the quarter-space approach. This method involves integrating Hetenyi's mirror pressure technique with Guilbault's factor approach to consider Hetenyi's iterative process. Consequently, the new method generates two factors, ψ_1 and ψ_2, along each axis to account for the impact of free edges on the contact zone. The expressions for these factors are provided by:

$$\psi_1 = 1.29 \tag{5.1}$$

$$\psi_2 = \frac{1}{1-\nu}\left\{0.17 - 0.25(1-2\nu)\right\} \tag{5.2}$$

This section details the extension of the quarter-space resolution method for addressing contact problems in an eighth space and a finite-length space with dimensions L_x along the x-axis and L_y along the y-axis.

For the eighth space, a normal loading is applied through a body, with the center of the contact positioned at a distance d_x from the edge along the x-axis and d_y from the edge along the y-axis, as depicted in Fig.5.2(a). The extension method involves seeking an axially symmetric loading, referred to as mirror loading. This loading is symmetric with respect to the axes that have free edges and centrally symmetric

concerning each corner of the space. In the case of the eighth space, this correction procedure is applied to the two free edges and the corner.

Likewise, for the finite-length space, a normal loading is applied via a sphere. In this case, the center of the contact is situated at a distance d_x from the first edge along the x-axis and at a distance $L_x - d_x$ from the second edge along the x-axis. Along the y-axis, the contact zone is located at a distance d_y from the first edge and at a distance $L_y - d_y$ from the second edge, as shown in Fig.5.2(a). To extend the resolution approach to this scenario, the correction procedure is applied to all four free edges and corners.

Figure.5.2(b) provides an overview of the extension method, focusing on the correction with the ψ_1 factor in the case of the eighth space, which has two free edges and one corner. A similar process is carried out for the second corrective factor, ψ_2. The extension process involves seeking mirror loading, which exhibits axial symmetry with respect to the axes that have free edges and central symmetry with respect to each corner of the space. For the finite-length space, the correction procedure is applied to all four free edges and the four corners.
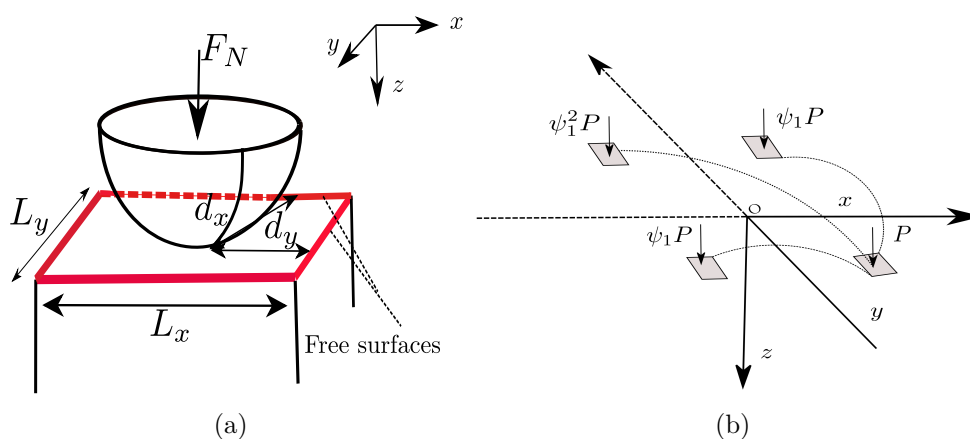
Figure 5.2: a) Finite-length-space subjected to a normal loading, b) Correction procedure with the corrective factors in the eighth-space

5.3   Contact model

As in Chapter 4, the boundary conditions for the contact problem between the eighth and the finite length can be represented by a set of equations and inequalities:

1. Surface Separation: The distance between the contacting bodies, denoted by $g(x,y)$, is the sum of the initial separation $g_i(x,y)$, the rigid body displacement δ_z, and the normal elastic surface displacement $u_3^{\Omega_1+\Omega_2}(x,y)$ of both bodies. It is given by the equation:

$$g(x,y) = g_i(x,y) + \delta_z + u_3^{\Omega_1+\Omega_2}(x,y) \tag{5.3}$$

2. Contact Condition: The contact pressure, denoted by $p(x,y)$, is always positive or zero when inside the contact area (Γ_c), and the surface separation is zero. Outside the contact area, the surface separation is positive, and the contact pressure is zero. This can be expressed as:

$$(x,y) \in \Gamma_c: \quad g(x,y) = 0 \quad \text{and} \quad p(x,y) > 0 \tag{5.4a}$$
$$(x,y) \notin \Gamma_c: \quad g(x,y) > 0 \quad \text{and} \quad p(x,y) = 0 \tag{5.4b}$$

3. Load Balance: The applied normal load F_N must equal the integral of the contact pressure distribution $p(x,y)$ over the contact area Γ_c. It can be expressed as:

$$F_N = \int_{\Gamma_c} p(x,y) dS \tag{5.5}$$

To solve the contact problem numerically, the surfaces of the two bodies in contact are meshed into a 2D regular grid of $N = N_x \times N_y$ points. Each point n is associated with a rectangular zone of size $dS = \Delta x \times \Delta y$, where the pressure is assumed to be constant. The pressure distribution $p(x,y)$ is discretized into patches of uniform pressure. Using linear elasticity theory, the normal displacement can be expressed in a discretized form as:

$$u_z(n) = \sum_{m=1}^{N} K_z^p(m,n) p(m) \tag{5.6}$$

K_z^p represents the influence coefficients, describing the effect of a rectangular patch of uniform pressure at point m on the normal elastic displacement at point n.

The surface displacement of the eighth space and the finite length space can be expressed as the sum of the surface elastic displacement of a homogeneous half-space (u_{zh}) and the perturbed normal displacement due to the presence of free edges near the contact area (u_{zspace}). It can be written as:

$$u_z = u_{zh} + u_{zspace} \tag{5.7}$$

The flowchart illustrating the process of solving the elastic eighth space and the finite length space contact problem is presented in Fig.5.3.

To correct for the stress state in the eighth space and the finite space, which is obtained from the numerical solution based on mirror loadings, a correction taking into account the factors is necessary. The stress solution obtained directly from the
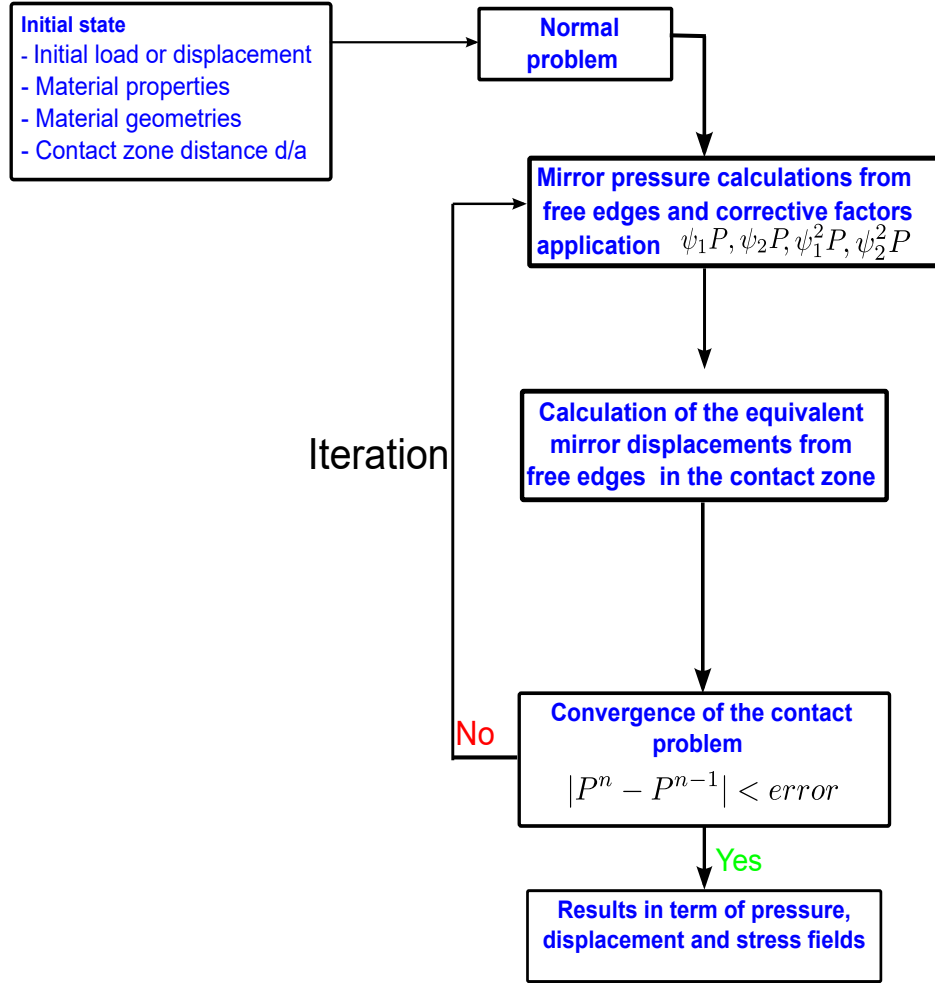
Figure 5.3: Flowchart for solving the eighth space and the finite length contact problem.

numerical method is only partially accurate, so a stress correction is required to improve the approximation.

Since the loadings are symmetrical, the tensile stress in the eighth space and the finite space can be approximated as the tensile stress in the corresponding half-space, with the addition of the tensile stress resulting from the mirror pressure acting on the free edge side. In this correction, only the effect of the ψ_1 factor will be considered, as the effect of the ψ_2 factor on the stress field is negligible. The distance d_x/a and d_y/a with respect to the free edges will affect the stress state.

The stress field can be approximated by the following expression:

$$\sigma_{xxeq} = \left[1 + (1-\psi_1)\frac{a}{d}\right]\left[1 + (1-\psi_1)\frac{a}{d}\right]\sigma_{xx} \tag{5.8a}$$

$$\sigma_{xzeq} = \left[1 - \frac{2(0.29a)}{4d}\right]\sigma_{xz} \tag{5.8b}$$

5.4 Numerical results and discussion

This section will analyze the frictionless contact between a sphere and two different surfaces: an eighth and finite-length space. The material properties of these surfaces are as follows: Young's modulus $E = 210$ GPa and Poisson's ratio $\nu = 0.3$.

The contact problem is investigated by varying two distance parameters, d_x and d_y, which represent the position of the contact center relative to the reference edges along the x and y directions, respectively, for both the eighth-space and the finite-length space.

Table 5.1 summarizes the analysis's material parameters and contact conditions. The outputs, such as pressure, stress, and length, are normalized by the maximum Hertzian pressure P_0 and the Hertz contact radius a obtained from the corresponding half-space solution to facilitate comparison and analysis.

For the analysis, a simulation domain of size $(-5a, 5a) \times (-5a, 5a) \times (0, 6a)$ is used, covering the x, y, and z directions. The domain is discretized uniformly into a grid of $251 \times 251 \times 40$ cuboids to represent the geometry and capture the contact behavior accurately.

Parameter	Symbol	Unit	Value
Normal load	P	(N)	1923
Indentor Young's modulus	E_1	(GPa)	Rigid
Indentor radius (sphere)	R	(mm)	20
Eighth and finite-length-space Young's modulus	E_2	(GPa)	210
Eighth and finite-length-space Poisson's ratio	ν_2		0.3
Hertz's maximum pressure	P_0	(MPa)	3672.76
Hertz's contact radius	a	(mm)	0.5
Eighth-space distance from the free surface	$d_x/a, d_y/a$		from 0 to 1.5
Finite-length-space distance from the free surface	$d_x/a, d_y/a$		from 0 to 1.5
Width of the finite-length-space along x and y	$L_x/a, L_y/a$		from 2 to 3

Table 5.1: Parameters and contact conditions

Simulations were performed using Abaqus 2019, a commercial software, to validate the different models on a computer with a 2.6 GHz i7 CPU. The region of interest was meshed using C3D8R elements, which are eight-node linear bricks with reduced integration, and had a mesh size of 0.04 mm. The remaining parts of the model were meshed with C3D4 elements, which are four-node linear tetrahedra. The sphere was modeled as an analytically rigid shell.

The simulations involved varying the dimensionless distances d_x/a and d_y/a to study their effect. Once again, The dimensionless pressure profiles along the x-axis of the eighth space and the finite length space were obtained using the SAM (Semi-Analytical Method) and FEM (Finite Element Method) approaches. Figure.5.4

shows the comparison of the pressure profiles obtained from the SAM and FEM methods for different values of d_x/a and d_y/a. This allows for a validation of the models and an assessment of their accuracy in predicting the pressure distribution along the x-axis.

5.4.0.1 Eighth space model validation

In this section, we validate the results obtained from the semi-analytical method (SAM) for the eighth space by comparing them with those obtained from finite element analysis (FEM). The validation is performed by comparing the pressure profiles obtained from both methods for various contact center positions relative to the free edges (d_x and d_y).

The comparison between SAM and FEM results shows good agreement, indicating the semi-analytical method's accuracy in capturing the eighth space's behavior as illustrated in Fig.5.4. It is observed that the pressure field in the eighth space experiences a more pronounced increase compared to the quarter-space case. This increase can be attributed to the mutual influence of the free edges present in the space.

Furthermore, the presence of the free edges induces a shift in the pressure field towards the infinite part of the space. This shift is more pronounced compared to the case of quarter-space modeling and is a consequence of the mutual influences of the free edges. Figure.5.5 presents the evolution of the pressure profile with the distance d_x/a and d_y/a.

The validation results confirm the accuracy of the developed method in capturing the influences of the two free edges and provide valuable insights into the pressure distribution.

Figure.5.6 provides a clear visualization of the pressure distribution and the evolution of the contact zone as a function of the distance d/a from the free edge of the eighth space. Several observations can be made based on Fig.5.6:

1. When a free edge is located very close to the contact zone, it results in an increased pressure field compared to the case of a half-space. This increase in pressure is due to the constraint imposed by the nearby free edge, which restricts the expansion of the contact zone and leads to higher pressures.

2. The presence of a nearby free edge causes a shift in the pressure field towards the infinite space direction compared to the case of a half-space. This shift occurs because the adjacent free edge influences the contact zone.

3. The mutual influence of the two free edges can further increase the maximum pressure. At a distance $d_x = d_y = a$ from the free edges, the maximum pressure can be approximately $1.04P_0$, where P_0 represents the maximum Hertzian pressure obtained from the corresponding half-space solution, in addition no truncated contact area is observed.

156
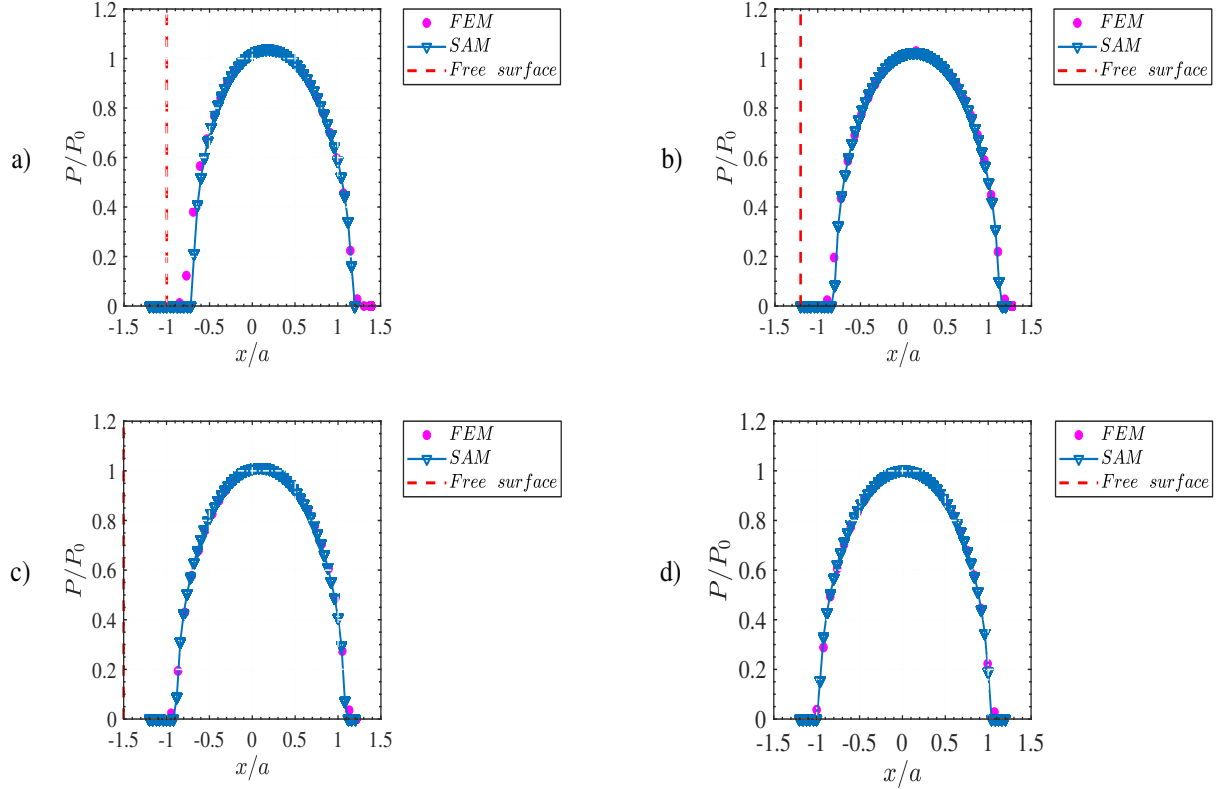
Figure 5.4: Pressure evolution respect to the distance d_x/a and d_y/a from each free edge on the eighth space: a) $d_x = d_y = a$, b) $d_x = d_y = 1.2a$, c) $d_x = d_y = 1.5a$ and d) $d_x = d_y = 3a$

5.4.0.2 Finite space model validation

In the finite-length space model, the influence of the free edges can come from all sides, which requires considering the entire model in the calculation. The simulations were conducted for various dimensionless distances d_x/a and d_y/a along the x and y axes, respectively, following the same conditions as in the quarter-space case.

The validation results demonstrate a good agreement between the SAM model and the FEM (see Fig.5.7). Figure.5.8(a) illustrates the pressure evolution with the distance showing the mutual influences of free edges on the contact zone.

In Figure.5.8(a), the highlighted case corresponds to the sphere being tangent to all four free edges of the finite-length space ($L_x = L_y = 2a$, $d_x = d_y = 2a$). In this configuration, the finite-length space experiences equal influences from all four edges. As a result, the pressure field becomes centered, exhibiting an increase in amplitude. In this case, the maximum pressure can reach up to 1.17 times the maximum Hertz pressure P_0, indicating the significant impact of the mutual edge influences on the contact behavior.

In Figure.5.8(b), the stress fields at a depth of $z = 0.72a$ in the finite-length space is validated by comparison with the FEM. The results from both models show good
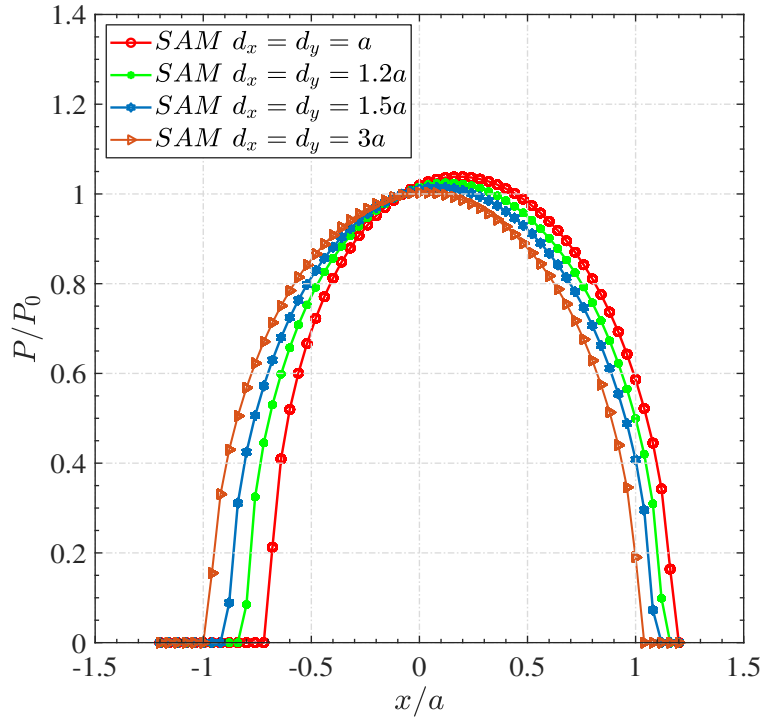
Figure 5.5: Pressure evolution respect to the distance d_x/a and d_y/a from each free edge on the eighth space: a) $d_x = d_y = a$, b) $d_x = d_y = 1.2a$, c) $d_x = d_y = 1.5a$ and d) $d_x = d_y = 3a$

agreement, confirming the accuracy of the semi-analytical method.

As previously observed, the presence of a free edge in proximity to the contact zone leads to an increase in the normal stress. This increase is particularly significant when approaching the free edges or simultaneously experiencing the mutual influence of multiple edges. The constraints imposed by the free edges contribute to the higher normal stress levels observed in the finite-length space compared to the quarter-space.

As in the previous cases, the shear and tensile stresses decrease in the finite-length space compare to the half space. Free edges introduce additional complexities and stress concentration effects, resulting in higher normal stress compared to the quarter-space caseas shown in Fig.5.8(b).

Figure.5.9 presents the contact zone pressure field in the finite-length space with the distance from the center of contact with respect to the four free edges.

The presence of free edges in the finite-length space has several effects on the contact problem responses:

- ✿ Firstly, the free edges tend to reduce the contact zone, resulting in a smaller contact area between the sphere and the finite-length space.

- ✿ Secondly, the presence of free edges increases the pressure field. The mutual
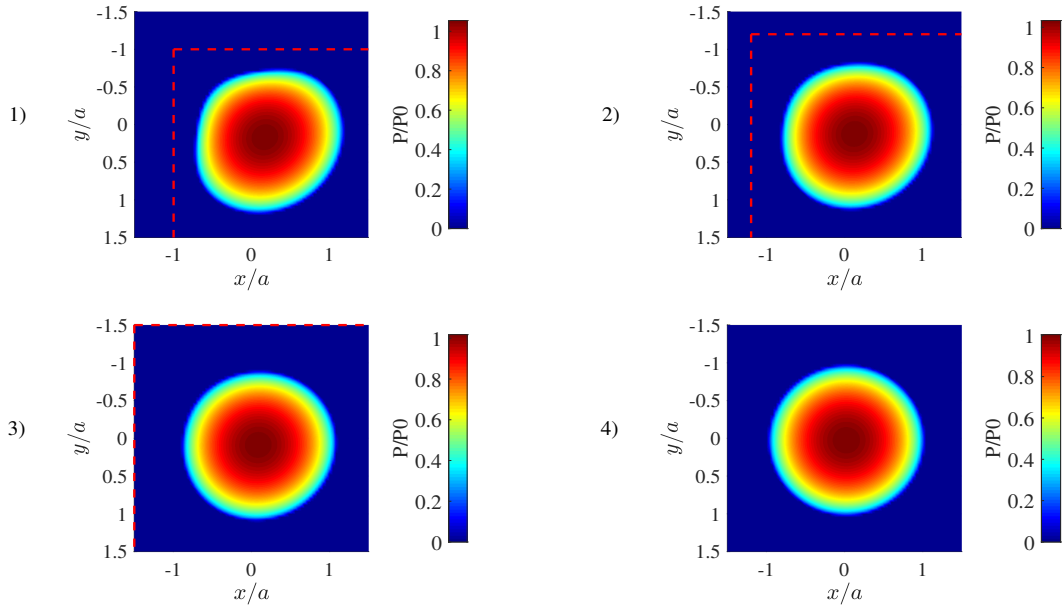
Figure 5.6: Pressure field evolution of length eighth space according to the distance d_x/a , d_y/a a-1) $d_x = d_y = a$ from the free edges   a-2) $d_x = d_y = 1.2a$ from the free edges   a-3) $d_x = d_y = 1.5a$ from the free edges   a-4) $d_x = d_y = 3a$ from the free edges

influence of the edges amplifies the stress concentration, leading to higher pressure values compared to the quarter-space case. This pressure increase results from the interaction and constraint effects induced by the adjacent free edges.

✿ Furthermore, the pressure field is shifted towards the side of the finite-length space that is farthest from the free edges. This shift occurs due to the asymmetric influence of the edges on contact behavior.

5.5   Synthesis

5.5.0.1   Effect of free surface distance d_x/a, d_y/a

Comparing the eighth space and the finite-length space with the half-space problem, we observe different pressure field profiles, leading to distinct deformation and stress fields due to the presence of free edges. The effects of the free edges depend on the distances d_x/a and d_y/a, as shown in Fig.5.5,5.9.

In Figure.5.6, a top view of the pressure evolution on the eighth space is presented. Figure.5.6 reveals an asymmetry in the pressure field and the contact zone as one approaches the free edge. Additionally, there is a shift of the pressure field towards the positive x-axis, indicating a shift towards the infinite part of the eighth
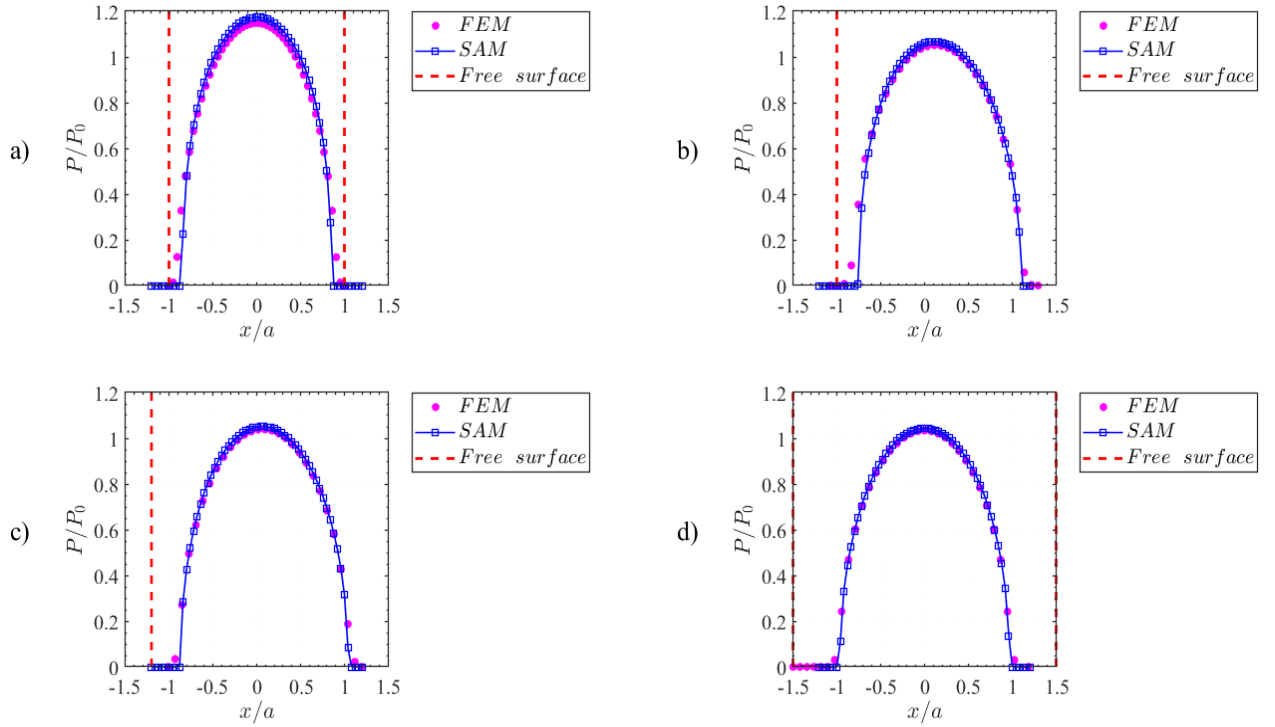
Figure 5.7: Pressure evolution respect to the distance d_x/a and d_y/a from each free edge on the finite length space   a) $L_x = L_y = 2a$ at $d_x = d_y = a$ b) $L_x = L_y = 3a$ at $d_x = d_y = a$ c) $L_x = L_y = 3a$ at $d_x = d_y = 1.2a$ d) $L_x = L_y = 3a$ at $d_x = d_y = 1.5a$

space. The presence of the free edge results in an increase in the pressure field due to the same loading being exerted on a smaller contact zone compared to the half-space case. Figure.5.5 illustrates the superposition of the pressure field according to the free edge distances d_x/a and d_y/a, providing a clearer view of the increased pressure field and their relative shifts.

In the case of the finite-length space model, we observe similar phenomena as in the eighth space, such as the asymmetry and the shift of the pressure field. However, we also observe the mutual influence of the four free edges, which is dependent on the distances d_x/a and d_y/a as shown in Fig.5.8(a). In the presence of these free edges, the maximum pressure field shifts more toward the direction of the edge farthest from the contact zone. The dissymmetry becomes more pronounced on the side of the edges closest to the contact zone. The mutual influence of the edges leads to an increased maximum pressure in the finite-length space solution. The maximum pressure in the finite-length space can reach up to 1.17 times the Hertz pressure P_0, as shown in Fig.5.9 and Fig.5.10, while it reaches up to $1.04P_0$ in the eighth space.

In the eighth and finite-length spaces, the presence of free edges has different effects on the stress fields compared to the half-space case. The normal stress increases in the presence of free edges, while the shear stresses decrease compared to the half-space. Moreover, the normal stress in the finite-length space is generally higher than
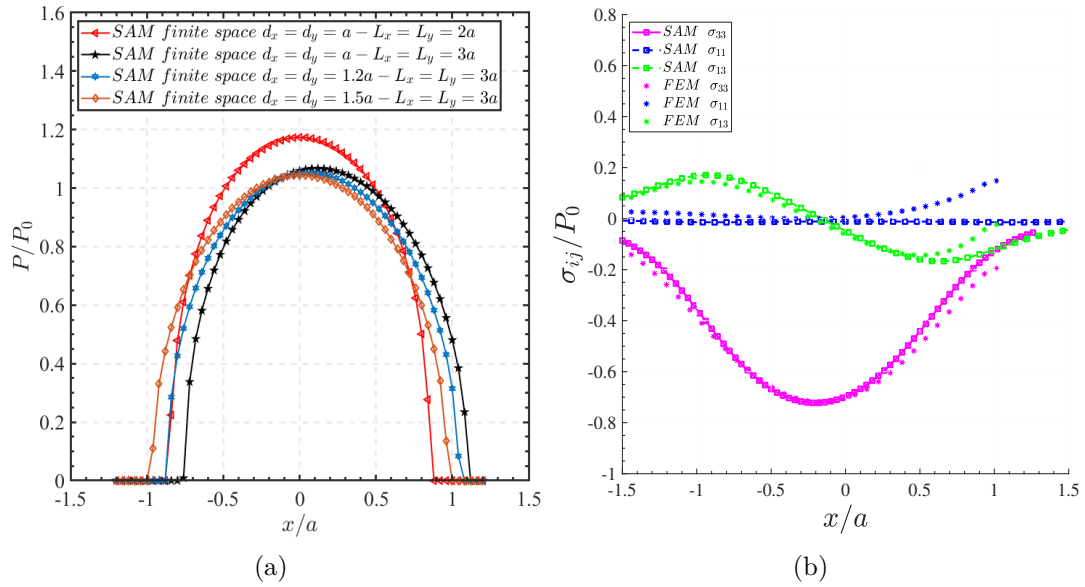
Figure 5.8: (a) Field evolution of finite length space according to the distance d_x/a, d_y/a, L_x/a and L_y/a, b) Finite length space stresses field for $L_x = L_y = 3a$, at $d_x = d_y = a$ from the free edges and at depth $z = 0.72a$
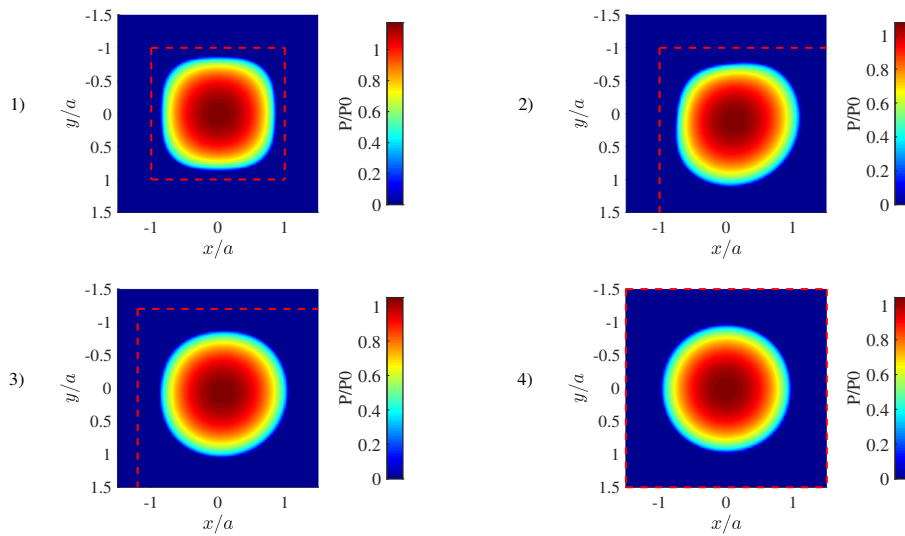
Figure 5.9: Pressure field evolution of finite length space according to the distances d_x/a, d_y/a, L_x/a and L_y/a for $P_0 = 3672 MPa$ a-1) $L_x = L_y = 2a$ and at $d_x = d_y = a$ from the free edges a-2) $L_x = L_y = 3a$ and at $d_x = d_y = a$ from the free edges a-3) $L_x = L_y = 3a$ and at $d_x = d_y = 1.2a$ from the free edges a-4) $L_x = L_y = 3a$ and at $d_x = d_y = 1.5a$ from the free edges

in the eighth space. Similar to the pressure field, the stress field also exhibits a shift towards the infinite side of the space and an increase in amplitude depending on the
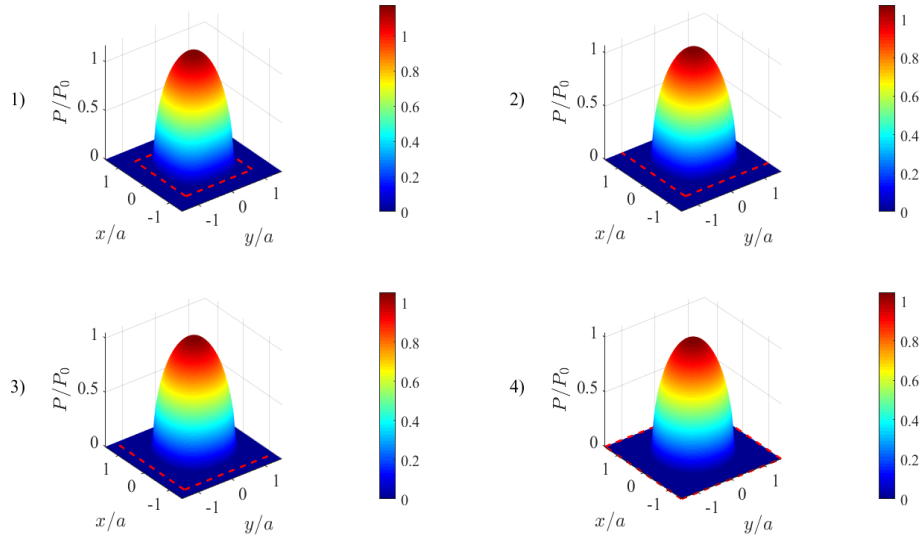
Figure 5.10: 3D view of the pressure distribution for finite-length-space function of the distance to the free edges, d_x/a and d_y/a, and size of the finite space, L_x/a and L_y/a: 1) $L_x = L_y = 2a$ and $d_x = d_y = a$, 2) $L_x = L_y = 3a$ and $d_x = d_y = a$, 3) $L_x = L_y = 3a$ and $d_x = d_y = 1.2a$ and 4) $L_x = L_y = 3a$ and at $d_x = d_y = 1.5a$

distance d/a from the free surface. As the distance d/a increases, the maximum tensile stress increases while the maximum compressive stress decreases and approaches the half-space solution. It is worth noting that as the contact center moves farther away from the free surface, the effects of the free edges diminish, and the stress field approaches the half-space solution. This occurs when the contact center is located at a distance $d/a \geq 4.0$, where the half-space solution can be considered valid.

5.6 Conclusion

This chapter presents the extension of the quarter-space method to analyze the eighth and finite-length spaces. The method incorporates corrective factors and the overlapping technique from the half-space solution to account for the presence of free edges and corners. The validity of the extended models has been demonstrated through comparison with the finite element method (FEM), showing good agreement between the two methods.

One notable observation is that when a free edge is located close to the contact zone in the eighth space, there is an increase in the maximum pressure. This increase can reach $1.04P_0$ at a distance $d_x = d_y = a$ from the free edges. The presence of free edges and corners leads to a reduction in the contact zone and a shift of the pressure field away from the free edges toward the infinite side of the space. These effects arise from the mutual influences of the two free edges and one corner.

In the case of the finite-length space, similar observations are made but with more pronounced effects. The maximum pressure can reach up to $1.17P_0$, indicating a higher stress level compared to the half-space case. The reduction in the contact zone and the shift of the pressure field are also more significant in the finite-length space, emphasizing the influence of the free edges.

Overall, both the eighth and finite-length spaces exhibit a higher normal stress level than the half-space case. The extension of the quarter-space method provides a valuable tool to analyze contact problems involving surfaces with free edges and finite-length spaces, capturing the complex interactions and stress distribution associated with these geometries.

The free edge effects vanish when the distance $d/a \geq 4$. It means that the influence of the free edges becomes less significant and can be neglected at greater distances. In this case, Hertz's solution can be considered. In terms of future perspectives, considering the effects of plasticity and heterogeneities in the developed models can provide a deeper understanding of the behavior of components and enable the analysis of more complex phenomena.

Chapter 6

Surface indentation process of rolling contact

In this chapter, our main focus is on investigating the indentation process on the surface of the raceway. To accomplish this, we employ a finite element modeling (FEM) approach, specifically utilizing the "Coupling-Euler-Lagrange" model developed by Bonetto. This model combines the strengths of both the Eulerian and Lagrangian methods, enabling us to simulate particle crushing in contact with reduced computational time. The primary objective of this study is to model and identify the crucial parameters that influence the formation of dents in rolling contacts. Following the investigation of the indentation process, we conducted an exhaustive parametric study to identify the most influential parameters. The results highlight the significance of the mechanical properties of the three bodies involved and the balance of these properties in dent formation. We found that the particle size is directly proportional to the size of the resulting dent as long as the particle size is smaller than the contact width. However, this relationship is significantly altered when the particle, after being crushed, becomes larger than the contact width. Furthermore, the presence of a slip in the contact considerably impacts the shape of the dent. It leads to increased spreading of the particle between the surfaces, resulting in more superficial dents. The numerical model enables the generation of realistic dents with asymmetrical profiles and the distribution of residual stresses they generate. This investigation aims to uncover new significant factors, including the particle's shape, orientation, position within the contact, the presence of a critical slip rate, and its variation. Furthermore, we have derived analytical expressions that approximate the variations of these key parameters as functions of other quantities. These expressions serve as the foundation for conducting Monte Carlo-type analyses, allowing us to determine dent dimensions' distribution. Additionally, this study enables us to establish criteria for evaluating the aggressiveness of dents based on particle size and contact conditions.

164

Sommaire

6.1 Introduction

In this chapter, we mainly focus on the real indentation process that occurs in rolling contacts using different bearing materials. Specifically, we will examine the indentation process on steel/steel bearing materials such as M50, 32CrMoV13, M50NiL, and M50NiLDH, as well as steel/ceramic bearings. To begin, we will briefly overview existing research on the topic, summarizing the key findings and current understanding of the indentation process in rolling contacts. Next, we will conduct a finite element modeling approach to reproduce the passage of a particle in rolling contact. For this purpose, we will employ the "Coupling-Eulerian-Lagrangian" model developed by Bonetto et al.(BON 19), which accurately captures the interaction between a spherical particle and a cylinder-plane contact. To make this study, we will modify and update the model to incorporate the specific operational conditions of main engine shaft line bearings. Additionally, we will consider additional crucial parameters for accurately modeling the indentation process. Furthermore, we will present a comprehensive parametric study to investigate the indentation process thoroughly. This study will focus on determining the influence of various factors, including the operating conditions of the bearing, the nature of its components (such as different bearing materials), and the characteristics of the particles involved. By systematically varying these parameters, we will be able to analyze their impact on the resulting dents and gain valuable insights into the indentation process in rolling contacts. Numerous studies have been conducted to enhance our comprehension of damage mechanisms in the presence of an indentation. Further information about these various studies is condensed and provided in the appendix.B.

6.2 Coupled Euler-Lagrange modeling

In Lagrangian finite element analysis, the mesh is typically fixed to the material and follows its motion, which can cause significant mesh distortion during large deformations. This can lead to inaccurate results and high computational costs due to the need for a large number of elements to accurately capture the deformation. Therefore, alternative methods such as Eulerian or Arbitrary Lagrangian-Eulerian (ALE) methods may be used where large deformations occur. These methods allow the mesh to remain fixed in space while the material moves through it, which can reduce distortion and improve accuracy. Reducing the size of the elements to limit their shape change is one way to improve the mesh quality and accuracy of the simulation. However, this improvement comes at the cost of increased memory usage and longer computation time. Additionally, reducing the element size may also reduce the critical time step, which is the maximum time step that can be used without introducing numerical instability in the simulation. The critical time step is usually calculated based on the material properties and the size of the elements used in the simulation. Equation 6.2 likely provides the expression for calculating the critical time step in the current simulation. Therefore, it is important to balance

the element size, computational cost, and accuracy of the results, considering the specific requirements of the simulation.

$$\Delta t_{critical} = \frac{L_c}{c_d} \tag{6.1}$$

$$c_d = \sqrt{\frac{E(1-\nu)}{\rho(1+\nu)(1-2\nu)}} \tag{6.2}$$

A critical time step is crucial in modeling dynamic phenomena with finite elements. It ensures that the simulation does not miss important events that occur within the material during the propagation of waves. The formula for the critical time step takes into account the characteristic distance L_c, which is the size of the smallest element in the model, and the speed of propagation of expansion waves in the medium c_d. In a structured mesh, L_c is close to the size of the smallest element. Therefore, the critical time step decreases with increasing mesh size and increases with increasing material density allowing the use of the principle of "Mass scaling" when inertial effects are ignored. This technique involves increasing the density of the material to obtain a higher critical time step and faster calculations. However, this approach is not used in this case.

The technique used by Xie et al.(XIE 15) is the Arbitrary Lagrangian-Eulerian (ALE) method, which is a hybrid Lagrangian-Eulerian technique. In this method, the mesh moves with the material but can also deform and adjust its position to reduce the distortion caused by large deformations. This technique is particularly suitable for modeling large deformation problems like those encountered in the indentation process. The mesh distortion can be reduced using the ALE method, and a more accurate simulation of the indentation process can be obtained without resorting to minimal elements, which would be computationally expensive. The ALE method also allows for simulating more complex geometries and material behaviors. Therefore, it is a promising technique for developing a complete and accurate indentation model at a reasonable computational cost.

In summary, the Eulerian modeling technique used in the present indentation model allows for more accurate and efficient simulations by avoiding the mesh distortion problems encountered in Lagrangian and ALE methods. This technique involves meshing 3-D space instead of the material and creating control points to observe the material. The mesh is fixed, ensuring the results' accuracy, and a reasonable size mesh can be used. The particle is modeled using Eulerian approach, while the other model components are modeled using Lagrangian approach, resulting in a coupled Euler-Lagrange model.

6.2.1 CEL Model

During the passage of a particle through contact, it undergoes significant deformation, causing the initial spherical shape to transform into a thin disc shape. However,

applying the traditional Lagrangian modeling method to the particle poses a considerable challenge due to mesh distortion. Like the particle, the mesh used in the modeling experiences substantial changes in shape, which can result in poor-quality results or discrepancies in the calculations.

To overcome this issue, Bonetto et al.(BON 20) adopted a Coupling-Eulerian-Lagrangian (CEL) approach, which combines both approaches methods in a single model. The Eulerian modeling is used to calculate the zones with large deformation, particularly the region occupied by the particle. On the other hand, the Lagrangian modeling is employed to calculate the zones with small deformation. The model's symmetry with respect to the rolling plane allows for the reduction of half of the modeling. The model comprises a roller, a raceway, a particle placed on the surface of the raceway at its center, and a rigid plane serving to apply the rolling load as shown in Figs.6.1,6.2 . The roller, as well as the raceway, are modeled using linear brick elements with eight nodes and reduced integration, called C3D8R. To remove the longitudinal wave reflections in the model caused by the displacement of the roller, CIN3D8 "infinity" elements are added around the edge of the raceway as illustrated in Fig.6.1, imitate the presence of boundary conditions located infinitely far away.
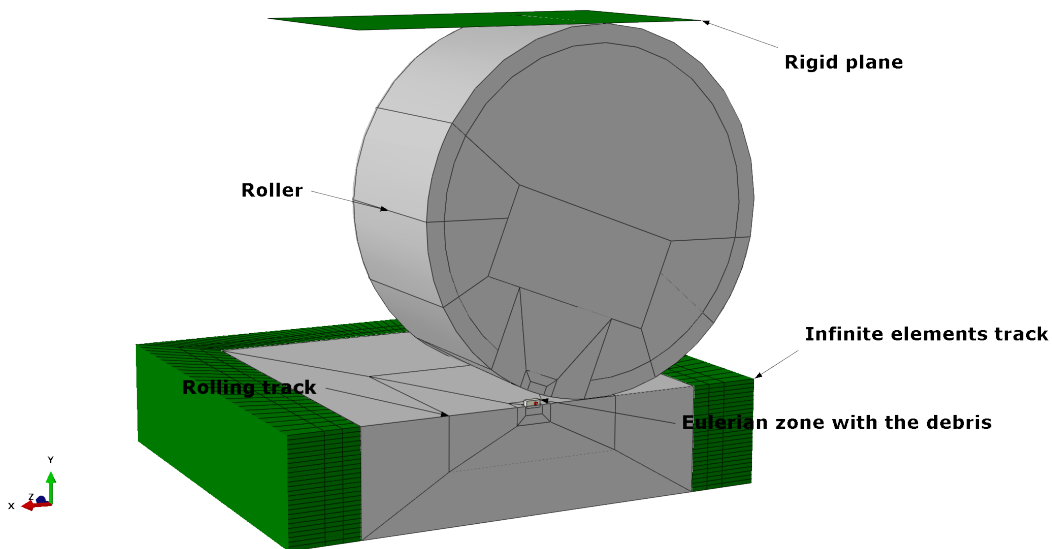
Figure 6.1: Finite elements model of indentation.

The Eulerian control domain used to track the behavior of the particle is defined in the same way as the Lagrangian solids in the previous model. However, the mesh used to model the particle is different, and linear Eulerian hexahedral elements with eight nodes and reduced integration EC3D8R are used. The particle is created in the model by defining a filling volume in the control space and applying the particle material to it. A filling rate variable is then assigned to each element of the Eulerian space, as shown in Fig.6.3. Initially, the Eulerian control space consists of empty

elements, full elements at the center of the particle, and partially filled elements on its surface. A rigid plate, modeled with R3D4 elements, is used to apply the load on the bearing during the first loading stage and to maintain it during the rolling phase.
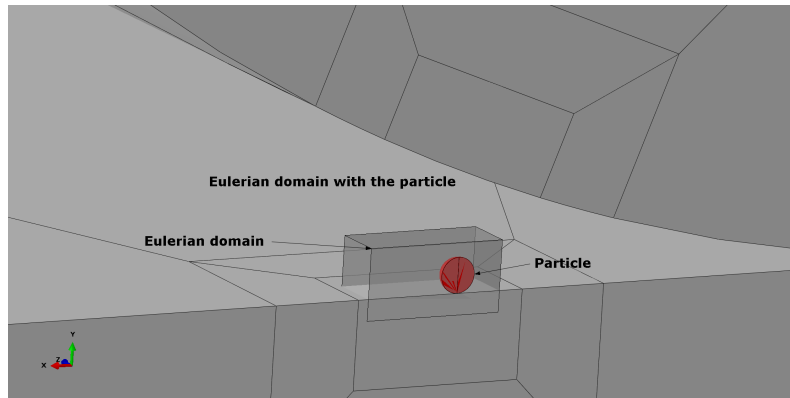
Figure 6.2: Area of the CEL model showing the Eulerian volume
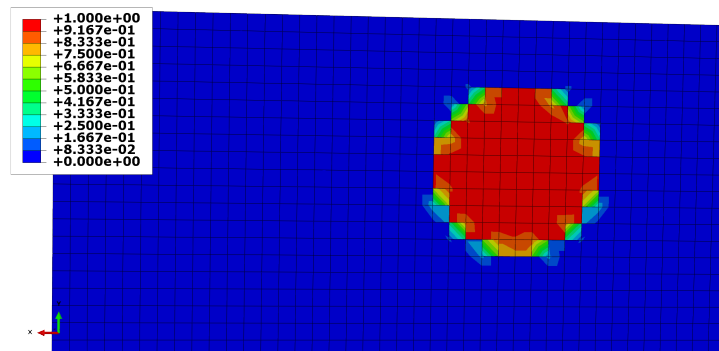
Figure 6.3: Filling the eulerian volume

6.2.2   Mechanical and thermal behavior

The mechanical and thermal behavior of the crushed particle in the contact can be complex and challenging to model accurately. The particle undergoes high levels of plastic deformation, generating heat and causing temperature increases. Additionally, the particle can experience fragmentation or even be completely crushed under extreme conditions. To model this behavior, a combination of experimental data and numerical simulations can be used. The Johnson-Cook model mentioned earlier is a popular choice for modeling the mechanical behavior of the particle. This model takes into account the strain rate, strain, and temperature dependence of the material's behavior. Thermal effects can be included in the simulation by incorporating the heat generated by plastic deformation into the model. This can be done

169

using techniques such as the Arbitrary Lagrangian-Eulerian (ALE) method, which allows for the modeling of material deformation and fluid-like behavior. In addition to modeling the mechanical and thermal behavior of the particle, it may also be necessary to consider the chemical reactions that occur during the indentation process. For example, oxidation or other chemical reactions can occur at the contact interface, leading to changes in material properties and behavior.

The passage of a particle through the contact and the resulting surface indentation occurs rapidly, typically within a short time interval of approximately 100 μs under typical operating conditions (VIL 99b). The indentation process generates high levels of inelastic deformations, resulting in very high strain rates and heat generation due to plastic work. Consequently, relying solely on modeling plastic deformations in the materials' constitutive behavior may not be sufficient to describe the indentation process accurately. It becomes necessary to introduce viscous and thermal effects into the constitutive law, as demonstrated by Nikas (NIK 13; NIK 14). To model the behavior of the roller, particle, and raceway, the Johnson-Cook law (JOH 83) is deployed. Its expression is given by:

$$\sigma_{eq} = (A + B\varepsilon^n)\left[1 + Cln(\dot{\varepsilon}/\dot{\varepsilon}_0)\right]\left[1 - \left(\frac{T - T_0}{T_m - T_0}\right)^m\right] \tag{6.3}$$

Where:

★ σ_{eq} is the equivalent stress

★ ε is the equivalent plastic strain

★ A, B, C, n, m are material constants

★ $\dot{\varepsilon}$ is the equivalent plastic strain rate

★ T is the temperature

★ $\dot{\varepsilon}_0$ is a reference strain rate

★ T_m is the melting temperature of the material

★ T_0 is the reference temperature of quasi-static test used to identify parameters

The first term of this expression represents the strain hardening effect, the second term represents the strain rate sensitivity, and the third term represents the thermal softening effect.

The determination of the parameters of the Johnson-Cook empirical law typically involves experimental tests using techniques such as the Hopkinson bar test, as described by Dorogoy and Rittel (DOR 09), or by correlating experimental tests with high-speed simulations, as done by researchers (SU 06; RAM 08; SHR 12). These

tests are used to measure the material response to high strain rates and determine the material parameters needed to accurately model the behavior using the Johnson-Cook law. Other techniques, such as high-speed photography and infrared imaging, can also be used to observe the deformation and thermal behavior of materials during high-speed impact or deformation.

The high speed at which the indentation process occurs assumes that the temperature increase in the materials is predominantly due to plastic deformation. In this context, the heat transfer between different materials and heat diffusion within each material can be neglected. Consequently, the only considered source of heat generation in the model is the plastic work, which is converted into heat energy and integrated into the model through Eq.6.4. This simplification is employed to facilitate the modeling process and ensure computational feasibility while still encompassing the fundamental physical phenomena of the process.

The equation is given as:

$$\Delta T = \frac{\eta}{\rho C_p} \underline{\underline{\sigma}} : \underline{\underline{\varepsilon}}_p \qquad (6.4)$$

Where:

- ✍ ΔT is the temperature increase due to plastic deformation

- ✍ η is the coefficient of Taylor-Quinney

- ✍ ρ is the density of the material

- ✍ C_p is the specific heat capacity of the material

- ✍ $\underline{\underline{\sigma}}$ is the stress tensor

- ✍ $\underline{\underline{\varepsilon}}_p$ is the plastic strain

The value of η (which is the fraction of inelastic dissipation trasformed into heat) is usually taken as 0.9 (TAY 34; CLI 84; SIM 92; ZHO 96).

The Johnson-Cook law parameters used in the model are obtained from the work of Su (SU 06) on residual stress modeling during high-speed machining operations. The parameters of the Johnson-Cook law used in the model are derived from the research conducted by Su (SU 06), which focused on residual stress modeling during high-speed machining operations. The material modeling parameters can be found in Table 6.1.

Table 6.1: Properties of the considered M50NiL steel

E (GPa)	ν	ρ (Kg.m^{-3})	C_p (J.kg^{-1}.K^{-1})	θ_m (K)	A (MPa)	B (MPa)	n	C	m
201	0.3	7800	472	σ_0	408	0.391	0.021	1.21	

According to tests conducted by Ville (VIL 98a) and Ville and Nélias (VIL 98b; VIL 99b), a hole is consistently observed at the bottom of the indentation mark, as illustrated in Fig.6.4, and its profile in pure rolling condition is shown in Fig.6.5. This hole is formed at the beginning of the indentation process, during the capture of the particle in the contact, as depicted in Fig.6.4. If the hole is not present at the end of the CEL model simulation, analysis of the dent profile during the indentation process reveals its formation during the initial stage of particle crushing.
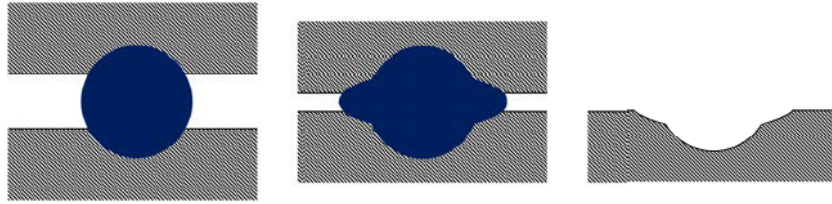
Figure 6.4: Theoretical process of indentation as described in (VIL 98a).
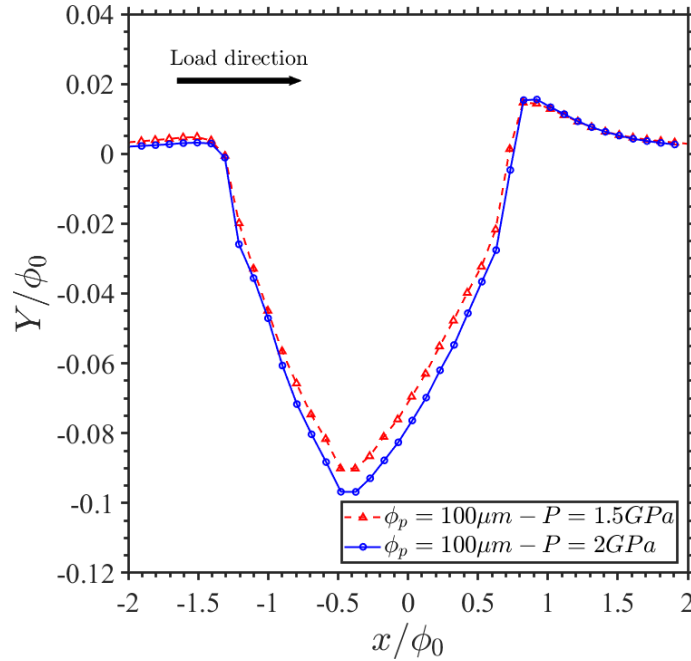
Figure 6.5: Dent profile in pure rolling condition

The non-axisymmetric nature of the dent in rolling contacts, as observed in the profile shown in Fig.6.5, can have significant consequences on the performance and durability of the contact. For example, a higher outlet pile-up which is 3.7 times higher than the inlet pile-up (indicating that the material is displaced in the direction of rolling), can lead to stress concentrations and potential crack initiation. On the other hand, the presence of a compression zone at the exit and a tension zone

172
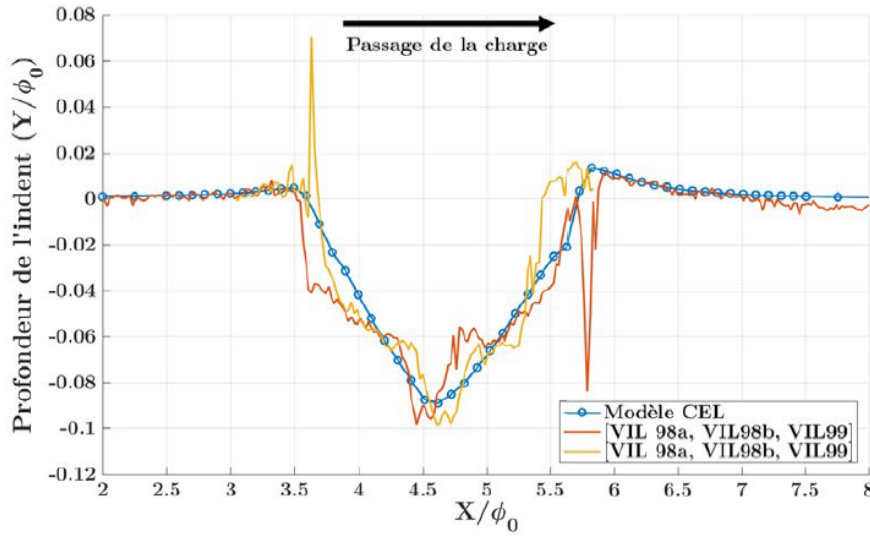
Figure 6.6: Numerical and experimental indentation profiles for a *SRR* of 6% (BON 20).

at the entrance of the dent suggests that the material experiences different loading modes during the indentation process. This can also affect the material's deformation behavior, fatigue life, and wear resistance. This non-axisymmetric nature of the real-dent generated by the CEL model, as shown in Fig.6.5, is a fundamental difference from the axisymmetric dents commonly used in current studies on fatigue (WAR 10; MOR 11b). The CEL model's ability to generate a more realistic initial dent makes it more suitable for fatigue calculations of indented surfaces. The importance of using a realistic dent in fatigue studies is highlighted by the fact that the stress distribution and loading conditions can significantly affect the fatigue life of the material.

The model developed by Bonetto et al.(BON 20) has undergone validation by comparing it with experimental data from Ville (VIL 98a). The validation was conducted under conditions of pure rolling and rolling + sliding. The profile of the numerical dent was compared to experimental profiles for particles with an initial diameter of 40-50 μm, and the graph was scaled by the nominal diameter of the particle (Fig.6.6). The shape of the numerical dent was found to be consistent with the observed tests. The depth of the numerical dent was equal to 8.15% of the initial particle diameter, while experimental values varied from 9 to 11%. The width of the numerical dent was measured to be 2.14 times the initial particle diameter , which falls perfectly within the experimental range of 1.8 to 2.5 times the initial diameter. Additionally, the numerical model produced beads around the dent, matching the experimental results in terms of height and width, showing good agreement overall.

However, it's worth noting that the results in the presence of model slip were only validated up to a slip rate of less than 20%. For an SRR (Slide-to-roll Ratio) of 20%, the dent profiles exhibited significant differences between the tests and the

simulation. The dimensions of the dents were lower by a factor of 2. These observed differences can be attributed to the fact that the slip rate becomes very significant, generating a high tangential loading. This tangential loading may be responsible for the phenomenon of breaking by shearing, exacerbating the spreading of the particle. It's important to mention that the CEL model used in the simulations does not take into account failure aspects, which could influence the results under high slip rates. Therefore, the model's validity is limited to slip rates below 20%, and beyond that, the simulations may need to accurately reflect the experimental behavior due to the lack of consideration of failure mechanisms by the CEL model.

When analyzing dents formed on a surface as presented in Fig.6.7, three main parameters can be used to characterize its profile:

- The depth of the dent.

- The diameter of the dent.

- The height of the pile-up.

Among these parameters, the most crucial is the pile-up height. This parameter is the critical one as it can generate an overpressure during the repeated passages of rolling elements. Therefore, special attention will be devoted to this parameter throughout the rest of this thesis.
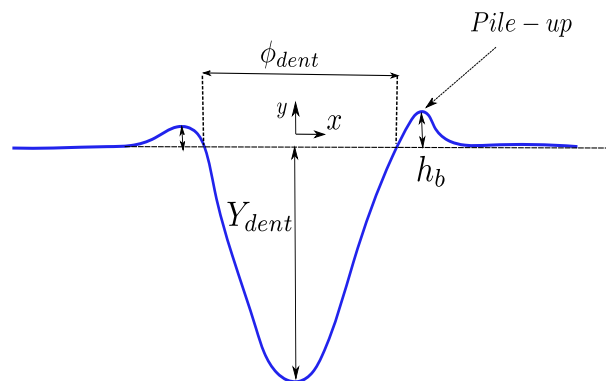
Figure 6.7:   Dent profile illustration

6.3   Indentation simulation by CEL model

In this section, a simulation will be conducted to study the resistance of bearing materials, including M50, 32CrMoV13, M50NiL, and M50NiLDH, against the indentation process. These rolling materials exhibit variations in hardness gradients and surface hardness levels, which are influenced by the specific treatments they

undergo, such as quenching, nitriding, carburizing, and carbonitriding, as well as their inherent characteristics. The primary objective of this simulation is to analyze the behavior of these steel grades when subjected to the indentation process. Since the particle crushing process primarily affects the surface (requiring a small volume of material on the surface), the surface properties can be considered representative of the entire material without significantly impacting the results.

6.3.1 Operating conditions

The operating conditions of the motor shaft line bearings are integrated into the model. The bearings rotate at high speed of 3200 rpm corresponding to a linear speed of 100 m/s, and the roller, which has a diameter of 10 mm and a useful length of 9 mm, is subjected to a force resulting in a maximum pressure of Hertz P_0. This pressure is comparable to those used in main engine shaft applications. In this study, the bearing elements were modeled as cylinders in a planar contact problem. This kind of contact is equivalent to bearing contact with some fixed geometry and loading. The friction resulting from the contact between the roller and the track is incorporated into the model using Coulomb's law. The contact is treated as an elastohydrodynamic (EHD) contact lubrication regime, commonly encountered in aeronautics. Zhu and Hu (ZHU 01) have demonstrated that the coefficient of friction (μ) in such regimes typically remains below 0.1. When the coefficient of friction is below this threshold, the impact of friction on the contact is limited, as shown by Johnson (JOH 85). Therefore, a coefficient of friction of $\mu = 0.01$ is employed to model the interaction between the roller and the track.

The second contact between the particle and the roller and track surfaces cannot be considered an elastohydrodynamic (EHD) contact due to its limited central thickness, which is only a few tens of nanometers and negligible compared to the particle size. However, there is lubricant present at the interface between the particle and the surfaces due to abundant lubrication, indicating that it is not a dry contact. In such a scenario, a mixed regime contact is assumed, resulting in a coefficient of friction $\mu_{particle} = 0.2$. This coefficient is consistent with the work of Nikas on indentation (NIK 12; NIK 13; NIK 14).

6.3.2 Material resistance

In this study, we focus on examining the response of four materials M50, 32Cr-MoV13, M50NiL, and M50NiLDH that have undergone thermochemical treatments to the indentation process. The primary goal is to assess how these treatments influence the materials' resistance to indentation. To achieve this, we will integrate the specified operating conditions from the previous section into the simulation models. The material parameters required for the simulations are provided in the Table.6.2.

Figure.6.8 illustrates the results of the simulations conducted under the condition of pure rolling. The focus is on comparing the materials' behavior in terms of

175

Table 6.2: Parameters of the nominal case

Parameter	Value
Loading	$P_0 = 1.5 GPa$
Roller dimensions	$Length = 9mm, \ \phi_{roller} = 10 \ mm$
Contact half-width	$b_0 = 133\mu m$
Particle diameter ϕ_0	$100 \ \mu$m
Particle nature	M50
Particle shape	Spherical
Particle position in the contact	Center of the contact
Bearing materials	M50, 32CrMoV13, M50NiL, M50NiLDH
Steel hardening	Isotrope
Velocity	$100 \ m.s^{-1}$
Rolling + sliding	SRR
Friction coefficients	$\mu_{particle} = 0.2/\mu_{roller} = 0.01$

the dent depth and the pile-up height. From the analysis of the indentation depth, it is evident that M50NiLDH demonstrates the highest resistance among the studied materials, indicating that it can withstand higher loads and exhibit the least indentation marks. On the other hand, M50 exhibits the weakest resistance, being the most susceptible to indentation. 32CrMoV13 falls in between, showing slightly lower resistance than M50NiL, which has a resistance level comparable to M50. Regarding the bead height, M50, 32CrMoV13, and M50NiL exhibit similar values, implying that their surface deformation and material displacement during the bearing process are relatively consistent. However, M50NiLDH exhibits a lower bead height, indicating less surface deformation or material displacement compared to the other materials. These observations from the suggest that M50NiLDH stands out as the most resistant material in terms of indentation depth, while M50NiLDH also shows a distinctive behavior with a lower bead height compared to the other materials. In the presence of surface carbonitriding treatment, the pile-up height of M50NiLDH steel is observed to be only half that of the bulk material. This emphasizes the significance of residual compressive stresses on the material's surface, which can vary depending on the type of heat treatment, the heat treatment application conditions, and the material's characteristics. Therefore residual stresses play a crucial role as one of the primary parameters influencing the indentation process.

To enhance our understanding of the indentation process, it is crucial to conduct parametric studies. These studies would involve systematically investigating various parameters that have an impact on both the geometry of the dent and the distribution of residual stresses. By carefully analyzing these factors, we can gain valuable insights into the indentation process and its influence on material behavior.
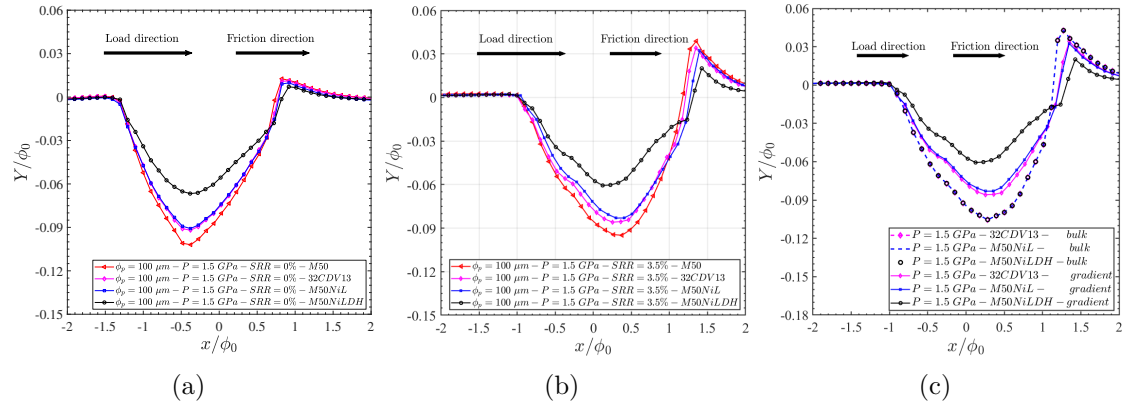
Figure 6.8: Dent profile evolution on bearing materials (a) In pure rolling condition, (b)In rolling/sliding condition and (c) Contrast between the dental profiles of the treated materials and the untreated materials.

6.4 Parametric studies

In this section, we will conduct an extensive parametric study to examine the effects of different parameters on the dent profile. To ensure a representative particle model, we will use M50NiL steel for our analysis. The same material M50NiL ise used for the roller and the track in the modeling except for the hybrid bearing where the rolling bearing can be in other material. Table.6.3 provides the values of various parameters used in the CEL model to study the indentation process. These parameters include the material properties of the roller, track, and particle, the particle's size and shape, and the contact conditions. In the following analysis, we consider particle size of 100 μm as the reference particle size. Consequently, in various simulations, the particle sizes will be reported and scaled relative to this reference size.

Table 6.3: Parameters definition for the parametric studies

Parameter	Value
Load	P_H
Particle diameter	ϕ_p
Particle nature	$E = 100 - 500 GPa$
Particle shape	Spherical, cubic
Particle position	Contact center and $r = 0.707a$
Roller/Ring/particle	$\sigma_0 = 0.5 - 3GPa$
Steel hardening	Isotrope
Velocity	20-60-100 m/s
Rolling + sliding	SRR
Friction coefficients	$\mu_{particle} = 0.2/\mu_{roller} = 0.01$

6.4.1   Friction coefficient influence

The coefficient of friction between surfaces under the EHD lubrication regime only varies significantly with operating conditions, material properties, and lubricant composition. However, the coefficient of friction between the particle and the surfaces in contact is more strongly dependent on these parameters and can vary more broadly. When the coefficient of friction increases, the frictional forces between the particle and the counter-face, oppose the spreading of the particle and generates deeper dents. For friction coefficients lower than 0.1, the CEL model predicts an expulsion of the particle upon contact with the roller. This analysis aligns with the conclusions drawn by Dwyer-Joyce et al. in their work (DWY 92), where they established a correlation between surface geometries, the coefficient of friction, and the maximum particle size capable of entering in contact. Specifically, the simulated scenario of planar cylinder contact reveals a critical particle size threshold for contact, which concurs with the outcomes depicted in Fig.6.9 for a coefficient of friction of 0.1. Thus, it establishes a criterion for capturing particles in contact, which combines the geometry of the contacting bodies, the particle size, and the coefficient of friction.
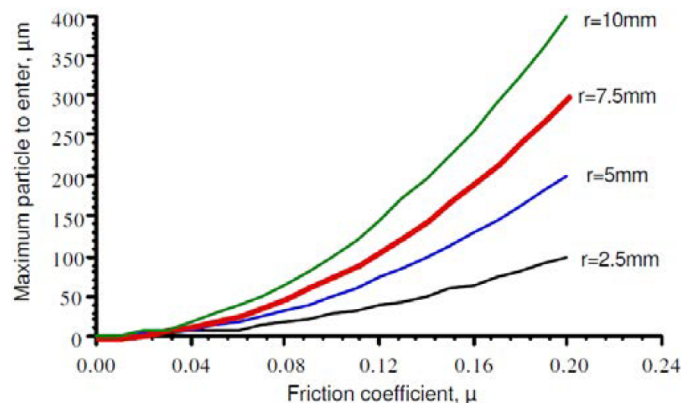
Figure 6.9: The maximum particle size introduced into the rolling contact is contingent upon the coefficient of friction for various radii, as indicated in (DWY 92)

The lubricated contact needs the definition of a coefficient of friction between the particle and the track. Within the mixed lubrication regime, various coefficient values have been examined. Notably, for friction coefficients below 0.2, the particle may be expulsed during crushing. Hence, a value of 0.2 is adopted for subsequent analyses as it proves suitable for the bearing lubrication regime. Nonetheless, it is important to note that during operation, this coefficient will fluctuate due to changes in temperature, load evolution, and other factors. Therefore, the coefficient of friction is not a fixed value and may vary under real operating conditions.

6.4.2 Particle size influence

The volume of material affected by the indentation is an important parameter in understanding the deformation and damage caused by the particle contact. The CEL model predicts that the volume of material affected by the indentation is dependent on the particle size. For example, for ductile particles, the volume can be a half-ellipsoid width of $2.8\phi_0$ and a depth of $1.7\phi_0$ depending on the particle, the bearing materials properties and the friction coefficient.

The comparison of the profiles, scaled by the reference diameter of 100 μm, as shown in Fig.6.10, reveals a noticeable modification in the shape of the dent for the largest particle. The obtained dent is less deep, measuring 8% of the initial diameter, however, it is also larger, measuring 2.5 times the initial diameter (2.5 ϕ_0).

Figure.6.10 illustrates the profiles of dents formed by different particle sizes, including particles of size ϕ_0 and $0.6\phi_0$. Notably, the dent profile and, consequently, the height of the bead, width, and depth of the dent undergo significant changes.

For ductile particles, the particle of size ϕ_0 generates a dent depth of $0.09\phi_0$, while the particle of size $0.6\phi_0$ results in a dent depth of $0.051\phi_0$. The corresponding bead heights for the two particle sizes are $0.0148\phi_0$ and $0.00693\phi_0$, respectively. In terms of dent diameter, the particle of size ϕ_0 yields a diameter of $2.2\phi_0$, whereas the particle of size $0.6\phi_0$ produces a diameter of $1.31\phi_0$.

In the case of elastic particles, the dent depths are $0.465\phi_0$ and $0.273\phi_0$ for particles of size ϕ_0 and $0.6\phi_0$, respectively. The resulting dent diameters are $1.3\phi_0$ and $0.82\phi_0$, while the bead heights are $0.033\phi_0$ and $0.012\phi_0$ for the two particle sizes, respectively.

In conclusion, it can be clearly observed that the particles' size substantially influences the dent's profile and the resulting height of the bead. The variations in particle size lead to significant differences in the dent's depth, diameter, and height, reflecting the significant role particle size plays in the overall indentation process.

6.4.3 Load influence

It is interesting to note that the geometry of the dent is weakly influenced by the normal load in indentation simulations, as shown in Fig.6.11. The depth of the dent and the height of its pile-up increases slightly with an increasing load but in limited proportions. This is consistent with previous studies by Ville, and Kang and Sadeghi (VIL 98a; KAN 04) on the effect of load on indentation. The von Mises stresses in the roller and the track at the particle's passage is also similar in all three loading cases, as shown in Fig.6.11, which explains the slight differences in results between loadings.
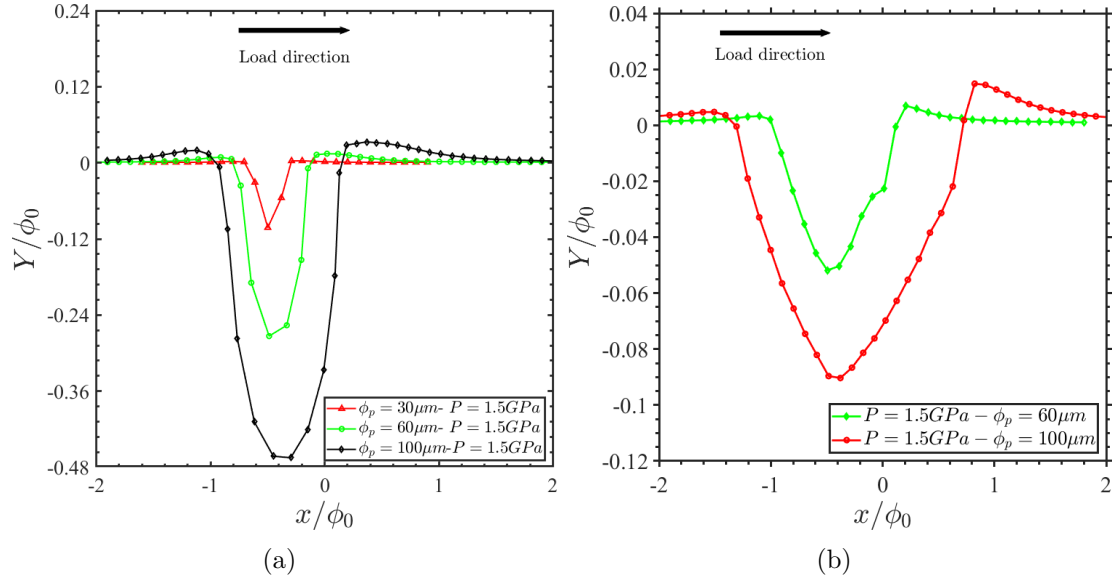
Figure 6.10: Indentation curve for different diameter a) for elastic particle b) for ductile particle
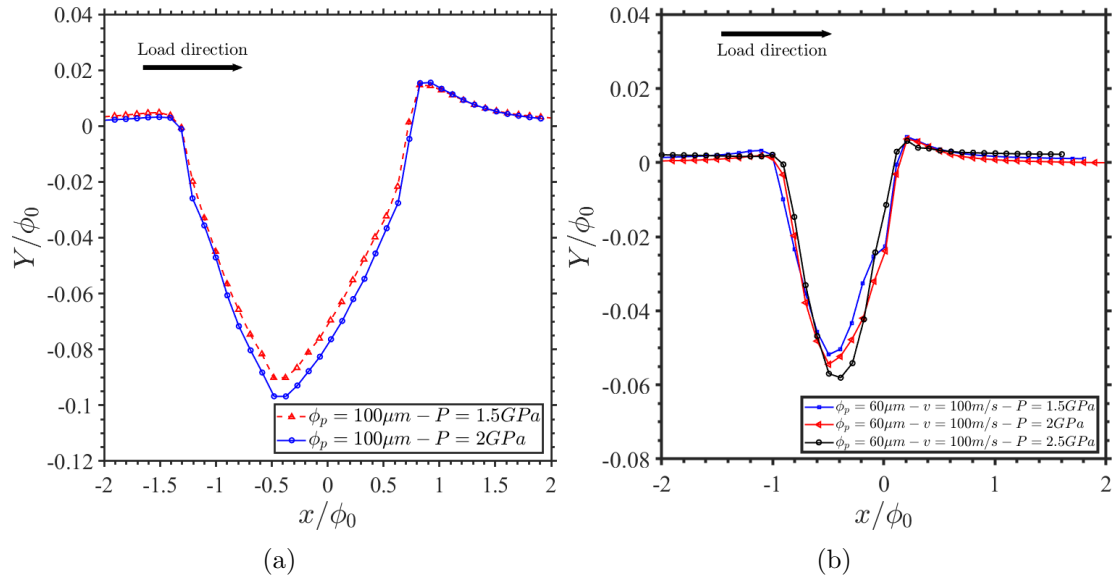
Figure 6.11: Indentation curve evolution of ductile debris for different load configurations (a)$P_H = 1.5\text{-}2\text{GPa}$ for particle diameter of $\phi_p = 100\mu m$; b)$P_H = 1.5\text{-}2\text{-}2.5\text{GPa}$ for particle diameter of $\phi_p = 60\mu m$

6.4.4   Particle position in the contact

The position of a particle in a rolling contact can significantly influence the resulting dent, particularly when there is sliding between the surfaces. For example, when a

particle is initially located near the edge of the contact area, it may be subjected to higher tangential force due to the relative motion between the surfaces, leading to a more severe indentation or even fracture of the particle. On the other hand, a particle located closer to the center of the contact area may experience a normal loading or a pure rolling loading. The presence of sliding between the surfaces can also be due to the position of the particle within the contact. For example, for a particle initially located near the edge of the contact area, it will experience a sliding during the loading because of its position as illustrated in Fig.6.12.
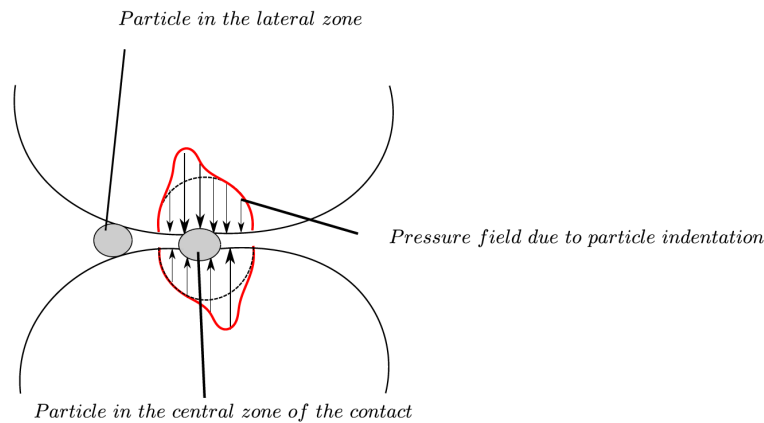
Figure 6.12: Illustration of debris position in the rolling contact

The particle's position can significantly influence the indentation, particularly when sliding occurs. Sliding introduces frictional forces that leads to wider dents. Thus, this study will focus on investigating two positions: the center of the contact, where the particle experiences pure rolling, and the position where the product PV reaches its maximum value, which will be determined later.
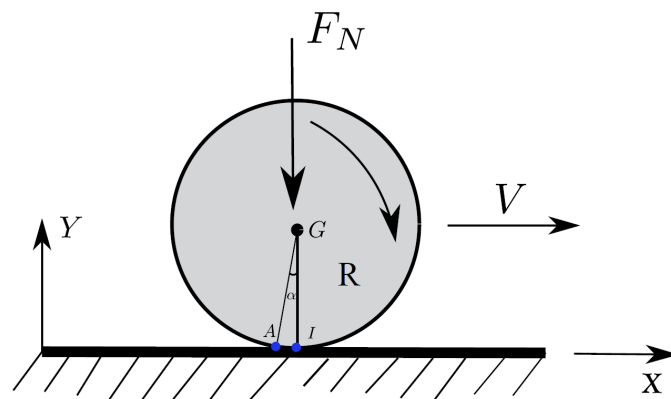
Figure 6.13: Illustration of position in rolling contat

To analyze these positions, the contact pressure will be considered using its Hertz expression, while the speed will be denoted by $V = rw$, where r is the radius and w is

the angular velocity. The product PV represents the pressure-velocity combination, where the pressure corresponds to the Hertz maximum pressure, and the velocity V represents the relative speed between the surfaces. The maximum value of PV indicates the position where the most significant energy dissipation occurs within the contact. This maximum value can be calculated by taking the derivative of the PV expression with respect to the parameter r.

When a roller is rolling on a plane as shown in Fig.6.13, the condition for rolling without slip is given by:

$$V_{I,1-2} = 0 \tag{6.5}$$

Therefore, considering a particle located at an angular position alpha relative to the vertical axis passing through the center, the relative velocity of the particle can be expressed as follows:

$$V_r = V_0(1 - \cos\alpha) \tag{6.6}$$

The Hertz 2D pressure is given by the expression:

$$P = P_0\sqrt{1 - \frac{r^2}{a^2}} \tag{6.7}$$

At the center of contact, the pressure is equal to P_0 (the Hertz maximum pressure), and there is no sliding, meaning the particle is experiencing pure rolling.

On the other hand, at the position $r = 0.707a$ (where a is the Hertz contact radius) where PV is at its maximum value, the corresponding pressure is $P = 0.707P_0$, with P_0 is the Hertz maximum pressure. At this specific position where $r = 0.707a$ and PV is at its maximum, the slip rate will be considered as 3%.

When conducting particle crushing simulations at the two mentioned positions (center of contact and $r = 0.707a$), we observe an increase in the pile-up height compared to the particle at the center. These simulations take into account both ductile particles and ceramic elastic particles.

Hence, considering the particle's position in the contact, we can clearly observe a substantial increase in both the height and width of the dent. As a result, the position emerges as a primary parameter influencing the entire indentation process.

6.4.5 Sliding influence

Sliding in a rolling contact in the presence of a particle can have a significant impact on the indentation process. The extent of sliding in the contact is quantified by the slide-to-roll ratio SRR. The SRR is defined as the ratio of the sliding velocity between the roller and the track to the local rolling velocity at the contact point. Mathematically, it can be expressed as:

$$SRR = \frac{U_1 - U_2}{U_1 + U_2} \tag{6.8}$$
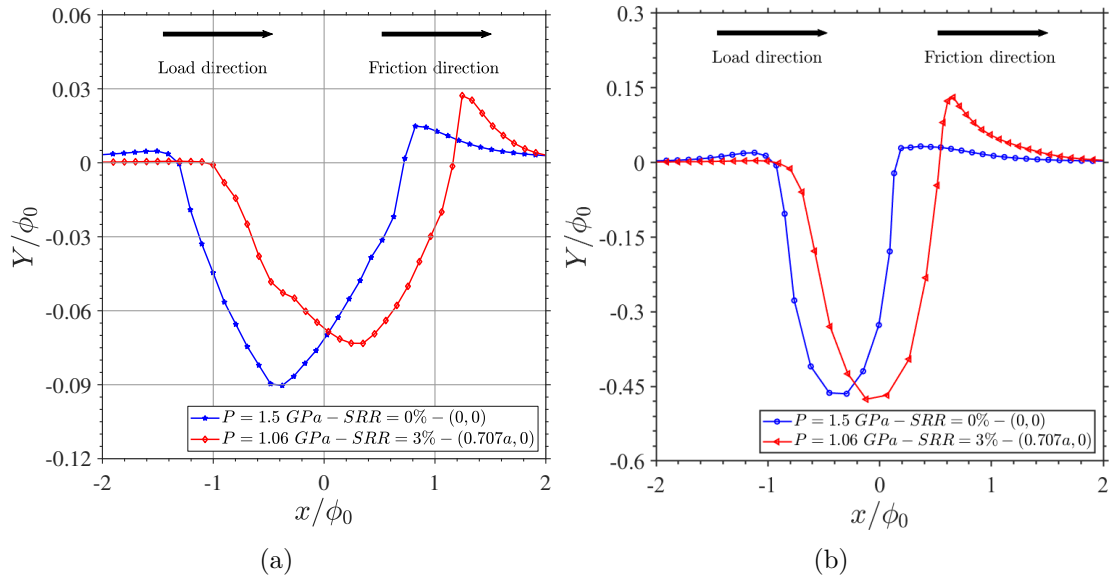
Figure 6.14: Dent profile of dent for the debris position in the contact (a) for ductile particle b) for elastic particle

where U_1 is the velocity of surface (1), and U_2 the velocity of surface (2). When $SRR = 0$, there is pure rolling, while a value of ± 1 corresponds to pure sliding. Intermediate values indicate a combination of rolling and sliding.

Depending on the Slid-to-roll ratio (SRR) sign as illustrated in Fig.6.15, we can distinguish positive and negative sliding:

1. Positive sliding refers to the case where the surface velocity of the rolling elements is smaller than that of the raceway in rolling direction, resulting in the particle being dragged backward in the opposite direction of the roller. This can cause the particle to become embedded in the surface and lead to surface damage. This results in a decrease in the contact area, a contraction of the particle in the direction of sliding, and a deeper indentation.

2. Negative sliding refers to the case where the surface velocity of the rolling elements is greater than that of the raceway in the direction of motion, resulting in the particle being pushed in the same direction as the rolling direction. This leads to a spreading of the particle and an offset of the dent. We can observe also an increase of the dent diameter and a spreading of the particle in the direction of sliding.

From the bearing kinematics point of view, the two bodies in contact do not always have the same linear speed in the contact zone. There is therefore, in addition to the rolling a combined slip. The direction of rolling is given by the direction of the linear speeds of the bodies in contact. To better understand the effect of this slide on the contact areas of the two bodies, let us look at what happens at the

$$U_2 < U_1 \qquad\qquad U_2 > U_1$$
$$SRR > 0 \qquad\qquad SRR < 0$$

U_2 → $\qquad\qquad$ U_2 →

U_1 → $\qquad\qquad$ U_1 →
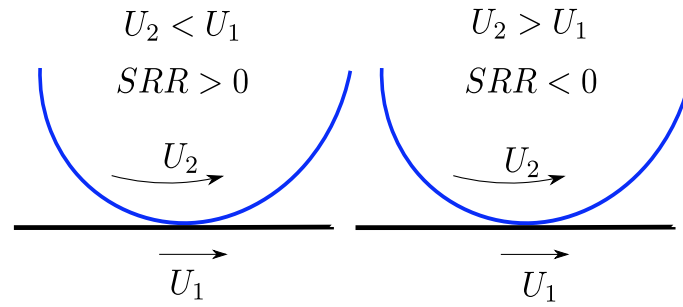
Figure 6.15: SRR illustration (a) in positive sliding (b) in the negative sliding

driving surface and the driven surface. The driving surface will tend to pull on the other surface and will therefore be braked by the second surface so the friction force is opposite to the rolling direction. As for the driven surface, it will be pulled by the fast surface, which leads to a friction force oriented in the direction of the rolling bearing as illustrated in Fig.6.16.

Driving surface $\qquad\qquad$ *Led surface*

(2) $\qquad\qquad$ (2)

Rolling $\qquad\qquad$ *Rolling*

Friction direction $\qquad\qquad$ *Friction direction*

Led surface (1) $\qquad$ *Driving surface* (1)

$U_2 > U_1 \qquad\qquad U_2 < U_1$
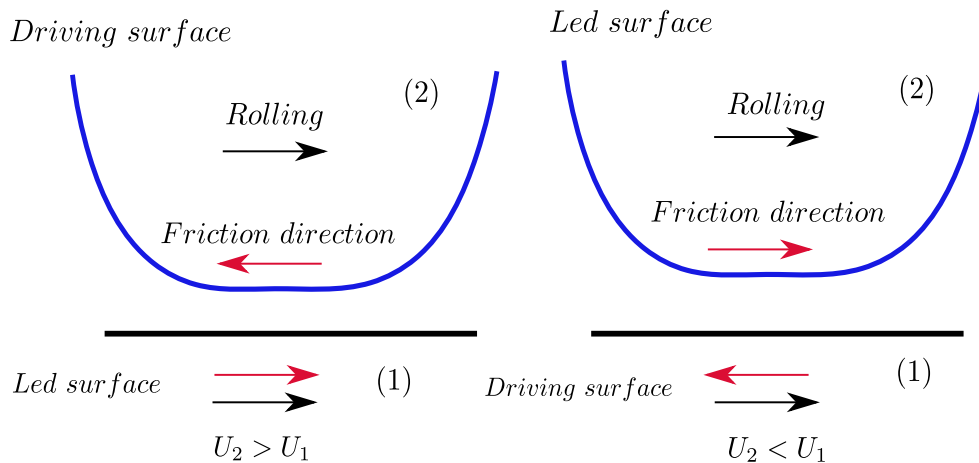
Figure 6.16: Representation depicting the directions of friction based on the relative speed of the surfaces.

For a SRR of 20%, the simulation results differ significantly from the experimental results. While the appearance of the numerical dent is similar to the experimental dent, with a shifted hole upstream of the dent, gradually increasing depth in the direction of rolling, and a steep ascent, the dimensions are smaller by a factor 2 as presented in Fig.6.17. This difference may be due to the very high sliding rate generating a high tangential load, which can cause the particle rupture by shearing and exacerbate its spreading. However, the CEL model used in the simulation does not account for failure, which may explain the significant difference in width between the numerical and experimental dents. Additionally, the spreading of the particle becomes very small due to the high SRR, and the mesh size used for the simulation may be too large to obtain accurate results. Therefore, the CEL model is valid for

low SRR but can only provide a general trend as SRR is greather than 20%.
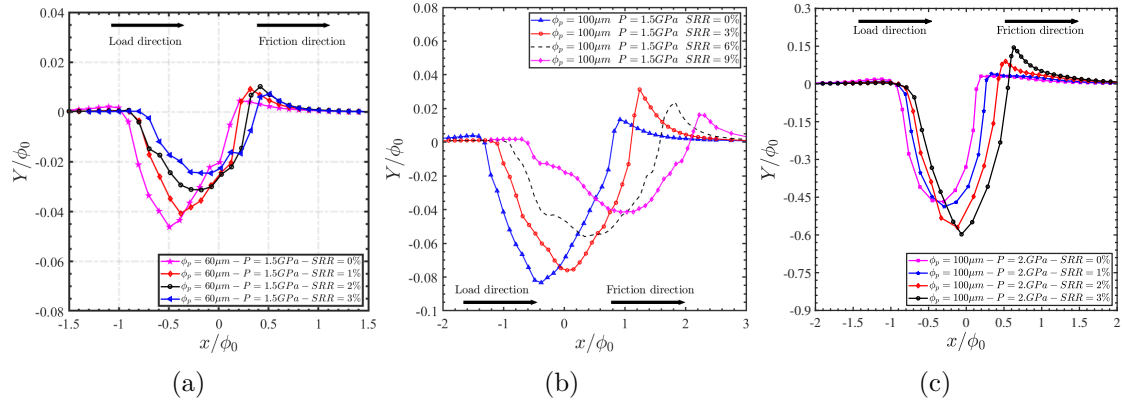
Figure 6.17: Dent profile evolution with the sliding rate (a) $\phi_p = 60\mu m$ for a ductile debris, (b) $\phi_p = 100\mu m$ for a ductile debris, c) $\phi_p = 100\mu m$ for an elastic debris

6.4.5.1 Sliding influence on ductile particle

In the presence of sliding, the crushing behavior of ductile particles indeed differs depending on whether positive sliding or negative sliding is present. Negative sliding, where the particle slides in the opposite direction of the applied force, leads to slightly larger dents than those formed during positive sliding. However, negative sliding results in lower bead heights compared to the case of positive sliding, as illustrated in Fig.6.18.

This distinction implies that positive sliding can be more detrimental in terms of the defect created on the surface. The larger dents formed during positive sliding, combined with the lower bead heights, indicate a potentially more significant impact on the surface, highlighting the potential harm associated with positive sliding in terms of surface damage.

Therefore, when considering the evolution of the SRR, the corresponding bead height undergoes a distinct evolution. As the slip rate increases, the bead height increases until it reaches a maximum value. However, beyond this critical slip rate, the bead height starts to decrease.

It is important to note that this critical slip rate, which leads to the maximum bead height, depends on the particle diameter. This relationship between the critical slip rate and particle diameter can be observed and analyzed, as depicted in Fig.6.18.

Thus, for a contact configuration with particle size, when we change the SRR, there will be a critical value for which the height of the bead generated will be the maximum. Thus, this value of the critical SRR is an influential parameter to be studied subsequently because it controls the maximum height of the bead. In the presence of sliding, the stresses around the dent in the material will elevate and

orient themselves in the direction of sliding, as depicted in Fig.6.19, in contrast to the rolling case where the stresses are comparatively lower.
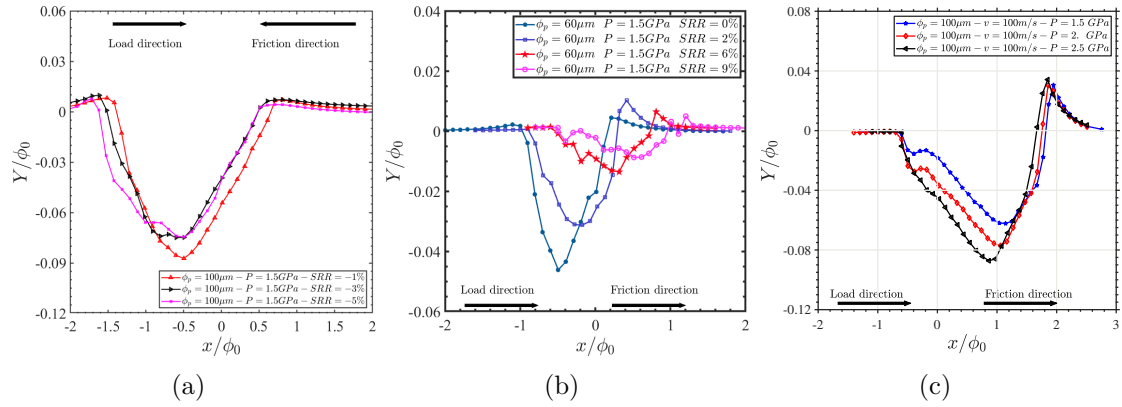
Figure 6.18: Dent profile evolution with the sliding rate (a) $\phi_p = 100\mu m$ for a ductile debris and negative sliding, (b) $\phi_p = 60\mu m$ for a ductile debris and positive sliding, c) $\phi_p = 100\mu m$ for a ductile debris and $SRR = 6\%$
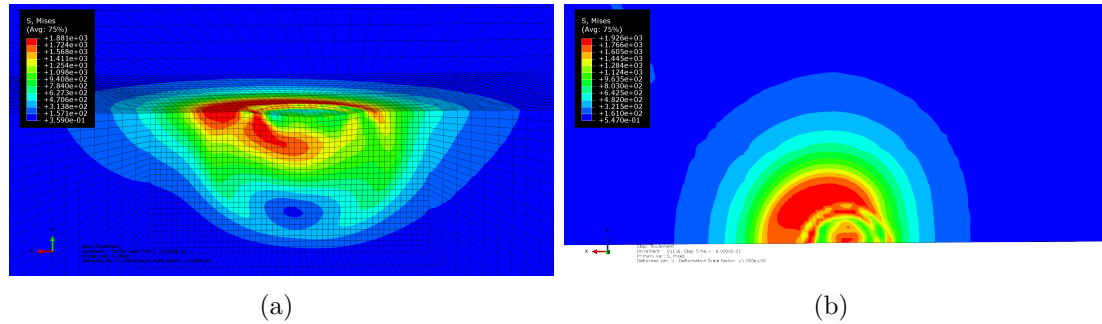
Figure 6.19: Indentation zone of particle of diameter $\phi_p = 100\mu m$ in M50 steel, after crushing in contact (a) In pure rolling condition (b) In presence of sliding $SRR = 3\%$.

6.4.5.2 Sliding influence with hard or elastic particle

In the case of an elastic particle, the dent's geometry on the surface changes as the slip rate evolves, considering a specific particle size. The created dent is narrower and deeper in comparison to the case of ductile particles as presented in Fig.6.20. The bead's depth, diameter, and height all increase with the progression of the sliding rate, as illustrated in Fig.6.21. This phenomenon can be explained by the fact that, in the presence of sliding, the elastic particle, being relatively harder, tends to cause more material to be torn off as it undergoes increased crushing against the surface. As the sliding rate increases, the particle's interaction with the surface

186

intensifies, resulting in a more significant deformation and subsequent alteration in the geometry of the dent. Fig.6.21(a) demonstrates that when an elastic or hard particle is present, both positive and negative sliding result in nearly identical bead heights.
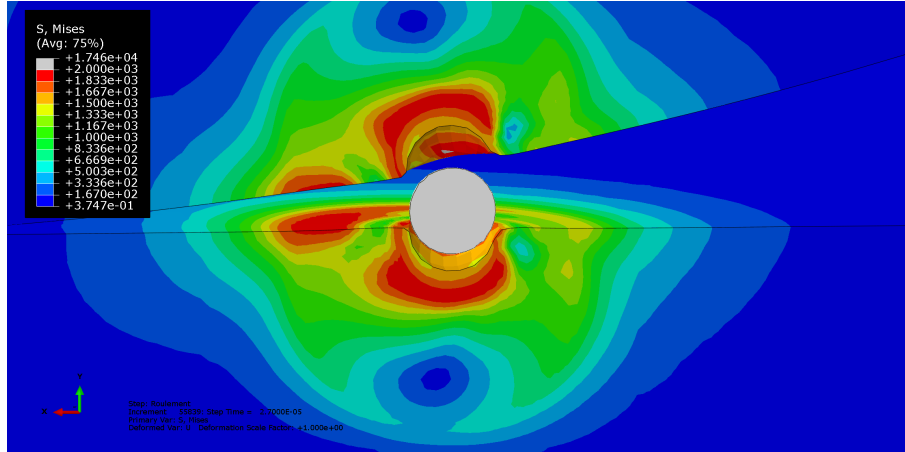
Figure 6.20: Indentation of an elastic particle in Si_3N_4 ($E = 310GPa$, $\nu = 0.26$) on a steel bearing in M50NiL at $P_H = 1.5GPa$ in pure rolling condition
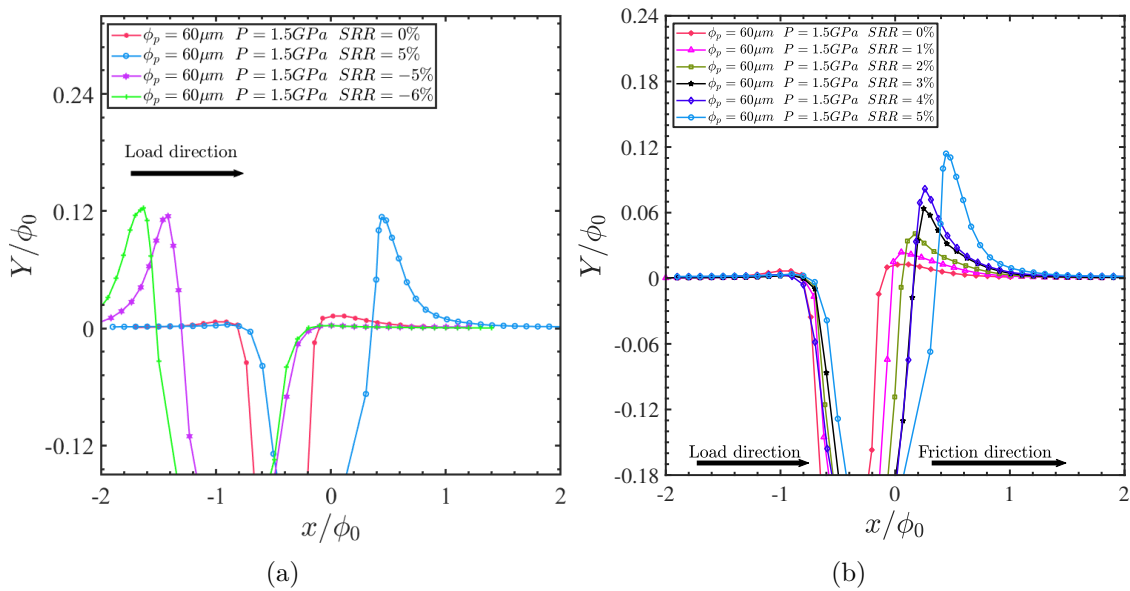
Figure 6.21: Evolution of the dent function of SRR for an elastic particle of diameter $\phi_p = 60\mu m$ in Si_3N_4 with roller and raceway in M50NiL a) In presence of positive and negative sliding b) In presence of positive sliding

6.4.5.3 Synthesis

To summarize, simulations have shown that the presence of positive slip in rolling contact with particles leads to an accentuation of particle spreading, resulting in more slender and shallower dents. The level of positive slip is quantified by the slide-to-roll ratio (SRR), and even low levels of positive slip can lead to an accentuation of the exit bead. As the level of positive slip increases, the lag of the hole upstream of the dent is well-reproduced in the simulations. On the other hand, negative slip reduces the depth of the dents but does not significantly increase the width of the dents. Negative slip also leads to a reduction in the exit bead and a significant increase in the entrance bead, but the proportions of this increase are less than in positive slip.

In summary, simulations carried out in the presence of both positive and negative slip in rolling contacts with particles show that slip has a significant effect on the indentation, as well as the formation and height of the exit and entrance beads. Positive slip tends to accentuate the spreading of the particle and create more slender and shallower dents, while negative slip reduces the depth of the dents but does not significantly increase their width. In addition, positive slip leads to an increase in the height of the exit bead and a reduction in the entrance bead, while negative slip leads to a reduction in the exit bead and a significant increase in the entrance bead. These effects become more pronounced as the level of slip increases.

The influence of the SRR on the indentation process has been extensively studied in the literature and has been shown to have a significant effect on the dent geometry, especially on the spreading of the material around the dent and the formation of the pile-up.

6.4.6 Influence of particle nature

The debris in transmission systems can come from various sources, such as organic materials during assembly, sand from the outside environment, and wear particles from within the system. The study has considered two categories of particles: ductile particles and very hard, brittle particles. The mechanical behavior of ductile particles will be modeled by the Johnson-Cook law, which has been used in previous work on indentation and is given in Table.6.2. On the other hand, hard brittle particles will be modeled by elastic behavior via Young's modulus. The study aims to investigate the effect of particle material properties on the behavior of rolling contacts, as different materials can have different responses to loading and deformation.

6.4.6.1 Ductile particles

This study focuses on ductile particles commonly found in industrial mechanisms. Specifically, we will be considering steels that exhibit variations in their elastic limit (yield strength). As a result, ductile particles create broader and shallower dents,

and the bead heights of these dents vary depending on the hardness of the particle (see Fig.6.23). Therefore, within the simulation framework, the materials used for the roller and the track will be M50NiL, possessing an elastic modulus of 200 GPa, a Poisson's ratio (ν) of 0.3, yield strength (σ_0), and exhibiting Johson-Cook viscoplastic behavior.

(a)   (b)
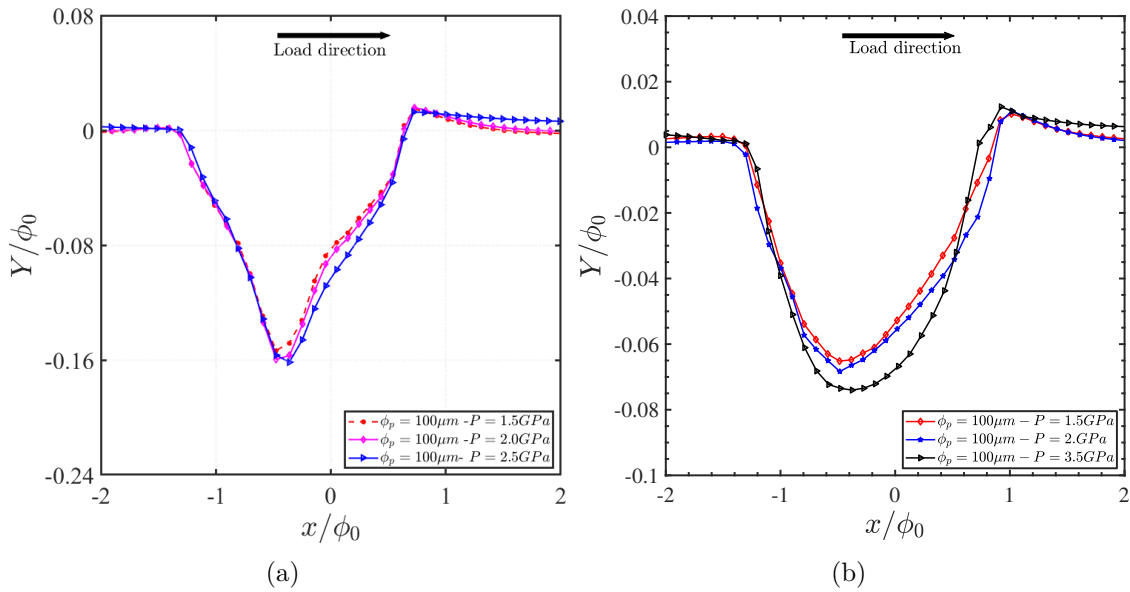
Figure 6.22: Dent profile evolution according to particle yield strength in a steel/steel bearing in M50NiL and particle of diameter $\phi_p = 100 \mu m$ (a) $\sigma_0 = 3GPa$, (b) $\sigma_0 = 0.5GPa$.
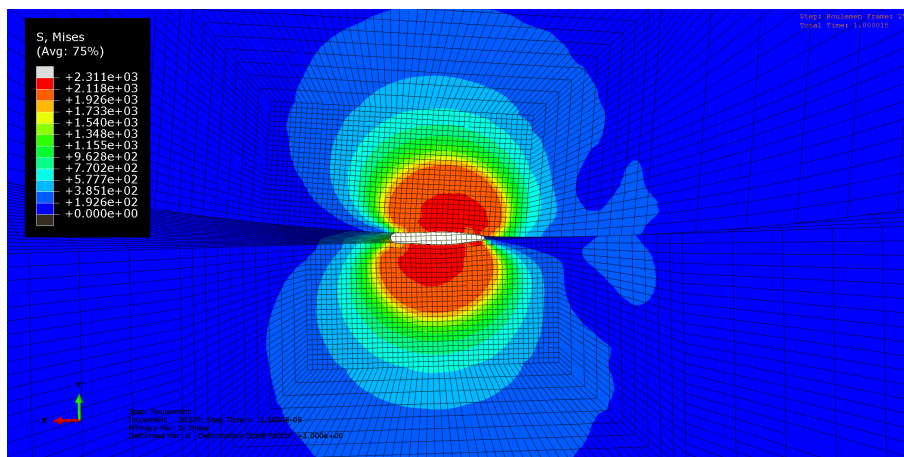
Figure 6.23: Particle of diameter $\phi_p = 100 \mu m$ in steel ($E = 200GPa$, $\nu = 0.45$, $\sigma_0 = 1.3GPa$) crushing process in rolling contact for $P_H = 1.6GPa$ (Roller and raceway in M50NiL)

Figure.6.22 illustrates that particles with an elastic limit of 3GPa create deeper but narrower dents with higher bead heights compared to particles with an elastic limit of 0.5GPa. Additionally, it is evident that the shape of the dents and the distribution of residual stresses undergo changes corresponding to the mechanical properties of the debris. Hence, Figure.6.23 displays the indentation zone after the ductile particle in M50 steel has been crushed. We observed that the regions experiencing the highest stress levels are the edges of indents in the direction of rolling in pure rolling conditions.

6.4.6.2 Elastic particles

The material of bearing components can vary, particularly due to the increased use of hybrid bearings that incorporate ceramic rolling elements. Just as the properties of particles affects the response to indentation, the material used for bearing components also influences this response. In this section, the brittle particles caracterized by the high elastic modulus and low plasticity are modeled using an elastic behavior based on their elastic modulus. Elastic particles are characterized by their modulus of elasticity and Poisson's ratio. An steel track and a Si_3N_4 ceramic roller are used to simulate a hybrid bearing. Therefore, a purely elastic behavior assumption is implemented for the simulation. In this section, we will systematically vary elastic properties, including the elastic modulus and Poisson's ratio, to examine how the compressibility of the particle influences the dent profile formed on the raceway. The compressibility modulus, often denoted as K (bulk modulus), measures a material's resistance to change in volume under pressure. It is related to the Young's modulus (E) and Poisson's ratio (ν) through the expression:

$$K = \frac{E}{3(1-2\nu)} \tag{6.9}$$

here: K is the compressibility modulus, E is the Young's modulus, and ν is the Poisson's ratio.

Consequently, when these elastic particles are crushed, they create deeper and narrower dents with significantly higher bead heights compared to ductile particles as illustrated in Fig.6.24. This difference is attributed to the harder nature of the particles, which results in a larger amount of material being displaced and forming agglomerates in the shape of beads on the surface.

In terms of stress distribution around the dent, the crushing of elastic particles leads to higher stress levels compared to those induced by ductile particles in the material. Consequently, the stress distribution around the dent is significantly greater (exacerbated by sliding), particularly with increased bead heights and deeper indentations as shown in Fig.6.25.

As shown in the Fig.6.26, the height of the bead is only slightly affected by its compressibility.

Figure.6.27 depicts the profile of the roller after crushing a ductile and elastic particle under pure rolling conditions. There is a slightly more pronounced roller
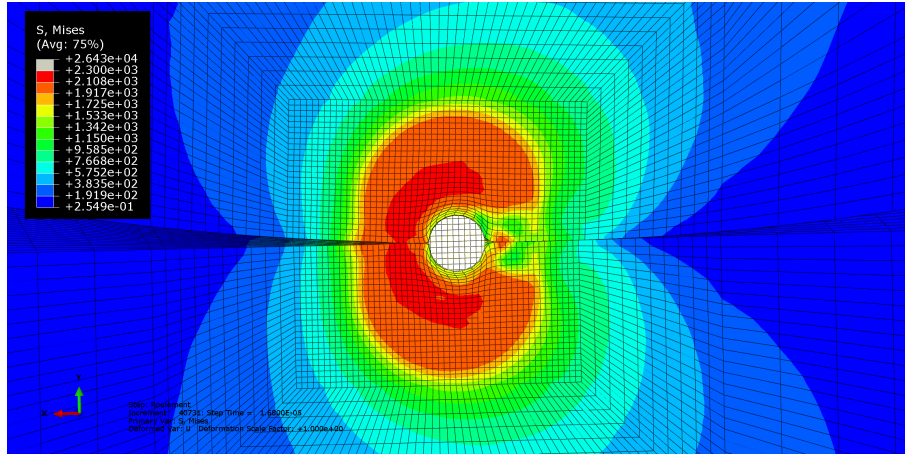
Figure 6.24: Crushing process of an elastic particle ($\phi_p = 100\mu m$) in Si_3N_4 on M50NiL/M50NiL bearing contact at $P_H = 1.5 GPa$

(a)   (b)
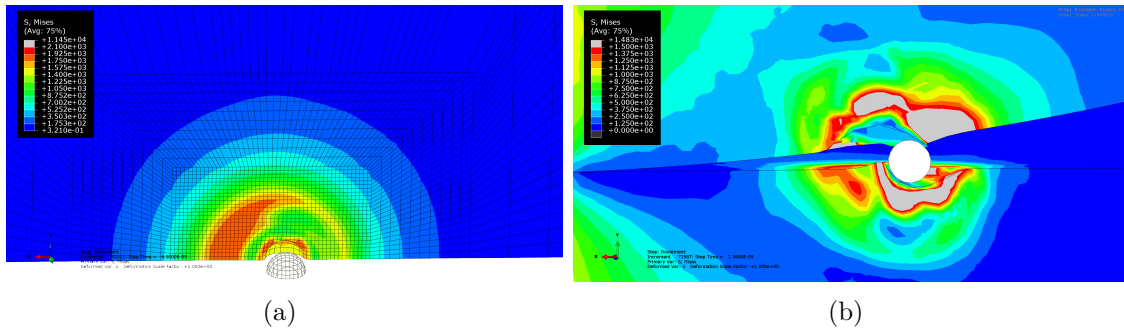
Figure 6.25: Denting zone in a M50NiL/M50NiL bearing contact with an elastic particle in Si_3N_4 (a) top view of the contact zone in pure rolling condition (b) face wiew of the elements in contact.

deformation in the rolling direction compared to the dent created on the raceway. Additionally, it can be observed that when both antagonists share similar mechanical properties, the height of the bead created is evenly distributed on each surface, effectively halving the bead height on both surfaces.

6.4.7 Particle material density influence

In this section, the effect of particle density on the indentation profile is investigated. Despite the increase in particle density, the indentation profile remains largely unaffected. This is attributed to the small size of the particles, which results in minimal inertia and, therefore, has little influence on the analysis results.

However, the advantage of increasing particle density is evident in terms of computational time efficiency. Although the indentation profile does not change significantly, using denser particles leads to an average time saving of 1 hour during the
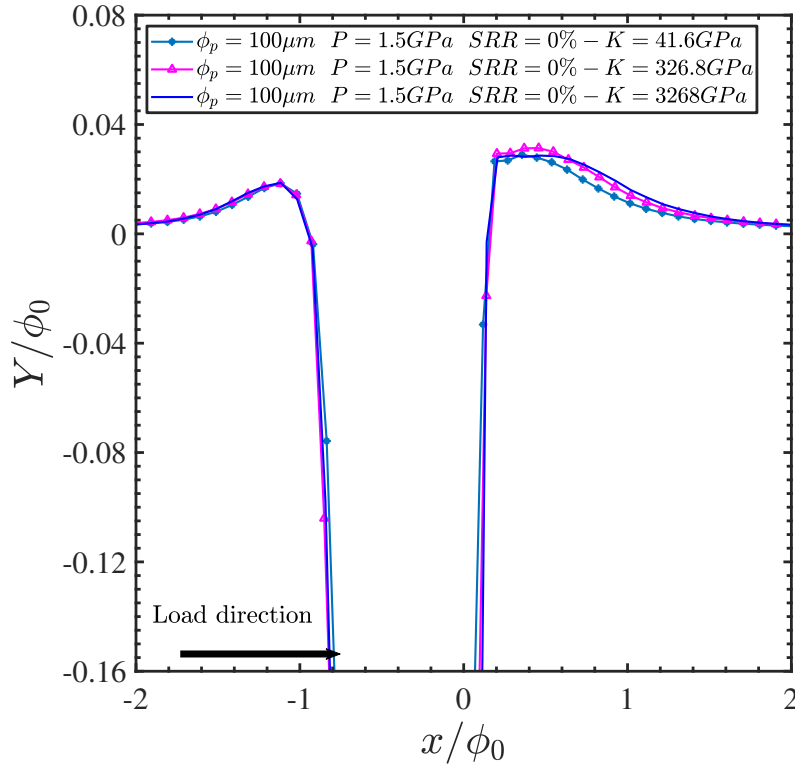
Figure 6.26: Dent evolution according to the debris compressibility

calculation process as illustrated in Fig.6.28.

In conclusion, while higher particle density may not alter the indentation profile substantially, it does offer the practical benefit of reducing the overall calculation time. This finding is valuable for researchers and engineers who wish to strike a balance between particle density, computational resources, and time optimization in their analyses.

Increasing the particle density up to 15 times the initial density shows negligible deviations in pure rolling conditions. However, these deviations become slightly more noticeable when sliding is present. Therefore, for optimal results and to minimize any significant errors in the dent profile, it is recommended to increase the density to 10 times the initial density.

6.4.8 Bearing material influence

In aeronautical applications, bearing materials face severe operational conditions, including high loading, speed, and temperature levels. Consequently, the rolling materials must exhibit exceptional strength, performance, and reliability. As a result, the commonly employed materials for these applications are steel/steel bearings (comprising steel rings and steel rolling elements) and hybrid steel/ceramic bearings (featuring steel rings and ceramic rolling elements).
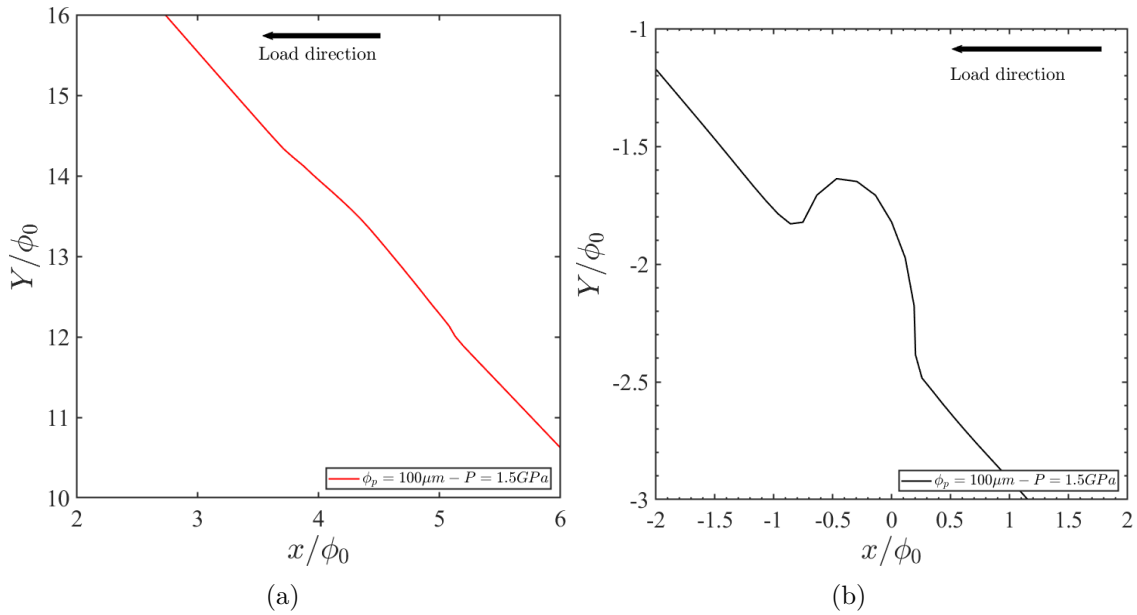
Figure 6.27: Roller profile after particle of diameter $\phi_p = 100\mu m$ indentation on M50NiL bearing (a) indentation of ductile particle in M50 (b) indentation of elastic particle in Si_3N_4.

During the particle's passage through contact, the interaction between the particle and the antagonists results in the observation of very high local overpressures. This phenomenon is influenced by the properties of both the antagonists and the particle, as illustrated in Figs.6.29,6.30.

Consequently, hybrid bearings will produce significantly deeper dents with more pronounced bead heights compared to steel/steel bearings at iso particle conditions, as shown in Fig.6.30. This can be attributed to the behavior observed when a steel/steel bearing is present. In such cases, the bearing race and the rolling element distribute the impact of particles in a similar manner, resulting in less pronounced dents. On the other hand, in hybrid bearings, the steel race absorbs most of the particle's impact, forming much deeper dents with considerably higher bead heights, as illustrated in Fig.6.31.

The more the elastic properties of the elements in contact increase, the more the particle sinks into the contact elements (roller and raceway) and will, therefore, penetrate the less hard element to the detriment of the harder one. Thus, from a certain particle size, the particle is trapped in the hole of the dent created, which slightly reduces the influence of the sliding as shown in Figs.6.32(b),6.33(a). We also observe a saturation of the evolution of the height of the bead due to the fact that the more the particle sinks into the material, the more it will cause the stricture of the zone, which will generate a collapse of the created bead. Another observed effect is that as the particle sinks further, the contact force responsible for creating the bead tends to reduce its height through matting, as illustrated in Fig.6.31,6.33(a).
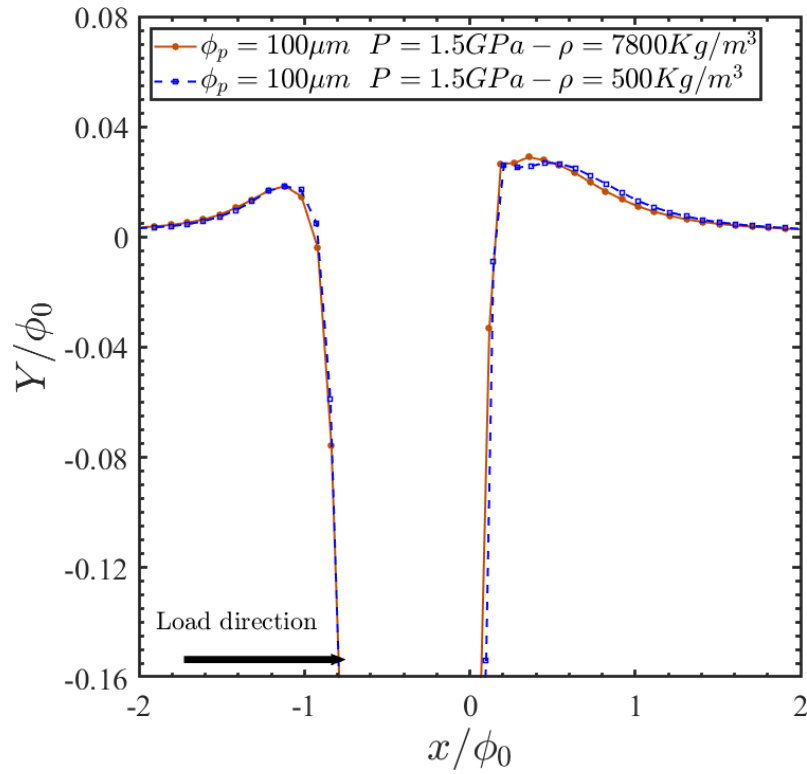
Figure 6.28: Dent evolution with the variation of particle density in pure rolling condition at iso-compressibility $K = 41.7 GPa$
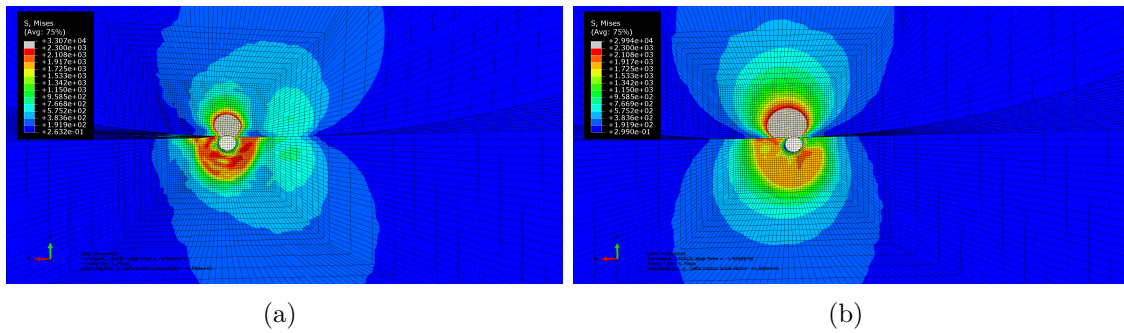
Figure 6.29: Denting process evolution in hybrid bearing contact (a) at time $t = 1.56.10^{-5}$ (b) $t = 1.92.10^{-5}$

Depending on the hardness of the ductile particle, it is possible to quickly attain bead height values comparable to those observed with elastic particles passing through a hybrid rolling contact as presented in Fig.6.33(b).
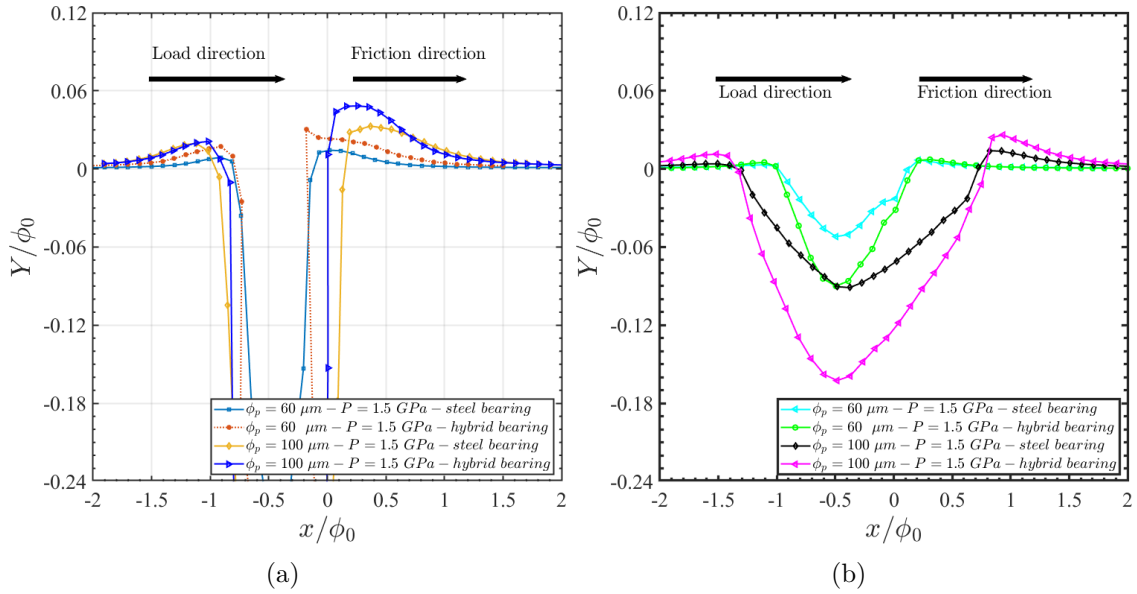
Figure 6.30: Dent profile comparaison according to the bearing material (a) Si_3N_4 elastic particle (b) M50 ductile particle.
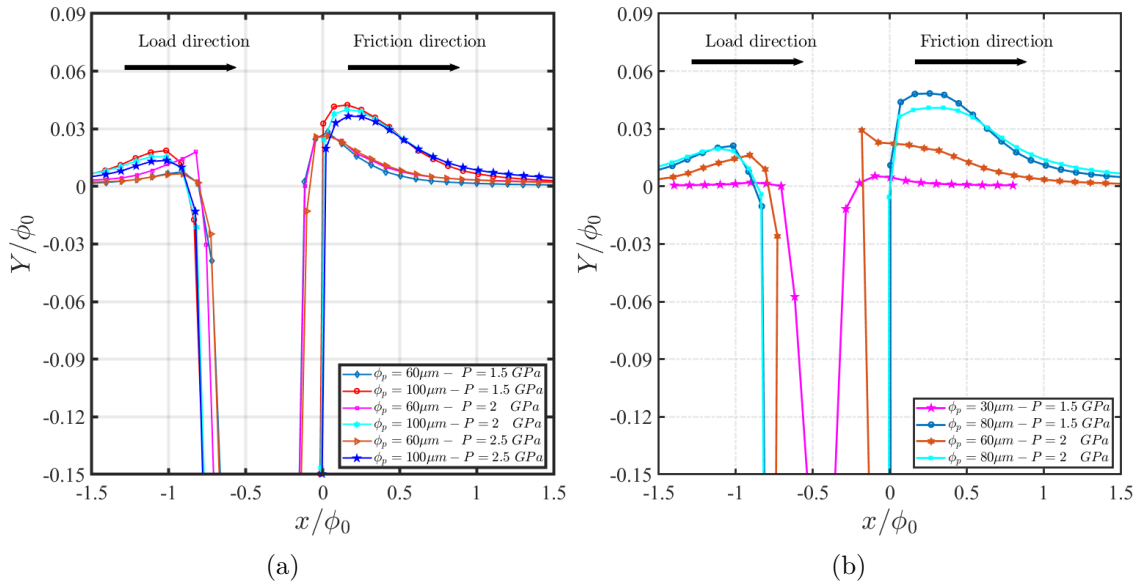
Figure 6.31: Dent profile for an elastic particle in pure rolling condition (a) $E = 100$ GPa, (b) $E = 310$ GPa.

6.4.9 Influence of particle shape

During operation, particles of varying natures and shapes traverse through the engine. Concerning the indentation of these particles on the bearing raceway, particle

(a)   (b)
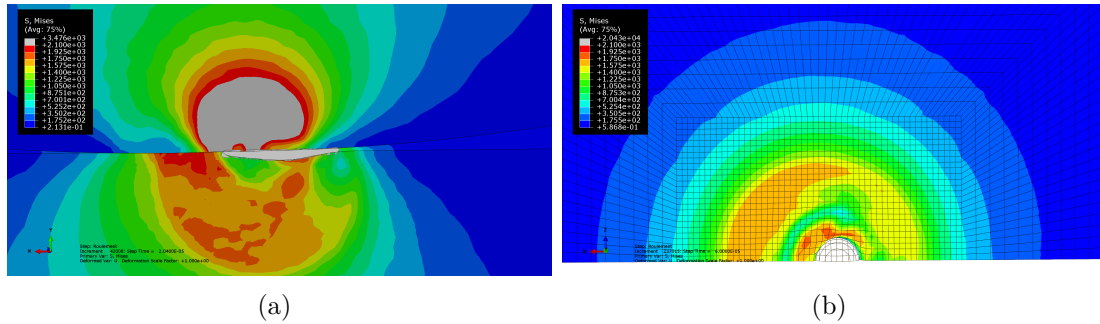
Figure 6.32: Denting zone for hybrid bearing contact (a) ductile particle in M50 (b) elastic particle in Si_3N_4.

(a)   (b)
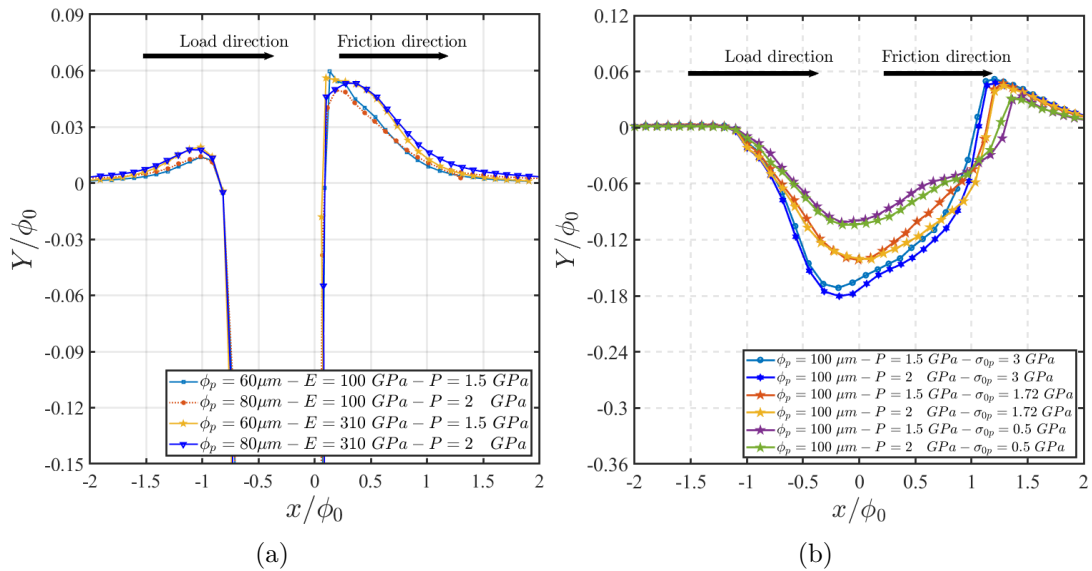
Figure 6.33: Dent profile in hybrid bearing of roller in Si_3N_4 and raceway in M50NiL (a) by variating the particle parameter (modulus and diameter) at $SRR = 1.5\%$ (b)Dent profile evolution in hybrid bearing in Si_3N_4 and M50NiL with ductile particle yield strenght variation (diameter $\phi_p = 100\mu m$ and $SRR = 3.5\%$).

shape (see Fig.6.34) is a significant factor affecting the dent profile and residual stress distribution. To investigate this, we will focus on two primary particle shapes: spherical and cubic. Moreover, we will ensure that the studied particles have equal volumes and edge lengths to assess their impact on the resulting dent geometry.

When particles with different geometries are subjected to the same crushing conditions, distinct dent profiles and stress distributions are observed, as show in Fig.6.35. Therefore, particle geometry emerges as a primary determining factor in shaping dent characteristics. In this context, with the same material properties, particle volume, and particle type, a cubic-shaped particle oriented at 45 degrees

196
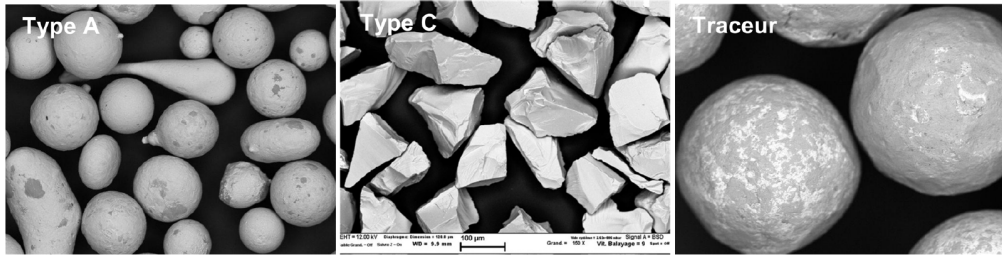
Figure 6.34: Presentation of different particle shapes
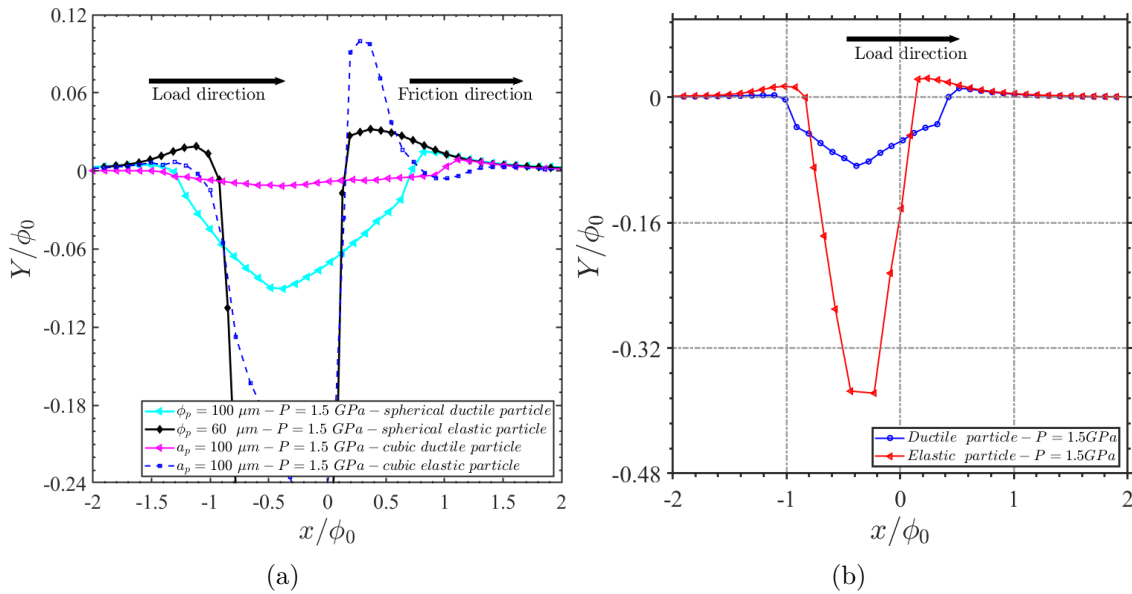
Figure 6.35: Dent profile comparaison according of the particle in M50NiL or Si_3N_4, in steel bearing in M50NiL, a) with spherical and cubic particle shape (b) with cubic shape.

will yield deeper dents with significantly greater bead dozer heights compared to a spherical particle. Conversely, a ductile cubic particle oriented at 0 degrees on the rolling track will produce flatter dents with slightly lower bead heights than those formed by spherical particles. This analysis highlights the crucial influence not only of the particle's geometry itself but also of the orientation of that geometry on the dent profile.

6.4.10 Influence of velocity

In this section, our focus lies in examining the impact of the rolling speed on the process of creating dents on the surface. As depicted in Fig.6.37, we can observe a moderate effect of the speed on the height evolution of the bead.
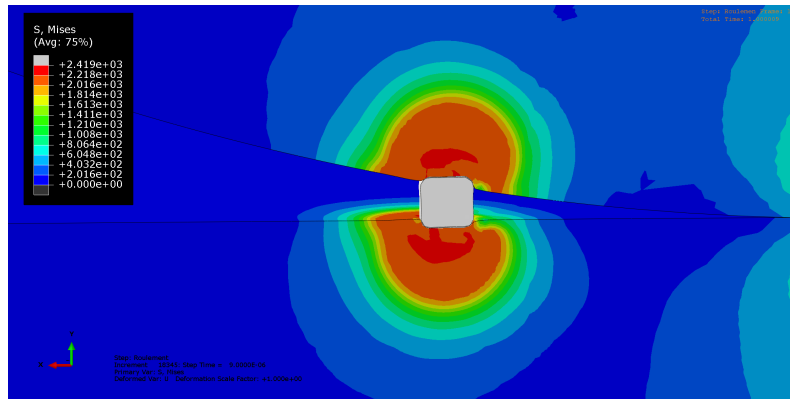
Figure 6.36: Indentation with presence of cubic particle of edge $a = 100\mu m$ in M50NiL bearing contact
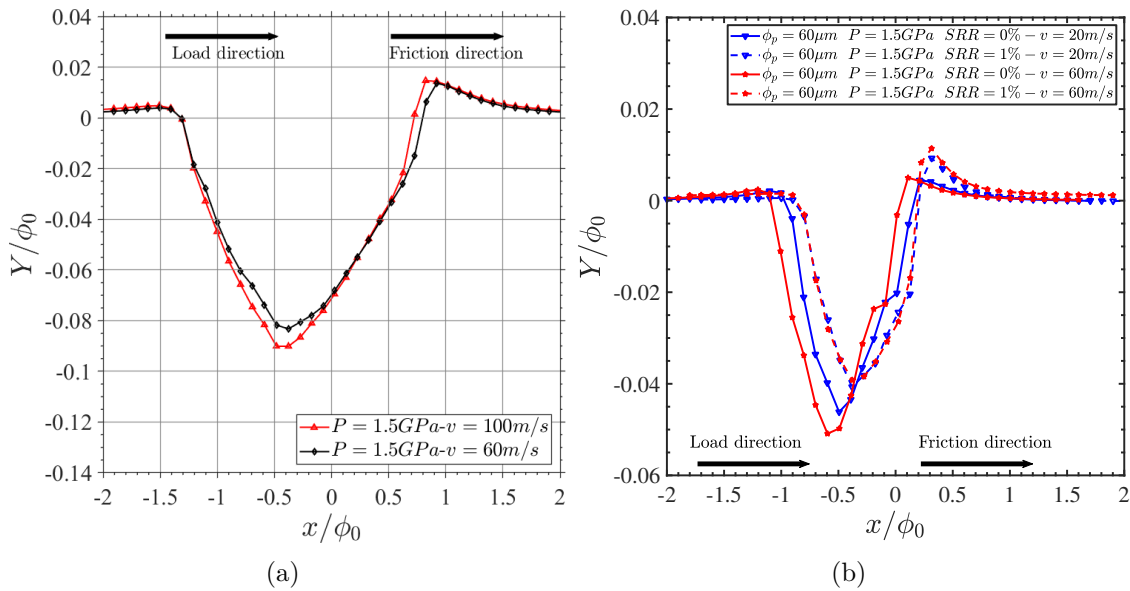
Figure 6.37: Dent profile evolution according to the velocity

6.4.11   Synthesis

In conclusion, the indentation process can be influenced by multiple parameters, and through a comprehensive study, their effects have been identified. Specifically, the load parameter has a weak influence, while the coefficient of friction, speed, and coefficient of friction have a moderate influence. On the other hand, certain parameters, such as the size and nature of the particle, presence of sliding, critical sliding, bearing material, particle shape and orientation, and the position of the particle in the contact and the residual stresses, have a significant first-order influence on the profile of the dent formed (see Table.6.4). The new parameters identified in this study are therefore the influence of the speed, the particle position, the bear-

198

ing material and the critical slip rate. An investigation was conducted to examine the impact of particle density on the results. The study revealed that the results remain consistent as long as the density ratio remains below 13. Furthermore, such lower-density ratios can significantly reduce the computation time, ranging from 30 minutes to 1 hour. Considering that computation time is a crucial aspect of this study, the subsequent sections will employ algebraic approximations to establish relationships between various parameters, facilitating faster calculations.

Table 6.4: Parameters influence

Parameter	Influence
Particle nature	+++
Particle diameter ϕ_p	+++
Particle position	+++
Particle shape	+++
Sliding	+++
Critical Sliding	+++
Bearing materials	+++
Residual stresses	+++
Friction coefficient	++
Velocity	+
Load	+
Particle compressibility	+

with

- +: Weak influence

- ++: Mean influence

- +++: High influence

A digital indentation database was established during this thesis for the purpose of implementing a meta-model. However, due to time constraints, the implementation of the meta-model could not be completed. The objective of the meta-model will be to incorporate input data distributions to predict output data by coupling with the Monte Carlo approach. The data encompasses various indentation configurations outlined in the Table.6.5 below.

6.5   Analytical approximations

In this section, we will introduce algebraic approximations to establish relationships between the key parameters identified in the previous simulations. These approximations provide convenient expressions that establish relationships between key

Table 6.5: Indentation database

Parameter	Steel/steel bearing	hybrid bearing
Different load range	1-2.5GPa	1-2.5GPa
Particle diameter ϕ_p	20-100μm	20-100μm
Particle shape	sphere	sphere
Sliding SRR	0-3.5%	0-1.5%
Particle nature	ductile $\sigma_0 = 1 - 3GPa$	ductile $\sigma_0 = 1 - 3GPa$
Particle nature	elastic $E = 100 - 500GPa$	elastic $E = 100 - 500GPa$
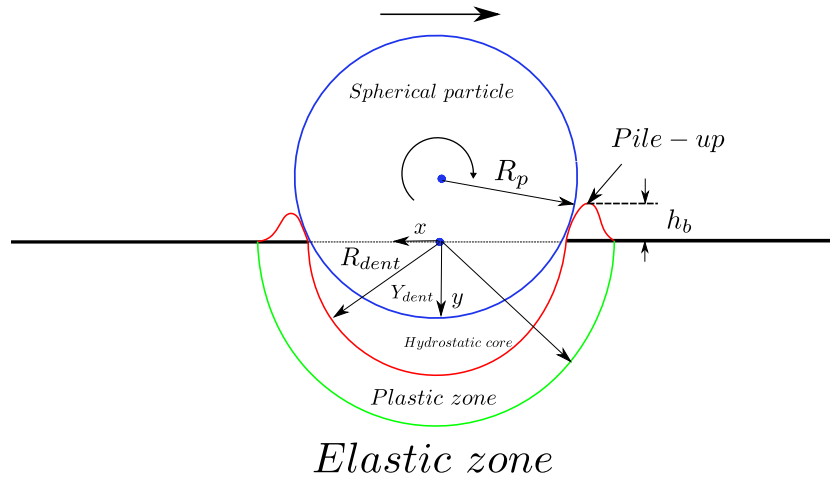
Figure 6.38: Dented zone illustration

parameters. The various analytical expressions developed in this section are applicable within an SRR (Slip-to-Roll Ratio) interval ranging from 0 to 20%.

When examining the particle crushing during rolling contact, we can represent the shape of the indentation as shown in Fig.6.38. The indentation's characteristics can be described by three parameters: the diameter of the dent, the depth of the dent, and the height of the bead. Among these parameters, the height of the bead is the most crucial, as it can lead to overstress and consequent damage when the dent is overrolled.

The geometry of dents is generally depicted by the product of a cosine with a decreasing exponential to dampen the ripples as shown in the expression below:

$$h(r) = h_p \cos(\frac{2\pi r}{4R}) \exp\left(-K\frac{r^2}{(4R)^2}\right) \tag{6.10}$$

with h_p, the depth of the dent, R, the radius of the indent, and K, the damping factor which is set to achieve the desired height of the raised area.

Numerous studies (NIK 16) have been conducted to develop algebraic approximations for first-order quantities that affect the static indentation process. In static indentation, the depth of the dent can be estimated based on the particle's radius and the radius of the dent. Its expression is as follows:

$$Y = R_p - \sqrt{R_p^2 - R_{dent}^2} \tag{6.11}$$

However, while these diverse expressions enable a depiction of the general geometry of the dent, they do not consistently ensure precision in describing the specific pile-up geometries. In order to accurately characterize this crucial parameter that dictates surface damage resulting from indentation, a new algebraic approximation will be introduced. This method will identify how the height of the raised area evolves as a function of the influential indentation parameters. The expressions introduced below are made dimensionless by considering the parameters of the nominal case of the dent (ϕ_0, b_0, h_0). Using dimensionless quantities removes the dependency on specific dent or particle sizes, allowing for a more generalized analysis. These normalized expressions enable a comprehensive understanding of the dent's profile and potential consequences during rolling contact, independent of specific dimensional values.

6.5.1 Dent diameter approximations

Various indentation simulations were conducted in the presence of ductile and elastic particles, and measurements of the dent's diameter were performed. As a result, algebraic approximations can be applied to follow the changes in the dent's diameter based on the operating conditions and the characteristics of the particle involved in the contact. To determine the diameter of the dent after the crushing of a ductile particle, the following expression, which depends on the half-width of contact and the diameter of the particle, has been proposed:

$$\phi_{dent} = 1.9 \frac{b}{b_0} \phi_p (1 + 0.1 SRR) \tag{6.12}$$

For an elastic particle, this expression is given by:

$$\phi_{dent} = 1.1 \frac{b}{b_0} \phi_p (1 + 0.1 SRR) \tag{6.13}$$

The contact half-width of the simulated case, denoted as b is compared to the half-width of the reference case, denoted as $b_0 = 133 \mu m$.

6.5.2 Sliding rate evolution approximations

As discussed earlier in this chapter, during particle crushing, according to the operating conditions and the particle size, a critical sliding rate exists at which the height of the bead reaches its maximum. The simulation results (for example in Fig.6.17) show how the critical slip rate changes concerning both the ductile particle diameter and the contact half-width. An algebraic approximation of this sliding rate is provided by the expression below:

$$SRR_c = 4.6 \frac{\phi_p}{b} \tag{6.14}$$

Its evolution with diameter is presented in Fig.6.39
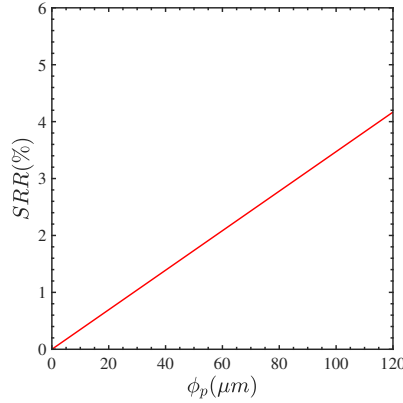
Figure 6.39: SRR evolution with the particle diameter for a steel bearing in M50NiL and $b = 133\mu m$.

6.5.3   Pile-up height approximations

The simulation results revealed that the size, position, shape of the particle, the presence of sliding, elastic properties of the materials (leading to the contact half-width), and plastic properties are the primary parameters influencing the height of the bead. Consequently, an algebraic approximation of the bead height's evolution as a function of these parameters has been proposed, specifically for iso-plastic properties for a spherical shape. In the case of pure rolling, the evolution of the bead height of a ductile particle in steel can be approximated using the following expression:

$$h_b = \frac{4}{3}\left(\frac{\phi^{1.9}b^{0.1}}{98\phi_0}\right) \tag{6.15}$$

To depict the evolution of the bead height as a function of parameters, one of the selected functions is $\frac{x}{(x+\text{cste})^2}$. This function can capture the bell-shaped behavior characterizing the particle's evolution based on the given parameters. The choice of this function is based on its ability to accurately represent the variation in height relative to the parameter variability. The pile-up height evolution for a ductile particle, considering various parameters, can be approximately represented by the following expression:

$$h_b = h_0\left(\frac{\phi}{\phi_0}\right)^{1.9}\left[1 + \frac{19.45 * SRR}{\left(SRR + 4.6\frac{\phi}{b}\right)^2}\right] \tag{6.16}$$

In the case of elastic particles where the height of the bead constantly evolves with sliding, the previous function proposed is no longer suitable. the evolution of the bead height in this case can be given by:

202

$$h_b = h_0 \left(\frac{\phi}{\phi_0} \right)^{1.6} \left[1 + \frac{1.32 \mid SRR \mid^3}{\left(\mid SRR \mid + 4.6 \frac{\phi}{b} \right)} \right] \qquad (6.17)$$
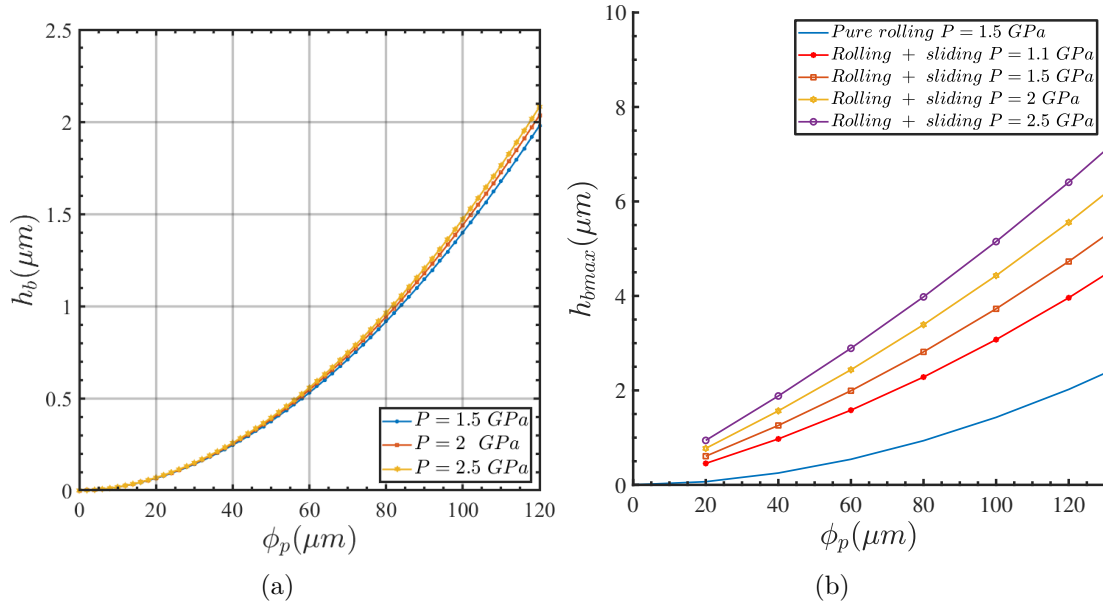
Figure 6.40: Pile-up height evolution (a) according to the particle diameter in pure rolling condition, (b) according to the particle diameter in rolling/sliding condition.

Figure.6.40(a) illustrates how the pile-up height changes with the diameter of the particle under pure rolling conditions. It becomes evident that the analytical approximations indicate a weak impact of the load on the pile-up height evolution.

Figure.6.40(b) shows an evolution of the height of the bead as a function of the diameter of the particle in rolling+sliding condition. It, therefore, emerges that in the presence of slip, the load has a more pronounced influence on the evolution of the pile-up height.

The approximations for the pile-up height evolution concerning the slip rate have been validated in both ductile and elastic particle scenarios. A good agreement has been observed between the approximations and the corresponding numerical results. This indicates that the approximations accurately capture the behavior of the pile-up height for both ductile and elastic particles.

6.5.4 Dent depth approximations

The indentation depth is a variable that relies on both the particle's size and the loading conditions. It can be estimated for a ductile particle using the following
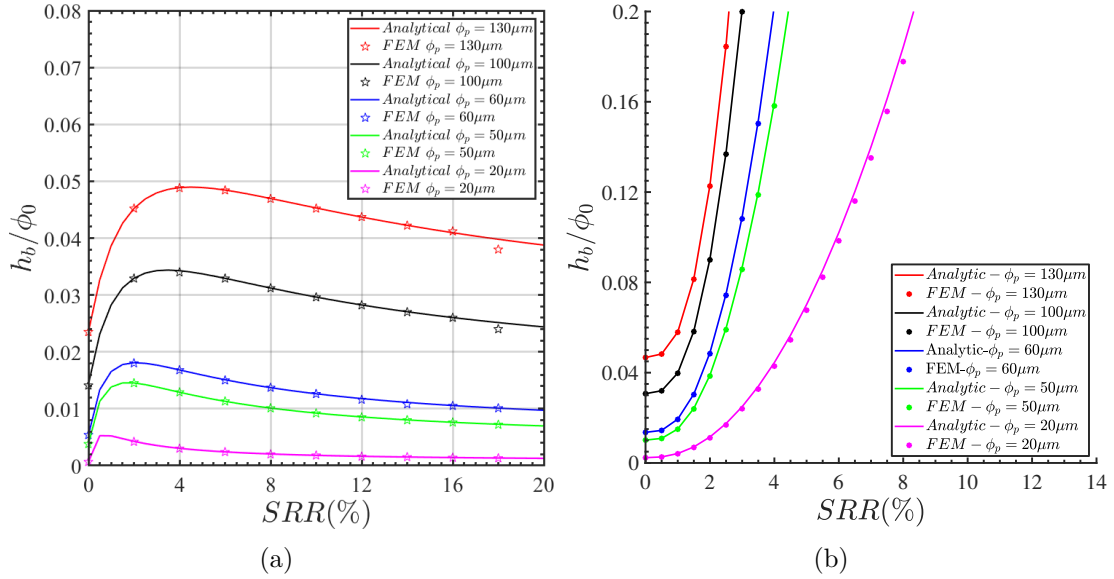
Figure 6.41: Validation of the anaytical expressions with the numerical results of the maximum pile-up height evolution with SRR (a) for a ductile particle (b) for an elastic particle.

approximation:

$$Y_{dent} = \phi_{dent} \frac{b^{1/4} \phi_p^{3/4}}{b0} \left(4.3.10^{-2} - 0.4.10^{-2} * SRR \right) \tag{6.18}$$

The dent's depth of an elastic particle can be given by:

$$Y_{dent} = \phi_{dent} \frac{b^{1/4} \phi_p^{3/4}}{b0} \left(0.031 * SRR^2 - 0.018 * SRR + 0.43 \right) \tag{6.19}$$

6.5.5 Particle harmfulness criteria

Dwyer-Joyce (DWY 92) formulated a criterion for assessing the penetrability of debris in a rolling contact, which asserts that the ability of a particle to penetrate depends on factors like the coefficient of friction and the geometry of the contacting components. In this section, we introduce criteria to assess the harmfulness of dents caused by suspended particles in the lubricant. These criteria help determine whether or not a particle possessing the mechanical properties required to create a dent in a rolling contact will result in dents with significantly higher pile-up heights or not. Through simulations involving various particle sizes as presented in Fig.6.42, we identified a critical size threshold. Beyond this threshold, particles undergo a laminating process, resulting in the particle enduring the maximum impact. These conditions vary based on the specific particle types.
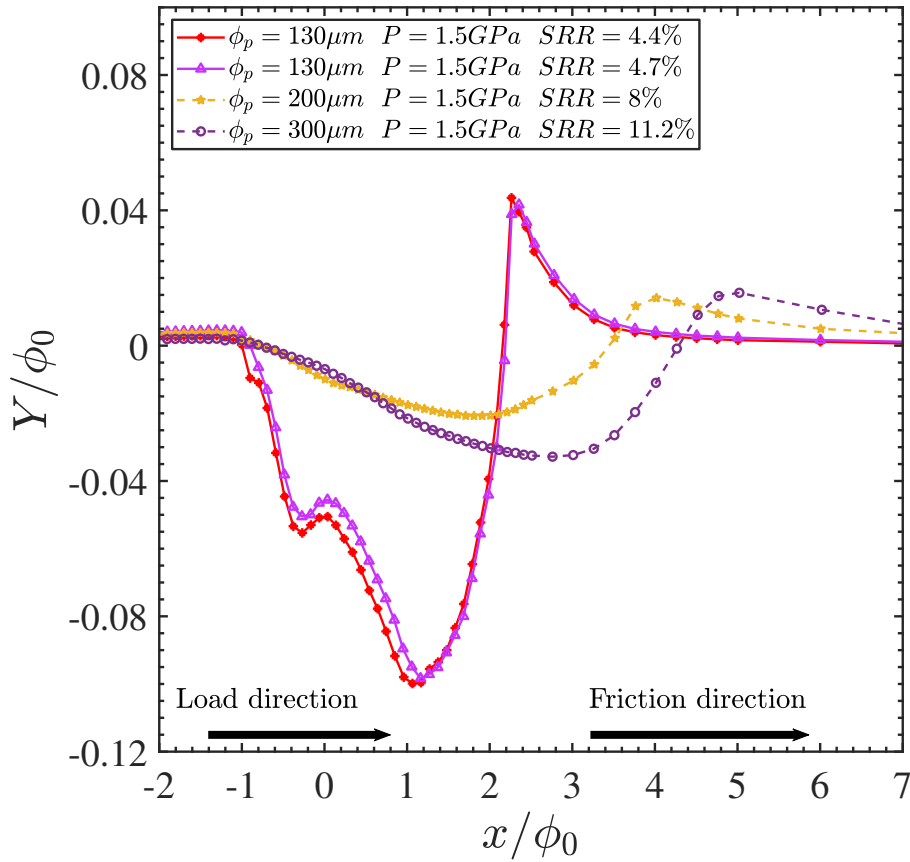
Figure 6.42: Dent evolution in fonction of the particle size and the sliding in M50NiL bearing contact (contact half-width $b = 133\mu m$) with particle in M50NiL

6.5.5.1 Ductile particle harmfulness criteron

For a ductile particle, the criterion for determining its harmfulness in relation to its geometry is as follows:

$$\frac{\phi_p}{2b} \le 1 \tag{6.20}$$

In this configuration, the dents formed will exhibit a greater bead height under iso-operating conditions. This is because the particle undergoes a complete crushing in the contact. When this ratio exceeds 1, the particle enters a laminating phase, wherein it bears the effects of indentation, thereby reducing the size of the dents on the raceway.

6.5.5.2   Elastic particle harmfulness criteron

When dealing with an elastic particle, the criterion for assessing its harmfulness based on its geometry is outlined as follows:

$$\frac{\phi_p}{2b} \leq \frac{1}{2} \tag{6.21}$$

Once again, when this ratio exceeds 1/2, the particle enters a laminating phase, wherein it bears the effects of indentation, thereby reducing the size of the dents on the raceway.

6.6   Modeling indentation in presence of lubrication

This section will introduce a model for particle crushing in the presence of lubrication.

6.6.1   Lubricant modeling

Incorporating the lubricant, which acts as a fluid capable of flowing through the contact area, involves the implementation of an Eulerian domain governed by a specific state law. To achieve this, the Coupled Eulerian Lagrangian' (CEL) modeling approach will be employed once again. This approach entails overlaying two Eulerian volumes, as shown in Fig.6.43,B.11, one for the particle and the other for the lubricant, the second subjected to the same loading conditions. Notably, the modeled lubricant volume remains unconstrained, allowing for free movement. It's important to note that, in this particular modeling, certain aspects, such as viscous behavior, glass transition, and thermal considerations, still need to be factored in. Consequently, the governing state law for fluid flow within the contact area will be that of Hugoniot.
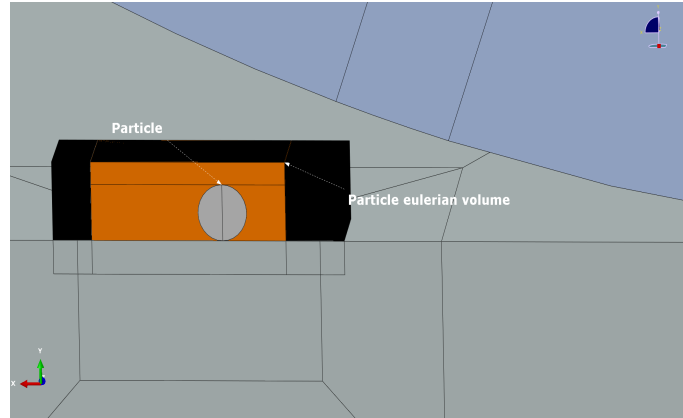
Figure 6.43: Superposition of two eulerian volume of particle and lubricant.

6.6.2 Linear $U_s - U_p$ Hugoniot form

The energy conservation equation relates the increase in internal energy per unit mass (E_m) to the rate of work done by stresses and the rate of heat addition. In the absence of heat conduction, the equation takes the form:

$$\rho \frac{\partial E_m}{\partial t} = (p - p_{bv}) \frac{1}{\rho} \frac{\partial \rho}{\partial t} + S : \dot{e} + \rho \dot{Q} \tag{6.22}$$

Where:

- p is the pressure stress (positive in compression)

- p_{bv} is the pressure stress due to bulk viscosity

- S represents the deviatoric stress tensor

- $\dot{e}$ is the deviatoric part of strain rate

- $\dot{Q}$ stands for the heat rate per unit mass

The equation of state defines pressure (p) as a function of current density (ρ) and internal energy per unit mass (E_m):

$$p = f(\rho, E_m) \tag{6.23}$$

This equation characterizes all attainable equilibrium states within a material. Eliminating E_m from the equation leads to a relationship between pressure (p) and volume (V), known as the Hugoniot curve. This unique curve describes achievable PV states behind shock waves. The linear relationship between the linear shock velocity (U_s) and the particle velocity (U_p) is defined as follows:

$$U_s = c_0 + sU_p \tag{6.24}$$

Here, s represents the coefficient that determines the linear relationship between the shock velocity and the particle velocity. This relationship describes the behavior of shock waves and their effect on particle velocities. With the above assumptions the linear Hugoniot form is written as:

$$P_H = \rho_0 c_0^2 \eta \left(1 - \frac{\Gamma_0 \eta}{2}\right) + \Gamma_0 \rho_0 E_m \tag{6.25}$$

This equation provides a description of the Hugoniot curve under certain conditions, involving the elastic bulk modulus ($\rho_0 c_0^2$) and other material properties. With c_0 ranged from 1.0 to 1.6, Γ_0, ρ_0 parameters that need to be set in the model.

A limiting compression, described by the denominator in the equation of state, is given by:

$$\eta_{lim} = \frac{1}{s} \tag{6.26}$$

At this limit, a tensile minimum occurs; beyond this point, negative sound speeds are calculated for the material.

(a)	(b)
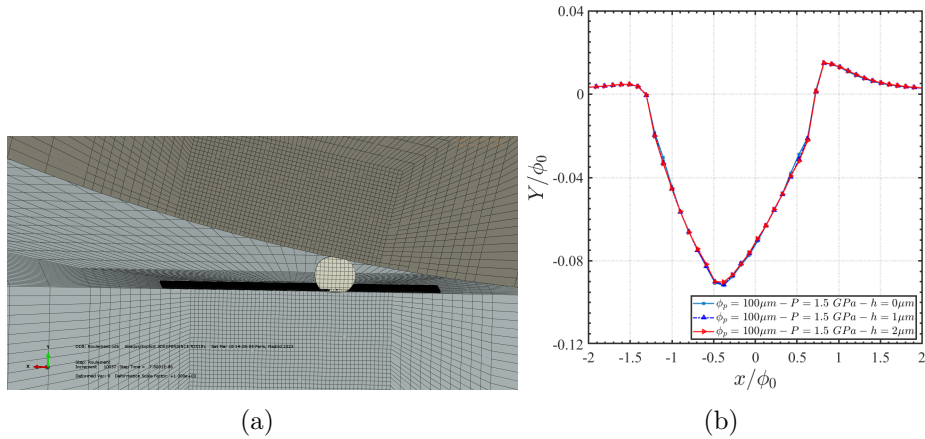
Figure 6.44: Lubricant passage in the denting contact (a) denting in presence of lubricant of thickness $e = 2\mu m$ in CEL model, (b) dent profile evolution according to lubricant thickness .

Figure.6.44(a) illustrates the process of particle crushing within a rolling contact environment in the presence of lubricant. The lubricant's effect is to diminish the depth of indentation and the size of the bead formed by the particles. However, at the current modeling stage, the lubricant's influence on the indentation profile still needs to be substantial, as the modeling still needs to be completed and comprehensive enough to capture its full impact, as illustrated in Fig.6.44(b).

Experiments focused on indentation in the presence of lubrication have yielded significant findings. When the dent is small, such as with a depth of 0.1 μm, any

surface irregularities are mitigated by the compression of the contacting surfaces. Consequently, the pressure remains relatively unaffected as the dent traverses the surface (as depicted in Fig.6.44(b)). However, as the dent's depth and the bead's height increase, the deformation of the surfaces becomes insufficient to compensate for the geometric irregularity. This leads to a modification in the distribution of pressure.

There is an observable correlation between the height of the indentation pads and the magnitude of the pressure peak they generate. This relationship aligns with findings from dry contact scenarios, where similar trends were previously noted. Hence, it becomes crucial to thoroughly investigate the progression of this bead height, alongside the factors and variables that impact its development, both in the context of indentation and fatigue analysis.

6.7 Conclusion

In this chapter, a comprehensive finite elements modelization of the indentation process has been executed, utilizing the CEL model developed by Bonetto. This model enables the application of an Eulerian approach for regions with substantial deformation and a Lagrangian approach for regions with minor deformations. Following this, an exhaustive parametric investigation was undertaken to discern the primary parameters that influence the dent's geometry.

The analysis has revealed that several significant parameters impact the dent's geometry. These include the particle's nature and diameter, the bearing materials, the presence of sliding, the existence of a critical indentation value, the particle's shape and orientation, the position of the particle within the contact area, and the presence of residual stresses. All these influential factors must be considered to enhance the accuracy of bearing lifespan estimation.

The impact of load on the denting process is minimal when indentation is present, particularly within the load ranges typical of aeronautical applications. The presence of slip exacerbates the formation of dents, and this aggravating effect is particularly pronounced when the slip occurs around the critical value for a ductile particle. We have also successfully identified the specific areas prone to damage around the dents:

- When subjected to rolling, all damage occurs downstream in the rolling direction.

- In sliding scenarios, damage is consistently observed downstream in relation to the frictional forces.

To reduce calculation costs, analytical expressions linking the most influential parameters have been developed.

Chapter 7

Rolling contact surface fatigue

This chapter focuses on the fatigue and life of surfaces in contact after indentation. When a surface is indented, fatigue can occur due to the formation of cracks that propagate until the surface spalls, which can ultimately lead to component failure. This chapter aims to identify the mechanisms that cause fatigue cracks to appear due to the presence of the fault. To achieve this, a semi-analytical tool simulates rolling cycles on indented surfaces. Several fatigue criteria are compared to determine which is most effective in locating the zones where cracks initiate at the edges of the indents. The study reveals that the formation of cracks is based on shear mechanisms, and the direction of the slip defines their location. Based on the results of this comparative study, a new criterion is developed by modifying the Dang Van II criterion. The parametric study that began in the previous chapter is continued, this time applying the new criterion to surfaces indented with the CEL pattern. The most critical parameters that influence the lifetime of indented surfaces are bearing load, slip, and the height of the beads.

Sommaire

7.1 Introduction

This chapter is dedicated to investigating fatigue in surfaces featuring irregularities. The aim is to uncover the underlying mechanisms that lead to premature fatigue in the presence of these irregularities. To achieve this goal, a simulation of rolling cycles on surfaces with indents will be conducted using the semi-analytical contact calculation tool introduced earlier. The modified Dang Van criterion, as adapted by Bonetto, will be employed to pinpoint sites of damage. Building upon the endurance limit findings established by Jacq's work, a damage criterion will be formulated using the analytical expressions developed in this study. The analysis will rely on key parameters, such as residual stresses,size and nature of debris, bearing materials, sliding, critical SRR and bead height, identified as first-order factors. A summary of the various fatigue criteria is provided in the appendix.C.

7.2 Presence of dent on the raceway

The presence of a dent on the raceway within a rolling contact can significantly compromise the functionality and longevity of the component. Dents introduce localized stress concentrations, which in turn can initiate and propagate fatigue cracks. Furthermore, they disrupt the uniform contact between rolling elements and the raceway, leading to heightened friction and wear. In severe cases, dents may even cause rolling elements to dislodge from the raceway, resulting in catastrophic component failure and potential engine shutdown. Consequently, meticulous inspection for dents and their appropriate management is essential to avert potential failures.

Empirical investigations carried out by Ville (VIL 98a), Ville and Nelias (VIL 98b; NEL 00), Jacq et al. (JAC 02; TON 12a) have underscored the influence of contact conditions. Their research has highlighted that the presence of slip between contacting surfaces can notably curtail the fatigue life of these surfaces. This is attributed to the elevated shear stresses induced by slip at the edges of indents, culminating in crack initiation and subsequent surface spalling and failure.

Accumulation of plastic deformation over successive rolling cycles emerges as a prominent contributor to micro-spalling and surface spalling. Xu et al. (XU 97; XU 98) have associated this phenomenon with cumulative plastic deformation in the region. They have proposed a damage model grounded in this accumulation to elucidate the chipping observed at dent edges. Likewise, other researchers, such as Warhadpande et al. (WAR 10; GOL 19), have also employed damage models to study fatigue on indented surfaces. These models aid in comprehending the mechanisms driving fatigue and can be utilized for prognosticating the component's fatigue life.

The presence of dents on surfaces can induce fatigue through distinct mechanisms. One such mechanism is micro-spalling as shown in Fig.7.1, arising from

212
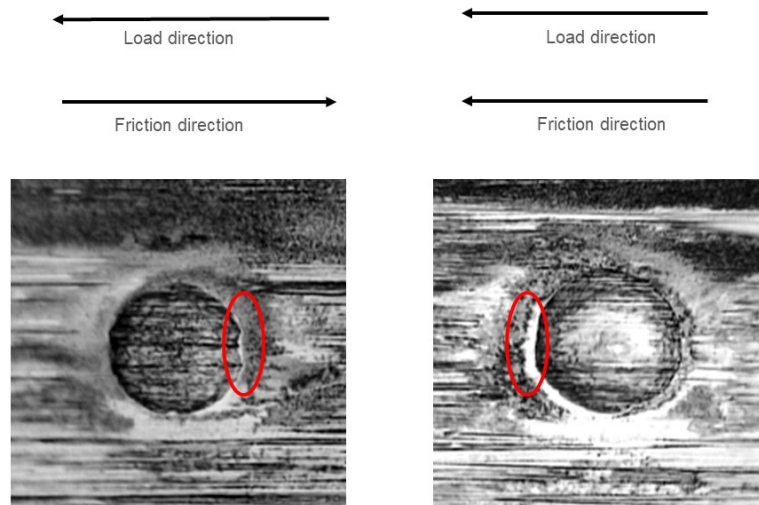
Figure 7.1: Influence of sliding direction on the area where micro-chipping becomes apparent around the indentation in cases of negative slip and positive slip as shown in (NEL 00)

plastic deformation of the material, while the other is spalling induced by the emergence and propagation of cracks that lead to material tearing as presented in Fig.7.2. These cracks can propagate in various orientations, including the direction of friction and the opposite direction. The latter form of cracking has been documented by researchers like Diab et al.(DIA 03; TON 12a) , and Morales-Espejel et al. (MOR 15a). These cracks typically form at an angle between 30° and 45° with respect to the surface, often resulting in a "V-shaped" spalling pattern. However, these values still surpass the experimentally observed range of 30° to 45°, as shown in Figs.7.3, and 7.4. Far from the surface, a reduction in the angles to around 30° is noted with only a minor increase in depth, typically a few tens of micrometers, which is in good agreement with the literature.

7.3   Fatigue analysis

During the initial load passages over the dent, plastic deformations occur, leading to significant modifications in geometry. Notably, the evolution of geometry modification during the initial cycles depends on the type of loading and material poperties. For instance, a pure rolling load results in a uniform reduction in bead height around the dent. Conversely, the introduction of slip induces an attenuation of the upper portion of the bead in the direction opposite to friction. In this study, the geometry of the dents created in Isaac was subjected to only two rolling cycles. Literature
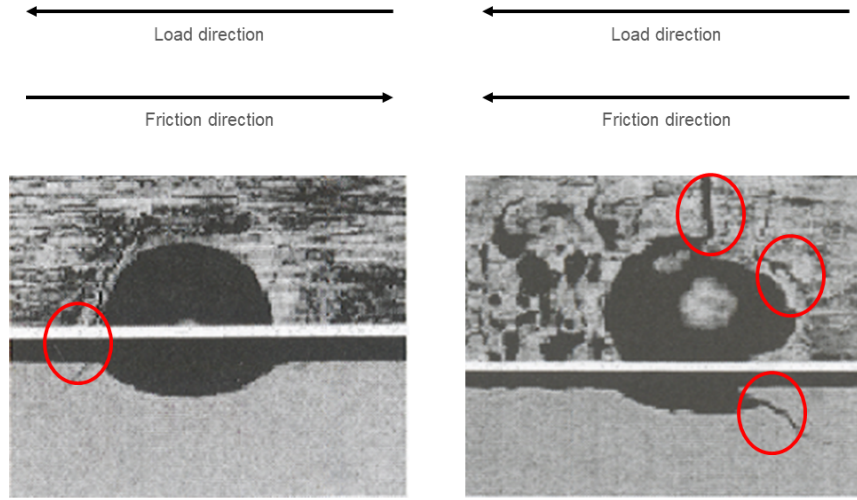
Figure 7.2: Influence of sliding direction on the side where cracks manifest around
the indentation during negative sliding and positive sliding (DIA 03) .

indicates that the height of the bead stabilizes rapidly at the end of the second cycle
with an isotrope hardening and relatively moderate loading, as depicted in Fig.7.6.

Consequently, when the load rolls over the indent, a slight reduction in indent
height becomes noticeable, particularly in the case of a steel-steel bearing. The
variation in height until stabilization amounts to roughly 92% of its initial height.

Existing literature indicates that this stabilization typically occurs after 2 to
3 cycles. In this study phase, the modified Dang Van type criterion, developed
by Bonetto (BON 20), is applied to rolling cycles on dents under rolling/sliding
conditions. Its expression is given by:

$$\sigma_{eq} = \max\left\{\tau_{pr}(t)\right\} + \alpha\Delta\sigma_n \tag{7.1}$$

The efficacy of a criterion in the context of this fatigue problem is assessed based
on its ability to predict the emergence of micro-cracks observed in existing litera-
ture, notably the work of Diab et al. (DIA 03). Thus, the quest is for a criterion
that effectively identifies the sites where these cracks initiate and, when possible,
accurately indicates the orientation of the critical plane. In this context, $\Delta\sigma_n$ repre-
sents the magnitude of the stress component normal to the plane defined by $\tau_{pr,max}$.
It is important to note that τ_{pr} is calculated using the principal directions, which
result in two orthogonal planes. The critical plane, crucial for maximizing the crite-
rion, is determined from these two planes, selecting the one where the normal stress
amplitude is highest.

Employing the term τ_{pr}, which relies on the alternating portion of the deviatoric
tensor, and incorporating the stress amplitude term normal to the plane eliminates

214
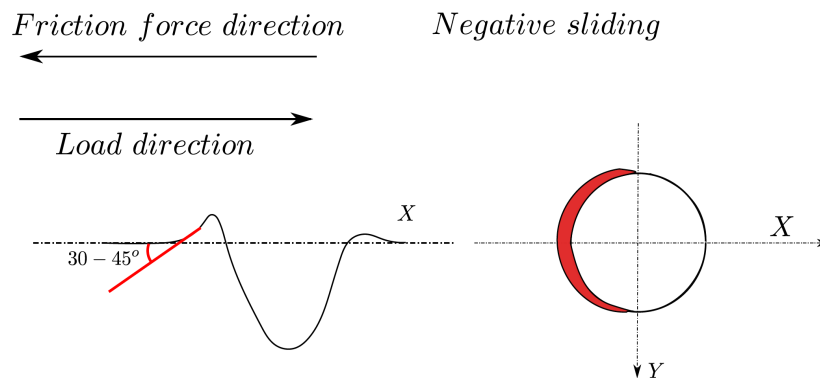
Figure 7.3: Definition of rolling and friction directions, along the zones where negative sliding and cracks occur.
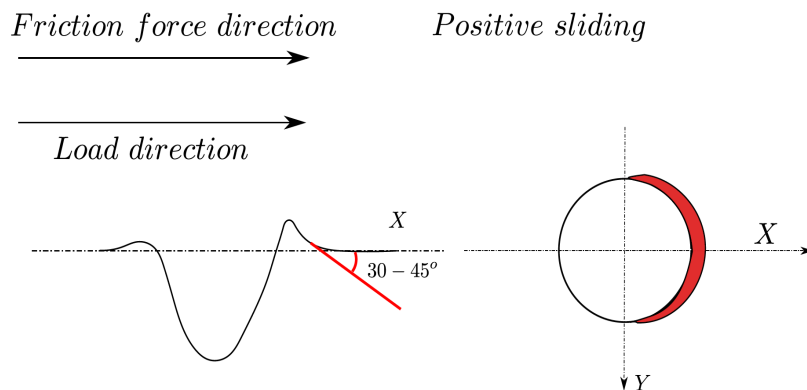
Figure 7.4: Definition of rolling and friction directions, along the zones where positive sliding and cracks occur.

the residual stresses originating from the indentation from the criterion calculation. It is crucial to underline that while residual stresses do not directly participate in the criterion computation, they still exert an influence on fatigue behavior. This is because their presence alters the initial phase of surface interaction and thus modifies the loading cycles during indentation.

Given the similarity of the new criterion formulation to Dang Van II criterion.(VAN 84; VAN 89), the constant α is adopted from the works of Morales-Espejel and Brizmer (MOR 11a), specifically $\alpha = 0.232$.
The Dang Van modified criterion identifies the edges of the dent as the most vulnerable regions. Interestingly as despicted in Fig.7.7 The sliding direction does not alter the location of the critical edge; it remains consistently positioned at the exit edge, aligned with the load's passage direction, where the highest criterion values concentrate. Positive slip significantly amplifies the criterion values on the entry edge, yet these values do not approach those obtained on the exit edge. This con-
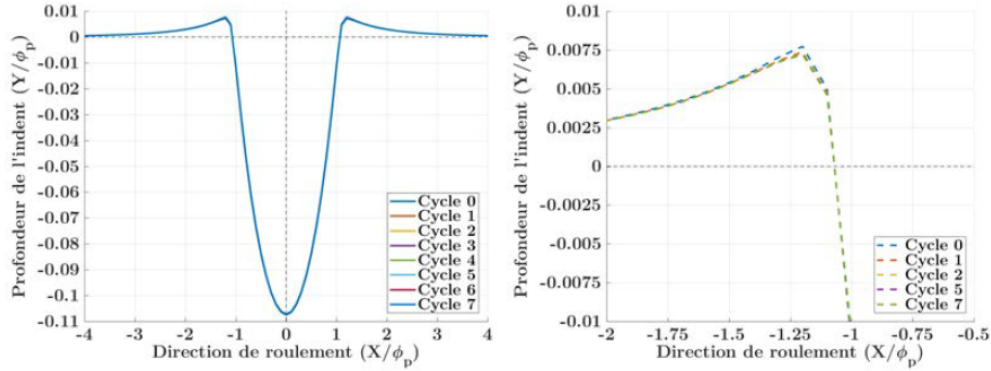
Figure 7.5: Evolution in the dent profile over the initial rolling cycles after indentation under in conditions of pure rolling (BON 20)
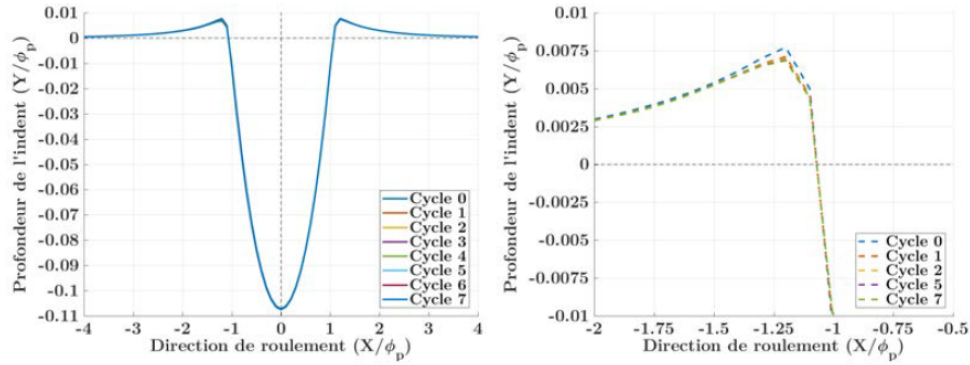
Figure 7.6: Evolution in the dent profile over the initial rolling cycles after indentation under in positive slip condition with a coefficient of friction $\mu = 0.1$ (BON 20).

sistent localization of the critical edge can be attributed to geometric distinctions between natural and artificial indents. Notably, the natural indent features an exit bead that is 3.7 times more pronounced than the entry bead. The examination of the critical planes identified by the criterion reveals a stronger alignment with experimental observations compared to earlier criteria. This is presented in Fig.

Hence, Figure.7.7 illustrate the regions where crack initiation occurs on the indent, as identified by the modified Dang Van criterion. The fatigue criteria utilized might not inherently consider the gradient effect caused by contact. In fact, these criteria are also susceptible to the influences of the criterion's parameters, which facilitate accurate prediction of critical planes and fatigue initiation zones.

So, Figure.7.7 depicts the evolution of damage around the dent and the location of crack initiation sites as a function of the number of cycles. For Figure.7.7, the calculations were conducted under pure rolling and rolling+sliding conditions with an outlet pile-up height of 3 times the inlet pile-up, resulting in a total number of cycles of 1230 under the considered operating conditions.

(a)   (b)
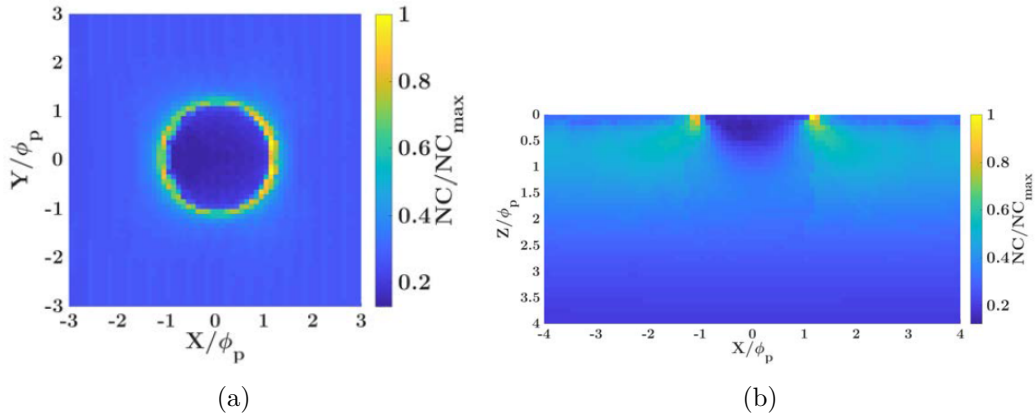
Figure 7.7: Application of the modified Dang Van criterion to an axisymmetric dent in positive sliding condition (BON 20).

7.4   Damage criterion

In this section, we focus on investigating the influence of indentation parameters on the determined endurance limit denoted as H_{1I} in the work by Jacq et al (JAC 03). To accomplish this, we have observed that the variation of H_{1I} exhibits a monotonic trend with the average slope of the dents s. This parameter, s, is defined as the ratio of the depth of the indent to its radius. Consequently, the expression for the average slope of the dent is given by:

$$s = \frac{Y_{dent}}{R_{dent}} \tag{7.2}$$

When a particle impacts the surface of the bearing, the resulting dent can be represented as shown in Fig.7.8.
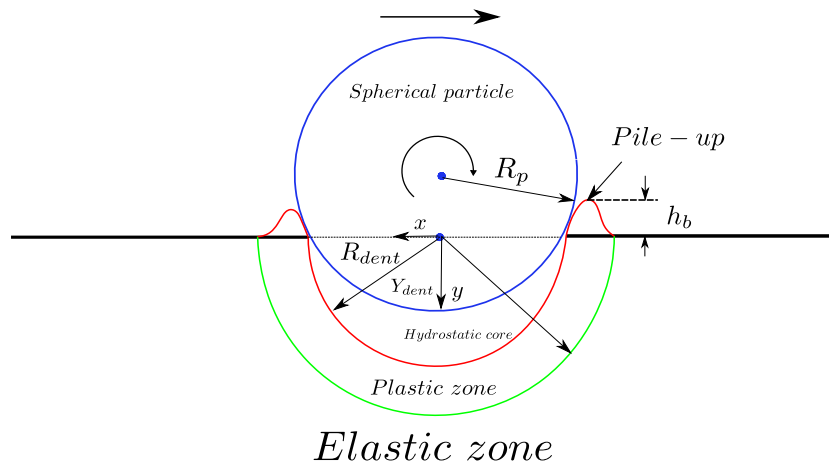
Figure 7.8: Dented zone illustration.

The lower limit of the rolling fatigue endurance threshold is attained when a specific point within the loaded blocks experiences a shear stress greater than the material's micro-elastic limit while the rolling body passes. Beyond this threshold, accumulated dislocations are likely to lead to damage.

The maximum load a contact can bear (expressed as the Hertz pressure of a smooth contact) without exceeding the micro-yield limit while considering potential overstresses and variations in the material's micro-elastic limit defines the lower boundary of the endurance limit referred to as H_{1I}.

For a smooth cylinder/plane or sphere/plane contact in pure rolling with a homogeneous material and no inclusions, H_{1I} is the Hertz pressure generating maximum shear stress equal to the micro-elastic shear limit:

$$H_{1I} = \frac{\tau_0}{3} \tag{7.3}$$

When inclusions are present, the overstress magnitude hinges on inclusion shape and mechanical properties relative to the matrix. Consequently, for each inclusion-matrix pairing, a unique H_{1I} value is determined by placing the inclusion in the most unfavorable position. In cases of pure rolling smooth contact on surface-treated steel, this unfavorable position typically coincides with the Hertz depth.

Furthermore, considering spherical inclusions, Lamagnére (LAM 96) identified the most harmful inclusions in M50 steel (like aluminas, with an overstress factor of 1.38). He calculated the value of H_1 for pure rolling smooth contact, amounting to 1.72 GPa at $100°C$.

Now, let us examine the scenario of nitrided 32CrMoV13 steel under smooth contact stress. The micro-elastic limit varies with depth due to the material's characteristics. Moreover, the residual stress distribution alters the stresses originating solely from the pressure field. Consequently, it becomes essential to compare the maximum shear stress at each micro-yield point meticulously. The shape of the shear stress profile and its compatibility with the micro-elastic limit profile are contingent upon the equivalent radius of the contacting bodies, denoted as R_{eq}.

Furthermore, the presence of a dent in the contact introduces localized pressure surges that trigger overstresses within the space. Additionally, the indentation procedure engenders substantial residual stresses and strengthens the material around the dent, subsequently modifying the stresses due to contact pressures only, as well as the micro-elastic limit of the material.

By considering the freshly indented state as the new initial condition prior to the passage of the rolling body over the indentation, H_{1I} can be defined as the maximum load (expressed by the maximum pressure of the smooth contact) for which the transfer of load onto the indentation does not lead to any breach of the micro-yield limit.

Based on the mechanical characterization made in this study and the simulations conducted for the creation of dents on the four steel grades M50, M50NiL, 32CrMoV13, and M50NiLDH, a clear trend emerges as presented in Fig.6.8. As discussed in the previous chapter.2 and 6, M50NiLDH exhibits the highest elastic limit

218

and, consequently, the highest indentation resistance among the various steel grades, followed by M50NiL, 32CrMoV13, and M50. The endurance limit of M50NiLDH is notably higher compared to that of M50NiL as illustrated in Fig.2.14. In turn, the endurance limit of M50NiL surpasses that of 32CrMoV13, and similarly, the endurance limit of 32CrMoV13 is higher than that of M50. This observation aligns well with the findings of Jacq et al., who also demonstrated that the endurance limit of 32CrMoV13 exceeds that of M50 as illustrated by (JAC 01) in Fig.7.9.

(a)   (b)
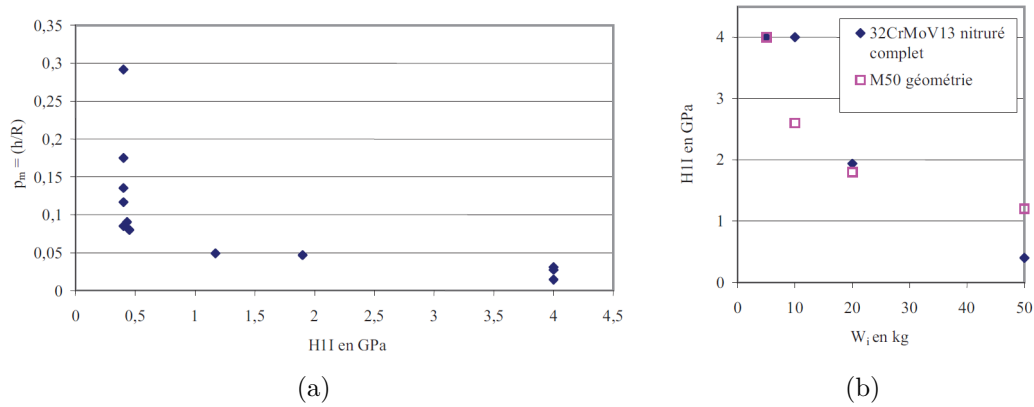
Figure 7.9: (a) Evolution of the average slope according to H_{1I}, (b) Influence of the material properties on the limit endurance of H_{1I} (JAC 03).

7.5 Indented contact life

To evaluate material resistance, this analysis employs bead heights that have not undergone cyclic passage of the dent. The average slope, denoted as s, can be defined as the quotient of the depth of penetration, h_{dent}, and the radius of the dent, R_{dent}. When sliding occurs, the particle spreads within the contact, resulting in a broader and shallower indent, mainly characterized by an increased bead height. Consequently, it becomes essential to modify the expression to incorporate the effect of sliding for ductile particles. For such particles, the average slope can be approximated using the following expressions:

$$s = \frac{Y_{dent}}{R_{dent}} \exp\left(\frac{\phi_{dr}}{\phi_{drs}} - 1\right) \tag{7.4}$$

$$s = 2\frac{\phi_p^{3/4} b^{1/4}}{b_0}\left(4.3.10^{-2} - 4.10^{-3} SRR\right)\exp\left(\frac{\phi_{dr}}{\phi_{drs}} - 1\right) \tag{7.5}$$

where ϕ_{drs} is the dent diameter created in rolling+ sliding condition while ϕ_{dr} would be the dent diameter in pure rolling condition.

219

Using the experimentally determined endurance limit by Jacq as a reference, it becomes evident that indents with an average slope equal to or exceeding 0.05 will exhibit a notably low endurance limit (<0.4GPa), thus leading to surface damage. Therefore, this value, leading to a drastic reduction in the endurance limit of the bearing materials, will be regarded as a threshold value, thus defining the domain of damage and non-damage based on the size of the surface defect created. Figure.7.10 illustrate the trend of the average slope in relation to the particle diameter and the half-width of contact, which characterizes the loading conditions. With slip levels in aeronautical bearings typically around 2%, it can be observed that under these circumstances, the average slope for M50NiL remains below 0.05 for particle diameters up to 40 μm. Consequently, for this particle size, the curve delineates the slope's behavior for varying values of the half-width of contact b. Hence, the key factors driving the damage will be the particle size and the contact size determined by the operating conditions. These results show of what occurs in the bearing surface in presence of a ductile particle with properties very close to steel.
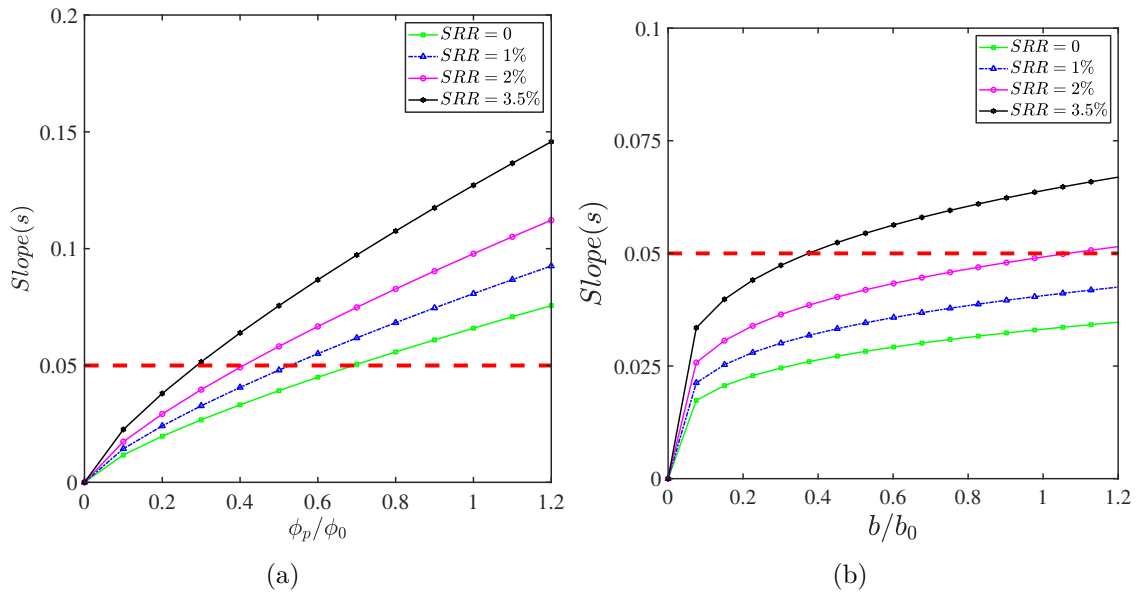
Figure 7.10:   Average slope evolution on ductile particles and M50NiL steel (a) with the particle diameter for $b = 133\mu m$ (b) with the contact half-width for a particle of diameter $\phi_p = 40\mu m$.

In the case of elastic particles, the supported particle sizes encompass very fine particles, and damage would occur rapidly even with 10 μm diameter particles, as shown in Fig.7.11. This approach to modeling hard particles holds certain limitations, as it doesn't incorporate their elastic limit or the subsequent rupture phenomena.

These results demonstrate the harmful effects of hard particles on the bearing's

lifespan. The harder the particle, the more abrupt the reduction in the material's endurance limit will be, compared to the case of a ductile debris.

The analyses conducted on hybrid bearings reveal a significant increase in the bead height as shown in Figs.6.30,6.31. In the presence of hybrid bearings, the heights of the dents resulting from particle crushing are increased. For instance, during the passage of a ductile M50 particle with a diameter of 100 μm in a hybrid rolling contact between M50NiL and Si_3N_4, the identified average slope is 0.3, up to the threshold of 0.05. which is above the threshold of 0.05. So the bearing gets damaged in such situations. For ductile particles, the size that the hybrid bearing can withstand in the presence of a slip around 2% is around 30 μm or less.

In the case of an elastic particle with a diameter of 100 μm and a loading level of 1.5 GPa in our operational conditions, the average rolling slope is approximately 0.75, accompanied by bead heights around 5 μm. The critical bead height to achieve an average slope of 0.05 is approximately 0.6 μm. Therefore, in a pure rolling scenario, the hybrid bearing can only support particle sizes less than or equal to 40 μm. Consequently, in a hybrid bearing, the impact of a particle, even if it's ductile, can quickly result in relatively high bead heights, damaging the bearing (see Fig.6.30). Therefore, the use of hybrid bearings should require a high level of cleanliness, thorough particle cleaning, and suitable particle control to mitigate bearing damage. An alternative approach could involve reducing the rolling element load or increase components dimensions, thereby lowering the risk of damage.
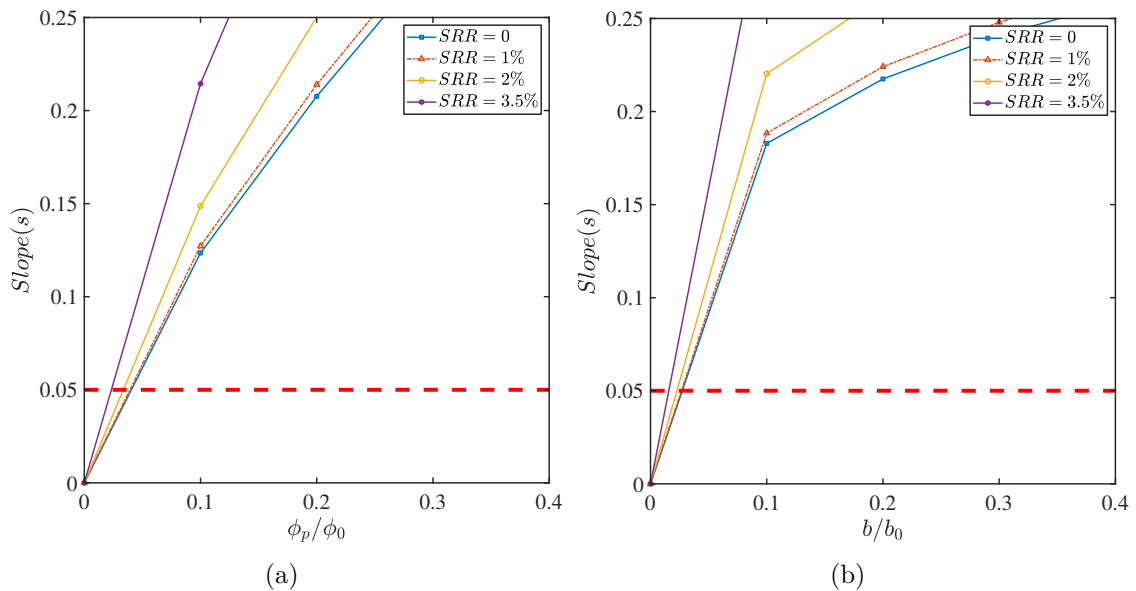
Figure 7.11: Average slope evolution on elastic particles and M50NiL steel (a) with the particle diameter for $b = 133\mu m$ (b) with the half contact width for $\phi_p = 40\mu m$.

The presented Figure.7.12 depicts the trend of slope evolution in relation to

particle diameter. It becomes evident that when considering M50NiLDH steel under the specified operational conditions, the material can withstand particle sizes under or equal 50 μm without experiencing a reduction in its endurance limit. This finding highlights the significant role of heat treatments in enhancing material resistance against surface damage.
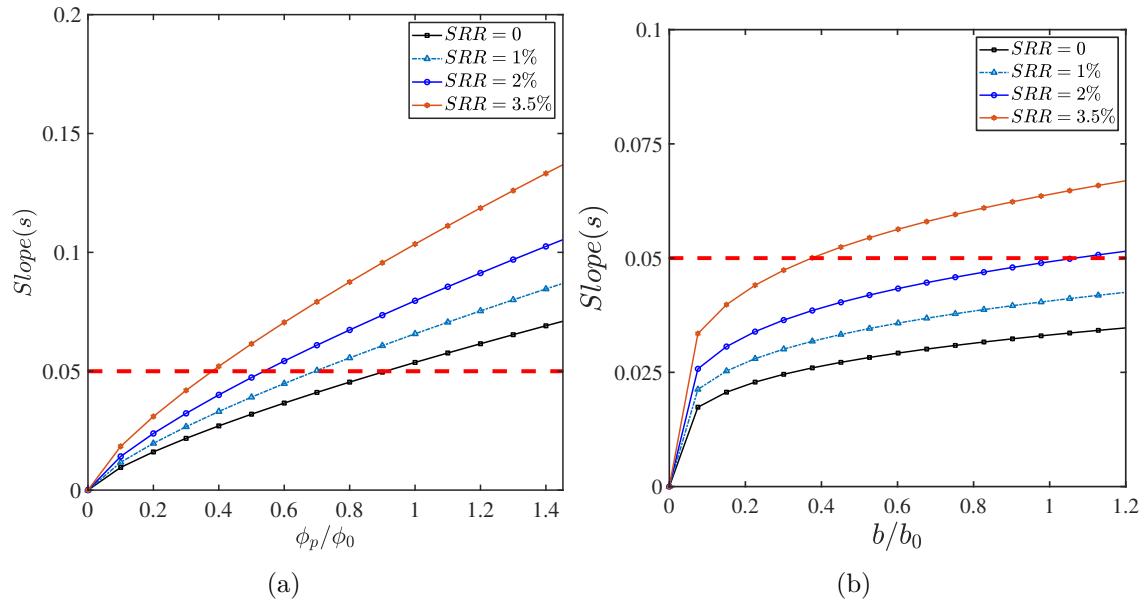
Figure 7.12: Average slope evolution on ductile particles and M50NiLDH steel (a) with the particle diameter for $b = 133\mu m$ (b) with the contact half-width for $\phi_p = 50\mu m$.

Using the average slope criterion, it became feasible to deduce a critical defect size threshold beyond which an indent's impact on the bearing's operational longevity becomes adverse. In our specific operating conditions, it has been determined that when the bead height of a dent exceeds 0.6 μm, the bearing's endurance limit experiences a rapid reduction, potentially resulting in surface spalling and subsequent damage. For a sliding level of 1% in steel/steel bearings, the sizes of ductile particles tolerable by the various grades of steel, namely M50, 32CDV13, M50NiL, and M50NiLDH, are respectively around: 40, 45, 50, and 70 μm. These sizes correspond to a threshold bead height of 0.6 μm. However, in the case of hybrid bearings, significantly larger bead heights are observed, even after subjecting them to rolling cycles as shown in Fig.6.30. Nonetheless, these bead heights remain sufficiently high to potentially cause premature damage to the raceway surfaces based on the criterion proposed in this study.

7.6 Industrial application

Within the framework of the SAE engine component initiative, a thorough examination of the bearing elements in bearing 1 as presented in Fig.7.13, of the CFM 56 engine exposed the existence of numerous dents on the bearing raceway surfaces. To comprehensively understand the characteristics and size of pollutants found on the bearing raceway, a study was initiated within Safran Aircraft Engine's IHENR division. This study aims to evaluate the distribution and dimensions of debris originating, and pile-up height distribution from the measured dents on the bearing surfaces.

7.7 Quantifying uncertainties

As previously discussed, mechanical structures are affected by uncertainties, and our goal is to measure how sensitive a system is to variations in its input parameters. These studies aim to assess the extent to which a system's behavior can vary due to uncertainties in the parameters governing it. The process of quantifying uncertainties involves three key steps: first, modeling both random and epistemic uncertainties; second, propagating these uncertainties through the model; and third, quantifying the observed variations in the system's outputs.

As example, lets consider an operator denoted as f, along with a set of behavior laws capable of predicting the physical behavior based on input data, x_i, expressed as $f(x_i) = y_i$. This allows for a direct approach in which the output values, y, are determined based on the input parameters, xi, and the operator f. By introducing uncertainties in the input parameters, these uncertainties can then be transferred to the outputs, which can be quantified using statistical tools. The primary advantage of this process is the ability to rank parameters according to their impact on the variability in the system's outputs.

So in the case of a mechanical structure that has a yield strength, if a failure criterion is in place, it becomes possible to calculate the associated probability of failure. Parameters associated with uncertainties that lead to critical behaviors deserve special attention. If these uncertainties cannot be reduced through further investigations, it becomes essential to closely monitor these parameters during the manufacturing and assembly of the component.

Conversely, the inverse approach involves quantifying the variations in input parameters based on the observed outputs. To accomplish this, stochastic calibration algorithms must be employed to account for output uncertainties and determine the range of input variations (TAF 13).

Much like the diverse nature of uncertainties, there is a variety of approaches available for modeling them. Each method offers a unique way of representing uncertainty. A well-informed user will choose the most suitable method based on

223

the type of uncertainty encountered. These methods can be broadly categorized into probabilistic and non-probabilistic approaches.

7.8 Modelisation in variable conditions

Turboreactors are vital and indispensable structures, subject to a multitude of constraints. The stresses they experience during flight vary according to the flight regime, spanning from takeoff to climb, then to cruise, and finally the landing phases. Throughout these distinct phases, aero, thermal, and centrifugal stresses are in constant flux. Relying solely on nominal load values during the cruise phase can be overly restrictive. Therefore, accounting for the variability in stresses based on actual conditions becomes an intriguing proposition.

However, conducting experiments under conditions closely mimicking the engine environment is both costly and intricate. Similarly, analyzing the variability in system responses typically necessitates increasing the number of samples to be measured. As a result, most tests are unitary and carried out under easily accessible laboratory conditions. Decision-makers thus seek to ascertain whether designed components meet reliability requirements, even if untested in operational conditions and for a limited population.

These observations have given rise to two key problem areas: How to resolve inconsistencies between two seemingly correct recalibrations that involve different physical behaviors? Is it possible to predict a structure's behavior under untested conditions? If so, with what degree of confidence?

Even on the scale of laboratory and technological tests, system responses to testing are influenced by uncertainties. Several types of uncertainties can affect numerical models and experimental results. Random uncertainty refers to inherent variations within the modeled system. These errors cannot be mitigated, even with more advanced analytical methods, as they are intrinsic to the physics involved. Some sources of random uncertainty include: Observation error where measurements are contaminated by noise, and the resulting errors are typically considered to be independent of time, following a normal distribution with a mean centered around zero. Parametric uncertainties is the case where two samples designed in the same way with identical materials can still differ. This is because most parameters (geometry, modulus, surface condition, etc.) are subject to manufacturing process variability. Residual variability concerns the situation where two measurements taken at different times exhibit differences, aside from observation errors and parametric uncertainties.

7.8.1 Probabilistic parametric methods

The most common way to represent uncertainties is by using probability density functions. Let A be an interval in R, and f be a function defined on A. We say that f is a probability density if:

1. f is continuous and positive on A.

2. $\int_A f(x)dx = 1$.

3. If the random variable X follows a density function f, then the probability of X falling within the real interval [a; b] is given by:

4. $P(X[a;b]) = \int_b^a f(x)dx$

where $a < b$. The most commonly used distribution is the normal distribution. The probability that the random variable X, following a normal distribution, takes the value x is defined by the probability density function:

$$p(x) = \frac{1}{\sqrt{2\pi\sigma^2}} \exp(-\frac{(x-\mu)^2}{2\sigma^2}) \tag{7.6}$$

where μ is the mean and σ is the standard deviation of the variable X. These distributions assume that we have sufficient information regarding the data under study to choose the most appropriate distribution form and to parametrize it credibly.

Stochastic parametric methods encompass sampling methods, reliability analysis methods, and stochastic finite element methods. Sampling methods involve drawing input parameters and their uncertainties and simulating a distribution of the relationships between different parameters to identify the output distribution. Reliability analysis methods are used to calculate the probability of failure of a mechanical structure. A criterion is defined to determine the system's state in the context of uncertainties. Stochastic finite element methods are an extension of classical finite element methods. The principle involves modeling the uncertain parameters of the system using stochastic functions rather than random variables.

7.8.2 Particle distribution and size identification using Monte-Carlo analysis

In this section, a study of variability using Monte Carlo methods based on experimental results of the bearings tests will be conducted. The initial phase of the investigation was conducted by experts and engineers from the BE team. This phase involved gathering data concerning the distribution and depth of dents within various quadrants of stage 1 in the CFM 56 engine bearing. Overall, the findings reveal that the areas displaying significant dents are those situated adjacent to the

unrestricted edges. As for the distribution and dimensions of the dents, they can be effectively modeled using either a normal or lognormal distribution. This modeling approach enables the determination of both an average value and a standard deviation based on the chosen distribution type. Using the various distributions identified within this study using the acquired data, the objective is to determine the distributions for several additional primary parameters linked to the indentation phenomenon. These parameters encompass attributes like particle size, bead height at the point where the dent is generated. Furthermore, a comprehensive examination of how uncertainty propagates through the analysis's ultimate output will also be conducted.
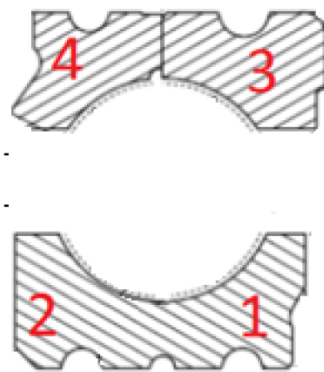
Figure 7.13: Illustration of bearing quadrants

Initially, a raw analysis of the data evolution was conducted, allowing for the fitting of various distributions associated with them.The fitted data includes the depth of the indentation and the diameter of the dent. Hence, Figures.7.14,7.15 provide a visual representation of the various distributions that will serve as the input data for our analysis.

Figure.7.15 depicts how the diameter and depth of the indentation vary with the number of dents. It's evident that dents with a diameter smaller than 20 μm are not detected, which can be attributed to the detectors' limitations concerning the size of the dents.

To obtain the distribution of the output concerning particle diameter and pile-up height, we computed the averages of the input data, resulting in the following findings:

- The diameter of the indents adheres to a normal mean distribution of approximately $\sim \mathcal{N}(40, 5)$.

- The contact half-width conforms to a normal mean distribution of approximately $\sim \mathcal{N}(88, 2)$.

- The depth of the indents follows an average normal distribution of approximately $\sim \mathcal{N}(4, 1)$.

226

(a)   (b)
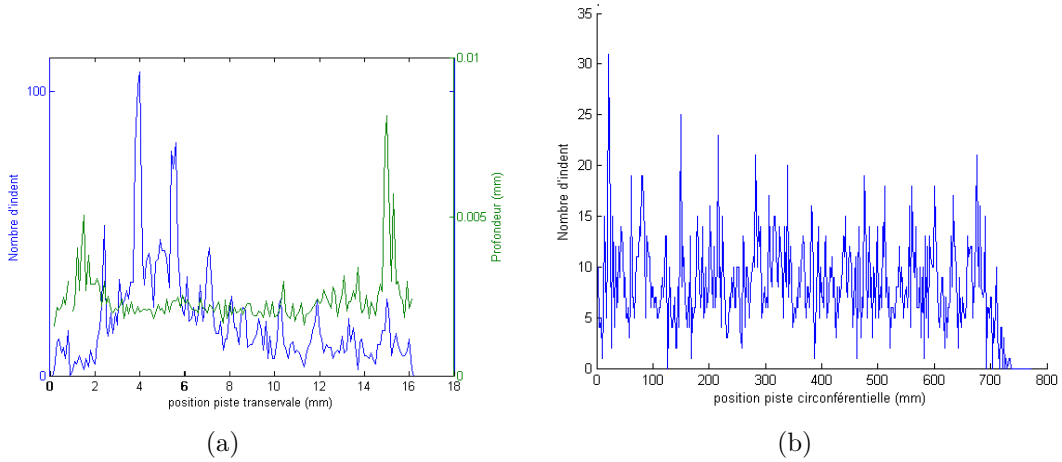
Figure 7.14: (a) Distribution of the dent number according to the transversal position on the raceway, (b) Distribution of the dent number according to the circonferencial position on the raceway.

(a)   (b)
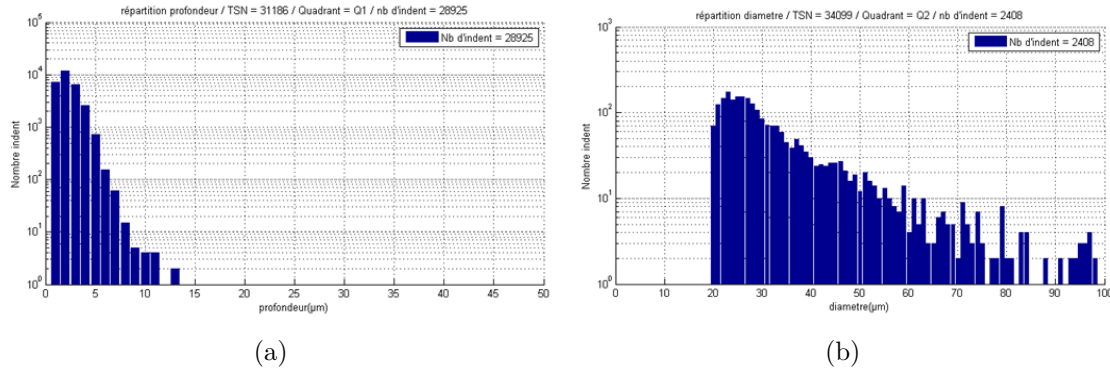
Figure 7.15: (a) Distribution of the dent number according to the dent depth, (b) Distribution of the dent number according to the dent size.

- The slip rate exhibits a mean normal distribution of $\sim \mathcal{N}(2, 0.5)$.

The problem is solved through a Monte Carlo approach, a set of 1000 pseudo-random variables was generated for each parameter involved in the problem. By utilizing the specific Matlab algorithm based on analytical expressions, the following outcomes were obtained:

- The particle diameter manifests a mean distribution of about $\sim \mathcal{N}(31, 5)$.

- The bead height demonstrates a mean normal distribution of roughly $\sim \mathcal{N}(0.096, 0.04)$.

Based on these results presented in Fig.7.16,7.17,7.18, it is evident that both the particle diameter and the bead height also exhibit Gaussian distributions. Given
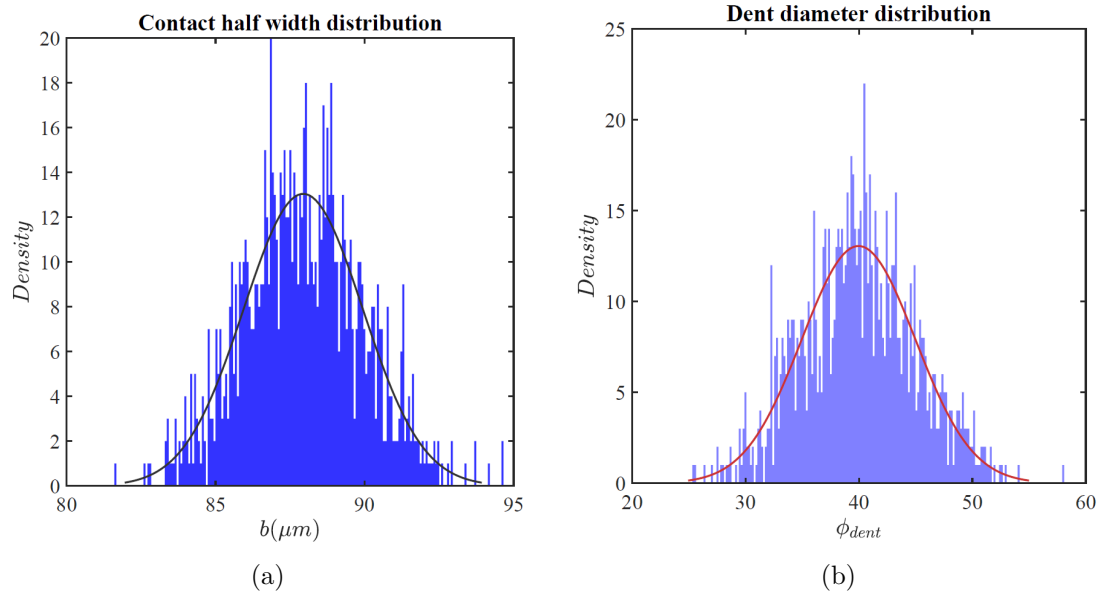
Figure 7.16: (a) Contact half-width following a gaussian distribution, (b) Dent diameter following a gaussian distribution.
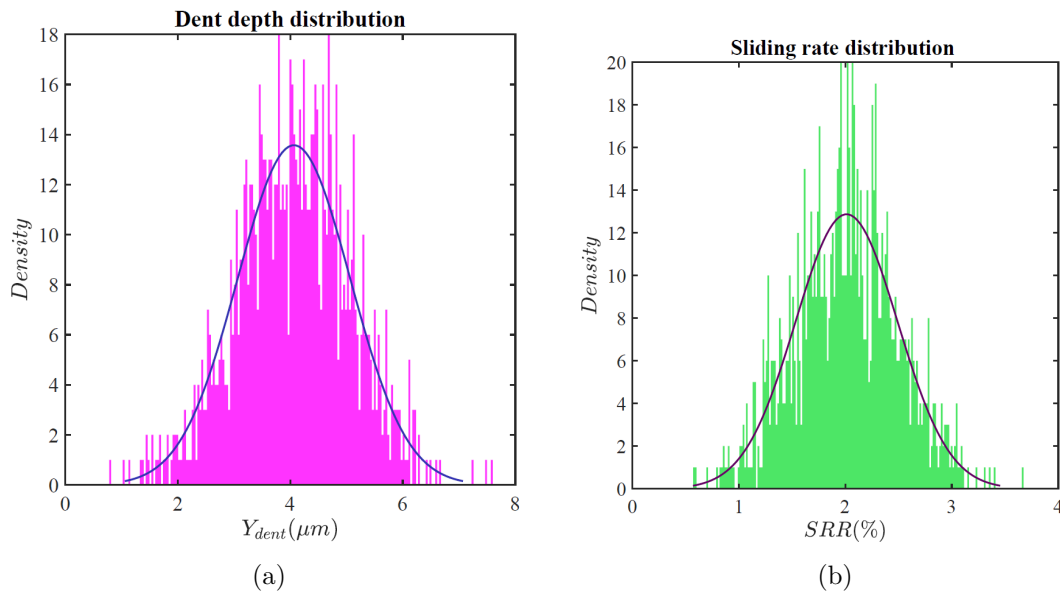
Figure 7.17: (a) Dent depth following a gaussian distribution, (b) SRR following a gaussian distribution.

that the bead height values are considerably lower than the threshold identified in this thesis, it becomes clear why no damage was detected on these bearings.
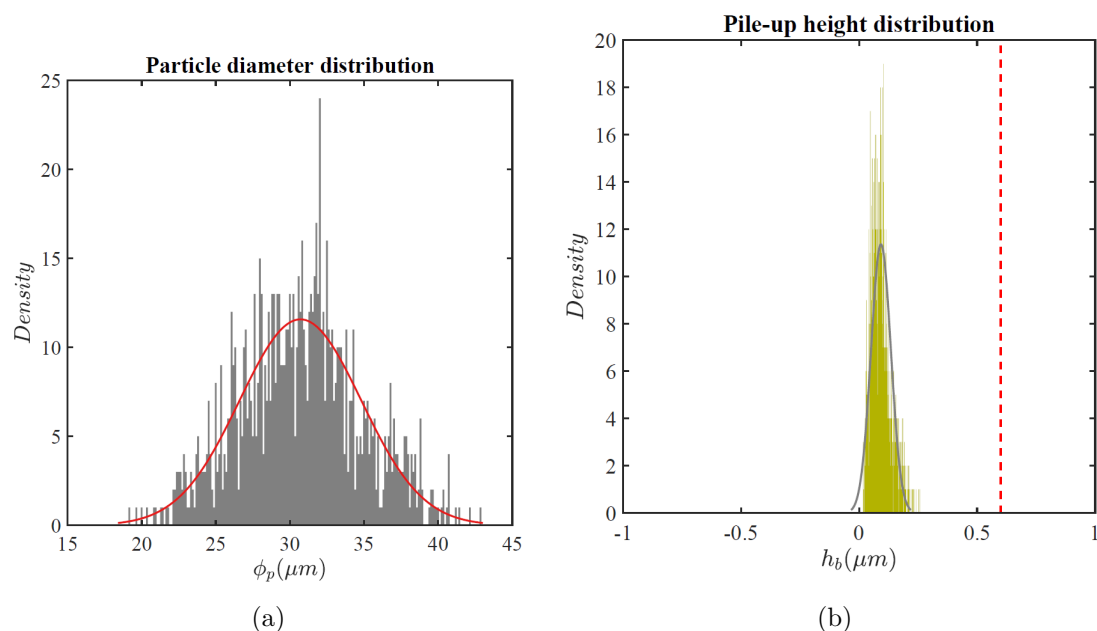
Figure 7.18: (a) Particles diameter following a gaussian distribution, (b) Pile-up height output following a gaussian distribution.

7.9   Conclusion

In this chapter, we conducted an in-depth analysis of the rolling cycle and applied the modified Dang van criterion proposed by Bonetto. This criterion helped identify the most susceptible areas, primarily the edges of the indent. Through the bearing cycle on the indent, we observed a reduction in bead height and a Swift stabilization of its geometry. The crucial factors influencing fatigue in the presence of an indent are the load, bead height, and slip. A damage criterion based on the endurance limit, as determined in Jacq's work on bearings, was introduced. This criterion enabled the identification of particle sizes ($< 40 \ \mu m$) that are tolerable for the bearings under the specified operating conditions of our study. Consequently, a defect size of bead exceeding $0.6 \ \mu m$ would lead to rapid damage to the bearing under normal operational conditions.

The analyses discussed above concern steel-steel bearings. However, in the case of hybrid bearings, significantly larger bead heights are observed, even after subjecting them to rolling cycles. Nonetheless, these bead heights remain sufficiently high to potentially cause premature damage to the raceway surfaces based on the criterion proposed in this study. Indeed, hybrid bearings result in the formation of indents with notably elevated bead heights. These increased bead heights have the potential to induce surface damage relatively quickly unless modifications are made to the prevailing loading conditions.

General conclusion

Presently, bearing damage predominantly occurs on the surface. The emergence of such damage is attributed to geometric imperfections, which could originate from inherent part defects like surface roughness or be generated during the system's operation, resulting in more pronounced defects such as indents. These indents are a consequence of lubricants carrying particles into the contact zones. The particles being crushed between the surfaces leading to the creation of dents, which subsequently alter the loading conditions for subsequent cycles. This alteration can culminate in the development of fatigue, taking the form of cracks or micro-spalling.

To address this, optimizing material properties involves focusing on surface properties. This optimization is achieved through thermochemical treatments such as quenching, cementation, nitriding, and carbonitriding. As a result, predicting and preventing surface damage necessitates a comprehensive understanding of the mechanical behavior of rolling materials. By grasping these material behavior principles, we conducted simulations to assess bearing resilience. These simulations indicated that for loadings involving a smaller volume, like fine particle indentation, surface properties prove sufficient for accurate modeling.

To identify suppression sources along the raceway, systematic modeling of free edge effects was undertaken using a semi-analytical development in a contact resolution tool. The outcome of this modeling endeavor unveiled a dual effect triggered by these edge influences: an amplification of pressure amplitude and a shift in the pressure distribution towards the less close free edge of the space. This pressure increase becomes particularly notable when numerous closely positioned free edges are present, owing to their mutual influence.

When the space is confined within finite dimensions along the x and y axes, relying solely on the Hertz solution would result in an error of approximately 20% when estimating the maximum pressure value. This discrepancy arises due to the intricate interplay among the various adjacent free edges. A comparable trend, albeit with more pronounced amplification, is discernible when dealing with a truncated contact zone. The influence of edge effects becomes negligible when the distance d/a exceeds four times the radius of the contact zone. Consequently, for $d/a \geq 4$, the Hertz solutions regain their validity and can be reliably applied.

The origins of pressure peaks can be attributed to various factors, including geometric irregularities, grooves, surface inclinations, fluctuations in surface roughness,

dents, edges, and rounded features. When these factors interact with the free edge's influence, they contribute to initiating damage within the system.

The study of surface indentation caused by the passage of a particle within a Hertzian contact is conducted through a finite element model. Applying the finite element method (FEM) for indentation modeling has proven highly effective in overcoming numerical challenges posed by the particle's substantial deformation during contact. The "coupled Euler-Lagrange" (CEL) model developed has been validated through correlation with indentation tests from existing literature. This validates the numerical tool.

Notably, the natural indentations in bearings are asymmetric, with the indent presenting a more prominent edge in the direction of the load passage. Using the CEL model, a comprehensive parametric analysis of the indentation process is conducted. This study highlights the importance of mechanical properties, particle size, nature, shape, and position, along with the presence of slip and critical slip rate and residual stresses in dent generation. A hard particle generates a narrow and deep dent with pronounced bead, while a ductile particle results in a wider, shallower dent with weaker bead. Under iso-loading conditions, particle size corresponds to the resulting indent size, with a tendency towards broader and shallower indents as the particle size increases. This elucidates a criterion for the harmfulness of indents based on particle size. The mechanical properties of the surface couple also play a significant role in indentation. It has been observed that steel bearings produce lower rim heights than hybrid bearings, where higher mechanical properties on the rolling elements induce lower deformation levels while the opposing surface experiences slightly more deformation.

The introduction of slip within the contact dramatically alters the shape of the obtained indents. As the particle spreads between surfaces due to increased sliding levels, the dents become broader and shallower. Additionally, a critical slip rate is noted, dependent on the operating conditions and particle size, where the rim height of a ductile particle is maximized. Ultimately, bearing loading has been found to have minimal influence on the indentation process.

In terms of fatigue on indented surfaces, it manifests particularly through the formation of cracks along the edge of the indent opposite to the direction of frictional forces in the presence of slippage. To study the formation of these cracks, a contact calculation tool based on semi-analytical methods is used to simulate the load passage on the indented surface. A fatigue criterion, a reformulation of the Dang Van criterion by Bonetto et al., is applied to these load passage cycles to determine the mechanisms behind the cracking. Shear has emerged as a driving mechanism for this type of fatigue, providing good results in localizing and predicting crack orientation. The parametric study conducted on the indentation process is extended to fatigue, highlighting three parameters increased load, sliding, and pile-up height that decrease the lifespan.

To mitigate the computational burden and establish relationships among influential parameters, analytical expressions have been devised to describe the evolution of various parameters, such as indent height and diameter, in the indentation process. These expressions account for parameters like particle size, slip rate, and loading. Utilizing these expressions, a framework for assessing the endurance limit evolution of bearings, as identified by Jacq, based on loading and particle size, has been established.

This analysis has revealed that within our operational conditions, specifically with slip levels at or below 2% and ductile particle sizes less than 40 μm, all studied rolling materials (M50, 32CDV13, M50NiL, M50NiLDH) have the potential for an endurance limit exceeding 1.5 GPa. Interestingly, the endurance limit tends to increase as the load decreases. In a slightly broader context, considering a bead height of 0.6 μm, the endurance limit is estimated to be around 0.5 GPa.

By leveraging these analytical expressions and findings, a deeper understanding has been achieved regarding how influential parameters impact the endurance limits of various rolling materials, offering valuable insights for optimizing their performance.

To go further, a modeling of the quarter space problem in presence of full plasticity can be realised to get a completed responce of components. Study of conducting a comprehensive exploration of the variability of the various parameters within the behavior law under both monotonic and cyclic loading conditions could significantly enhance the calibration process. Similarly, increasing the CEL indentation model by integrating thermal effects and refining its capabilities for indentations in the presence of lubrication promises more accurate and high-quality results.

Furthermore, including fracture mechanisms for brittle particles would extend the model's applicability to encompass all particles encountered in transmission systems. Additionally, developing a streamlined model for indentation, coupled with a Monte-Carlo analysis, would enable an optimal study of parameter variability and its impact on output responses. This approach would prove particularly valuable in the context of bearing contact studies involving indents.
It would be valuable to examine the progression of rolling cycles on an indentation caused by ceramic rolling elements. This analysis could reveal the cycle at which the stabilization of the bead height occurs and provide insight into the final height of the bead. Considering practical enhancements, incorporating a plastic damage model into the existing tools employed in this study could effectively replicate the micro-chipping phenomenon that occurs at an indent's exit. Finally, embarking on a campaign of fatigue tests on indents holds the potential to calibrate the novel fatigue criterion and damage model, thereby quantifying the remaining lifetimes of components during their operational lifecycle and maintenance periods. This comprehensive approach not only advances understanding but also empowers informed decision-making and enhances the reliability of systems.

Appendix A

Elliptical contact

A.1 Contact Mechanics

This section provides a concise overview of contact mechanics, tracing its inception from Hertz's work (HER 82) in optics to the establishment of a theory for ellipsoidal contact pressure on elastic solid bodies. Before the rise of advanced numerical methods, the historical development of contact mechanics is well-documented in Johnson's publication "Contact Mechanics" (JOH 85). Subsequently, the section proceeds to covering the fundamentals of contact mechanics, encompassing Hertz's influential theory, non-Hertzian contact particularly in rolling contact and culminates with an exploration of contemporary numerical methods employed in solving contact problems.

A.1.1 Hertzian Contact

Hertz developed analytical relationships for determining the maximum surface pressure in contact between cylinders or spheres and on a semi-infinite plane. These relationships were based on the findings of Boussinesq, who studied the deformation of a semi-infinite body under the effect of a concentrated force applied to a plane. The Hertz equations determine the maximum pressure, deformations of the parts, and stress distribution inside them. The Hertz theory makes several simplifying assumptions, including:

✤ The materials are assumed to be elastic, homogeneous, and isotropic, with no internal voids or cracks.

✤ The contact surfaces are assumed to be smooth and perfectly spherical or cylindrical, without roughness or asperities.

✤ The deformation of the contact surfaces is assumed to be small so that linear elasticity theory can be applied.

❋ The contact is assumed to be non-sliding, meaning there is no relative tangential motion between the two surfaces.

The Hertzian contact theory provides analytical expressions for the contact pressure distribution, the contact area, and the deformation of the bodies under load. This contact theory has wide applications in various fields, including mechanical engineering, materials science, and biomechanics, and is often used as a benchmark for validating numerical simulations of contact problems.

A.1.1.1 Circular contact area

In the Hertz solution for circular contact regions, two elastic bodies with radii of curvature R_1 and R_2 are brought into contact under a normal load F_N as shown in Fig.A.1. The resulting contact area is a circle with radius a, and the Hertz theory provides the contact pressure distribution $p(r)$ as a function of the radial distance r from the center of the contact area. The Hertz solution assumes that the bodies are linearly elastic, homogeneous, and isotropic and that the contact is frictionless.

For instance, considering the contact between two spheres, the following expression gives the equivalent radius:

$$\frac{1}{R_{eq}} = \frac{1}{R_1} + \frac{1}{R_2}, \tag{A.1}$$

The expression for the equivalent modulus is:

$$\frac{1}{E_{eq}} = \frac{(1-\nu_1^2)}{E_1} + \frac{(1-\nu_2^2)}{E_2} \tag{A.2}$$

Where ν_1 and ν_2 are the Poisson's ratios of the bodies.

The Hertz maximum pressurea and the pressure field are given by:

$$P_{Hertz} = \frac{3F_N}{2\pi a^2} = \left(\frac{6F_N E_{eq}^2}{\pi^3 R_{eq}^2}\right)^{1/3} \tag{A.3}$$

$$p(x,y) = \frac{3F_N}{2\pi a^2}\left[1 - \left(\frac{x^2}{a^2} + \frac{y^2}{a^2}\right)\right]^{\frac{1}{2}} \tag{A.4}$$

The contact radius is given by the expression:

$$a = \left(\frac{3F_N R_{eq}}{4E_{eq}}\right)^{1/3} \tag{A.5}$$

The expression for rigid body displacement is given by:

$$\delta_z = \frac{a^2}{R_{eq}} = \left(\frac{9F_c^2}{16R_{eq}E_{eq}^2}\right)^{1/3} \tag{A.6}$$
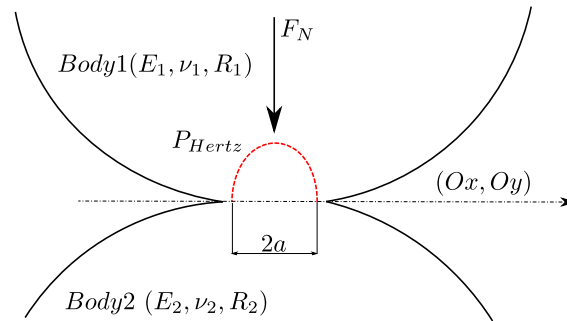
Figure A.1: The general problem of Hertzian contact illustration

In the case of contact problem between rolling elements bearings, the contact area is often approximated as elliptical due to the non-circular shapes of the bearing components. The elliptical contact area can calculate the maximum surface pressure and stress distribution as presented in this section, similar to the Hertz theory for circular contact areas.

A.1.1.2 Quarter space contact problem

Quarter-space contact problem denotes a specific type of contact problem occurring when two bodies interact near a free edge, a situation often observed in engineering applications like bearings and gears. In contrast to the more straightforward Hertzian contact, solving quarter-space contact requires complex numerical methods. Numerous studies in the field of contact mechanics, as noted in the literature (HET 60; HET 70; HAN 89; HAN 90; HAN 91; GUI 11; WAN 12; WAN 17), have concentrated on developing diverse numerical techniques to address the intricacies of this problem.

Understanding the behavior of free edges, particularly in raceways, holds significant importance in comprehending the emergence of pressure peaks. Defining the contact area becomes challenging when bodies come into contact, leading to intricate stress and strain distributions. Free edges, like those found on raceways, further complicate stress distribution, resulting in concentrated local stress.

In the context of rolling element bearings, the presence of free edges on raceways can lead to pressure peaks where the rolling element and raceway meet. These peaks can cause considerable damage to the bearing over time, reducing its overall lifespan.

This part of the thesis focuses on numerically modeling the impact of free edges on the bearing contact zone. By combining advanced analytical techniques with numerical methods, it becomes feasible to simulate and analyze the behavior of rolling tracks in the presence of edge effects. These numerical models offer valuable insights into the complex interactions and phenomena at the contact interface. The objective is to enhance our understanding of the fundamental mechanisms and contribute to strategies for optimizing raceway performance and durability.

A.1.1.3   Numerical methods for solving contact problems

Numerical methods (ODE 84; ODE 86; LUB 86; TER 88; BOF 12; BOF 14; BLA 16; BLA 18; AND 81)play a crucial role in contact mechanics research and engineering design by providing valuable tools for solving contact problems. However, it is important to recognize that each method has its own set of strengths and weaknesses, making them suitable for different types of problems (KAR 87; PAR 85; LAC 00; WRO 02; BEN 68; KAL 90b; POL 99; LIU 00). Semi-analytical methods combine analytical solutions with numerical techniques, such as the boundary element method (BEM) and the fast Fourier Transform (FFT). These methods are advantageous when dealing with contact problems involving complex geometries and boundary conditions. By leveraging analytical solutions in specific regions and numerical techniques in others, they can provide approximate solutions efficiently.

On the other hand, finite difference and multigrid methods discretize the contact problem into a grid of points and approximate the solutions at these points using finite differences. These methods are particularly efficient for problems with regular geometries and uniform material properties. Multigrid methods further enhance their effectiveness by accelerating convergence and improving solution accuracy.

Finite element methods (FEM) are widely utilized in contact mechanics due to their flexibility in handling complex geometries and material properties. FEM discretizes the problem into small elements, where the equations of motion are solved using numerical techniques. This approach allows for accurately modeling various contact problems and has become one of the most popular numerical methods in simulating contact phenomena across different engineering disciplines.

There are several numerical methods that can be used to solve contact problems in mechanics. Here are some of the main methods:

In the field of contact mechanics, various numerical methods can be employed to solve contact problems with different complexities and requirements. Here are some commonly used numerical methods:

- **The Finite Element Method (FEM):** FEM discretizes the problem domain into small elements and approximates the solution within each element using basis functions. It can handle both linear and nonlinear contact problems, large deformations, and complex material behavior.

- **The Boundary Element Method (BEM):** BEM discretizes only the boundary of the problem domain, making it suitable for problems with infinite or semi-infinite domains. It is useful for modeling elastic, viscoelastic, and viscoplastic materials.

- **The Discrete Element Method (DEM):** DEM models the contact between individual particles or bodies and is commonly used in granular mechanics and geomechanics. It simulates both normal and tangential contact forces and can account for particle breakage and sliding.

- **The Finite Volume Method (FVM):** The Finite Volume Method (FVM) is a numerical technique commonly used to solve various problems, including contact problems. It is particularly well-suited for problems involving complex geometries and discontinuities, making it applicable to contact analysis.

- **The Semi-analytical methods:** Semi-analytical methods combine the advantages of analytical and numerical approaches. They are useful for solving contact problems involving bodies with complex geometries and material properties.

The selection of the most suitable numerical method depends on the specific characteristics of the contact problem, such as geometry, material behavior, and boundary conditions. Researchers choose the appropriate method that can provide accurate and efficient solutions for their particular application.

A.2   The Semi-analytical method for the Contact Problem

This section will discuss the resolution approach for the contact problem using the semi-analytical method. The semi-analytical approach is a powerful technique that combines the benefits of both analytical and numerical methods to solve contact problems. The semi-analytical method can handle various types of contact, including normal and tangential contact. It considers the complex geometries of the contacting bodies, taking into account their intricate shapes and surface features. Additionally, it can accurately model the material behavior, capturing nonlinearities, viscoelasticity, and other complexities (AHM 83; JOH 85; ANT 05; GAL 06b; CHA 11; KOU 14; KOU 15a; AMU 16a; BEY 19; WAL 20).

A.2.1   The normal contact problem

When considering the contact between two purely elastic bodies, B_1 and B_2, occurring in the tangent plane of the contact in the $(x - y)$ plane. We need to solve the elastic deformation problem for the bodies subject to appropriate boundary conditions at the contact interface to determine the contact pressure and deformation. The surface profiles of the bodies are defined by the functions:

$$z_1 = h_1(x, y) \tag{A.7}$$
$$z_2 = h_2(x, y), \tag{A.8}$$

where z_1 and z_2 are the heights of the surfaces of Ω_1 and Ω_2 above the $x - y$ plane, respectively.

The contact pressure and deformation will be determined by solving the elastic deformation problem for the bodies subject to the appropriate boundary conditions at the contact interface. The contact problem is defined by the following equations:

1. The surface separation:

   The distance between the contacting bodies $g(x)$ is given by the summation of the initial separation $g_i(x)$, the rigid body displacement δ_z and the normal elastic surface displacement of both bodies $u_z^{\Omega_1+\Omega_2}(x)$:

   The initial separation function can be written as:

   $$g_i(x,y) = h_1(x,y) - h_2(x,y). \tag{A.9}$$

   $$g(x,y) = g_i(x,y) + \delta_z + u_3^{\Omega_1+\Omega_2}(x,y) \tag{A.10}$$

2. The contact condition:

   $$(x,y) \in \Gamma_c; \quad g(x,y) = 0 \quad and \quad p(x,y) > 0 \tag{A.11a}$$

   $$(x,y) \notin \Gamma_c; \quad g(x,y) > 0 \quad and \quad p(x,y) = 0 \tag{A.11b}$$

   where $p(x,y)$ denotes the pressure field and g the final surface gap between the two bodies.

3. The load balance:

   The normal applied load F_N must be equal to the integral of the contact pressure distribution $p(x,y)$ over the contact zone Γ_c. It is given by:

   $$F_N = \int_{\Gamma_c} p(x,y) dS \tag{A.12}$$

A.2.2 The tangential contact problem

To address the tangential contact problem, understanding the distribution of shear tractions resulting from relative tangential motion between contacting bodies is crucial. Resolving this problem involves assessing the equilibrium of forces and moments at the contact interface while applying friction laws or contact models to depict the contact behavior. This solution closely intertwines with the resolution of the normal contact problem, as the distribution of tangential forces relies on body deformation and the normal contact pressure distribution.

An essential component in the analysis of tangential contact is the slip vector, denoted by $\mathbf{s}$. At time t, let $\mathbf{s}^t$ represent the slip vector, where $\dot{}$ indicates the time derivative operator. Consider two points on the surfaces of bodies 1 and 2 in contact at time t, located at coordinates x_1^t and x_2^t, respectively. Additionally, let $u_{\tau,1}^t$ and $u_{\tau,2}^t$ denote the tangential elastic displacements of the surfaces.

The slip between times t' and t is defined as follows:

$$\bar{\mathbf{s}}^t = \begin{bmatrix} \Delta u_x^t - \Delta \delta_x^t \\ \Delta u_y^t - \Delta \delta_y^t \\ 0 \end{bmatrix} \tag{A.13}$$

When tangential displacements are non-zero, the tangential contact problem needs to be addressed. This occurs when a tangential force $\bar{Q}$ is applied or when there is a coupling between the normal and tangential problems due to differences in elastic properties of the contacting surfaces. The tangential contact problem involves the relative tangential displacements of surfaces u_x^q and u_y^q, the displacements of tangential rigid bodies δ_x and δ_y. The slip amplitudes s_x and s_y as well as the slip vector $\bar{\mathbf{s}}$, the shears q_x and q_y, the slip zone Γ_{sl}, the stick zone Γ_{st} and the tangential force Q.

Coulomb's law is used to define the relationship between pressure and shear. In discrete form, the tangential problem is expressed as follows:

$$\Delta u_{\tau,ij}^t - \Delta \delta_\tau^t = s_{ij}^t \neq 0, q_{ij} = -\mu p_{ij} \frac{s_{ij}^t}{s_{ij}^t}, \quad \forall (i,j) \in \Gamma_{sl} \tag{A.14a}$$

$$\Delta u_{\tau,ij}^t - \Delta \delta_\tau^t = s_{ij}^t = 0 \tag{A.14b}$$

$$q_{ij} < \mu p_{ij}, \quad \forall (i,j) \in \Gamma_{st} \tag{A.14c}$$

$$\sum_{\Gamma p} q_{ij}.S_{ij} = Q \tag{A.14d}$$

where S_{ij} is the discretisized elementary area.

A.2.3 Variational Formulation of contact problem

The variational formulation of the contact problem involves expressing the problem in terms of a variational principle or function, which allows us to derive the governing equations and boundary conditions. The variational formulation is commonly used in contact mechanics to find the equilibrium configuration and contact forces between two contacting bodies. To formulate the contact problem variationally, researchers(DUV 72; KAL 90b) typically consider the total potential energy functional, the sum of the elastic strain energy, and the work done by external loads. The goal is to find the configuration that minimizes the total potential energy, subject to the appropriate boundary conditions and constraints. So solving the contact problem is equivalent to minimizing the complementary energy, i.e., the energy of elastic deformation expressed as a function of p and q. This minimization is accompanied by constraints that must be satisfied, namely, the positivity of pressures and Coulomb's law, which limits the shear. The variational formulation of the problem is then written as:

$$\min_{p,q} \left(\int_{\Gamma_c} \left[\frac{1}{2} \left(h_0 - \delta z + \frac{1}{2} \bar{u}_z \right) p dS + \int_{\Gamma_c} \left(-\Delta \delta_\tau^t + \frac{1}{2} (\bar{u}_\tau^t - \bar{u}_\tau^{t-1}) \right) q \right] dS \right) \tag{A.15}$$

Subject to the following constraints:

$$p \geq 0 \tag{A.16}$$

$$q \leq \mu p \tag{A.17}$$

In this context, Γ_c denotes the domain of integration, where h_0 is a constant, δz and $\Delta \delta_\tau^t$ are a provided displacements. The variables $\bar{u}_z$ and $\bar{u}_t^\tau$ represent unknown displacements, while p represents the pressure, and q the shear.

The aim is to minimize the function across the domain Γ_c by determining the optimal values for p and q.

Assuming the contact problem is decoupled, and the tangential problem has been previously resolved, the variational expression for the normal contact problem is provided by the equation:

$$\min_p \left(\frac{1}{2} \mathbf{p}^T \mathbf{A_z^p} \mathbf{p} + \mathbf{h}^{*T} \mathbf{p} + c_\tau \right), \tag{A.18a}$$

$$p_{ij} \geq 0, \tag{A.18b}$$

where $\mathbf{p}$ is the vector for the pressure field; $\mathbf{A_z^p}$ the influence coefficients of the normal displacement at the surface due to the pressure; $\mathbf{h}^*$ the vector for the initial gap, the rigid body displacements and the normal displacements induced by the shear fields at the surface since they do not induce any work. c_τ is the complementary energy due to the tangential problem that is supposed already solved.

Assuming that the normal problem has been solved, we can express the discrete variational formulation of the tangential contact problem as:

$$\min_q \left(\frac{1}{2} \mathbf{q}^T \mathbf{A}_\tau^q \mathbf{q} + \mathbf{W}^{*T} \mathbf{q} + c_p \right) \tag{A.19}$$

where $\mathbf{q}$ represents the shear pressure vector, and $A_\tau^q \mathbf{q}$ the influence coefficients of the tangential displacement on the surface due to the pressure. The vector $\mathbf{W}^*$ is defined by the expression:

$$\mathbf{W}^* = -\Delta \delta_\tau^t + \mathbf{A}_\tau^p \mathbf{p} - \bar{\mathbf{u}}_{\boldsymbol{\varnothing}}^{\mathbf{t-1}} \tag{A.20}$$

Here, c_p stands for the complementary energy resulting from the normal problem, which is assumed to have been previously resolved.

To address this problem described by Eq.(A.19), both the normal and tangential contact problems can be formulated as minimization problems with specific constraints:

$$\min_{\phi(x) \in \mathbf{R}^n} \phi(\mathbf{x}), \text{ with } \begin{cases} c_i(\mathbf{x}) = 0, & i \in \mathcal{E}, \\ c_i(\mathbf{x}) \geq 0, & i \in \mathcal{I}. \end{cases}$$

where $\mathcal{E}$ represents the set of points i associated with equality constraints, and $\mathcal{I}$ stands for the set of points i linked to inequality constraints, the general Lagrangian formulation for the problem presented in equation (A.21) can be expressed as follows:

$$\mathcal{L}(\phi(x), \lambda) = \phi(\mathbf{x}) - \sum_{i \in \mathcal{E} \cup \mathcal{I}} \lambda_i c_i(\mathbf{x}) \tag{A.21}$$

Where λ_i are the Lagrange multipliers. The number of Lagrange multipliers is equal to the number of constraints. Solving the constrained minimization problem is equivalent to solving the Karush-Kuhn-Tucker (KKT) optimality conditions, which are written as follows:

$$\nabla_x \mathcal{L}(x, \lambda) = 0, \tag{A.22a}$$

$$c_i(x) = 0, \forall i \in \mathcal{E} \tag{A.22b}$$

$$c_i(x) \geq 0, \forall i \in \mathcal{I} \tag{A.22c}$$

$$\lambda_i(x) \geq 0, \forall i \in \mathcal{I} \tag{A.22d}$$

$$\lambda_i(x) c_i(x) = 0, \forall i \in \mathcal{E} \cup \mathcal{I} \tag{A.22e}$$

The complementarity condition, defined by the last line of the above equation, can be rewritten in the following form:

$$c_i(\mathbf{x}) > 0, \ \lambda_i = 0, \tag{A.23a}$$

$$c_i(\mathbf{x}) = 0, \ \lambda_i \geq 0, \tag{A.23b}$$

The application of the KKT conditions to the normal contact problem allows its formulation to be rewritten in the following form:

$$\min \left(\frac{1}{2} \mathbf{p}^T \mathbf{A}_z^p \mathbf{p} + \mathbf{h}^{*T} \mathbf{p} + c_\tau - \sum \lambda_{ij} p_{ij} \right) \Leftrightarrow \mathbf{A}_z^p \mathbf{p} + \mathbf{h}^{*T} - \lambda = 0 \tag{A.24a}$$

$$p_{ij} > 0, \quad \lambda_{ij} = 0 \tag{A.24b}$$

$$p_{ij} = 0, \quad \lambda_{ij} \geq 0 \tag{A.24c}$$

The tangential problem can also be rewritten, by applying the conditions of KKT, by the expression:

$$\min \left(\frac{1}{2} \mathbf{q}^T \mathbf{A}_\tau^q \mathbf{q} + \mathbf{W}^{*T} \mathbf{q} + c_p - \sum \lambda_{ij} \left(\frac{q_x^2 + q_y^2}{2fp} - \frac{fp}{2} \right) \right) \Leftrightarrow \mathbf{A}_\tau^q \mathbf{q} + \mathbf{W}^{*T} - \begin{pmatrix} \vdots \\ \lambda_{ij} \frac{q_{xij}}{fp_{ij}} \\ \vdots \\ \lambda_{ij} \frac{q_{yij}}{fp_{ij}} \\ \vdots \end{pmatrix} = 0 \tag{A.25a}$$

$$\|\mathbf{q}_{ij}\| < fp_{ij}, \quad \lambda_{ij} = 0 \tag{A.25b}$$

$$\|\mathbf{q}_{ij}\| = fp_{ij}, \quad \lambda_{ij} \geq 0 \tag{A.25c}$$

where λ_{ij} is here the norm of the slip vector s_{ij}

A.2.4 Contact problem resolution methods

The computation of displacements is an essential step in the resolution process. However, it can become computationally expensive due to the requirement for a double summation over the entire domain at each calculation point. With a discretization grid containing N_p points, computing displacements at a single point necessitates $O(N_p^2)$ operations. Therefore, it is imperative to reduce the computational cost in order to maintain reasonable computation times. A method proposed by Ju and Farris (JU 96), later refined by Liu et al. (LIU 00), leverages the properties of discrete convolution products in the frequency domain to address this issue.

A.2.4.1 The DC-FFT method

The Fourier transform of a function $f(t)$ is defined by the integral:

$$\tilde{f}(\omega) = \int_{-\infty}^{\infty} f(t)e^{-i\omega t}dt \tag{A.26}$$

The inverse Fourier transform from the frequency domain to the time domain is expressed as:

$$f(t) = \frac{1}{2\pi} \int_{-\infty}^{\infty} \tilde{f}(\omega)e^{i\omega t}d\omega \tag{A.27}$$

For continuous linear convolution, given functions $g(t)$ and $h(t)$, the convolution $f * g$ is calculated as:

$$(f * g)(t) = \int_{-\infty}^{\infty} g(\tau)h(t-\tau)d\tau \tag{A.28}$$

Utilizing the Fourier transform on the convolution product yields:

$$\tilde{f}(\omega) = \tilde{g}(\omega) \cdot \tilde{h}(\omega) \tag{A.29}$$

This allows the convolution product to be computed through the inverse Fourier transform of the product of the Fourier transforms.

The discrete convolution product, defined for a domain with N values, is given by:

$$f_j = \sum_{r=0}^{N-1} g_r \cdot h_{j-r}, \quad j = [0, N-1] \tag{A.30}$$

The discrete Fourier transform and its inverse are expressed as:

$$\hat{f}_s = \frac{1}{N} \sum_{r=0}^{N-1} f_r e^{-2i\pi rs/N}, \quad s = [0, N-1] \tag{A.31}$$

$$f_j = \frac{1}{N} \sum_{r=0}^{N-1} \hat{f}_r e^{2i\pi rj/N}, \quad j = [0, N-1] \tag{A.32}$$

The discrete convolution theorem is then articulated as:

$$\hat{f}_s = \hat{g}_s \cdot \hat{h}_s, \quad s = [0, N-1] \tag{A.33}$$

The Fast Fourier Transform (FFT) is a highly efficient method that significantly decreases computational load, using algorithms optimized for different dataset sizes. While the direct approach to discrete Fourier transform calculations is computationally expensive, the use of FFT algorithms substantially reduces the number of operations, allowing convolutions to be computed with remarkable efficiency. These methods, like Singleton's FFT algorithms, make it feasible to perform computations at a significantly reduced computational cost, particularly for larger datasets. Consequently, convolutions conducted in the Fourier frequency domain necessitate $O(N)$ operations as opposed to $O(N^2)$ operations in the spatial domain. By leveraging FFT algorithms, the overall computational load is trimmed down to $O(N+3N)$ instead of $O(N^2$, a substantial advantage, especially for large values of N. However, it is important to note that these approaches may introduce errors. Nonetheless, there exists a trade-off between the method's swiftness and the potential errors associated with FFT utilization.

The procedure for implementing the Discrete Convolution and Fast Fourier Transform (DC-FFT) method encompasses the following steps:

a) Find the influence coefficients, $\{K_j\}_N$;

b) Extension of the influence coefficients by wrap-around order, $\{K_j\}_{2N}$;

c) Apply the FFT to the extended influence coefficients, $\{\tilde{K}_s\}_{2N}$;

d) Enter the pressures, $\{p_j\}_N$;

e) Extend the pressures using the zero-padding, $p_j = p_j, \quad j \in [0, N-1]$ and $p_j = 0, \quad j \in [N, 2N-1]$;

f) Apply the FFT to the extended pressures, $\{\tilde{p}_j\}_{2N}$;

g) Term to term product in the Fourier frequency domain, $\{\tilde{\nu}_j\}_{2N}$;

h) Apply the IFFT to obtain the wanted quantity $\{u_j\}_{2N}$;

i) Truncation to keep $\{u_j\}_{2N}$, $j \in [0, N-1]$.

The Discrete Convolution and Fast Fourier Transform (DC-FFT) method proposed embodies the wrap-around order and zero-padding techniques.

Zero Padding and wrap-around order

The discrete convolution product introduces periodicity in the calculation. However, the calculation of the normal displacement involves the pressure and the influence coefficients, which are not inherently periodic. The periodicity of the pressure introduced by the convolution leads to overlapping with the influence coefficients K,

as illustrated in Fig.A.4. The "zero-padding" method can address this issue by extending the terms from N to 2N by adding zeros. This effectively neutralizes the overlap, as shown in Fig. A.5.

Applied to the influence coefficients, the wrap-around order consists of two steps.

➤ Firstly, the initial coefficients are extended with zero values for the index N.

➤ Secondly, for the indices $N + 1$ to $2N - 1$ we write the initial (0 to $N - 1$) indices symmetrically with respect to the index N. In function of the parity of the influence coefficients, an opposite sign is applied to the extended range of coefficients. In this respect, for even coefficients the coefficients have to be extended like in Fig.A.4 and for odd coefficients they should be extended like in Fig.A.5.
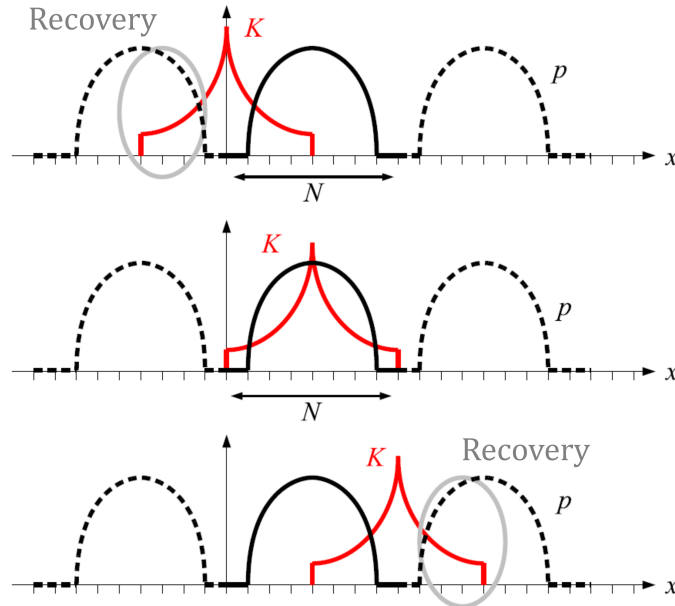
Figure A.2: Illustration of the recovery phenomenon due to periodicity of the signal when performing discrete convolutions(GAL 07).

The DC-FFT method presented above for one dimension can be applied for the two dimensional case. For calculation of the 3D fields, two possibilities arise:

❖ Use the 2D-DC-FFT for every value of the third component or

❖ Implement the 3D-DC-FFT in analogy with what has been done previous.

The latter technique is mainly used when dealing with inhomogeneities or when 3D images are involved. In the context of this study, the use of only the 2D-DC-FFT algorithm is sufficient to have a good gain in term of simulation time.

244
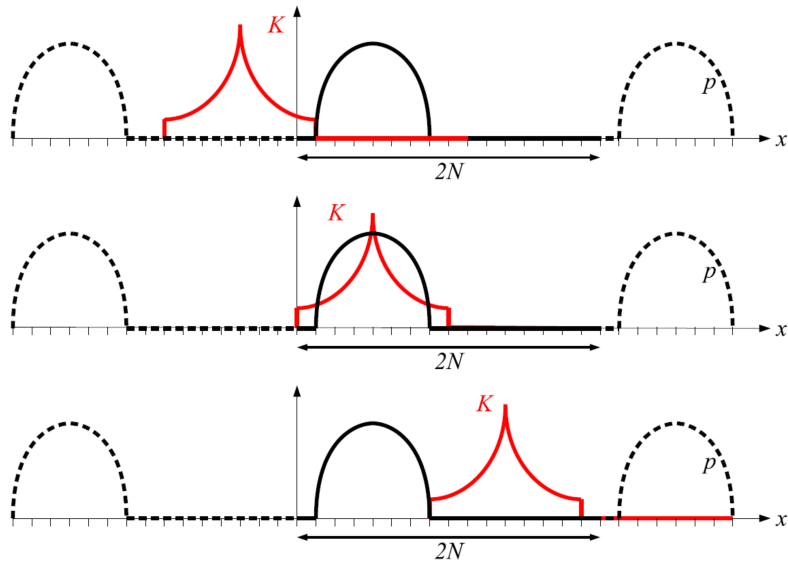
Figure A.3: Illustration of the zero padding technique to avoid the recovery phenomenon for discrete convolutions(GAL 07).

Moreover, the calculation using eventually 3D-DC-FFT would be considered only for the calculation of the 3D stresses. Those stresses are not always calculated in the process, thus the gain would not be much.

Finally, using the DC-FFT technique, the calculation of the elastic fields is guaranteed in an efficient way. However, the contact problem is not solved yet. To solve the contact problem, the numerical process used is the Conjugate Gradient Method (CGM) which is described in the next section.

A.2.5   The Conjugate Gradient Method

The Conjugate Gradient Method (CGM) is an optimization technique introduced by Hestenes and Stiefel in 1980 (HES 80) based on Conjugate Direction methods. It is commonly used to solve systems of linear equations and can also be applied to unconstrained optimization problems such as energy minimization.

Let's consider the problem of solving a system of linear equations represented by the equation:

$$\mathbf{A}\mathbf{x} = \mathbf{b} \tag{A.34}$$

where $\mathbf{A}$ is an $N \times N$ real symmetric matrix (i.e., $\mathbf{A}^T = \mathbf{A}$) that is positive-definite (i.e., $\mathbf{x}^T\mathbf{A}\mathbf{x} > 0$ for all non-zero vectors $\mathbf{x} \in \mathbb{R}^N$), and $\mathbf{b}$ is a real vector of size N.

To introduce the concept of conjugacy, let's consider two vectors $\mathbf{u}$ and $\mathbf{v}$. These vectors are conjugate if $\mathbf{u}^T\mathbf{A}\mathbf{v} = 0$. A set of mutually conjugate vectors $Q = \{\mathbf{p}_1, \cdots, \mathbf{p}_N\}$ with respect to $\mathbf{A}$ can be used to find the solution $\mathbf{x}_*$ of the
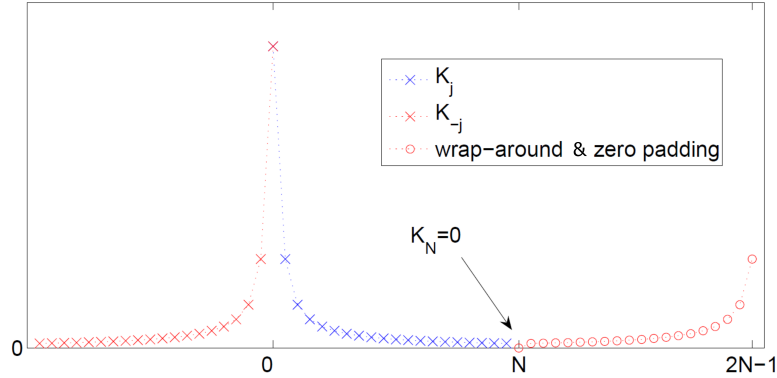
Figure A.4: Illustration of the wrap-around and zero padding of the even influence coefficients while doing the DC-FFT (GAL 07).
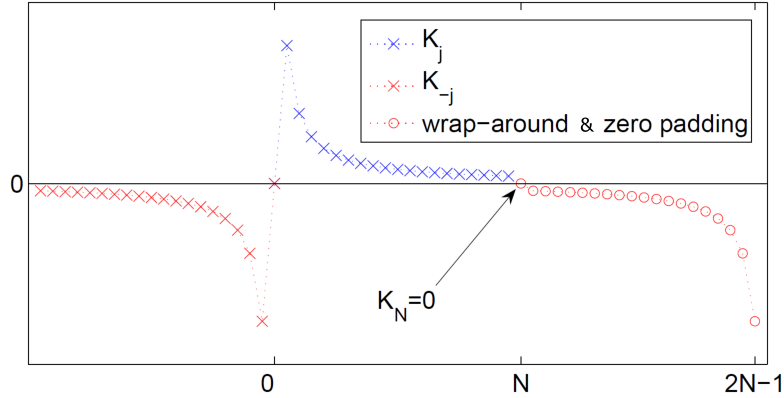
Figure A.5: Illustration of the wrap-around and zero padding of the odd influence coefficients while doing the DC-FFT (GAL 07).

system, given by:

$$\mathbf{x}_* = \sum_{i=1}^{N} \alpha_i \mathbf{A} \mathbf{p}_i \tag{A.35}$$

where $\alpha_i = \frac{\mathbf{p}_k^T \mathbf{b}}{\mathbf{p}_k^T \mathbf{A} \mathbf{p}_k}$. This solution is known as the direct solution for a well-chosen set of conjugate vectors Q. However, finding all the $\mathbf{p}_k$ vectors can be computationally expensive for large N. The CGM provides an iterative approach that can approximate the solution without explicitly computing all the conjugate vectors.

In the iterative formulation of the CGM, we start from an initial point $\mathbf{x}_0$ and use a metric to approach the solution $\mathbf{x}_*$. The problem is reformulated as a quadratic function:

$$\phi(\mathbf{x}) = \frac{1}{2}\mathbf{x}^T \mathbf{A} \mathbf{x} - \mathbf{x}^T \mathbf{b}, \qquad \mathbf{x} \in \mathbb{R}^N \tag{A.36}$$

that needs to be minimized. The gradient of the quadratic function provides the

246

solution to the original problem:

$$\nabla\phi(\mathbf{x}) = \mathbf{A}\mathbf{x} - \mathbf{b}. \tag{A.37}$$

The first conjugate direction vector $\mathbf{p}_0$ is obtained as $\mathbf{p}_0 = \mathbf{b} - \mathbf{A}\mathbf{x_0}$, which is equivalent to the gradient. The name "Conjugate Gradient Method" comes from the fact that the subsequent vectors $\mathbf{p}_k$ will be conjugate to this initial vector $\mathbf{p}_0$.

It's important to note that the gradient in the equation above is also known as the residual $\mathbf{r}(\mathbf{x})$ of the system:

$$\mathbf{r}(\mathbf{x}) = \nabla\phi(\mathbf{x}) = \mathbf{A}\mathbf{x} - \mathbf{b}. \tag{A.38}$$

At each step k, the optimal next location is determined by:

$$\mathbf{x}_{k+1} = \mathbf{x}_k + \alpha_k \mathbf{p}_k \tag{A.39}$$

where

$$\alpha_k = \frac{\mathbf{p}_k^T(\mathbf{A}\mathbf{x_k} - \mathbf{b})}{\mathbf{p}_k^T \mathbf{A}\mathbf{p_k}} = \frac{\mathbf{p}_k^T \mathbf{r_k}}{\mathbf{p}_k^T \mathbf{A}\mathbf{p_k}}. \tag{A.40}$$

The general algorithm for the CGM can be summarized as follows: Choose the starting point $\mathbf{x}_0$

$$\mathbf{r}_k \leftarrow \mathbf{A}\mathbf{x_0} - \mathbf{b}$$

if $\mathbf{r}_0$ is smaller than the chosen error, then return $\mathbf{x}_0$ as the result
$\mathbf{p}_0 \leftarrow \mathbf{r}_0$
$k \leftarrow 0$
repeat

$$\alpha_k \leftarrow \frac{\mathbf{r}_k^T \mathbf{r_k}}{\mathbf{p}_k^T \mathbf{A}\mathbf{p_k}};$$

$$\mathbf{x}_{k+1} \leftarrow \mathbf{x}_k + \alpha_k \mathbf{p}_k;$$

$$\mathbf{r}_{k+1} \leftarrow \mathbf{r}_k + \alpha_k \mathbf{p}_k;$$

if $\mathbf{r}_{k+1}$ is smaller than the error, then exit the loop

$$\beta_k \leftarrow \frac{\mathbf{r}_{k+1}^T \mathbf{r}_{k+1}}{\mathbf{r}_k^T \mathbf{r}_k};$$

$$\mathbf{p}_{k+1} \leftarrow -\mathbf{r}_{k+1} + \beta_k \mathbf{p}_k;$$

$$k \leftarrow k+1$$

end repeat
return $\mathbf{x}_{k+1}$ as the result

The CGM algorithm has also been extended to solve constrained linear systems, where the problem is formulated as follows:

$$\min_{\mathbf{x} \in \mathfrak{R}^n} \phi(\mathbf{x}) = \frac{1}{2}\mathbf{x}^T \mathbf{A}\mathbf{x} - \mathbf{b}^T\mathbf{x}, \quad \text{with} \begin{cases} c_i(x) = 0, & i \in \mathcal{E} \\ c_i(\mathbf{x}) \geq 0, & i \in I \end{cases} \tag{A.41}$$

The CGM algorithm is applied in the context of contact problems by formulating the problem in the constrained minimization form called the variational formulation of the contact problem. This formulation encompasses both the normal and tangential components of the contact problem.

A.2.6   Algorithms of contact problem resolution

In 1999, Polonsky and Keer (**?**) have proposed an algorithm that combines the conjugate gradient method with the variational formulations described earlier to solve the contact problem. This algorithm was implemented by Gallego (GAL 07) in the developpment of the homemade Isaac code. So the different steps of the algorithm are:

1. Initialization: Set the pressure field $\mathbf{p}$ to satisfy the equilibrium equation A.42.
$$\sum_{(i,j) \in \Gamma'_c} p_{ij} S_{ij} = P. \tag{A.42}$$

   where Γ'_c represents the potential contact zone, and $\lambda_{ij} = 0$ and $\zeta = 0$.

2. Surface Normal Displacement: Use DC-FFT to calculate the surface normal displacement $\bar{\mathbf{u}}_z^p$. Approximate the rigid body displacement δ_z by summing the gaps in the contact zone according to equation A.43.
$$\sum_{(i,j) \in \Gamma_c} \bar{u}_{zij}^p + h_{ij}^* = 0. \tag{A.43}$$

3. Gap Calculation: Compute the gap g_{ij} for each contact point (i,j) in the actual contact zone using $g_{ij} = \bar{u}_{zij}^p + h_{ij}^*$.
$$g_{ij} = \bar{u}_{zij}^p + h_{ij}^*, \quad (i,j) \in \Gamma'_c. \tag{A.44}$$

4. Descent Direction: Calculate the descent direction d_{ij} based on the gap g_{ij} and the previous descent direction. For contact points (i,j) in the contact zone, update $d_{ij} \leftarrow -g_{ij} + \zeta \frac{G}{G_{\text{old}}} d_{ij}$, where G is the sum of squared gaps. For non-contact points, set $d_{ij} \leftarrow 0$. Update $G_{\text{old}} \leftarrow G$ and $\zeta \leftarrow 1$.
$$d_{ij} \leftarrow -g_{ij} + \zeta \frac{G}{G_{\text{old}}} d_{ij}, \quad (i,j) \in \Gamma'_c, \tag{A.45a}$$

$$d_{ij} \leftarrow 0, \quad (i,j) \notin \Gamma'_c, \tag{A.45b}$$

where

$$G = \sum_{(i,j)\in\Gamma'_c} g_{ij}^2. \tag{A.45c}$$

Finally, $G_{\text{old}} \leftarrow G$ and $\zeta \leftarrow 1$.

5. DC-FFT on Descent Direction: Apply DC-FFT to the descent direction $\mathbf{d}$ to obtain $\mathbf{r}_z^p = \mathbf{A}_z^p \mathbf{d}$.

$$\mathbf{r}_z^p = \mathbf{A}_z^p \mathbf{d}. \tag{A.46}$$

The descent step is calculated as follows:

$$\alpha = \frac{\sum_{(i,j)\in\Gamma'_c} g_{ij}^2}{\sum_{(i,j)\in\Gamma'_c} d_{ij} r_{ij}}. \tag{A.47}$$

6. Descent Step Calculation: Compute the descent step size α as
$\alpha = \frac{\sum_{(i,j)\in\Gamma'_c} g_{ij}^2}{\sum_{(i,j)\in\Gamma'_c} d_{ij} r_{ij}}$.

7. Pressure Update: Update the pressures using $p_{ij} \leftarrow p_{ij} + \alpha d_{ij}$.

$$p_{ij} \leftarrow p_{ij} + \alpha d_{ij}. \tag{A.48}$$

8. Complementary Conditions Enforcement: Enforce complementary conditions by setting negative pressures to zero and adjusting the contact zone. If $p_{ij} < 0$ for contact points (i,j), set $p_{ij} \leftarrow 0$ and remove (i,j) from Γ'_c. If $g_{ij} = \lambda_{ij} < 0$ for non-contact points, set $p_{ij} \leftarrow -\alpha g_{ij}$, $\zeta \leftarrow 0$, and add (i,j) to Γ'_c.

$$\text{if } p_{ij} < 0, \quad (i,j) \in \Gamma'_c, \tag{A.49a}$$

$$p_{ij} \leftarrow 0, \quad \Gamma'_c \leftarrow \Gamma'_c \setminus (i,j), \tag{A.49b}$$

$$\text{if } g_{ij} = \lambda_{ij} < 0, \quad (i,j) \notin \Gamma'_c, \tag{A.50a}$$

$$p_{ij} \leftarrow -\alpha g_{ij}, \quad \zeta \leftarrow 0, \quad \Gamma'_c \leftarrow \Gamma'_c \cup (i,j). \tag{A.50b}$$

9. Equilibrium Equation Enforcement: Multiply the pressure field by a factor a to satisfy the equilibrium equation A.42, where

$$a = \frac{P}{\sum_{\Gamma'_c} p_{ij} S_{ij}}$$

Check the convergence criterion ε, given by

$$\varepsilon = \frac{\sum_{(i,j)\in\Gamma'_c} (p_{ij} - p_{ij\,\text{old}})}{\sum_{(i,j)\in\Gamma'_c} p_{ij}} < \varepsilon_0$$

If ε is below the threshold, terminate the algorithm; otherwise, go back to step 2.

$$a = \frac{P}{\sum_{\Gamma'_c} p_{ij} S_{ij}}, \tag{A.51}$$

And then the convergence criterion is tested:

$$\varepsilon = \frac{\sum_{(i,j)\in\Gamma'_c}(p_{ij} - p_{ij \text{ old}})}{\sum_{(i,j)\in\Gamma'_c} p_{ij}} < \varepsilon_0. \tag{A.52}$$

The semi-analytical solver employed in this study allows for the resolution of both normal and tangential contact problems using the methods described earlier. By solving the contact problem, the solver provides pressure and shear fields on the contact surface. These fields can be used to calculate elastic stresses within the semi-infinite space and the coefficients of influence outlined in Annex B. A "return mapping" algorithm is utilized for elastoplastic calculations to compute plastic deformations and the resulting displacements on the surface. A contact resolution loop ensures the contact problem is properly resolved on the geometrically deformed surface. The semi-analytical solver also offers additional functionalities, such as handling heterogeneities and incorporating viscoelasticity, although they need to be covered in this context. Figure A.6 shows the general algorithm for the contact problem.

A.2.7 Stress and displacement field in bodies in contact

In solving contact problems involving normal or normal + tangential forces, it is necessary to establish a relationship between the load distribution and the resulting displacements and stresses. In the case of semi-infinite elastic, homogeneous, and isotropic space, Boussinesq (BOU 85) and Cerruti(CER 82) used the theory of potentials to define the relationship between loading and stress fields and induced deformations. Love(LOV 29) later developed a similar approach for the relationship between uniform pressure acting on a rectangular area and the resulting normal displacement. Finally, Vergne (VER 85) extended this solution to the tangential problem, defining the relationship between the distribution of tangential forces and the resulting tangential displacements. These methods are still widely used today in the field of contact mechanics.

The discretization of the contact surface and the volume is a common approach to solving contact problems numerically. By discretizing the surface and volume into small rectangular and hexahedral elements, respectively, the problem is transformed into a finite number of algebraic equations that can be solved using numerical methods. Each element is centered at a specific point, and the pressure, displacement, and other relevant quantities are assumed to be constant within that element. The discretization step size Δx and Δy determine the size of each element, and the number of elements N_p is determined by the number of points in the discretization grid, which is given by $N_p = N_x \times N_y$. The pressure distribution on the contact surface
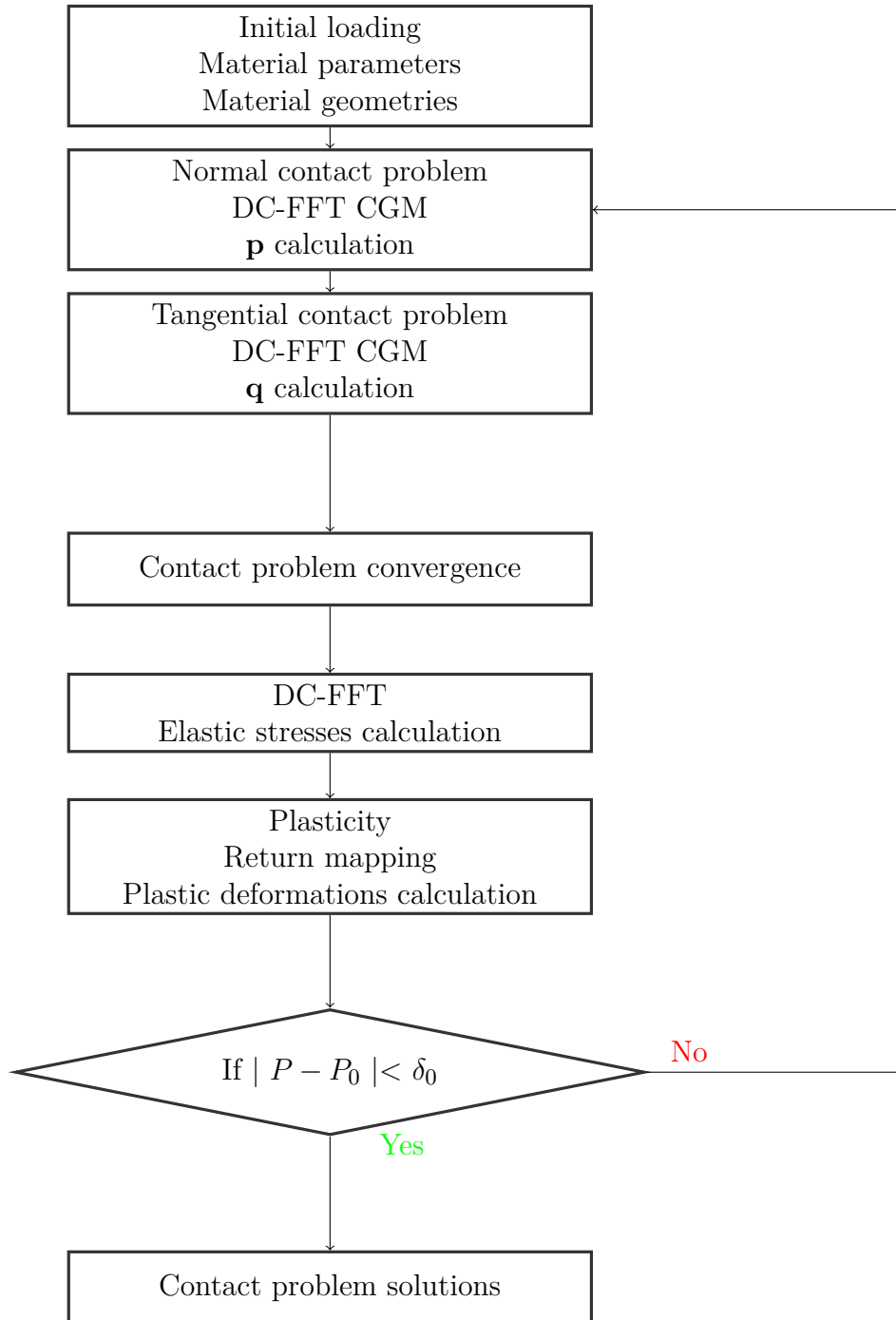
Figure A.6: General algorithm for solving the Contact Problem.

can then be approximated by a sum of pressure values on each element.

The stresses induced by the loading on a rectangular area of size $*$ centered at O and subjected to loading p, q_x, or q_y constant can be calculated using the theory of potentials. At any point $M(x, y, z)$ in the massif, the stresses induced by the loading can be expressed as follows:

$$\begin{aligned}
\frac{\sigma_{i,j}}{p} &= C_{i,j}^p(x, y, z, E, \nu) \\
&= S_{i,j}^p(x + \frac{\Delta x}{2}, y + \frac{\Delta y}{2}, E, \nu) + S_{i,j}^p(x - \frac{\Delta x}{2}, y - \frac{\Delta y}{2}, E, \nu) \\
&\quad + S_{i,j}^p(x - \frac{\Delta x}{2}, y + \frac{\Delta y}{2}, E, \nu) + S_{i,j}^p(x + \frac{\Delta x}{2}, y - \frac{\Delta y}{2}, E, \nu)
\end{aligned} \tag{A.53}$$

$$\begin{aligned}
\frac{\sigma_{i,j}}{q_x} &= C_{i,j}^{q_x}(x, y, z, E, \nu) \\
&= S_{i,j}^{q_x}(x + \frac{\Delta x}{2}, y + \frac{\Delta y}{2}, E, \nu) + S_{i,j}^{q_x}(x - \frac{\Delta x}{2}, y - \frac{\Delta y}{2}, E, \nu) \\
&\quad + S_{i,j}^{q_x}(x - \frac{\Delta x}{2}, y + \frac{\Delta y}{2}, E, \nu) + S_{i,j}^{q_x}(x + \frac{\Delta x}{2}, y - \frac{\Delta y}{2}, E, \nu)
\end{aligned} \tag{A.54}$$

$$\begin{aligned}
\frac{\sigma_{i,j}}{q_y} &= C_{i,j}^{q_y}(x, y, z, E, \nu) \\
&= S_{i,j}^{q_y}(x + \frac{\Delta x}{2}, y + \frac{\Delta y}{2}, E, \nu) + S_{i,j}^{q_y}(x - \frac{\Delta x}{2}, y - \frac{\Delta y}{2}, E, \nu) \\
&\quad + S_{i,j}^{q_y}(x - \frac{\Delta x}{2}, y + \frac{\Delta y}{2}, E, \nu) + S_{i,j}^{q_y}(x + \frac{\Delta x}{2}, y - \frac{\Delta y}{2}, E, \nu)
\end{aligned} \tag{A.55}$$

Analogously, the displacements caused by the loading at a point $M(x, y, z = 0)$ of the contact surface are given by the following relations:

$$\begin{aligned}
\frac{u_{i,j}}{p} &= K_{i,j}^p(x, y, z = 0, E, \nu) \\
&= U_{i,j}^p(x + \frac{\Delta x}{2}, y + \frac{\Delta y}{2}, E, \nu) + U_{i,j}^p(x - \frac{\Delta x}{2}, y - \frac{\Delta y}{2}, E, \nu) \\
&\quad + U_{i,j}^p(x - \frac{\Delta x}{2}, y + \frac{\Delta y}{2}, E, \nu) + U_{i,j}^p(x + \frac{\Delta x}{2}, y - \frac{\Delta y}{2}, E, \nu)
\end{aligned} \tag{A.56}$$

$$\begin{aligned}
\frac{u_{i,j}}{q_x} &= K_{i,j}^{q_x}(x, y, z = 0, E, \nu) \\
&= U_{i,j}^{q_x}(x + \frac{\Delta x}{2}, y + \frac{\Delta y}{2}, E, \nu) + U_{i,j}^{q_x}(x - \frac{\Delta x}{2}, y - \frac{\Delta y}{2}, E, \nu) \\
&\quad + U_{i,j}^{q_x}(x - \frac{\Delta x}{2}, y + \frac{\Delta y}{2}, E, \nu) + U_{i,j}^{q_x}(x + \frac{\Delta x}{2}, y - \frac{\Delta y}{2}, E, \nu)
\end{aligned} \tag{A.57}$$

$$
\begin{aligned}
\frac{u_{i,j}}{q_y} &= K_{i,j}^{q_y}(x, y, z = 0, E, \nu) \\
&= U_{i,j}^{q_y}\left(x + \frac{\Delta x}{2}, y + \frac{\Delta y}{2}, E, \nu\right) + U_{i,j}^{q_y}\left(x - \frac{\Delta x}{2}, y - \frac{\Delta y}{2}, E, \nu\right) \\
&\quad + U_{i,j}^{q_y}\left(x - \frac{\Delta x}{2}, y + \frac{\Delta y}{2}, E, \nu\right) + U_{i,j}^{q_y}\left(x + \frac{\Delta x}{2}, y - \frac{\Delta y}{2}, E, \nu\right)
\end{aligned}
\tag{A.58}
$$

Using the principle of superposition and the elementary solutions, we can solve the contact problem on a discretized grid of points on the surface of semi-infinite masses. Let us define a grid of $N_p = N_x * N_y$ points with a spacing of x in the x-direction and y in the y-direction. Each point is the center of a rectangular zone of area $S = \Delta x * \Delta y$, where normal and tangential loadings are considered constant. The stress field at any point $M(x, y, z)$ in the space is then obtained by summing the contributions of all the rectangular zones centered on each grid point, taking into account the loading and displacement influence coefficients, as follows:

$$
\sigma_{i,j}(x, y, z) = \sum_{k=1}^{N_p} C_{i,j}^{p,k} p_k + \sum_{k=1}^{N_p} C_{i,j}^{qx,k} q_{x,k} + \sum_{k=1}^{N_p} C_{i,j}^{qy,k} q_{y,k}
\tag{A.59}
$$

Where $\sigma_{i,j}(x, y, 0)$ is the stress tensor component $\sigma_{i,j}$ at point M(x, y, z = 0), $C_{i,j}^{p,k}$, $C_{i,j}^{qx,k}$, and $C_{i,j}^{qy,k}$ are the normal stress, x-direction shear stress, and y-direction shear stress influence coefficients at the k-th grid point, respectively, and p_k, $q_{x,k}$, and $q_{y,k}$ are the normal pressure, x-direction shear force, and y-direction shear force applied at the k-th grid point, respectively.

The stress field at any point $M(x, y, z)$ in the solid mass is given by the sum of the contributions from all the rectangular zones centered on each grid point, taking into account the loading and pressure influence coefficients, as follows:

$$
\begin{aligned}
\sigma_{i,j}(x, y, z) &= \sum_{k=1}^{N_p} \sum_{l=1}^{N_q} C_{p,i,j}(x - x_k, y - y_l, z, E, \nu) p(x_k, y_l) \\
&\quad + \sum_{k=1}^{N_p} \sum_{l=1}^{N_q} C_{qx,i,j}(x - x_k, y - y_l, z, E, \nu) q_x(x_k, y_l) \\
&\quad + \sum_{k=1}^{N_p} \sum_{l=1}^{N_q} C_{qy,i,j}(x - x_k, y - y_l, z, E, \nu) q_y(x_k, y_l)
\end{aligned}
\tag{A.60}
$$

Where $C_{p,i,j}$, $C_{qx,i,j}$ and $C_{qy,i,j}$ are the normal pressure, tangential force along the x-axis and tangential force along the y-axis influence coefficients, respectively. p_k, $q_{x,k}$ and $q_{y,k}$ are the values of the normal pressure, tangential force along the x-axis and tangential force along the y-axis, respectively, applied on the rectangular zone centered on the k-th grid point with coordinates $(x_k, y_k, 0)$. N_p is the total number of grid points, which is equal to $N_x \times N_y$, and ν and E are the Poisson's ratio and Young's modulus of the solid mass, respectively.

The relative displacements of surfaces can be obtained using a similar approach as for the stress field. For a point M(x, y) on the surface, the relative displacements are given by:

$$u_x = \sum_{i=1}^{N_p} U_{x,i} \cdot p_i \tag{A.61}$$

$$u_y = \sum_{i=1}^{N_p} U_{y,i} \cdot p_i \tag{A.62}$$

$$u_z = \sum_{i=1}^{N_p} S_{xy,i} \cdot q_{y,i} - S_{yx,i} \cdot q_{x,i} \tag{A.63}$$

where $U_{x,i}$ and $U_{y,i}$ are the influence coefficients for the displacement in the x and y directions respectively, caused by a unit normal load p_i applied at the center of the ith rectangular zone, and $S_{xy,i}$ and $S_{yx,i}$ are the influence coefficients for the displacement in the z direction caused by unit shear loads $q_{y,i}$ and $q_{x,i}$ applied at the center of the ith rectangular zone. Here the alert is put on the difference in the reference frame between surfaces 1 and 2 and that there is an opposition of signs for the shear terms q_x and q_y between the two surfaces.

$$\frac{\sigma_{i,j}}{q_x} = C_{i,j}^{q_x}(x,y,z,E,\nu) \tag{A.64a}$$

$$\frac{\sigma_{i,j}}{q_y} = C_{i,j}^{q_y}(x,y,z,E,\nu) \tag{A.64b}$$

$$\frac{u_j}{p} = K_j^p(x,y,E,\nu) \tag{A.65}$$

With

$$K_j^p(x,y,E,\nu) = U_j^p(x+\frac{\Delta x}{2},y+\frac{\Delta y}{2},E,\nu) + U_j^p(x-\frac{\Delta x}{2},y-\frac{\Delta y}{2},E,\nu)+$$

$$U_j^p(x+\frac{\Delta x}{2},y-\frac{\Delta y}{2},E,\nu) + U_j^p(x-\frac{\Delta x}{2},y-\frac{\Delta y}{2},E,\nu) \tag{A.66}$$

where i,j denotes the direction of the stress component, E is the elastic modulus of the material, and ν is its Poisson's ratio. The coefficients $C_{p,i,j}$, $C_{qx,i,j}$, and $C_{qy,i,j}$ are known as the influence coefficients and depend on the geometry of the loaded area and the location of the point M.

Appendix B

Parametric study on denting process

B.1 Denting problem

The denting problem refers to the occurrence of dents or depressions on the surface of a material or component. It is a common issue in various industries, including automotive, aerospace, and manufacturing. Dents can be caused by various factors, such as impact or collision with other components, excessive loads or pressure, improper handling or storage, or particle crushing in two components contact. The dent's severity can range from minor surface imperfections to deep deformations that compromise the component's structural integrity. The study of surface fatigue caused by lubricant contamination is a complex undertaking that necessitates careful consideration of the conditions that give rise to dents. While naturally occurring dents can display various characteristics, researchers often prefer to utilize artificial dents generated through techniques such as spherical indenters or finite element models in plane strain or axisymmetric configurations in fatigue studies. The use of artificial dents offers the advantages of repeatability and generalizability.

Several researchers, including Xu et al. (XU 20), Warhadpande and Sadeghi (WAR 10), Morales and Gabelli (DIA 03; COU 05; NEL 05; ANT 08; MOR 11b; MOR 15a; MOR 15b; MOR 16; VIE 16) and others (JAC 01; JAC 02; JAC 03), have employed artificial dents to investigate the impact of residual stresses, microstructure, and lubrication conditions on the behavior of dented surfaces.

While natural dents may pose challenges in experimental design and interpretation, dedicated efforts in this area can still yield valuable insights into the mechanisms underlying surface fatigue. However, for studies that require precise control and reproducibility, artificial dents remain a valuable tool.

The behavior of particles in suspension within the lubricant during their passage through contact has been investigated by researchers such as Wan and Spikes (WAN 88), Dwyer-Joyce et al. (DWY 90; DWY 92; CAN 96; DWY 05) and others (VIL 98a; VIL 98b; VIL 99a; VIL 99b). These studies utilized optical setups capa-

ble of capturing microphotographs, as exemplified in Fig.B.1, to observe and analyze particle behavior. The researchers observed distinct differences in the behavior of particles depending on their nature. Ductile particles were found to undergo crushing as they passed through the contact. This crushing process occurred continuously throughout their passage, resulting in particle shape and size changes. In contrast, brittle particles shatter early in the process, creating clouds of dents. Figure.B.1 schematically illustrates this behavior. The shattering of brittle particles leads to generating numerous dents in the surrounding area. Dwyer-Joyce et al. (DWY 92)

(a)   (b)
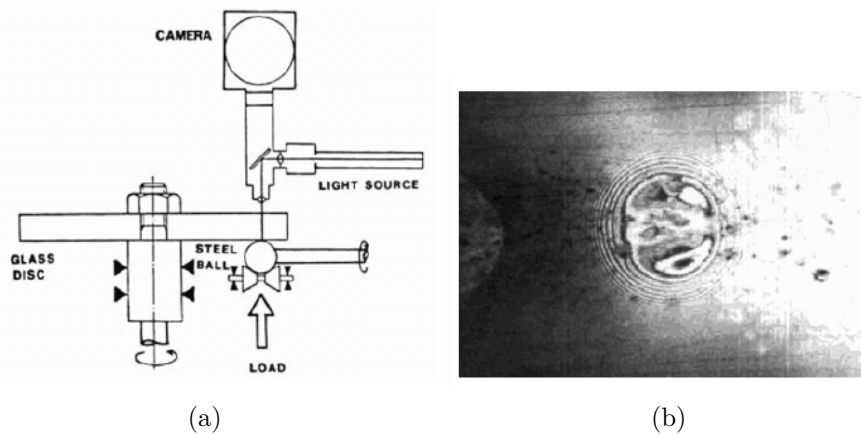
Figure B.1: Observation montage of the EHD contact (a) and photomicrograph showing the passage of SAE 30 particles in the contact (b), according to (WAN 88)

established a relationship between particle size, surface geometry, and the coefficient of friction to define the maximum particle size that can enter the contact. Finally, Cann et al.(CAN 96) compared the profiles of dents obtained with and without lubricant for iron particles with a diameter of $30-60\mu m$. In the presence of lubricant, a reduction in the depth of the dent is observed, as illustrated in Fig.B.1,B.3. This reduction is of the same order of magnitude as the thickness of the lubricant film.

(a)   (b)
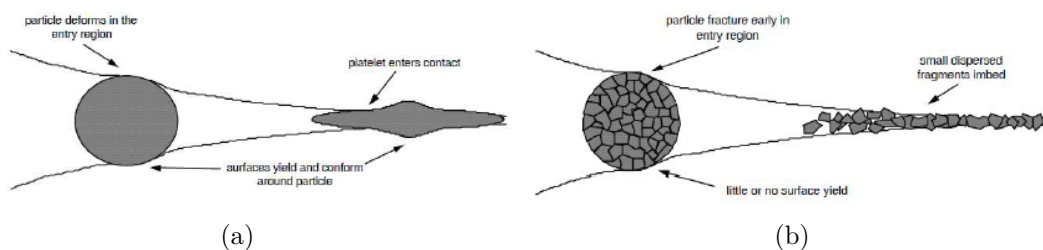
Figure B.2: The behavior of a ductile particle (a) and a fragile particle (b) when passing through the contact, according to (DWY 92)

.

256

In their research, Ville and Nélias have conducted various studies (VIL 98a; VIL 98b; VIL 99b; NEL 00) where they developed a pollution test rig, originally imagined by Nelias (NEL 99). This test rig enables them to introduce a known number of particles into the lubricant and control the concentration of particles. Using this setup, they studied the contact indentation between bi-disc steel rollers made of AISI 52100. Through their experiments, Ville and Nélias observed that the number of dents counted on the surfaces of the rollers exhibited a linear relationship with the product of the particle concentration in the lubricant and the duration of the test. This relationship is illustrated in Fig.B.4. The linear correlation between the number of dents and the particle concentration and test duration suggests that these factors significantly influence the indentation process. In their study, the authors investigated the behavior of different particle types: ductile M50 steel particles and fragile SiC silica carbide or sand SAE AFTD particles. They confirmed the previously observed differences in behavior between these particle types. By conducting experiments with particles of varying sizes, ranging from 10-20 μm to 40-50 μm, the authors established a direct relationship between particle size and the dimensions of the dent. Larger particles resulted in larger dents, indicating that particle size plays a significant role in indentation.
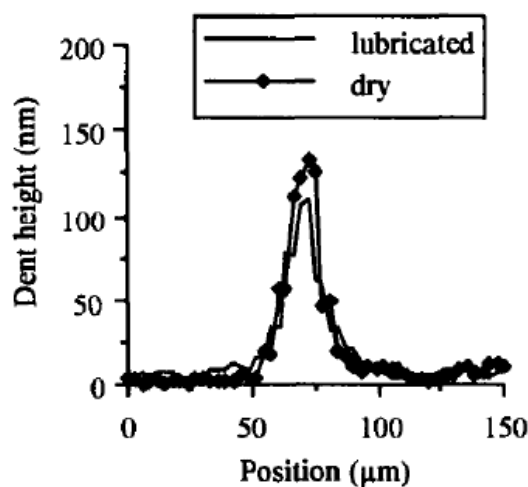
Figure B.3: Indentation profiles acquired from iron particles from initial diameter of 30-60 μm under both dry and lubricated contact conditions, as outlined in (CAN 96)

The authors also examined the effect of relative slip between the surfaces. They found that the relative slip tends to spread the particles in the direction of friction, leading to longer dents and the embedding of particles in the surfaces. Furthermore, the authors compared tests conducted at different speeds and observed a reduction in the dent depth in lubricated contact. This reduction, on the order of the lubricating film thickness, aligns with the observations made by Cann et al. (CAN 96).
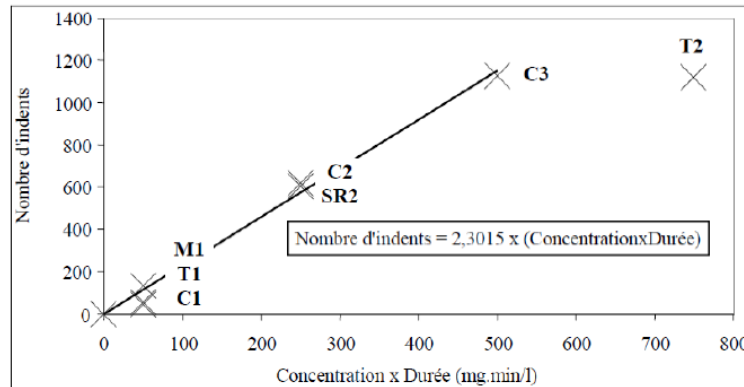
Figure B.4: Count of dents observed on surfaces based on variations in product concentration and duration (VIL 99b).

This consistency supports the understanding that lubrication plays a crucial role in modifying the behavior and characteristics of dents.
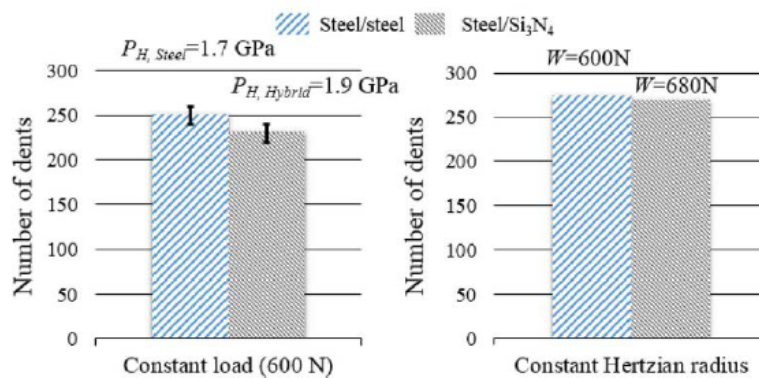
Figure B.5: Rate of particle capture in steel-steel or hybrid contacts under conditions of constant head and a consistent Hertz zone size, as detailed in (STR 16).

So it appears that the use of ceramic rolling bodies in hybrid bearings can provide protection against indentation for the ceramic body but at the expense of the facing surface, which experiences deeper dents. This observation is supported by studies conducted by Tonicello et al.(TON 12b) and Strubel et al.(STR 16; STR 17). Additionally, the nature of the contact does not seem to affect the capture rate of particles, as demonstrated by Fig.B.5.

In modeling the passage of a particle in rolling contact, relatively fewer analytical or numerical studies have been conducted. One of the early approaches was presented by Hammer et al. (HAM 87; HAM 89), who approximated the phenomenon by relating it to crushing a spherical particle between two flat surfaces. They provided an analytical expression for the axisymmetric pressure field and the shape of the dent. This approach was supported by experimental tests conducted by the same

authors and demonstrated the ability of soft particles to cause damage to harder surfaces through confinement.

Ko and Ioannides (KO 89) developed two finite element models, one axisymmetric and the other in plane strain, based on the work of Hammer presented in Fig.B.6. These models replicated the crushing of a spherical and cylindrical particle and allowed for the study of residual stresses after indentation. Kang et al. (KAN 04) later introduced the rolling effect into the modeling by developing a finite element model for the passage of a particle in a two-disc contact. This model enabled a parametric study of indentation and produced results in agreement with the experimental tests conducted by de Ville and Nelias (VIL 98a; VIL 98b; VIL 99b; NEL 00). The study also examined the effect of the coefficient of friction between the particle and the surfaces, showing that a reduction in friction led to decreased frictional forces opposing the spreading of the particle and resulted in wider and more superficial dents.

When the coefficient of friction between the particle and the surfaces is reduced, the opposing frictional forces decrease, allowing the particle to spread more easily. This leads to wider and more superficial dents, as observed in indentation experiments. Finite element analysis can be used to model and simulate this phenomenon, providing valuable insights into the behavior of particles during indentation.

(a)   (b)
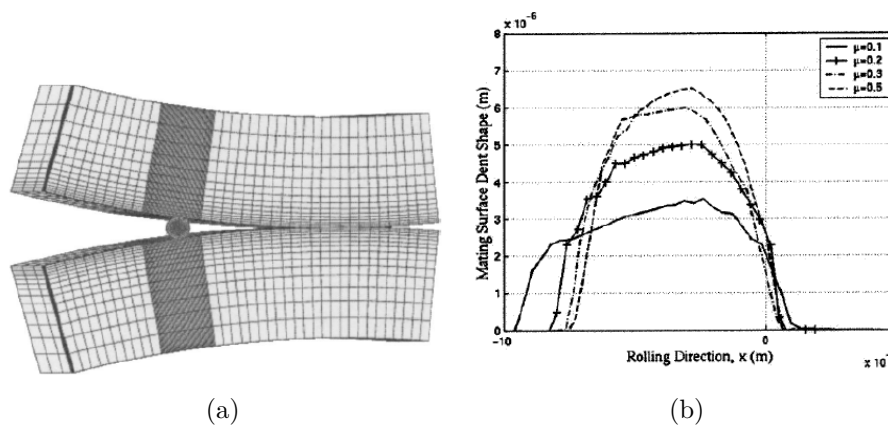
Figure B.6: (a) Axisymmetric finite element (FE) model and plane strain representation (KO 89). (a) Finite element model depicting the passage of a spherical particle within a two-disc contact and profiles of dents acquired through this model for varying friction coefficient values (KAN 04).

Recently, Nikas's analytical model enables to take into account multiple factors, including plasticity, sliding, lubrication, thermal effects, and strain rate effects. The model has been further improved by incorporating thermal and strain rate effects in subsequent studies, demonstrating ongoing efforts to enhance the accuracy of modeling and simulations in the field of rolling contact mechanics. A significant finding of Nikas's model is the generation of high temperatures within the particle during its

passage through contact. Plastic work and friction contribute to this heating, and in some cases, the temperatures can reach the melting point locally. This emphasizes the importance of considering thermal effects in accurately predicting the behavior of particles during indentation.
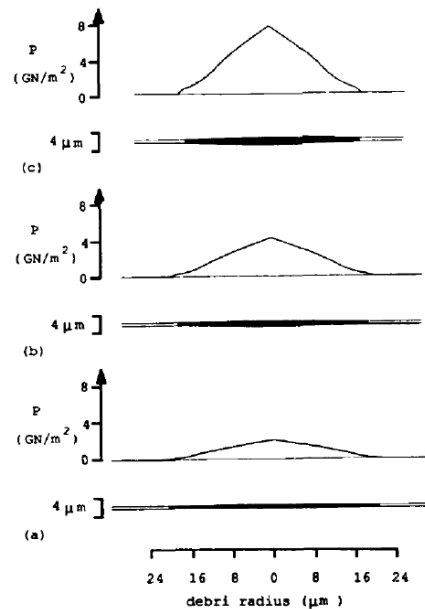
Figure B.7: The pressure profile and indentation shape for particles on top of low alloy steel, mild steel, and copper surfaces were sourced from (HAM 87).

Additionally, Nikas (NIK 12; NIK 13; NIK 14) highlights the significance of incorporating visco-plastic effects in the model. This can be achieved through a Johnson-Cook-type behavior law, which captures the time-dependent deformation behavior of the particle and the influence of strain rate on its response.

Studying the fatigue of indented surfaces requires careful consideration of the operating conditions and the ability to create dents with specific parameters. A flexible numerical indentation tool is essential for this purpose as it allows for the accurate and reproducible creation of dents with controlled parameters such as size, shape, and depth. Such a tool enables researchers to precisely control the contact parameters and explore the effects of different materials and surface coatings on the fatigue behavior of the indented surfaces. This capability enhances understanding how dents respond to varying conditions and contribute to developing more effective fatigue mitigation strategies.

In parallel with experimental studies, developing a versatile finite element model that incorporates thermal and visco-plastic effects is crucial for a comprehensive understanding of indented surfaces. While previous models discussed in the text have limitations, incorporating these effects can significantly improve the accuracy of simulations. However, it is important to consider the computational cost associated

with such models, as high computational requirements can hinder their practical use in industrial applications.

Therefore, the challenge lies in balancing accuracy and computational cost when developing a finite element model. It should accurately capture the thermal and visco-plastic effects while being computationally efficient enough for practical utilization. This balance allows for wider adoption of the model in industrial contexts, where time and computational resources are often limited. With an accurate and efficient model, researchers can investigate the fatigue behavior of indented surfaces under realistic conditions and explore the influence of various parameters and operating conditions on fatigue life.

The Coupled-Euler-Lagrange model, developed by Bonetto et al.(BON 20), is an example of a sophisticated numerical approach that addresses the challenges of incorporating thermal and visco-plastic effects while maintaining reasonable computational costs. This model provides a framework for implementing a versatile finite element model capable of capturing these effects accurately. Additionally, the ongoing efforts to update and extend the model to consider operating conditions and new parametric studies further enhance its applicability and relevance in studying indented surfaces.

Figure.B.9 depicts how the elastic modulus and the yield strength of the particle impact the dent profile. It's noticeable that the modulus has a minimal effect, while the elastic limit moderately affects the dent profile.
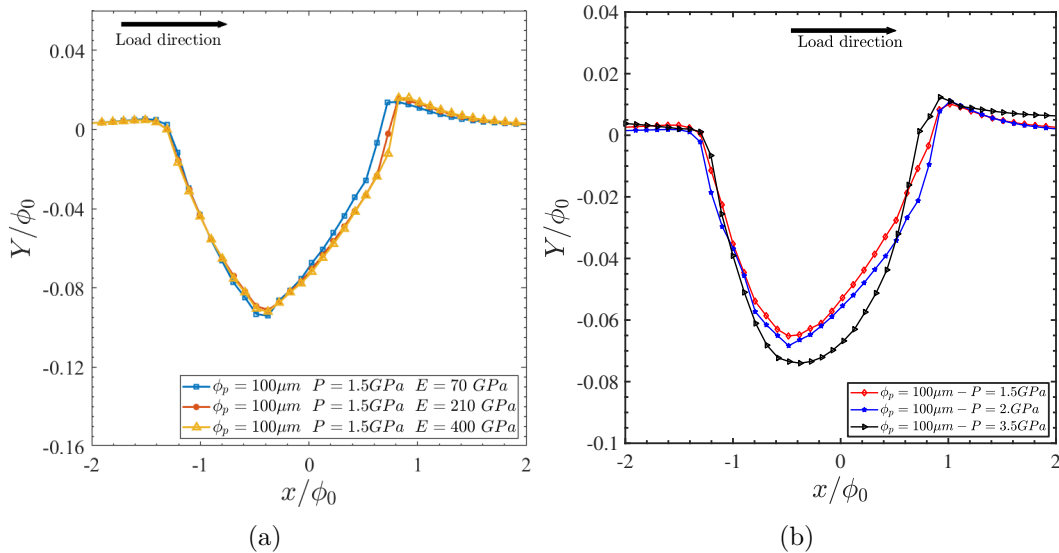
Figure B.8: Dent profile according (a) Influence of the modulus, (b)Dent profile for yield strength $\sigma_0 = 0.5GPa$.

When examining hybrid rolling, it becomes evident that the indentation profiles differ, characterized by greater indent depths, smaller indent diameters, and notably elevated bead heights, as depicted in the illustrations figure Fig.B.10. Specifically,
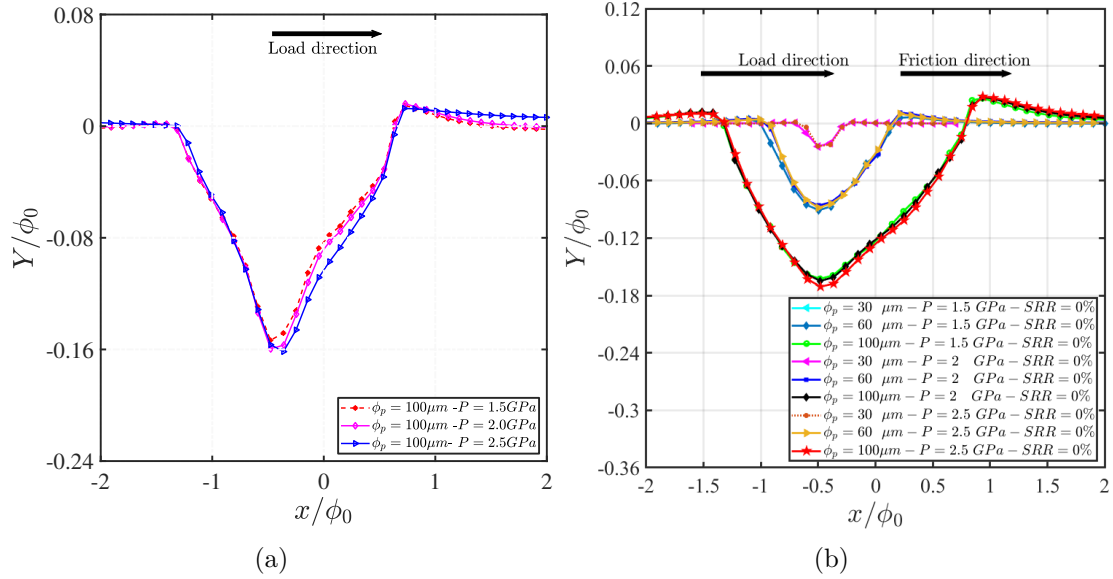
Figure B.9: Dent profile according (a) For a particle elastic limit of $\sigma_0 = 3GPa$, (b) Influence of the particle size and loading.

in pure rolling scenarios, the bead heights are comparatively lower than those seen in the presence of sliding. In hybrid bearing conditions, a protrusion becomes noticeable around the material bead. This is primarily attributed to the expulsion of material from the interior, which is then slightly smoothed on the surface due to the movement of rolling elements.

The harder a particle is, the more fishy effect it will create on the track. The fish effect consists of the deformation in the direction transverse to the loading of the track due to the poisson ratio of the materials which tends to shrink the surface section of the indent.

The loading effect of the particles on the tracks which is an effect combining the level of loading and the hardness of the particles consisting in crushing a level of bead by the loading which induced it.

In the scenario of the hybrid bearing, a swift saturation in the evolution of bead height was observed in relation to various parameters. This phenomenon can be rationalized by the increase in these parameter values, leading to the particle's penetration reaching a threshold beyond which the bead height diminishes. This reduction occurs due to the material pressing against itself, prompted by the constriction effect.

262
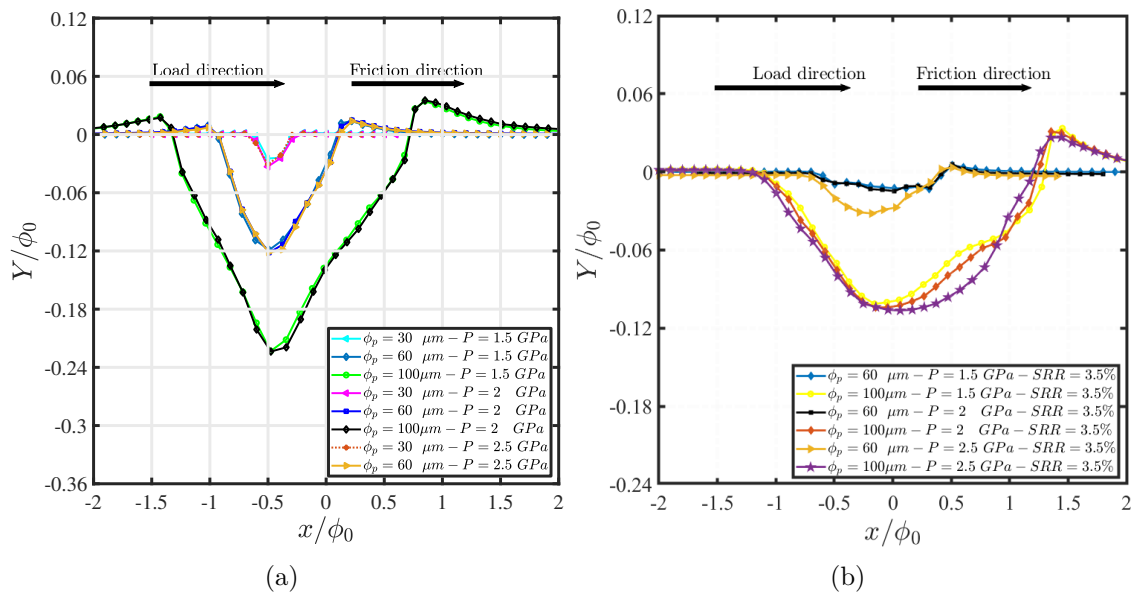
Figure B.10: (a) Dent profile in pure rolling for particle yield strenght $\sigma_0 = 1712$ MPa, (b) Dent profile in pure rolling for particle yield strenght $\sigma_0 = 3000$ MPa, (c) Dent profile in rolling/sliding for particle yield strenght $\sigma_0 = 500$ MPa.
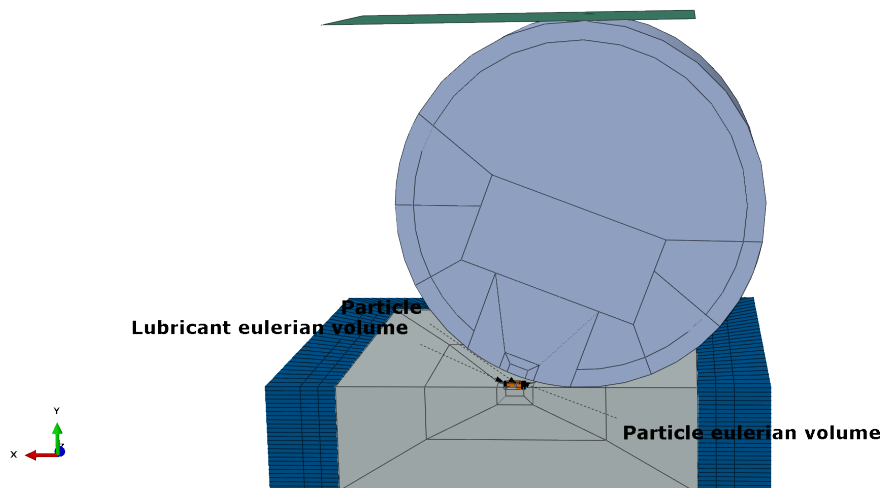
Figure B.11: Presence of lubricant in CEL model.

Appendix C

Fatigue criteria

C.1 Stress invariants

Consider a volume of matter subjected to a stress tensor $\overline{\overline{\sigma}}$. The tensor can be decomposed into a deviatoric part s and a hydrostatic part:

$$\overline{\overline{\sigma}} = \overline{\overline{s}} + \sigma_H \overline{\overline{I}} \tag{C.1}$$

The hydrostatic stress σ_H is the first invariant of the stress tensor $\overline{\overline{\sigma}}$ and $\overline{\overline{I}}$ is the identity tensor.

$$\sigma_H = \frac{1}{3} tr(\overline{\overline{\sigma}}) \tag{C.2}$$

In fatigue rolling, two constraint invariants are commonly used: the first invariant of the deviatoric stress tensor and the second invariant of the von Mises equivalent stress tensor.

The first invariant of the deviatoric stress tensor is denoted as J_2 and represents the magnitude of the deviatoric stresses. It is defined as:

$$\overline{\overline{J_2}} = (1/2)s_{ij}s_{ij} \tag{C.3}$$

Where s_{ij} is the deviatoric stress tensor, defined as:

$$s_{ij} = \sigma_{ij} - \frac{1}{3}\sigma_{kk}\delta_{ij} \tag{C.4}$$

Where s_{ij} is the stress tensor, and δ_{ij} is the Kronecker delta.

The second invariant of the von Mises equivalent stress tensor is denoted as J_3 and represents the magnitude of the equivalent stress. It is defined as: Over a loading cycle, the maximum hydrostatic stress, as well as the mean hydrostatic stress is defined as:

Maximum hydrostatic stress:

264

$$\sigma_{H,max} = \max_{t \in [0,T]} (\sigma_H(t))$$

Mean hydrostatic stress:

$$\sigma_{H,mean} = \frac{1}{T} \int_0^T \sigma_H(t) dt$$

where $\sigma_H(t)$ is the hydrostatic stress at time t during the loading cycle and T is the total time of the loading cycle.

The deviatoric stress tensor s is used to define the second invariant of constraints, noted J_2:

$$\overline{\overline{J_2}} = \frac{1}{2} s_{ij} s_{ij} \tag{C.5}$$

Where s_{ij} represents the deviatoric stress tensor. The value of J_2 corresponds to the square of the von Mises equivalent stress, commonly used in fatigue analysis. It takes into account both the normal and shear stresses acting on the material and is defined as:

$$\sigma_{eq} = \sqrt{(3\overline{\overline{J_2}})} \tag{C.6}$$

Where $tr(\overline{\overline{\sigma}})$ is the trace of the stress tensor, and $\overline{\overline{I}}$ is the identity tensor. The deviatoric part represents the contribution of the shear stresses, while the hydrostatic part represents the contribution of the normal stresses. The use of the deviatoric part is common in fatigue analysis as it is more sensitive to the presence of shear stresses, which are often the primary cause of fatigue failure.

In the context of fatigue, the deviatoric stress tensor is used to evaluate the damage accumulation in a material during cyclic loading. The average part of the deviatoric stress tensor, smoy, is related to the mean stress while the alternating part, sa, is related to the amplitude of the stress variation. These parameters are used in fatigue criteria to predict the fatigue life of a material. To determine the values of smoy and sa, we need to evaluate the deviatoric stress tensor over a loading cycle. The curve traced by the deviatoric stress tensor in the 6-dimensional space is generally complex and irregular. Therefore, to obtain representative values of smoy and sa, we need to find the smallest 6-dimensional hypersphere that encloses the curve traced by the deviatoric stress tensor. This hypersphere is called the minimum enclosing hypersphere, and its center corresponds to the average value of the deviatoric stress tensor, while its radius corresponds to the alternating part. Finding the minimum enclosing hypersphere is a non-trivial problem in high-dimensional spaces. Still, it allows us to obtain representative values of smoy and sa from the irregular loading path. This is important because the fatigue life of a material depends on the

amplitude and mean of the cyclic stress and not on the details of the loading path. Therefore, by using smoy and sa obtained from the minimum enclosing hypersphere, we can predict the fatigue life of a material more accurately.

The search for the center and radius of the smallest hypersphere circumscribed to a curve can be achieved through minimization algorithms. The most commonly used algorithm is the Welzl algorithm, which can determine the center and radius of the smallest sphere circumscribing a set of points up to dimension 3. For higher dimensions, Gartner extended the algorithm to hyperspheres of dimension $n = 10$. These algorithms can be implemented in software such as Matlab or through dedicated algorithms.

The Tresca criterion states that material failure occurs when the maximum shear stress in a material exceeds a critical value. In the case of rolling fatigue, this criterion is applied to the alternating part of the tensor of deviatoric stresses, sa. The component τ_{pr} is defined as half of the difference between the maximum and minimum values of the shear stress, which can be written as:

$$\tau_{pr} = \frac{1}{2}(s_1 - s_3) \tag{C.7}$$

where s_1 and s_3 are the maximum and minimum principal stresses, respectively, obtained from the eigenvalues of the deviatoric stress tensor. The critical shear stress τ_c can be obtained experimentally or from theoretical models, and material failure occurs when $\tau_{pr} > \tau_c$.

C.2 Variables acting on a plane

The critical plane fatigue criteria use plane invariant variables to predict the onset of fatigue failure. These variables are derived from the stress and strain tensors on a specific plane called the critical plane. The critical plane is the plane of maximum shear stress range over a loading cycle. The plane invariant variables commonly used in critical plane fatigue criteria include:

❀ Normal stress amplitude (σ_a): This is the average absolute value of the critical plane's maximum and minimum normal stress.

❀ Shear strain amplitude (γ_a): This is the average absolute value of the critical plane's maximum and minimum shear strain.

❀ Maximum shear stress range ($\Delta\tau_{max}$): This is the maximum difference between the maximum and minimum shear stress on the critical plane.

❀ Shear stress amplitude (τ_a): The average absolute values of the maximum and minimum shear stress on the critical plane.

❈ Normal strain amplitude (ε_a): This is the average absolute value of the critical plane's maximum and minimum normal strain.

These variables can be used to calculate the fatigue damage or life of a material under cyclic loading based on empirical or theoretical models. The accuracy of the prediction depends on the validity of the model and the accuracy of the input data.

The stress vector $\overline{T}$ acting on the plane with normal vector $\overline{n}$ can be decomposed into a normal stress vector $\overline{N}$ and a vector of shear stress $\overline{\tau}$, $\overline{N}$ is defined as the projection of $\overline{T}$ onto the normal direction $\overline{n}$, while $\overline{\tau}$ is defined as the projection of $\overline{T}$ onto the plane perpendicular to $\overline{n}$. In equations, this can be expressed as:

$$\overline{N} = \overline{T}\,\overline{n} \tag{C.8}$$

$$\overline{\tau} = \overline{T} - \overline{N} \tag{C.9}$$

C.3   Fatigue criteria with stress invariants

The fatigue criteria based on stress invariants do not provide information about the orientation of fatigue cracks. These criteria are based on invariant scalar quantities under coordinate transformations, such as the first and second stress invariants or the maximum shear stress. They provide a way to assess the potential for failure based on the magnitude of the stress state but do not consider the stress's direction or orientation. Criteria based on the critical plane can be used to obtain information about the orientation of fatigue cracks. These criteria consider the stress state's variation as the plane's orientation changes. They are based on the assumption that the plane of maximum shear or normal stress is the most critical for crack initiation and propagation. There are several critical plane-based fatigue criteria, such as the Smith-Watson-Topper (SWT) criterion (SMI 70), the Fatemi-Socie (FS) criterion (FAT 88), and the Brown-Miller (BM) criterion (BRO 73). These criteria use different combinations of stress components on the critical plane to calculate a fatigue damage parameter, which can be compared to a fatigue limit or S-N curve to assess the potential for failure. The critical plane-based criteria are more complex to apply and require more computational effort, but they can provide more accurate predictions of fatigue life and crack orientation.

C.4   Stress fatigue criteria

The Dang Van criterion is a fatigue criterion considering the effect of multiaxial stress states. Dang Van proposed it in 1984 (VAN 84), and has been widely used in the industry. The criterion is based on the stress invariants and is expressed in

terms of the maximum shear stress amplitude and the normal stress amplitude on the critical plane. The original Dang Van criterion (1984) involves searching for the critical plane where the maximum shear stress amplitude is maximum. The criterion can be expressed as follows:

$$\frac{\tau_{max}}{\sigma_a} + k\frac{\sigma_{max}}{\sigma_a} \leq 1 \tag{C.10}$$

Where τ_{max} is the maximum shear stress amplitude, σ_{max} is the maximum normal stress amplitude, σ_{max} is the stress amplitude, and k is a material parameter. However, the search for the critical plane is computationally expensive in 3D problems. Therefore, in 1989, Dang Van.(VAN 89) proposed a simplified version of the criterion that does not require the search for the critical plane. The simplified criterion can be expressed as:

$$(\frac{\tau_a}{\sigma_a})^2 + (\frac{\sigma_n}{\sigma_a})^2 \leq 1 \tag{C.11}$$

Where τ_a is the amplitude of the shear stress on the plane perpendicular to the mean stress, σ_n is the normal stress on the same plane, and σ_a is the stress amplitude. This criterion is simpler but may be less accurate than the original one. The Dang Van criterion is widely used in the industry due to its simplicity and effectiveness in predicting fatigue failure under multiaxial loading.

Bibliography

[AHM 83] AHMADI N., KEER L. M., MURA T.
Non-Hertzian Contact Stress Analysis for an Elastic Half Space-Normal and Sliding Contact. *International Journal of Solids and Structures*, vol. 55, 1983, p. 357-373.

[AHY 22] AHYEE A. K., CHAISE T., DUVAL A., NÉLIAS D.
Nouvelle résolution numérique du problème de quart de massif en présence de bords libres. *15ème colloque national en calcul des structures*, , 2022.

[ALV 04] ALVES J., OLIVEIRA M., MENEZES L.
An advanced constitutive model in sheet metal forming simulation: the Teodosiu microstructural model and the Cazacu Barlat yield criterion. *International Journal of Mechanical Sciences*, vol. 51, nº 5, 2004, p. 357–381.

[AMU 16a] AMUZUGA K.
Damage mechanism related to plasticity around heterogeneous under rolling contact loading in hybrid bearings ceramic/steel. Thèse de doctorat, INSA Lyon, Lyon, 2016.

[AMU 16b] AMUZUGA K., CHAISE T., DUVAL A., NÉLIAS D.
Fully Coupled Resolution of Heterogeneous Elastic-Plastic Contact Problem. *Journal of Tribology*, vol. 138, nº 2, 2016, Page 021403.

[AND 81] ANDERSSON T.
The Boundary Element Method applied to Two-Dimensional Contact Problems with Friction. BREBBIA C., Ed., *Boundary Element Methods*, p. 239–258 Springer Berlin Heidelberg, Berlin, Heidelberg, 1981.

[ANT 05] ANTALUCA E.
Contribution á l'étude des contacts élasto-plastiques et d'un chargement normal et tangentiel. Thèse de doctorat, INSA de Lyon, 2005.

[ANT 08] ANTALUCA E., NÉLIAS D.
Contact fatigue analysis of a dented surface in a dry elastic-plastic circular point contact. *Tribology Letters*, vol. 29, nº 2, 2008, p. 139–153.

[ARM 66] ARMSTRONG P., FREDERICK C.
A mathematical representation of the multiaxial Bauschinger effect. Technical Report nº RD/B/N731, 1966, Berkeley Nuclear Laboratories.

[ARZ 98] ARZT E.
Size effect in materials due to microstructural and dimensional constraints: a comparative review. *Acta Materialia*, vol. 46, nº 1, 1998, p. 5611–5626.

[BEN 67] BENTALL R. H., JOHNSON K. L.
Slip in the rolling contact of two dissimilar elastic rollers. *International Journal of Mechanical Science*, vol. 9, nº 6, 1967, p. 389–404.

[BEN 68] BENTALL R., JOHNSON K.
An elastic strip in plane rolling contact. *International Journal of Mechanical Sciences*, vol. 10, nº 8, 1968, p. 637–663.

[BEY 19] BEYER T., CHAISE T., LEROUX J., NELIAS D.
A damage model for fretting contact between a sphere and a half space using semi-analytical method. *International Journal of Solids and Structures*, vol. 164, 2019, p. 66–83.

[BLA 91] BLAKE J. W., CHENG H. S.
A surface pitting life model for spurs gears: ASME Journal of Tribology. vol. 113, 1991, p. 712–718.

[BLA 16] BLANCO-LORENZO J., SANTAMARIA J., VADILLO E., CORREA N.
On the influence of conformity on wheel-rail rolling contact mechanics. *Tribology International*, vol. 103, 2016, p. 647–667.

[BLA 18] BLANCO-LORENZO J., SANTAMARIA J., VADILLO E., CORREA N.
A contact mechanics study of 3D frictional conformal contact. *Tribology International*, vol. 119, 2018, p. 143–156.

[BOF 12] BOFFY H., BAIETTO M.-C., SAINSOT P., LUBRECHT A.
An Efficient 3D Model of Heterogeneous Materials for Elastic Contact Applications Using Multigrid Methods. *Journal of Tribology*, vol. 134, nº 2, 2012, p. 021401 1–8.

[BOF 14] BOFFY H., VENNER C.
Multigrid solution of the 3D stress field in strongly heterogeneous materials. *Tribology International*, vol. 74, 2014, p. 121–129.

[BOL 98] BOLSHAKOV A., PHARR P.
Influences of pile-up on the measurement of mechanical properties by load and depth sensing indentation techniques. *J Mater Res*, vol. 13, 1998, Page 1049.

[BOL 13] BOLZON G., TALASSI M.
An effective inverse analysis tool for parameter identification of anisotropic material models. *International Journal of Mechanical Sciences*, vol. 77, 2013, p. 130–144.

[BON 19] BONETTO A., NÉLIAS D., CHAISE T., ZAMPONI L.
A Coupled Euler-Lagrange Model for More Realistic Simulation of Debris Denting in Rolling Element Bearings. *Tribology Transactions*, vol. 62, n° 5, 2019, p. 760–778.

[BON 20] BONETTO A.
Etude de l'indentation et de la fatigue des contacts roulants. Thèse de doctorat, INSA Lyon, 2020.

[BOU 85] BOUSSINESQ J.
Application des potentials à létude de l'équilibre et des mouvements des solides elastiques. 1885.

[BOU 05] BOUCLY V., NÉLIAS D., LIU S., WANG Q. J., KEER L. M.
Contact analyses for bodies with frictional heating and plastic behavior. *Journal of Tribology*, vol. 127, n° 2, 2005, p. 355–364.

[BOW 87] BOWER A. F., JOHNSON K. L., KALOUSEK J.
A ratchetting limit for plastic deformation of a quarter-space under rolling contact loads. *In: Proc. Int. Symp.on Contact Mechanics and Wear of Rail/Wheel Systems II. University of Waterloo Press*, , 1987, p. 117–131.

[BRA 18] BRANCO R., PRATES P., COSTA J., BERTO F., KOTOUSOV A.
New methodology of fatigue life evaluation for multiaxially loaded notched components based on two uniaxial strain-controlled tests. *International Journal of Fatigue*, vol. 111, 2018, p. 308–320.

[BRO 73] BROWN M. W., MILLER K. J.
A Theory for Fatigue Failure under Multiaxial Stress-Strain Conditions. *Proceedings of the Institution of Mechanical Engineers*, vol. 187, n° 1, 1973, p. 745–755.

[BRO 08] BROGGIATO G., CAMPANA F., CORTESE L.
The Chaboche nonlinear kinematic hardening model: Calibration methodology and validation. *Meccanica*, vol. 43, 2008, p. 115–124.

[BUC 03] BUCAILLE J. L., STAUSS S., FELDER E., MICHLER J.
Determination of plastic properties of metals by instrumented indentation using different sharp indenters. *Acta Materialia*, vol. 51, 2003, p. 1663–1678.

[BUR 20] BURGOLD A., DROSTE M., SEUPEL A., BUDNITZKI M., BIERMANN H., KUNA M.

Modeling of the cyclic deformation behavior of austenitic TRIP-steels. *International Journal of Plasticity*, vol. 133, 2020, Page 102792.

[CAN 96] CANN P. M., SAYLES R., SPIKES H., IOANNIDES E., HAMER J.
Direct observation of particle entry and deformation in a rolling EHD contact. *Tribology Series*, vol. 31, 1996, p. 127–134.

[CAO 04] CAO Y. P., LU J.
A new scheme for computational modelling of conical indentation in plastically graded materials. *Acta Materialia*, vol. 9, 2004, p. 1703–1716.

[CAO 21] CAO W., YANG J., ZHANG H.
Unified constitutive modeling of Haynes 230 including cyclic hardening/softening and dynamic strain aging under isothermal low-cycle fatigue and fatigue-creep loads. *International Journal of Plasticity*, vol. 138, 2021, Page 102922.

[CAR 13] CARBONE G., PUTIGNANO C.
A novel methodology to predict sliding and rolling friction of viscoelastic materials: Theory and experiments. *Journal of the Mechanics and Physics of Solids*, vol. 61, n° 8, 2013, p. 1822–1834.

[CER 82] CERRUTI V.
Ricerche intorno all'equilibrio dei corpi elastici isotropi, Reale Accademia dei Lincei. *Roma*, , 1882.

[CHA 86] CHABOCHE J.
Time-independent constitutive theories for cyclic plasticity. *International Journal of Plasticity*, vol. 2, 1986, p. 149–188.

[CHA 88] CHAMPAUD P.
Contribution á l'étude de la fatigue d'un alliage Fe-C-Cr (100Cr6) soumis á un champ de contraintes de Hertz. Thèse de doctorat, Institut National des Sciences Appliquées de Lyon, 1988.

[CHA 97a] CHABOCHE J., JUNG O.
Application of a kinematic hardening viscoplasticity model with thresholds to the residual stress relaxation. *International Journal of Plasticity*, vol. 13, 1997, p. 785–807.

[CHA 97b] CHAMPIOT F.
Contribution á l'analyse et á la modélisation de la propagation des fissures courtes dans les aciers soumis á la fatigue de roulement. Thèse de doctorat, Institut National des Sciences Appliquées de Lyon, 1997.

[CHA 08a] CHABOCHE J.
A review of some plasticity and viscoplasticity constitutive theories. *International Journal of Plasticity*, vol. 24, 2008, p. 1642–1693.

[CHA 08b] CHAPARRO B., THUILLIER S., MENEZES L., MANACH P., FERNAN-
DES J.
Material parameters identification: Gradient-based, Genetic and Hybrid Opti-
mization Algorithms. *Computational Materials Science*, vol. 44, 2008, p. 339–
346.

[CHA 11] CHAISE T.
Mechanical simulation using a semi-analytical method: from elasto-plastic rolling
contact to multiple impacts. Thèse de doctorat, INSA Lyon, 2011.

[CHA 12] CHABOCHE J., KANOUTÉ F.
Cyclic inelastic constitutive equations and their impact on the fatigue life predic-
tions. *International Journal of Plasticity*, vol. 35, 2012, p. 44–66.

[CHE 97] CHENG W., CHENG H. S.
Semi Analytical Modelling of Crack Initiation Dominant Contact Fatigue Life for
Roller Bearings. *ASME Journal of Tribology*, vol. 119, 1997, p. 233–239.

[CHE 05] CHENG Y-T C. C.-M.
Relationships between initial unloading slope, contact depth, and mechanical
properties for spherical indentation in linear viscoelastic solids. *Mater Sci Eng A*,
, 2005.

[CHE 10a] CHEN W. W., ZHOU K., KEER L. M., WANG Q. J.
Modeling elasto-plastic indentation on layered materials using the equivalent in-
clusion method. *International Journal of Solids and Structures*, vol. 47, nᵒ 20,
2010, p. 2841–2854.

[CHE 10b] CHEN W., ZHOU K., KEER L., WANG Q.
Modeling elasto-plastic indentation on layered materials using the equivalent in-
clusion method. *International Journal of Solids and Structures*, vol. 47, nᵒ 20,
2010, p. 2841–2854.

[CHE 18] CHEONG W., GAO W., CHIU W., TAN V.
The Prediction of isothermal cyclic plasticity in 7175-T7351 aluminium alloy using
an evolving microstructure model. *International Journal of Fatigue*, vol. 108,
2018, p. 21–33.

[CHO 13] CHOUDHARY S., DUTTA B., DUTTA K.
Evaluation of stress-strain based approaches for the prediction of ratcheting in
alloy 800 under in-phase and out-of-phase cyclic loading. *International Journal
of Pressure Vessels and Piping*, vol. 108, 2013, p. 56–65.

[CHO 17] CHOUDHARY S., DUTTA B.
Constitutive modeling of cyclic hardening/softening behavior of alloy 617 based
on cyclic plasticity models. *Journal of Nuclear Materials*, vol. 495, 2017, p. 499–
509.

[CIZ 05] Cizelj L., Leskovar M.
Combined viscoplasticity, creep and damage model for prediction of structural behavior at high temperature. *Nuclear Engineering and Design*, vol. 235, 2005, p. 659–677.

[CLI 84] Clifton R., Duffy J., Hartley K., Shawki T.
On critical conditions for shear band formation at high strain rates. *Scripta Metallurgica*, vol. 18, nº 5, 1984, p. 443–448.

[CON 86] Constantinou M. C., Gazetas G.
Soil-structure interaction effects for laterally excited bridges. *Journal of Engineering Mechanics*, vol. 112, nº 5, 1986, p. 503–521.

[COU 05] Coulon S., Ville F., Lubrecht A. A.
Experimental investigations of rolling contact fatigue of dented surfaces using artificial defects. *Tribology and Interface Engineering Series*, vol. 48, 2005, p. 691–702.

[COU 17] Couqué H., Capelle J., Michel B.
A cooperative quantitative modeling approach of anisothermal cyclic plasticity and creep of high-chromium steels. *Materials Science and Engineering: A*, vol. 682, 2017, p. 632–643.

[DAO 01] Dao M., Chollacoop N., Van Vliet K. J., Venkatesh T. A., Suresh S.
Computational modelling of the forward and reverse problems in instrumented sharp indentation. *Acta Materialia*, vol. 49, 2001, p. 3899–3918.

[DAR 15] Darvizeh M., Jahed H., Abbasi M., Paknahad M.
Experimental study of multiaxial cyclic ratchetting of ASTM SA508 Gr. 4N steel. *International Journal of Pressure Vessels and Piping*, vol. 126, 2015, p. 27–38.

[DAU 21] Daud N., Abdalla A., Radzi N., Khan S.
Experimental and numerical study on the fatigue life of S275 mild steel under proportional and non-proportional loading conditions. *International Journal of Fatigue*, vol. 148, 2021, Page 106307.

[DES 20] De Sousa R., Faria A., Rosa P., Tavares S.
A combined numerical-experimental approach for the prediction of high-cycle fatigue lifetime under non-proportional loading conditions. *International Journal of Fatigue*, vol. 135, 2020, Page 105619.

[DIA 03] Diab Y., Coulon S., Ville F., Flamand L.
Experimental investigations on rolling contact fatigue of dented surfaces using artificial defects: Subsurface analyses. *Tribology Series*, vol. 41, 2003, p. 359–366.

274

[DIA 13] Diao H., Yao Z., Chen L., Wang Q., Li Y.
Uniaxial ratcheting behavior and its modeling of new cast heat-resistant steel under cyclic plastic deformation. *International Journal of Plasticity*, vol. 49, 2013, p. 62–81.

[DOE 86] Doener M. F., Nix W. D.
A method for interpreting the data from depth-sensing indentation instruments. *Journal of Materials Research*, vol. 1, 1986, p. 601–616.

[DON 19] Dong Y., Chen X., Xu Z., Wang Y., Song Y., Ma Z., Zhang Z.
High-temperature low-cycle fatigue behavior of P92 steel under non-proportional cyclic loading. *Materials*, vol. 12, n° 15, 2019, Page 2439.

[DOR 09] Dorogoy A., Rittel D.
Determination of the Johnson-Cook material parameters using the SCS specimen. *Experimental Mechanics*, vol. 49, n° 6, 2009, Page 881.

[DOW 66] Dowson D., Higginson G.
Elastohydrodynamic Lubrication: The Fundamentals of Roller and Gear Lubrication. Pergamon Press, Oxford, 1966.

[DUV 72] Duvaut G., Lions J.-L.
Les Inequations en Mecanique et en Physique, vol. 1. Dunod, Paris, 1972.

[DWY 90] Dwyer-Joyce R., Hamer J., Sayles R., Ioannides E.
Surface damage effects caused by debris in rolling bearing lubricants, with an emphasis on friable materials. *Rolling Element Bearings: Towards the 21st Century* Mechanical Engineering Publications for the I. Mech. E., 1990, p. 1–8.

[DWY 92] Dwyer-Joyce W. R. S., Hamer J. C., Sayles R. S., Ioannides E.
Lubricant Screening for Debris Effects to Improve Fatigue and Wear Life. *Tribology Series*, vol. 21, 1992, p. 57–63.

[DWY 05] Dwyer-Joyce R.
The life cycle of a debris particle. *Tribology and Interface Engineering Series*, vol. 48, 2005, p. 681–690.

[EHL 16] Ehlers S., Petrovski B., Jäger A., Körner C., Drummer D.
Cyclic deformation behavior of as-built and heat-treated IN718 processed by selective laser melting. *International Journal of Fatigue*, vol. 82, 2016, p. 214–224.

[ELM 03] Elmustafa A. A., Stone D. S.
Nanoindentation and the indentation size effect: kinetics of deformation and strain gradient plasticity. *Journal of the Mechanics and Physics of Solids*, vol. 51, 2003, p. 357–381.

[ENO 12] Enomoto Y., Kubo K., Kadoi K.
Microstructural and crystallographic effects on the ratcheting behavior of type 316 stainless steel. *International Journal of Plasticity*, vol. 30, 2012, p. 1–20.

[ERT 39] Ertel A.
Hydrodynamic lubrication based on new principles. *Akad. Nauk. SSSR, Prikladnaya Matematika i Mekhanika*, vol. 3, nᵒ 2, 1939, p. 41–52.

[ESH 59] Eshelby J. D.
The Inclusion Equivalent Method. *Proceedings of the Royal Society of London. Series A, Mathematical and Physical Sciences*, vol. 252, 1959, Page 561.

[FAN 93] Fan H., Keer L. M., Cheng W., Cheng H. S.
Competition Between Fatigue Crack Propagation and Wear. *ASME Journal of Tribology*, vol. 115, 1993, p. 141–147.

[FAR 19] Faria A., de Sousa R., Rosa P., Tavares S.
Comparison of experimental tests and numerical simulations for the fatigue behavior of welded joints under multiaxial loading. *International Journal of Fatigue*, vol. 122, 2019, p. 126–138.

[FAT 88] Fatemi A., Socie D. F.
A critical plane approach to multiaxial fatigue damage including out-of-phase loading. *Fatigue Fracture of Engineering Materials Structures*, vol. 11, nᵒ 3, 1988, p. 149–165.

[FEI 18] Fei W., Peng X., Li S.
Low-cycle fatigue behavior of 100Cr17Ni14Mo2 austenitic stainless steel under uniaxial, torsional and combined non-proportional loadings. *International Journal of Fatigue*, vol. 108, 2018, p. 25–38.

[FEI 20] Fei W., Peng X., Yang X., Li S.
Multiaxial ratcheting behavior of GH4169 superalloy under different stress states. *Materials*, vol. 13, nᵒ 7, 2020, Page 1605.

[FIE 93] Field J., M.V. S.
A simple predictive model for spherical indentation. *Journal of Materials Research*, vol. 8, 1993, p. 297-306.

[FIS 06] Fischer Cripps A. C.
Critical review of analysis and interpretation of nanoindentation test data. *Surf Coat Technol*, vol. 200:4153, 2006.

[FIS 12] Fischer F., Moosbrugger V., Ruch D.
High cycle fatigue of pearlitic ductile iron under variable amplitude loading: Experimental study and damage modeling. *International Journal of Fatigue*, vol. 39, 2012, p. 119–129.

[FRE 06] Freitas M., Barreiros J., de Jesus A.
Ratcheting of AISI 316L(N) stainless steel at room temperature under cyclic loading with a mean stress. *International Journal of Fatigue*, vol. 28, 2006, p. 682–690.

[FRI 64] Friedel J.
Dislocations, vol. 3. Pergamon Press, Oxford, 1964.

[FU 16] Fu J., Barlat F., Kim J., Pierron F.
Identification of nonlinear kinematic hardening constitutive model parameters using the virtual fields method for advanced high strength steels. *International Journal of Solids and Structures*, vol. 102–103, 2016, p. 30–43.

[FU 19] Fu Y., Peng X., Li S.
Multiaxial ratcheting fatigue behavior of AA7075-T651 aluminum alloy under different strain rate. *Materials*, vol. 12, nº 19, 2019, Page 3137.

[GAL 06a] Gallego L., Nelias D., Jacq C.
A comprehensive method to predict wear and to define the optimum geometry of fretting surfaces. *Journal of Tribology*, vol. 128, nº 3, 2006, p. 476-485.

[GAL 06b] Gallego L., Nelias D., Jacq C.
A Comprehensive Method to Predict Wear and to Define the Optimum Geometry of Fretting Surfaces. *Journal of Tribology*, vol. 128, nº 3, 2006, p. 476–485.

[GAL 07] Gallego L.
Fretting et Usure des Contacts Mecaniques: Modelisation Numerique. Thèse de doctorat, INSA Lyon, 2007.

[GAL 10] Gallego L., Nelias D., Deyber S.
A fast and efficient contact algorithm for fretting problems applied to fretting modes I, II and III. *Wear*, vol. 268, nº 1-2, 2010, p. 208–222.

[GAL 12] Gallardo-Hernandez E., Huanca-Quispe M., Casellas D., Suarez R.
Cyclic ratchetting in thermally aged cast duplex stainless steels. *International Journal of Fatigue*, vol. 37, 2012, p. 16–23.

[GAL 13] Gallardo-Hernandez E., Torres-Valle A., Casellas D., Suarez R.
High cycle fatigue behavior of cast stainless steel centrifugal pump impellers under axial/torsional loading. *International Journal of Fatigue*, vol. 47, 2013, p. 100–108.

[GAO 92] Gao H., Chui C.-H., Lee J.
NIST Special Publication 896: International Workshop on Instrumented Indentation. *International Journal of Solids and Structures*, vol. 2471, 1992, Page 29.

[GAO 20] GAO X., YANG X., XIONG X., LI Z., DENG D.
Multiaxial high cycle fatigue behavior and life prediction of 30CrNiMo8 steel under non-proportional loading. *International Journal of Fatigue*, vol. 135, 2020, Page 105599.

[GAR 20] GARCIA-CASTILLO F., PORTUONDO-ARIAS E., SÁNCHEZ-SOTO M., BERRUETA J., FLORES J.
Fatigue and ratcheting behavior of 304L stainless steel at room and elevated temperatures under uniaxial and multiaxial loadings. *International Journal of Fatigue*, vol. 133, 2020, Page 105391.

[GAR 21a] GARCÍA-PEDROZA U., HUÉTINK J., FLORES J., PORTUONDO-ARIAS E.
Multiaxial fatigue and ratcheting behavior of titanium alloy Ti-6Al-4V under in-phase and out-of-phase loading. *International Journal of Fatigue*, vol. 145, 2021, Page 106042.

[GAR 21b] GARUD Y., KATTIMANI V., NAIK N.
Multiaxial fatigue behavior and life prediction of Al 7050 alloy under various non-proportional loadings. *Engineering Failure Analysis*, vol. 129, 2021, Page 105469.

[GIA 99] GIANNAKOPOULOS A. E., SURESH S.
Determination of elastoplastic properties by instrumented sharp indentation. *Scripta Mater*, vol. 40, 1999, p. 1191-1198.

[GIA 02] GIANNAKOPOULOS A.
Indentation of plastically graded substrates by sharp indentors. *Int. J. Solids Struct.*, vol. 39, 2002, p. 2495-2515.

[GOL 19] GOLMOHAMMADI Z., SADEGHI F.
A coupled multibody finite element model for investigating effects of surface defects on rolling contact fatigue. *Journal of Tribology*, vol. 141, nᵒ 4, 2019.

[GRU 49] GRUBIN A.
Fundamentals of the hydrodynamic theory of lubrication of heavily loaded cylindrical surfaces. *Investigation of the Contact Machine Components*, vol. 2, 1949.

[GUE 10] GUENFOUD S., BOSAKOV S. V., LAEFER D. F.
A Ritz's Method Based Solution for the Contact Problem of a Deformable Rectangular Plate on an Elastic Quarter-Space. *International Journal of Solids and Structures*, vol. 47, nᵒ 14-15, 2010, p. 1822–1829.

[GUI 11] GUILBAULT R.
A Fast Correction for Elastic Quarter-Space Applied to 3D Modeling of Edge Contact Problems. *Journal of Tribology ASME*, vol. 133, nᵒ 3, 2011, Page 031402.

278

[GUO 17a] GUO L., WANG W., ZHANG Z. M., WONG P. L.
Study on the free edge effect on finite line contact elastohydrodynamic lubrication. *Tribology International*, vol. 116, 2017, p. 482–490.

[GUO 17b] GUO L., ZHANG Z. M., WANG W., WONG P. L.
An explicit matrix algorithm for solving three-dimensional elastic wedge under surface loads. *International Journal of Solids and Structures*, vol. 128, 2017, p. 231-242.

[GUO 20] GUO L., ZHANG Z. M., WANG W., ZHAO Y., WONG P. L.
An Explicit Solution to a three-dimensional wedge problem considering two edges effect. *International Journal of Solids and Structures*, vol. 8, n° 2, 2020, p. 370–383.

[HAM 76] HAMROCK B. J., DOWSON D.
Isothermal Elastohydrodynamic Lubrication of Point Contacts - Part 1: Theoretical Formulation. *Journal of Lubrication Technology*, vol. 98, n° 2, 1976, p. 223–228.

[HAM 77] HAMROCK B. J., DOWSON D.
Isothermal Elastohydrodynamic Lubrication of Point Contacts - Part III: Fully Flooded Results. *Journal of Lubrication Technology*, vol. 99, n° 2, 1977, p. 264–275.

[HAM 87] HAMER J., SAYLES R., IOANNIDES E.
Deformation mechanisms and stresses created by 3rd body debris contacts and their effects on rolling bearing fatigue. *Tribology Series*, vol. 12, p. 201–208 1987.

[HAM 89] HAMER J., SAYLES R., IOANNIDES E.
Particle deformation and counterface damage when relatively soft particles are squashed between hard anvils. *Tribology Transactions*, vol. 32, n° 3, 1989, p. 281–288.

[HAN 89] HANSON M. T., KEER L. M.
Stress Analysis and Contact Problems for an Elastic Quarter Space. *Quarterly Journal of Mechanics and Applied Mathematics*, vol. 42, n° 3, 1989, p. 363–381.

[HAN 90] HANSON M. T., KEER L. M.
A Simplified Analysis for an Elastic Quarter-Space. *Quarterly Journal of Mechanics and Applied Mathematics*, vol. 43, n° 4, 1990, p. 561–587.

[HAN 91] HANSON M. T., KEER L. M.
An Analysis for an Elastic Quarter-Space. *Wear*, vol. 144, n° 1, 1991, p. 39–48.

[HAR 79] Hartnett M. J.
The analysis of contact stresses in rolling element bearings. *Journal of Lubrication Technology*, vol. 101(1), 1979, p. 105-109.

[HAR 80] Hartnett M. J., Cheng H. S., Keer L. M.
A General Numerical Solution for Elastic Body Contact Problems. *Solid Contact and Lubrication, ASME*, vol. 39, 1980, p. 51–66.

[HAY 00] Hay JL. P. P.
Instrumented indentation testing. vol.8. Materials Park, OH: ASM International;. *ASM Handbook*, vol. vol.8., 2000, p. p. 232-43.

[HEL 06] He LH. Fujisawa N. S. M.
Elastic modulus and stress-strain response of human enamel by nanoindentation. *Biomaterials*, vol. 27:4388, 2006.

[HEN 95] Hendrix B.
The use of shape correction factors for elastic indentation measurements. *J. Mater. Res.*, vol. 10, 1995, p. 255-257.

[HER 82] Hertz H.
Ueber die Beruhrung fester elastischer Korper. *Journal fur die reine und angewandte Mathematik*, , 1882, p. 156–171.

[HER 14] Herrera-Solaz V., LLorca J., Dogan E., Karaman I., Segurado J.
An inverse optimization strategy to determine single crystal mechanical behavior from polycrystal tests: application to AZ31 Mg alloy. *International Journal of Plasticity*, vol. 57, 2014, p. 1–15.

[HER 15] Herrera-Solaz V., Segurado J., LLorca J.
On the robustness of an inverse optimization approach based on the Levenberg–Marquardt method for the mechanical behavior of polycrystals. *European Journal of Mechanics*, vol. 53A, 2015, p. 220–228.

[HES 80] Hestenes M.
Conjugate Direction Methods in Optimization. Springer, New York, NY, 1980.

[HET 60] Hetenyi M.
A Method of Solution for the Elastic Quarter-Plane. *Journal of Applied Mechanics*, vol. 223, 1960, p. 289–296.

[HET 70] Hetenyi M.
A General Solution for the Elastic Quarter Space. *Journal of Applied Mechanics*, vol. 37, n° 1, 1970, p. 70–76.

[JAC 01] Jacq C.
Limite d'endurance et durée de vie en fatigue de roulement du 32CrMoV13 nitruré en présence d'indentations. Thèse de doctorat, INSA de Lyon, 2001.

[JAC 02] Jacq C., Nélias D., Lormand G., Girodin D.
Development of a three-dimensional semi-analytical elastic-plastic contact code. *Journal of Tribology*, vol. 124, nº 4, 2002, p. 653–667.

[JAC 03] Jacq C., Nelias D., Lormand G., Dudragne G.
Rolling contact fatigue of nitrided 32CrMoV13 steel. *Tribology and Interface Engineering Series*, vol. 41, nº 41, 2003, p. 299–308.

[JEG 12] Jegou S., Barrallier L.
Determination of residual stresses within submicroscopic and coherent precipitates. *Materials Science and Engineering: A*, vol. 543, 2012, p. 109–116.

[JL. 95] J-L. Loubet B. L., Oliver W.
NIST Special Publication 896: International Workshop on Instrumented Indentation. *National Institute of Standards and Technology, San Diego, CA*, , 1995, p. 31-34.

[JLL 86] JL Loubet JM Georges G. M. P. B. B. L.
Microindentation techniques in materials science and engineering. *ASTM STP*, vol. 43, 1986, Page 106.

[JOH 83] Johnson G. R.
A constitutive model and data for materials subjected to large strains, high strain rates, and high temperatures. *Proceedings of the 7th International Symposium on Ballistics*, 1983, p. 541–547.

[JOH 85] Johnson K. L.
Contact Mechanics. Cambridge University Press, Cambridge [Cambridgeshire] New York, 1985.

[JU 96] Ju Y. Q., Farris T. N.
Spectral analysis of two-dimensional contact problems. *Journal of Tribology*, vol. 118, 1996, p. 320–328.

[JUE 22] Juettner M., Bartz M., Tremmel S., Correns M., Wartzack S.
Edge Pressures Obtained Using FEM and Half-Space: A Study of Truncated Contact Ellipses. *Lubricants*, vol. 10, 2022, Page 107.

[KAL 67] Kalker J.
On the rolling contact of two elastic bodies in the presence of dry friction. Thèse de doctorat, Delft University, 1967.

[KAL 90a] KALKER J. J.
Three Dimensional Elastic Bodies in Rolling Contact. Kluwer Academic Publishers, Dordrecht, 1990.

[KAL 90b] KALKER J.
Three-Dimensional Elastic Bodies in Rolling Contact, vol. 2 of *Solid Mechanics and Its Applications.* Springer Netherlands, Dordrecht, 1990.

[KAN 74] KANNEL J. W.
Comparison between predicted and measured axial pressure distribution between cylinders. *Journal of Lubrication Technology*, vol. 96(3), 1974, p. 508-514.

[KAN 04] KANG Y. S., SADEGHI F., HOEPRICH M. R.
A finite element model for spherical debris denting in heavily loaded contacts. *Journal of Tribology*, vol. 126, nº 1, 2004, p. 71–80.

[KAR 87] KARAMI G., FENNER R.
A Two-Dimensional BEM Method for Thermo-Elastic Body Forces Contact Problems. *Proc. Boundary Elements IX, Southampton (1987)*, vol. 417 Computational Mechanics Publications, 1987, p. 417–437.

[KEE 83a] KEER L. M., BRYANT M. D.
A Pitting Model of Contact Fatigue. *ASME Journal of Lubrication Technology*, vol. 105, nº 2, 1983, p. 198–205.

[KEE 83b] KEER L. M., LEE J. C., MURA T.
Hetenyi's Elastic Quarter Space Problem Revisited. *International Journal of Solids and Structures*, vol. 19, nº 6, 1983, p. 497–508.

[KEE 84] KEER L. M., LEE J. C., MURA T.
A contact problem for the elastic quarter space. *International Journal of Solids and Structures*, vol. 20, nº 5, 1984, p. 513–524.

[KLE 93] KLEIBER M.
Parameter sensitivity of elastic-plastic response. *2nd US National Congress on Computational Mechanics*, 1993.

[KLO 06] KLOTZER D., ULLNER C., TYULYUKOVSKIY E., HUBER N.
Identification of visco-plastic material parameters from spherical indentation data: Part II. Experimental validation of the method. *Journal of Materials Research*, vol. 21, nº 3, 2006, p. 677–684.

[KO 89] KO C., IOANNIDES E.
Debris denting - The associated residual stresses and their effect on the fatigue life of rolling bearing: An FEM analysis. *Tribology Series*, vol. 14, p. 199–207 1989.

[KOU 14] Koumi K. E., Nelias D., Chaise T., Duval A.
Modeling of the contact between a rigid indenter and a heterogeneous viscoelastic material. *Mechanics of Materials*, vol. 77, 2014, p. 28–42.

[KOU 15a] Koumi K. E.
Modélisation du contact entre matériaux hétérogénes: Application au contact Aube/Disque. Thèse de doctorat, INSA de Lyon, 2015.

[KOU 15b] Koumi K. E., Chaise T., Nélias D.
Rolling contact of a rigid sphere/sliding of a spherical indenter upon a viscoelastic half-space containing an ellipsoidal inhomogeneity. *Journal of the Mechanics and Physics of Solids*, vol. 80, 2015, p. 1–25.

[KUO 97] Kuo C. H., Keer L. M., Bujold M. P.
Effects of Multiple Cracking on Crack Growth and Coalescence in Contact Fatigue. *ASME Journal of Tribology*, vol. 119, 1997, p. 385–390.

[LAC 00] de Lacerda L., Wrobel L.
Frictional Contact Analysis of Coated Axisymmetric Bodies Using the Boundary Element Method. *The Journal of Strain Analysis for Engineering Design*, vol. 35, nᵒ 5, 2000, p. 423–440.

[LAM 96] Lamagnere P.
Etude et modélisation de l'amorcage de fissures de fatigue de roulement au voisinage des microhétérogénéités dans l'acier M50 (80MoCrV4). Thèse de doctorat, Institut National des Sciences Appliquées de Lyon, 1996.

[LEE 86] Lee J. K., Keer L. M.
Study of a Three-Dimensional Crack Terminating at an Interface. *ASME Journal of Applied Mechanics*, vol. 108, 1986, p. 316–331.

[LEE 97] Lee J. K., Mal A. K.
A Volume Integral Equation Technique for Multiple Inclusion and Crack Interaction Problems. *ASME Journal of Applied Mechanics*, vol. 119, 1997, p. 23–31.

[LEE 04] Lee J., Lee J.
Proceedings of the Numiform'04 on Materials Processing and Design: Modelling, Simulation and Applications. *AIP Conference Proceedings*, , 2004, Page 1645, American Institute of Physics.

[LEG 04] Leggoe J.
Determination of the elastic modulus of microscale ceramic particles via nanoindentation. *J Mater Res*, , 2004, Page 19:2437.

[LEM 90] Lemaitre J., Chaboche J.-L.
Mechanics of Solid Materials. Cambridge University Press, 1990.

[LIN 86] LIN M., FINE M., MURA T.
Fatigue crack initiation on slip bands: theory and experiment. *Acta Metallurgica*, vol. 34, n⁰ 4, 1986, p. 619–628.

[LIU 00] LIU S., WANG Q., LIU G.
A versatile method of discrete convolution and FFT (DC-FFT) for contact analyses. *Wear*, vol. 243, n⁰ 1, 2000, p. 101–111.

[LIU 02] LIU S. B., WANG Q.
Studying Contact Stress Fields Caused by Surface Tractions With a Discrete Convolution and Fast Fourier Transform Algorithm. *Journal of Tribology*, vol. 124, n⁰ 1, 2002, p. 36–45.

[LOV 29] LOVE A. E. H.
The Stress Produced in a Semi-Infinite Solid by Pressure on Part of the Boundary. *Philosophical Transactions of the Royal Society of London*, , 1929, p. 377–420.

[LUB 86] LUBRECHT A. A., TEN NAPEL W. E., BOSMA R.
Multigrid, an alternative method for calculating film thickness and pressure profiles in elastohydrodynamically lubricated line contacts. *Journal of Tribology*, vol. 108, n⁰ 4, 1986, p. 551–556.

[LUN 47] LUNDBERG G., PALMGREN A.
Dynamic Capacity of Rolling Bearings. *Acta Polytehnica–Mechanical Engineering Series*, vol. 1, n⁰ 3, 1947, p. 1–50.

[Mat 02] MATHWORKS INC.
User's Guide and Optimization Toolbox, Release 6.13. The MathWorks Inc., Natick, MA, version 6.13 edition, 2002.

[MEN 16] MENG L., BREITKOPF P., LE QUILLIEC G.
Identification of material parameters using indentation test-study of the intrinsic dimensionality of P-h curves and residual imprints. *MATEC Web of Conferences*, vol. 80, 2016, Page 10012.

[MER 22] MERAY F., CHAISE T., GRAVOUIL A., DEPOUHON P., B. D., NÉLIAS D.
A Novel SAM/X-FEM Coupling Approach for the Simulation of 3D Fatigue Crack growth under Rolling Contact Loading. *Finite Elements in Analysis and Design*, vol. 206, 2022, Page 103752.

[MOH 16] MOHAMMADPOUR A., CHAKHERLOU T.
Numerical and experimental study of an interference fitted joint using a large deformation Chaboche type combined isotropic–kinematic hardening law and mortar contact method. *International Journal of Mechanical Sciences*, vol. 106, 2016, p. 297–318.

284

[MOR 11a] MORALES-ESPEJEL G. E., BRIZMER V.
Micropitting Modelling in Rolling-Sliding Contacts: Application to Rolling Bearings. *Tribology Transactions*, vol. 54, nº 4, 2011, p. 625–643.

[MOR 11b] MORALES-ESPEJEL G. E., GABELLI A.
The behavior of indentation marks in rolling-sliding elastohydrodynamically lubricated contacts. *Tribology Transactions*, vol. 54, nº 4, 2011, p. 589–606.

[MOR 15a] MORALES-ESPEJEL G. E., GABELLI A.
The progression of surface rolling contact fatigue damage of rolling bearings with artificial dents. *Tribology Transactions*, vol. 58, nº 3, 2015, p. 418–431.

[MOR 15b] MORALES-ESPEJEL G. E., GABELLI A., DE VRIES A. J. C.
A Model for Rolling Bearing Life with Surface and Subsurface Survival-Tribological Effects. *Tribology Transactions*, vol. 58, nº 5, 2015, p. 894–906.

[MOR 16] MORALES-ESPEJEL G. E., GABELLI A.
A model for rolling bearing life with surface and subsurface survival: sporadic surface damage from deterministic indentations. *Tribology International*, vol. 96, 2016, p. 279–288.

[MOY 11] MOY C., BOCCIARELLI M., RINGER S., RANZI G.
Identification of the material properties of Al 2024 alloy by means of inverse analysis and indentation tests. *Materials Science and Engineering: A*, vol. 529, 2011, p. 119–130.

[MUR 85] MURAKAMI Y., KANETA M., YATSUZUKA H.
Analysis of Surface Crack Propagation in Lubricated Rolling Contact. *ASLE Transactions*, vol. 28, nº 1, 1985, p. 60–68.

[MUR 94] MURAKAMI Y., ENDO M. D.
Effects of Defects, Inclusions and Inhomogeneities on Fatigue Strength. *International Journal of Fatigue*, vol. 16, 1994, p. 163–182.

[NAJ 14] NAJJARI M., GUILBAULT R.
Modeling the Edge Contact Effect of Finite Contact Lines on Subsurface Stresses. *Tribology International*, vol. 77, 2014, p. 78-85.

[NAK 00] NAKAMURA T., WANG T., SAMPATH S.
Determination of properties of graded materials by inverse analysis and instrumented indentation. *Acta Materialia*, vol. 48, nº 17, 2000, p. 4293–4306.

[NAK 07] NAKAMURA T., GU Y.
Identification of elastic-plastic anisotropic parameters using instrumented indentation and inverse analysis. *Mechanics of Materials*, vol. 39, nº 4, 2007, p. 340–356.

[NAT 21] NATH A., BARAI S., RAY K.
Studies on the experimental and simulated cyclic-plastic response of structural mild steels. *Journal of Constructional Steel Research*, vol. 182, 2021, Page 106652.

[NEL 65] NELDER J., MEAD R.
A simplex method for function minimization. *The Computer Journal*, vol. 7, n° 4, 1965, p. 308–313.

[NEL 99] NELIAS D.
Contribution à l'étude des roulements. Modélisation globale des roulements et avaries superficielles dans les contacts EHD pour des surfaces réelles ou indentées. Thèse de doctorat, INSA de Lyon, 1999.

[NEL 00] NELIAS D., VILLE F.
Detrimental effects of debris dents on rolling contact fatigue. *Journal of Tribology*, vol. 122, n° 1, 2000, p. 55–64.

[NEL 05] NELIAS D., JACQ C., LORMAND G., DUDRAGNE G., VINCENT A.
New methodology to evaluate the rolling contact fatigue performance of bearing steels with surface dents: application to 32CrMoV13 (nitrided) and M50 steels. *Journal of Tribology*, vol. 127, n° 3, 2005, p. 611–622.

[NEL 07] NELIAS D., ANTALUCA E., BOUCLY V., CRETU S.
A Three-Dimensional Semianalytical Model for Elastic-Plastic Sliding Contacts. *Journal of Tribology*, vol. 129, n° 4, 2007, p. 761–771.

[NIK 12] NIKAS G. K.
An experimentally validated numerical model of indentation and abrasion by debris particles in machine-element contacts considering micro-hardness effects. *Proceedings of the Institution of Mechanical Engineers, Part J: Journal of Engineering Tribology*, vol. 226, n° 5, 2012, p. 406–438.

[NIK 13] NIKAS G. K.
Debris particle indentation and abrasion of machine-element contacts: An experimentally validated, thermoelastoplastic numerical model with micro-hardness and frictional heating effects. *Proceedings of the Institution of Mechanical Engineers, Part J: Journal of Engineering Tribology*, vol. 227, n° 6, 2013, p. 579–617.

[NIK 14] NIKAS G. K.
Strain-rate effects on the plastic indentation and abrasion of elastohydrodynamic contacts by debris particles. *Proceedings of the Institution of Mechanical Engineers, Part J: Journal of Engineering Tribology*, vol. 228, n° 1, 2014, p. 22–45.

[NIK 16] NIKAS G. K.
Algebraic equations for the pile-up geometry in debris particle indentation of rolling elastohydrodynamic contacts. *ASME Journal of Tribology*, vol. 138, n° 2, 2016, Page 0215003, American Society of Mechanical Engineers.

286

[NIX 98] Nix W.D. G. H.
Indentation size effects in crystalline materials: a law for strain gradient plasticity. *J. Mech. Phys. Solids*, vol. 46, 1998, p. 411−425.

[NOC 06] Nocedal J., Wright S.
Numerical Optimization. Springer, New York, 2006.

[ODE 84] Oden J. T., Martins J. A. C.
Models and computational methods for dynamic friction phenomena. *Computer Methods in Applied Mechanics and Engineering*, vol. 52, 1984, p. 527–634.

[ODE 86] Oden J. T., Lin T. L.
On the general rolling contact problem for finite deformations of a viscoelastic cylinder. *Computer Methods in Applied Mechanics and Engineering*, vol. 57, 1986, p. 297–367.

[OLI 92] Oliver WC. P. P.
An improved technique for determining hardness and elastic modulus using load and displacement sensing indentation experiments. *Philosophical Transactions of the Royal Society of London*, , 1992, Page 7:1564.

[OLI 04] Oliver W. C., Pharr G. M.
Measurement of hardness and elastic modulus by instrumented indentation: Advances in understanding and refinements to methodology. *J. Mater. Res.*, vol. 19, n° 1, 2004, Page 19.

[O'S 88] O'Sullivan T. C., King R. B.
Sliding contact stress field due to a spherical indenter on a layered elastic halfspace. *Journal of Tribology*, vol. 110, n° 2, 1988, p. 235–240.

[PAR 85] Paris F., Garrido J. A.
On the Use of Discontinuous Elements in 2D Contact Problems. *Boundary Elements VII* Computational Mechanics Publications, 1985.

[PAU 81] Paul B., Hashemi J.
Contact Pressure on Closely Conforming Elastic Bodies. *Journal of Applied Mechanics*, vol. 48, n° 3, 1981, p. 543–548.

[PHA 02] Pharr G., Bolshakov A.
NIST Special Publication 896: International Workshop on Instrumented Indentation. *J. Mater. Res*, vol. 2660, 2002, Page 17.

[PIO 00] Piot D.
Prévision de la distribution des durées de vie en fatigue de roulement á partir des caractéristiques mécaniques et inclusionnaires de l'acier. Thèse de doctorat, Institut National des Sciences Appliquées de Lyon, 2000.

[POL 99] POLONSKY I. A., KEER L. M.
A numerical method for solving rough contact problems based on the multi-level multi-summation and conjugate gradient techniques. *Wear*, vol. 231, nº 2, 1999, p. 206–219.

[PRA 09] PRADHAN SK. NAYAK BB. S. S. M. B.
Mechanical properties of graphite flakes and spherulites measured by nanoindentation. *Carbon*, , 2009, p. 47-2290.

[RAM 08] RAMESH A., MELKOTE S. N.
Modeling of white layer formation under thermally dominant conditions in orthogonal machining of hardened AISI 52100 steel. *International Journal of Machine Tools and Manufacture*, vol. 48, nº 3-4, 2008, p. 402–414.

[ROB 16] ROBITAILLE C.
Etude de la fatigue des roulements hybrides en conditions de fonctionnement aggravées. Thèse de doctorat, INSA Lyon, 2016.

[ROC 94] ROCHER S.
Contribution á l'analyse et la modélisation de la propagation des fissures courtes dans l'acier 100Cr6 soumis á la fatigue de roulement. Thèse de doctorat, Institut National des Sciences Appliquées de Lyon, 1994.

[SAN 93] SANCHETTE-GOSSET L.
Contribution á l'analyse et á la modélisation de l'amorcage des fissures dans l'acier 100Cr6 soumis à la fatigue de roulement. Thèse de doctorat, Institut National des Sciences Appliquées de Lyon, 1993.

[SHE 35] SHEPHERD W. M.
Stress systems in an infinite sector. *Proceedings of the Royal Society*, vol. A 148, nº 864, 1935, p. 284–303.

[SHR 12] SHROT A., BAKER M.
Determination of Johnson-Cook parameters from machining simulations. *Computational Materials Science*, vol. 52, nº 1, 2012, p. 298–304.

[SIM 92] SIMO J., MIEHE C.
Associative coupled thermoplasticity at finite strains: Formulation, numerical analysis and implementation. *Computer Methods in Applied Mechanics and Engineering*, vol. 98, nº 1, 1992, p. 41–104.

[SMI 70] SMITH K. N., WATSON P., TOPPER T. H.
A stress-strain function for the fatigue of metals. *Journal of Materials*, vol. 5, 1970, p. 767–778.

[SMI 19] SMITH M.
ABAQUS/Standard User's Manual, Version 6.9. 2019.

[SNE 65] Sneddon I.
The relation between load and penetration in the axisymmetric Boussinesq problem for a punch of arbitrary profile. *Int. J. Eng Sci.*, vol. 3:47, 1965.

[SNE 71] Sneddon I. N.
Fourier Transform Solution of the Quarter Plane Problem in Elasticity. *Applied Mathematics Research Group, North Carolina State University*, vol. File PSR-99/6, 1971, p. 497–508.

[SON 14] Song Z., Komvopoulos K.
An elastic–plastic analysis of spherical indentation: Constitutive equations for single-indentation unloading and development of plasticity due to repeated indentation. *Mechanics of Materials*, vol. 76, 2014, p. 93–101.

[S.P 09] S. Pathak J. Shaffer S. K.
Elastic-Plastic Rolling-Sliding Contact on a Quarter Space. *Scr. Mater*, vol. 60, 2009, p. 439-442.

[STI 09] Stienon A.
Contribution à la modélisation de la durée de vie des roulements à partir des caractéristiques inclusionnaires des aciers: concentration, morphologie, propriétés mécaniques. Thèse de doctorat, Institut National des Sciences Appliquées de Lyon, 2009.

[STR 16] Strubel V., Fillot N., Ville F., Cavoret J., Vergne P., Mondelin A., Maheo Y.
Particle entrapment in hybrid lubricated point contacts. *Tribology Transactions*, vol. 59, nᵒ 4, 2016, p. 768–779.

[STR 17] Strubel V., Fillot N., Ville F., Cavoret J., Vergne P., Mondelin A., Maheo Y.
Particle Entrapment in Rolling Element Bearings: The Effect of Ellipticity, Nature of Materials, and Sliding. *Tribology Transactions*, vol. 60, nᵒ 2, 2017, p. 373–382.

[SU 06] Su J.-C.
Residual stress modeling in machining processes. Thèse de doctorat, Georgia Institute of Technology, 2006.

[TAB 51] Tabor D.
The Hardness of Metals. *Oxford University Press*, , 1951.

[TAF 13] Taflanidis J. L. B. . A. A.
Prior and posterior robust stochastic predictions for dynamical systems using probability logic. *International Journal for Uncertainty Quantification,vol. 3 no. 4*, vol. 23, 46, 2013, p. 271-288.

[TAN 81] Tanaka K., Mura T.
A dislocation model for fatigue crack initiation. *Journal of Applied Mechanics*, vol. 48, 1981, p. 97–103.

[TAY 34] Taylor G. I., Quinney H.
The latent energy remaining in a metal after cold working. *Proceedings of the Royal Society of London. Series A, Containing Papers of a Mathematical and Physical Character*, vol. 143, nº 849, 1934, p. 307–326.

[TER 88] Terzopoulos D., Fleiseher K.
Modeling Inelastic Deformation: Viscoelasticity, Plasticity, Fracture. *Computer Graphics*, vol. 22, nº 44, 1988, p. 269–278.

[TON 12a] Tonicello E.
Etude et modélisation de la fatigue de contact en présence d'indentation dans le cas de roulements tout acier et hybrides. Thèse de doctorat, INSA de Lyon, 2012.

[TON 12b] Tonicello E., Girodin D., Sidoroff C., Fazekas A., Perez M.
Rolling bearing applications: some trends in materials and heat treatments. *Materials Science and Technology*, vol. 28, nº 1, 2012, p. 23–26.

[TRA 48] Tranter C. J.
The Normal Indentation of an Elastic Half-space by a Rigid Sphere. *Journal of Applied Mechanics*, vol. 1, 1948, p. 125–130.

[VAN 84] Van K. D., Le Douaron A., Lieurade H.
Multiaxial fatigue limit: a new approach. *Fracture 84*, , 1984, p. 1879–1885.

[VAN 89] Van K. D., Griveau B., Message O.
On a new multiaxial fatigue limit criterion: theory and application. *Biaxial and Multiaxial Fatigue*, , 1989, p. 479–496.

[VAN 03] VanLandingham. M.
Review of instrumented indentation. *International Journal of Solids and Structures*, vol. 108, 2003, Page 249.

[VER 85] Vergne F.
Calcul des déplacements et des contraintes dans un demi-espace élastique chargé en surface par des actions distribuées normales ou tangentielles quelconques. *Master's thesis,INSA Lyon*, , 1985.

[VIE 16] Vieillard C., Kadin Y., Morales-Espejel G. E., Gabelli A.
An experimental and theoretical study of surface rolling contact fatigue damage progression in hybrid bearings with artificial dents. *Wear*, vol. 364, 2016, p. 211–223.

290

[VIL 98a] VILLE F.
Pollution solide des lubrifiants, indentation et fatigue des surfaces. Thèse de doctorat, INSA de Lyon, 1998.

[VIL 98b] VILLE F., NELIAS D.
Influence of the nature and size of solid particles on the indentation features in EHL contacts. *Tribology Series*, vol. 34, 1998, p. 399–409.

[VIL 99a] VILLE F., NELIAS D.
Early fatigue failure due to dents in EHL contacts. *Tribology Transactions*, vol. 42, n° 4, 1999, p. 795–800.

[VIL 99b] VILLE F., NELIAS D.
An Experimental Study on the Concentration and Shape of Dents Caused by Spherical Metallic Particles in EHL Contacts. *Tribology Transactions*, vol. 42, n° 1, 1999, p. 231–240.

[WAL 20] WALLACE E. R., CHAISE T., NELIAS D.
Three-dimensional rolling/sliding contact on a viscoelastic layered half-space. *Journal of the Mechanics and Physics of Solids*, vol. 143, 2020, Page 104067.

[WAN 88] WAN G. T. Y., SPIKES H. A.
The Behavior of Suspended Solid Particles in Rolling and Sliding Elastohydrodynamic Contacts. *Tribology Transactions*, vol. 31, n° 1, 1988, p. 12–21.

[WAN 97] WAN G. T. Y., GABELLI A., IOANNIDES E.
Increased performance of hybrid bearings with silicon nitride balls. *STLE Tribol. Trans.*, vol. 40, 1997, p. 701–707.

[WAN 07] WANG W., WONG P. L., HE F., WAN G. T. Y.
Experimental study of the smoothing effect of a ceramic rolling element on a bearing raceway in contaminated lubrication. *Springer Tribol. Lett.*, vol. 28, 2007, p. 89–97.

[WAN 12] WANG Z. J., JIN X. Q., WANG Q., KEER L. M.
Numerical Methods for Contact Between Two Joined Quarter Spaces and a Rigid Sphere. *International Journal of Solids and Structures*, vol. 49, n° 18, 2012, p. 2515–2527.

[WAN 17] WANG W., GUO L., WONG P. L., ZHANG Z. M.
Surface normal deformation in elastic quarter-space. *International Journal of Solids and Structures*, vol. 114, 2017, p. 358-364.

[WAR 10] WARHADPANDE A., SADEGHI F.
Effects of surface defects on rolling contact fatigue of heavily loaded lubricated contacts. *Proceedings of the Institution of Mechanical Engineers, Part J: Journal of Engineering Tribology*, vol. 224, n° 10, 2010, p. 1061–1077.

[WAY 11] WAYNE CHEN W., JANE WANG Q., HUAN Z., LUO X.
Semi-Analytical Viscoelastic Contact Modeling of Polymer-Based Materials. *Journal of Tribology*, vol. 133, n⁰ 4, 2011, Page 041404.

[WEI 49] WEIBULL W.
A statistical representation of fatigue failures in solids. *Acta Polytechnica, Mech. Eng. Serie*, vol. 1, n⁰ 9, 1949.

[WRO 02] WROBEL L., ALIABADI M., Eds. *The boundary element method.* J. Wiley, Chichester ; New York, 2002.

[XIE 15] XIE J., NELIAS D., WALTER-LE BERRE H., OGAWA K., ICHIKAWA Y.
Simulation of the cold spray particle deposition process. *Journal of Tribology*, vol. 137, n⁰ 4, 2015, Page 041101.

[XU 97] XU G., SADEGHI F., COGDELL J. D.
Debris Denting Effects on Elastohydrodynamic Lubricated Contacts. *Journal of Tribology*, vol. 119, n⁰ 3, 1997, p. 579–587.

[XU 98] XU G., SADEGHI F., HOEPRICH M. R.
Dent Initiated Spall Formation in EHL Rolling/Sliding Contact. *Journal of Tribology*, vol. 120, n⁰ 3, 1998, p. 453–462.

[XU 20] XU J., WANG K., LIANG X., GAO Y., LIU Z., CHEN R., WANG P., XU F., WEI K.
Influence of viscoelastic mechanical properties of rail pads on wheel and corrugated rail rolling contact at high speeds. *Tribology International*, vol. 151, 2020, Page 106523.

[YAN 48] YAN W. SUN Q. F. X.-Q. Q. L.
Determination of transformation stresses of shape memory alloy thin films: a method based on spherical indentation. *Appl Phys Lett*, , 1948.

[YAN 06] YAN W. SUN Q. L. H.-Y.
Spherical indentation hardness of shape memory alloys. *Mater Sci Eng A*, vol. 425:278, 2006, p. 357-373.

[YAN 10] YAN W. P. C.
Spherical indentation of metallic foams. *Mater Sci Eng A*, vol. 527:3166, 2010, Page 70â€"76.

[YAN 11] YAN W. PUN CL. W. Z.-S. G.
Some issues on nanoindentation method to measure the elastic modulus of particles in composites. *Compos: Part B-Eng*, , 2011, Page 42:2093.

[ZAN 72] Zantopulos H.
Comparison between predicted and measured axial pressure distribution between cylinders. *Journal of Lubrication Technology*, vol. 94(2), 1972, p. 181-186.

[ZHA 13] Zhang Z. M., Wang W., Wong P. L.
An Explicit Solution for the Elastic Quarter-Space Problem in Matrix Formulation. *International Journal of Solids and Structures*, vol. 50, nᵒ 6, 2013, p. 976–980.

[ZHA 14] Zhang S. G., Wang W. Z., Zhao Z. Q.
The Effect of Surface Roughness Characteristics on the Elastic-Plastic Contact Performance. *Tribology International*, vol. 79, 2014, p. 59–73.

[ZHA 16] Zhang H. B., Wang W. Z., Zhang S. G., Zhao Z. Q.
Modeling of Finite-Lenght Line Contact Problem With Consideration of Two Free-End Surfaces. *Journal of Tribology*, vol. 138, nᵒ 2, 2016, Page 021402.

[ZHA 17] Zhang H. B., Wang W. Z., Zhang S. G., Zhao Z. Q.
Elastohydrodynamic lubrication analysis of finite line contact problem with consideration of two free end surfaces. *Journal of Tribology*, vol. 139(3), 2017, Page 031501.

[ZHO 89] Zhou R. S., Cheng H. S., Mura T.
Micropitting in Rolling and Sliding Contact Under Mixed Lubrication. *ASME Journal of Tribology*, vol. 111, 1989, p. 605–613.

[ZHO 96] Zhou M., Ravichandran G., Rosakis A.
Dynamically propagating shear bands in impact-loaded prenotched platesâ€"II. Numerical simulations. *Journal of the Mechanics and Physics of Solids*, vol. 44, nᵒ 6, 1996, p. 1007–1032.

[ZHU 01] Zhu D., Hu Y.-Z.
A computer program package for the prediction of EHL and mixed lubrication characteristics, friction, subsurface stresses and flash temperatures based on measured 3-D surface roughness. *Tribology Transactions*, vol. 44, nᵒ 3, 2001, p. 383–390.

FOLIO ADMINISTRATIF

THESE DE L'INSA LYON, MEMBRE DE L'UNIVERSITE DE LYON

NOM : AHYEE   DATE de SOUTENANCE : 26 Janvier 2024

Prénoms : Amakoe Komlanvi

TITRE : Etude expérimentale et numérique de l'impact de la microstructure sur l'endommagement des roulements de lignes d'arbres moteurs sous indentation

NATURE : Doctorat   Numéro d'ordre : 2024ISAL0012

Ecole doctorale : MEGA

Spécialité : Mécanique- Génie Mécanique- Génie civil

RESUME :

La fatigue de surface est la principale cause de défaillances des roulements. Elle résulte de la rugosité et des défauts de surface comme les indents. La gestion de la pollution des lubrifiants, qui provoque ces indents, est coûteuse et difficile à réaliser dans certaines conditions. Les particules drainées par les huiles sont entraînées dans les contacts et écrasent les surfaces en créant des indents et des défauts propices à la fatigue. Comprendre les mécanismes d'indentation et de fatigue liée aux indents est essentiel pour garantir la fiabilité des roulements et réduire les coûts de maintenance.
   Dans le cadre de cette thèse, une caractérisation des matériaux des roulements (M50, 32CrMo13, M50NiL, M50NiLDH) a permis d'identifier le gradient de micro-dureté ainsi que les lois de comportement et leur évolution. Des modèles semi-analytiques prenant en compte les effets des bords ont été élaborés, mettant en évidence que les bords libres induisent une augmentation de l'amplitude de la pression de contact de Hertz ainsi qu'un décalage de cette dernière. L'utilisation des solutions de Hertz pour résoudre le contact peut entraîner des erreurs pouvant atteindre jusqu'à 20 % de la pression maximale de Hertz dans le cas d'un massif de dimension finie. Les effets de bords disparaissent et peuvent être négligés à partir d'une distance d/a≥4. Pour simuler l'indentation sur les pistes de roulement, un modèle par éléments finis de type « couplé Euler-Lagrange » a été adapté afin de reproduire le processus d'indentation réel des roulements et d'en étudier les effets. Une étude paramétrique exhaustive du processus d'indentation a été menée, révélant ainsi que la taille, la nature, la forme et la position de la particule, les matériaux des roulements, la présence de glissement et son taux critique, ainsi que les contraintes résiduelles ont une influence significative sur la formation du bourrelet. L'étude de la fatigue de surface a impliqué l'utilisation de critères d'endommagement et de fatigue afin de localiser les sites d'amorçage des fissures et de déterminer la hauteur de bourrelet critique.

MOTS-CLÉS : Nanoindentation, Effet de bords, Roulement, Ecrouissage, Contraintes résiduelles, Fatigue, Limite d'endurance, CEL, Méthode semi-analytique, Contact roulant, Analytique

Laboratoire (s) de recherche : Laboratoire de Mécanique des Contacts et des Structures, UMR CNRS 5259 - INSA de Lyon   18-20 rue des Sciences
                 69621 Villeurbanne Cedex FRANCE

Directeur de thèse : Daniel NELIAS

Présidente de jury :   Caroline   RICHARD

Composition du jury : Daniel   NELIAS
                 Thibaut   CHAISE
                 Caroline   RICHARD
                 Frederic   LEBON
                 Djimédo   KONDO